40Ar/39Ar Dating of the Late Cretaceous

Jonathan Gaylor

Université Paris Sud 11

UFR des Sciences d'Orsay

École Doctorale 534 MIPEGE, Laboratoire IDES

Sciences de la Terre

$^{40}Ar/^{39}Ar$ Dating of the Late Cretaceous

Thèse de Doctorat

Présentée et soutenue publiquement par

Jonathan GAYLOR

Le 11 juillet 2013 devant le jury compose de:

Directeur de thèse:	Xavier Quidelleur, Professeur, Université Paris Sud (France)
Rapporteurs:	Sarah Sherlock, Senoir Researcher, Open University (Grande-Bretagne)
	Bruno Galbrun, DR CNRS, Université Pierre et Marie Curie (France)
Examinateurs:	Klaudia Kuiper, Researcher, Vrije Universiteit Amsterdam (Pays-Bas)
	Maurice Pagel, Professeur, Université Paris Sud (France)

$^{40}Ar/^{39}Ar$

Dating of the Late Cretaceous

Acknowledgements

I would like to begin by thanking my supervisor Xavier Quidelleur without whom I would not have finished, with special thanks on the endless encouragement and patience, all the way through my PhD!

Thank you all at GTSnext, especially to the directors Klaudia Kuiper, Jan Wijbrans and Frits Hilgen for creating such a great project. Working within this team has been a great pleasure and I have enjoyed tremendously the opportunity to work in such a strong network of professionals. A big thank you to Benjamin Heredia, whom I also owe to finishing my PhD. I thoroughly enjoyed every field trip and discussion we had in the middle of no-where in Canada! Also a big thank you all of the work and data you have provided as part of the joint project. Canada would not of been the same without him.

I would also like to thank all of the fellow students on the GTSnext project for providing a great insight into the world of academia. I would also like to thank Diederik Liebrand and Tiffany Rivera for all of the banter on the workshops funded by GTSnext. Special thanks to Christian Zeeden and Anne Fischer for helping me in the Netherlands.

A big thank you to all others associated with the GTSnext project, especially Willem Langenberg who helped us forge great contacts with Canadian geologists and without whom we would not of been able to complete the work submitted. Additionally I would like to thank, Arts Sweet, Jack Lerbekmo (deceased) and David Eberth for again helping us locate new field sites suitable for this project. I am especially thankful to Silja Husing whom helped me considerably with my paleomagnetic work at Fort Hoofdjjk and providing such an excellent insight to this interesting topic. Thank you to Roel Elsas for developing such a great mineral separation technique, saving me countless hours in the laboratory.

I would like to send my thanks to Reishi Takashima and Hiroshi Nishi for involving me in their work and allowing me to understand a new insight in the world of geochronology.

Thank you to all of the volcanology team in Bât 504 for helping me with work and helping my transition in France from the UK succeed. Especially to Damien for putting up with me in the office and helping me with all my logistical needs. Thank you to all the other PhD students who have provided many interesting times and have became friends. A big thank you to Kim Ho whom I am extremely grateful for helping me settle in at Paris Sud. Thank you to Sarah Sherlock, Bruno Galbrun and Maurice Pagel for their thoughtful insights.

Finally, I would like to finishing thanking my family, my Mum and Dad who were always there encouraging and supporting me. Thanks to all my friends in Paris in particular Steffi, Matt and Liesa for helping me have the best three years of my life. I would also like to thank my home friends especially to Thomas, Louise and Dawes, with thanks also to Wiltshire who constantly supported me.

The European Community's Seventh Framework Program (FP7/2007 2013) under Grant agreement no. [215458] has funded this research.

Contents

Résumé

Dans le cadre du projet européen GTS Next, nous proposons de calibrer l'échelle des temps du Crétacé Supérieur (66-100 Ma) en utilisant la méthode de datation $^{40}Ar/^{39}Ar$ sur des minéraux de haute température (sanidine) extraits de cendres volcaniques. L'objectif de cette approche est de contraindre, au cycle d'excentricité de 405 ka le plus proche, les séries sédimentaires européennes de référence du Crétacé aux séries étudiées dans le cadre de ce travail. Cette corrélation pourra être effectuée pour les séries présentant une cyclicité bien définie reliée aux variations des paramètres orbitaux de la Terre. La meilleure approche pour acquérir des âges de très haute résolution et de haute qualité pour le Crétacé Supérieur est d'utiliser les cendres volcaniques riches en silice du bassin du Western Interior (WIB; Amérique du Nord), qui se trouvent intercalées dans les successions sédimentaires marines peu profondes. Ce projet nécessite une approche multi-disciplinaire incluant l'utilisation des techniques de datation par isotopes radiogéniques, associées aux méthodes magnétostratigraphique, chimiostratigraphique et cyclostratigraphique.

Le Crétacé, subdivisé en deux époques (Crétacé Supérieur et Crétacé Inférieur), est caractérisé par son climat à effet de serre, par un niveau des mers élevé (150 m plus élevé que les niveaux actuels; Frakes et al, 1999) et par des événements anoxiques globaux. Il se termine brusquement autour de 66 Ma à la limite correspondant à l'extinction massive du Crétacé / Tertiaire (ou plus précisément, Crétacé / Paléogène) incluant la disparition des dinosaures. Durant le Crétacé, le supercontinent Pangée a poursuivi sa dislocation pour former les continents d'aujourd'hui. Ce processus, associé à une hausse du volcanisme sous-marin et du taux d'expansion du plancher océanique au niveau des dorsales, contribue à une augmentation des émissions de CO_2 (1700 ppm) conduisant par effet de serre aux températures maximales observées au milieu du Crétacé (Seller, 2005). Le Crétacé, riche en faune marine et terrestre a préservé de nombreux fossiles de vertébrés, mammifères et dinosaures, témoins de cette période, importante et intéressante à étudier pour notre compréhension du système climatique dans un contexte de réchauffement climatique global. Pour cette raison, il est important de contraindre précisément les âges de ces événements et de leurs limites.

Des enregistrements marins européens, bien contraints par leur contenu en fossiles, ont permis d'élaborer des interprétations cyclostratigraphic précises des derniers 125 Myr. De nombreux travaux, tels que Obradovitch (1993), Gradstein et al. (2004; 2012), ont permis de mettre en place une échelle des temps à haute résolution temporelle. Cependant, certaines parties de l'échelle des temps ne sont pas fixes mais plutôt contraintes par des durées relatives flottantes dues à l'utilisation de séries d'origine géographique différentes dont la corrélation paléontologique est délicate. Cette échelle doit donc être calibrée par des âges absolus pour déterminer avec précision l'histoire géologique, environnementale et climatique globale du Crétacé.

En Europe, l'un des principaux problèmes est l'absence de matériel permettant de déterminer l'âge des limites d'étages des principales inversions ou paléomagnétiques. La majorité des coupes stratigraphiques dédiées à l'étude cyclostratigraphique sont principalement situées en Italie, au sud-est de la France et de l'Angleterre. Malheureusement, les couches de tuf volcanique sont trop altérées et les minéraux à basse température (glauconite) montrent des âges radiométriques sous-estimés pour le Crétacé inférieur (Fiet et al., 2006), suggérant un délais important dans la formation des glauconites et donc dans la fermeture du chronomètre K-Ar.

La majorité des âges de la plus récente échelles des temps géologiques (GTS2012; Gradstein et al., 2012) a été calculée en utilisant une courbe d'ajustement des âges $^{40}Ar/^{39}Ar$ d'Obradovitch (1993), recalculés par rapport à des standards re-calibrés (Kuiper et al., 2008). Cependant, certaines données ont été révisées car les horizons d'ammonites du Western Interior Basin (WIB) n'étaient pas cohérents avec les sections européennes GSSP (Global Boundary Stratotype Section and Point) de référence. Cette dernière révision de l'échelle des temps du Crétacé intègre des corrélations cyclostratigraphiques avec les coupes européennes (Herbert et al., 1995; Fiet et al., 2001; Grippo et al., 2004), elles mêmes datées à partir des paramètres orbitaux (Laskar et al., 2004; 2011).

Néanmoins, de nombreuses incertitudes demeurent et ces datations sont souvent seulement relatives. Il est à présent nécessaire d'obtenir des âges radiométriques absolus pour caler ces séries et proposer des âges stables pour les principales limites d'étages du Crétacé supérieur.

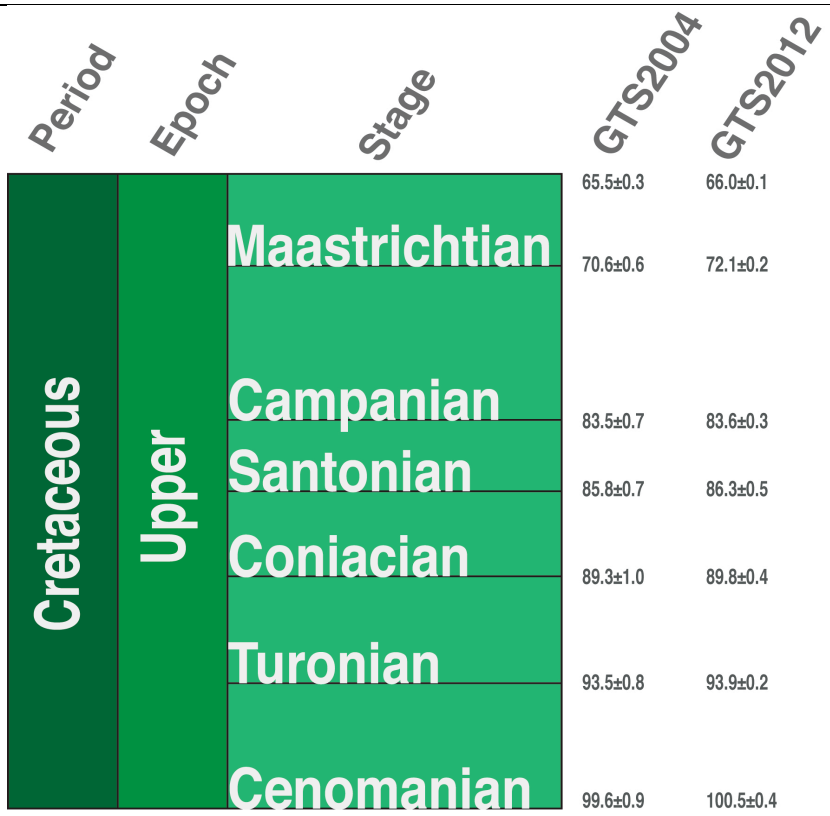

Fig.1 Echelle des temps géologiques du Crétacé Supérieur. Ages (en Ma) d'après les échelles des temps GTS2004 et GTS2012 (Gradstein et al., 2004; 2012).

La méthode de datation radiométrique $^{40}Ar/^{39}Ar$ a été inventée par Merrihue et Turner (1966). Il s'agissait d'analyser de petits échantillons en mesurant les isotopes père et fils grâce à un spectromètre de masse gaz rare en utilisant une technique dérivée de la méthode de datation K-Ar développée par A. Nier (1948). Cette méthode est également basée sur la décroissance de l'isotope ^{40}K en $^{40}Ar^*$ (^{40}Ar radiogénique), mais elle utilise l'isotope stable ^{39}K irradié en ^{39}Ar, par bombardement de neutrons dans un réacteur nucléaire. Cette production sera quantifiée par un nombre sans dimension, le facteur J, calculé à partir de mesures d'âges d'échantillons standards aussi appelés les moniteurs de flux. Connaissant le taux de désintégration de l'isotope ^{40}K en ^{40}Ar *, la production du ^{39}Ar à partir de ^{39}K pendant l'irradiation et les rapports isotopiques du potassium, nous sommes en mesure de calculer l'âge radiométrique. La datation $^{40}Ar/^{39}Ar$ est un outil très utilisé pour la datation dans de nombreux contextes géologiques.

Les incertitudes de cette méthode sont dominées par les incertitudes systématiques qui sont celles associées à l'âge des standards utilisés comme moniteurs de flux pour le calcul du facteur J, et celles liées à la constante de décroissance. Elles limitent sa justesse à environ 1-2%. Les incertitudes analytiques liées aux conditions de la mesure sont négligeables, de l'ordre de 0.1%, pour les analyses effectuées sur des minéraux riches en K, comme les feldspaths sanidines étudiés ici. Concernant la détermination de l'incertitude sur le facteur J, il est important de dissocier l'incertitude analytique liée à la mesure et l'incertitude associée à la régression polynomiale utilisée pour obtenir la valeur de J en fonction de la hauteur h dans le tube irradié. En effet, le flux neutronique varie dans l'espace à l'intérieur du réacteur nucléaire et il faut en tenir compte. Pour calculer objectivement l'incertitude sur ce facteur J, nous avons suivi une approche originale qui consiste à analyser des standards à la fois comme moniteurs de flux et comme inconnus. Pour cela, trois produits majeurs du champ volcanique de San Juan (Colorado, USA) PPD, FCT et NCD ont été mesurées sur l'instrument multi-collection $^{40}Ar/^{39}Ar$ développé au laboratoire de géochronologie multi-technique de l'Université Paris Sud, et décrit en détail dans Coulié et al. (2004). Le calcul des valeurs de J est effectué à partir des âges FCT et TCR de 28.201 ± 0.046 Ma et 28.53 ± 0.02 Ma, respectivement, d'après Kuiper et al. (2008). Ces deux âges standards ont un rapport de R^{FCT}_{TCR} = 1.011 ± 0.001 (± 1σ), d'après Renne et al. (1998). Une courbe de régression polynomiale a été obtenue pour chaque tube et pour l'ensemble des tubes des deux séances d'irradiation effectuées lors de cette étude (Fig. 2a). On peut remarquer que la valeur maximale de la variation de J sur les 7 cm de hauteur des tubes est de 4%, ce qui impose une détermination précise de la fonction J=f(h) qui sera ensuite appliquée à chaque échantillon à dater.

En règle générale, une incertitude constante de 0.2% est appliquée pour le facteur J (e.g., Kuiper et al., 2008; Renne et al., 2010). Cependant, en utilisant des échantillons d'âge connu comme "inconnus", nous avons été en mesure de quantifier plus précisément cette incertitude. En utilisant FCT comme référence à 28.201 Ma pour l'âge des moniteurs de flux (FCT ou TCR), pour ce même échantillon FCT, ou des échantillons de même âge NCD et PPD, traités comme inconnus, nous avons calculé une valeur moyenne pondérée de 28.190 ± 0.125 Ma. Nous obtenons une différence d'âge de seulement 0.011 Ma, validant l'ensemble de l'approche suivie ici (Fig. 2b).

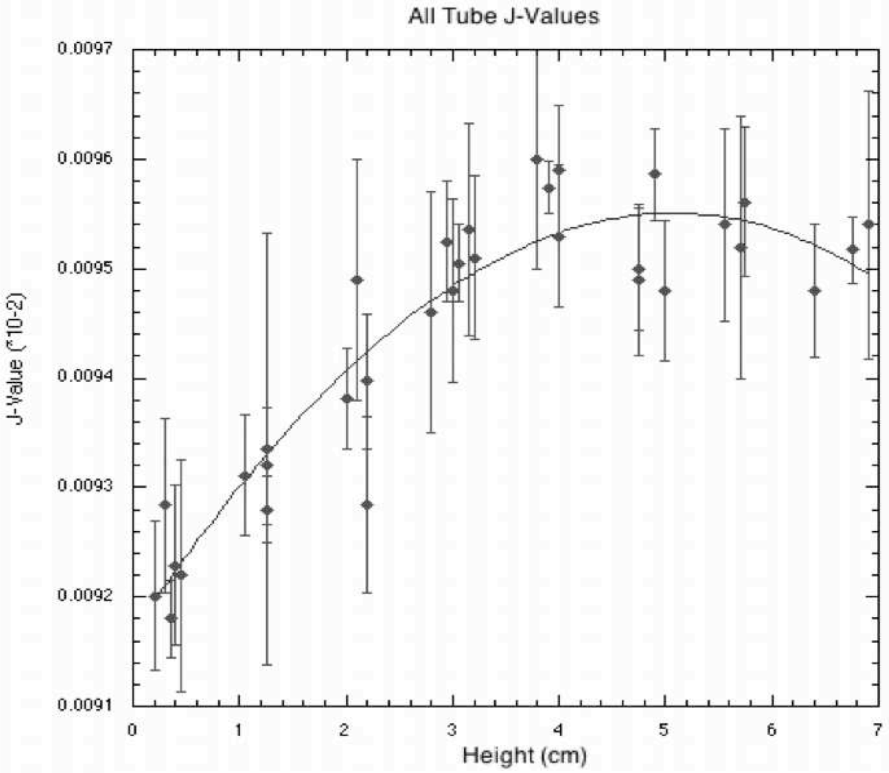

Fig. 2a : Valeur … ards d'âge relatif à FCT c … régression polynomiale de …

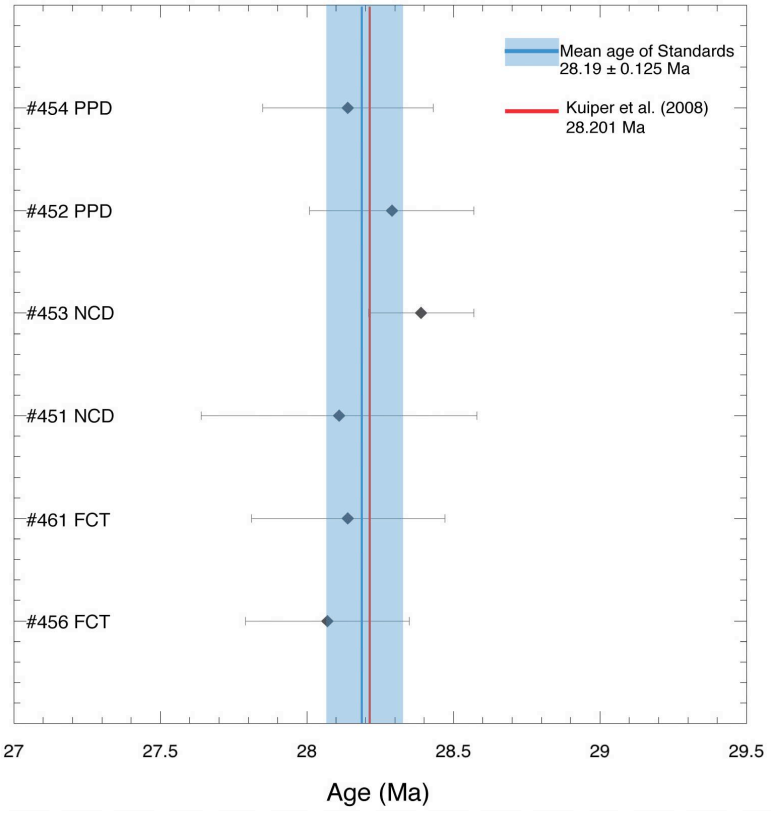

Fig. 2b : Ages $^{40}Ar/^{39}Ar$ fusion-totale des produits volcaniques de San Juan (Colorado, USA) calculés à partir de standards d'âge relatif à FCT de 28.201 Ma. PPD (Pagosa Peak Dacite), NCD (Nutras Creek Dacite) et FCT (Fish Canyon Tuf) sont contemporains.

De plus, l'incertitude relative (0.125 Ma) obtenue sur cette moyenne est de 0.45%. On peut donc conclure que l'incertitude sur la détermination du facteur J est ici de 0.45%. Cette valeur sera appliquée à toutes les déterminations d'âge $^{40}Ar/^{39}Ar$ obtenues tout au long de cette thèse.

Les âges radiométriques du Crétacé Supérieur, notamment de l'échelle GTS2012 (Gradstein et al., 2012), proviennent de coupes du Western Interior Basin et sont principalement dérivés des résultats obtenus par Obradovitch (1993). La formation de Horseshoe Canyon (Eberth, 2011) dans le bassin sédimentaire de l'Ouest Canadien est particulièrement bien adaptée pour déterminer l'âge des derniers étages du Crétacé, notamment, les limites Crétacé / Paléogène et Campanien / Maastrichtien qui seront détaillées ci-dessous. En effet, cette formation se compose d'une couche épaisse de sédiments marins qui comprend des niveaux de cendres volcaniques, et est particulièrement bien exposée le long de la rivière Red Deer, dans le sud de l'Alberta, Canada (Eberth, 2011). En parallèle de cette étude effectuée au Canada, nous nous sommes également intéressés à la partie inférieure du Crétacé supérieur, du Cénomanien au Santonien, échantillonné à Hokkaido au Japon. Ces deux études ont été effectuées en complémentarité des travaux de thèse de Benjamin Heredia (Université de Berne, Suisse) qui a daté par la méthode U/Pb les même niveaux de téphra que ceux datés en $^{40}Ar/^{39}Ar$, quand des zircons en qualité et quantité suffisante ont pu être séparés. Cette méthode ne souffre pas des incertitudes systématiques affectant les âges $^{40}Ar/^{39}Ar$, et, si le temps de résidence du magma dans la chambre magmatique est suffisamment bref pour être négligé, étant donné que les constantes de décroissance sont très bien déterminées, elle est la plus précise et juste des méthodes de datations radiométriques.

Limite Crétacé / Paléogène (K/Pg)

Notre âge de la limite Crétacé/ Paléogène (K/Pg) de 65.75 ± 0.06 Ma a été obtenu par l'utilisation d'une multitude de techniques géochronologiques associées à des interprétations stratigraphiques dans la coupe de la rivière Red Deer (Alberta, Canada). La localisation de la limite K/Pg dans la région de la rivière Red Deer est déterminée par la présence de quartz choqués (e.g., Grieve et Alexopoulos, 1988), par une anomalie en Ir (e.g., Lerbekmo et St. Louis, 1986), et par un enrichissement en

micro-diamants, acides aminés et isotopes lourds d'origine extraterrestre (e.g., ^{107}Ag, ^{236}U, ^{244}Pu; Carlisle et al., 1995). Toutes ces études ont permis de mettre en évidence la limite proche de la base de la couche de charbon No.13, représentée par un niveau d'argile de 1-2 cm d'épaisseur (e.g., Sweet et al., 1999). Le niveau de cendres volcaniques altérées dans la couche de charbon No.13 a été trouvé ~ 30 cm au-dessus de la limite argileuse (Therrien et al, 2007; ce travail). Par conséquent, et en supposant que le niveau contenant la couche de charbon No.13 représente un cycle de précession, la limite K/Pg est à l'incertitude analytique près dans la population de zircon la plus jeune, à 65.746 ± 0.058 Ma (Fig. 3b).

Ces deux mêmes niveaux de téphras ont été datés en ^{40}Ar/^{39}Ar. Le téphra supérieur a été dupliqué et donne un âge de 65.51 ± 0.21 Ma, tandis que le téphras inférieur, situé à la limite K/Pg, donne un âge de 65.88 ± 0.30 Ma (Fig. 3a). Ces âges ^{40}Ar/^{39}Ar sont en parfait accord avec les âges U/Pb. Néanmoins, comme leur incertitude est nettement inférieure, nous utiliserons ces derniers pour dater cette limite majeure de l'échelle des temps géologiques.

Bien que l'excentricité module l'amplitude de la précession, l'expression de l'excentricité n'a pas été bien développée dans l'alternance sédimentaire étudiée ici, probablement parce que la section est trop courte et que l'interférence possible des horizons de sable masque cette cyclicité. Cependant, nous avons pu caler cyclostratigraphiquement les sédiments dans un environnement fluvial non-marin en utilisant les enregistrements haute-résolution de proxy suggérant qu'une cyclicité liée à une précession se retrouve à la base du chron magnétique C29r. On peut noter que notre âge de 65.746 ± 0.058 Ma n'est pas compatible avec les âges publiés dans GTS2012 (66.0 ± 0.1 Ma) et l'âge révisé de Renne et al. (2013; 66.043 ± 0.043 Ma). Des contraintes supplémentaires peuvent être apportées si on en déduit l'âge de la base du chron magnétique inverse C29r. Afin de valider notre âge radiométrique, nous avons donc contraint la position de la base de C29r en utilisant le paléomagnétisme appliqué directement sur notre coupe de Red Deer.

Compte tenu de la durée séparant cette inversion de la limite K/Pg, de notre résultat, nous pouvons déduire un âge de 65.988 ± 0.031 Ma pour la base du chron magnétique inverse C29r.

L'âge apparent obtenu pour cette inversion magnétique par Husson et al. (2011), par calibration astronomique du Maastrichtien à partir de sédiments océaniques profonds, suggère que la limite K/Pg tombe entre les excentricités maxima et minima, ce qui conduit ces auteurs à proposer un âge pour la base de C29r de 65.89 ± 0.08 Ma (option 1) ou de 66.30 ± 0.08 Ma (option 2). Clairement, nos travaux valident leur option 1 qui est en accord, en tenant compte des incertitudes, avec notre résultat.

Les estimations d'âge présentées dans ce travail peuvent avoir une forte influence sur l'interprétation concernant le nombre de cycles présent entre la base de l'Eocène et l'inversion C29r.

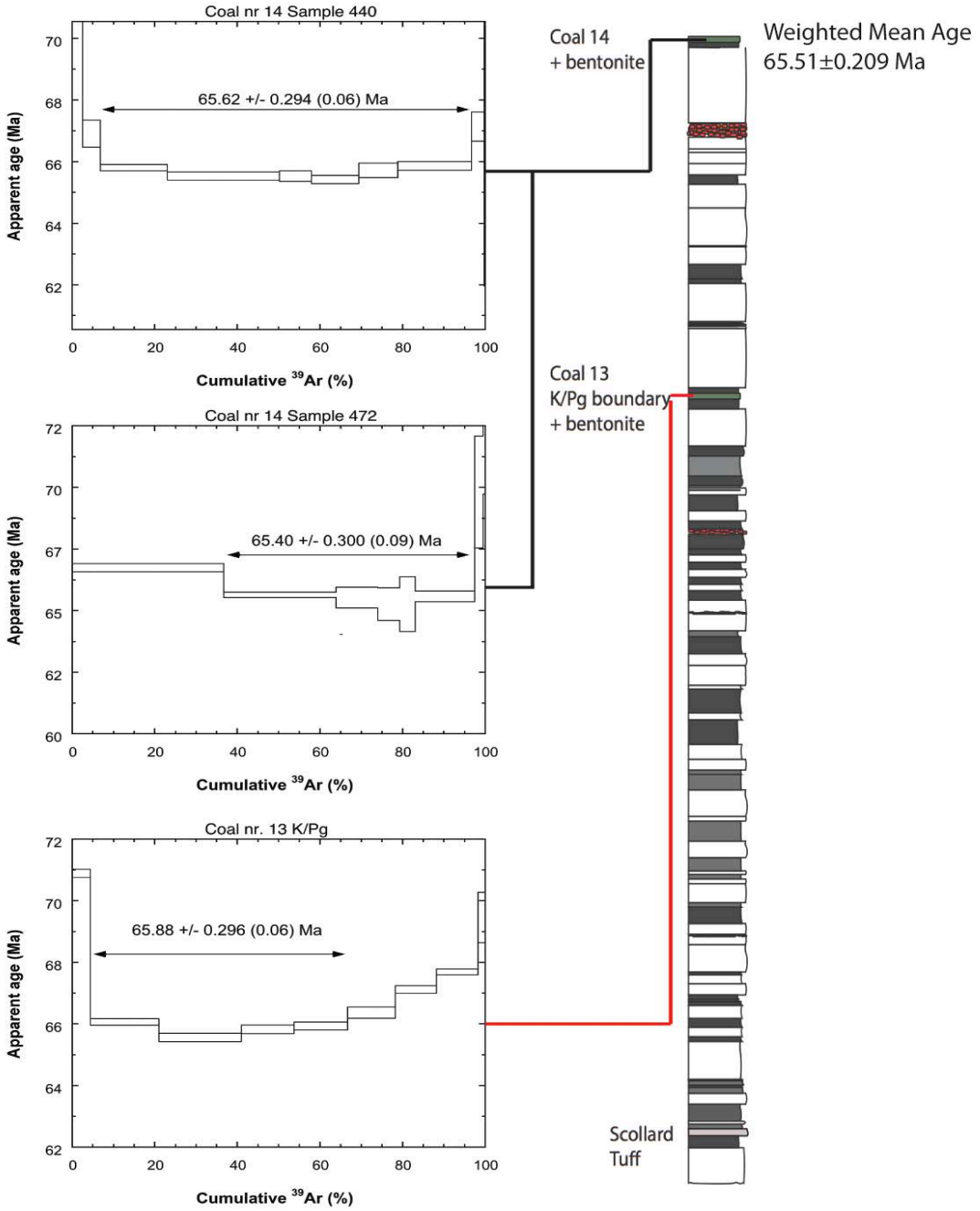

Fig. 3a. (ci-dessus) Spectres d'âges $^{40}Ar/^{39}Ar$ pour deux niveaux de téphra échantillonnés près des couches de charbon No. 13 et 14 de la coupe Knudsen le long de la rivière Red Deer.

Fig. 3b. (page suivante) Comparaison entre les différentes calibrations astrochronologiques du Maastrichtien indiquant les cycles d'excentricité de la limite K/Pg identifiés à 405 ka et vers le bas dans des forages provenant de l'Océan Atlantique et de Zumaia (d'après Westerhold et al., 2008; Husson et al., 2011; Batenburg et al., 2012). La limite K/Pg est indiquée dans les différentes sections et directement reliée au développement de la cyclostratigraphie dans cette étude ainsi qu'aux âges $^{40}Ar/^{39}Ar$ et U/Pb moyens pondérés.

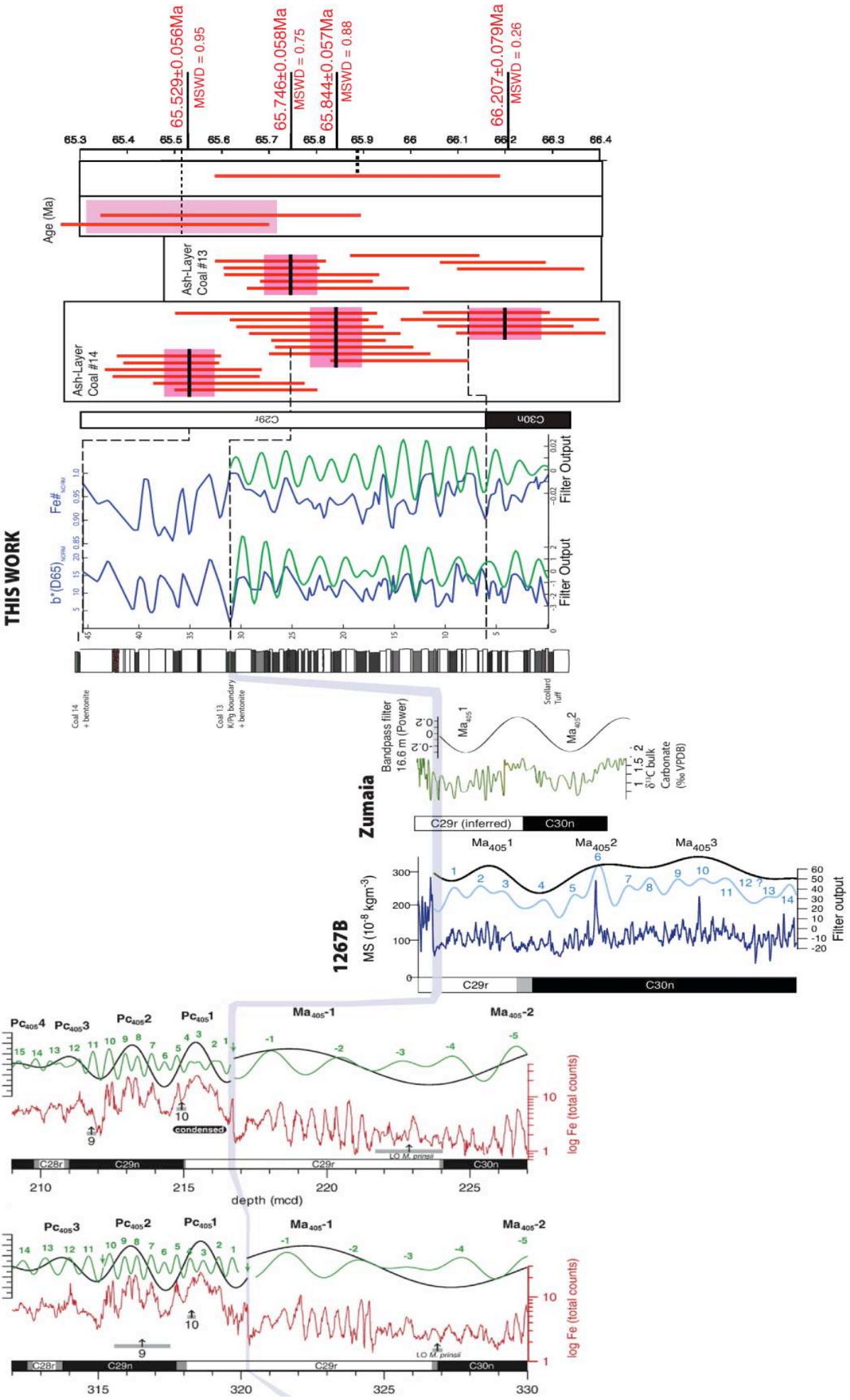
65.529±0.056Ma
MSWD = 0.95
65.746±0.058Ma
MSWD = 0.75
65.844±0.057Ma
MSWD = 0.88
66.207±0.079Ma
MSWD = 0.26
65.3 65.4 65.5 65.6 65.7 65.8 65.9 66 66.1 66.2 66.3 66.4
Age (Ma)
Ash-Layer Coal #13
Ash-Layer Coal #14
C29r
C30n
THIS WORK
Fe#NCRM
b*(D65)NCRM
Filter Output
Filter Output
Coal 14 + bentonite
Coal 13 K/Pg boundary + bentonite
Scollard Tuff
Zumaia
Bandpass filter 16.6 m (Power)
Ma405 1
Ma405 2
δ13C bulk Carbonate (‰ VPDB)
C29r (inferred)
C30n
1267B
MS (10-8 kgm-3)
Ma405 1
Ma405 2
Ma405 3
Filter output
C29r
C30n
Pc405 4
Pc405 3
Pc405 2
Pc405 1
Ma405 -1
Ma405 -2
filter output
condensed
LO M. prinsii
log Fe (total counts)
1262
C28r
C29n
C29r
C30n
210 215 220 225
depth (mcd)
1267
315 320 325 330

Dans le bassin sédimentaire de l'Ouest canadien, la limite Campanien / Maastrichtien (C/M) palynomorphique est préservée dans la succession sédimentaire de la formation de Horseshoe Canyon. Cette limite a été placée à ~ 8 m au-dessous du niveau de charbon No. 10 (e.g., Lerbekmo et Braman, 2002; Hamblin, 2004; Eberth, 2010) d'après des corrélations magnétostratigraphiques avec la section Bottaccione, Italie (e.g., Alvarez et al., 1977; Silva et al., 1994), près de la limite des chrons magnétiques C31r - C32n. La formation de ces séquences sédimentaires (alternances) à toutes les échelles est directement influencée par les variations du niveau des mers en raison de la précession. Elle est plus dominée encore par les cycles d'excentricité, comme le montre notre analyse cyclostratigraphique, et elle est principalement contrôlée par les horizons de sable, qui ont été interprétés par auto-cyclicité dans un cadre dynamique sédimentaire. En outre, le laps de temps entre les deux populations les plus jeunes des âges U-Pb sur zircon obtenus pour les deux couches de cendres volcaniques montre que les cendres volcaniques sont séparées par ~ 800 kyr, c'est-à-dire huit cycles d'excentricité de 100 kyr. La limite Campanien / Maastrichtien dans le bassin sédimentaire de l'Ouest canadien coïncide avec ~ 2,5 cycles d'excentricité au-dessus de la plus jeune population de zircon à la base de la section et ~ 4.9 Myr avant la limite Crétacé-Paléogène (K/Pg), et correspond donc à un âge absolu de 70.65 ± 0.09 Ma (Fig. 4).

Notre travail suggère que la limite C/M précédemment placée dans la section de Morrin Bridge par rapport aux travaux de Eberth (2011) et Lerbekmo (2005) est inexacte. Des difficultés dans la définition de la limite couplée avec la complexité de la magnétostratigraphie et bio-stratigraphie ont entravé le positionnement de cette limite dans l'ouest du Canada. Contrairement à la coupe de la rivière Red Deer où nous avons daté la limite K/Pg, nous n'avons pas pu obtenir une magnétostratigraphie fiable, puisque chaque échantillon a présenté un fort signal de ré-aimantation magnétique. L'estimation de l'âge de cette limite est donnée à 70.65 ± 0.09 Ma et n'est pas cohérent avec l'estimation proposée par Voigt et al. (2012) et Husson et al. (2011), conduisant ainsi un âge environ 1.4 Myr plus jeune. Cela met en évidence la nécessité d'améliorer l'interprétation bio-stratigraphique et magnétostratigraphique pour la section de Red Deer. Plutôt que de définir un nouvel âge de la limite, les âges

obtenus ici peuvent constituer des contraintes d'âges importantes dans l'Ouest du Canada. Malheureusement, il n'a pas été possible d'obtenir des âges $^{40}Ar/^{39}Ar$ fiables. Les spectres d'âges montrent un comportement très perturbé en forme de selle de cheval, caractéristique d'une contamination par excès d'argon.

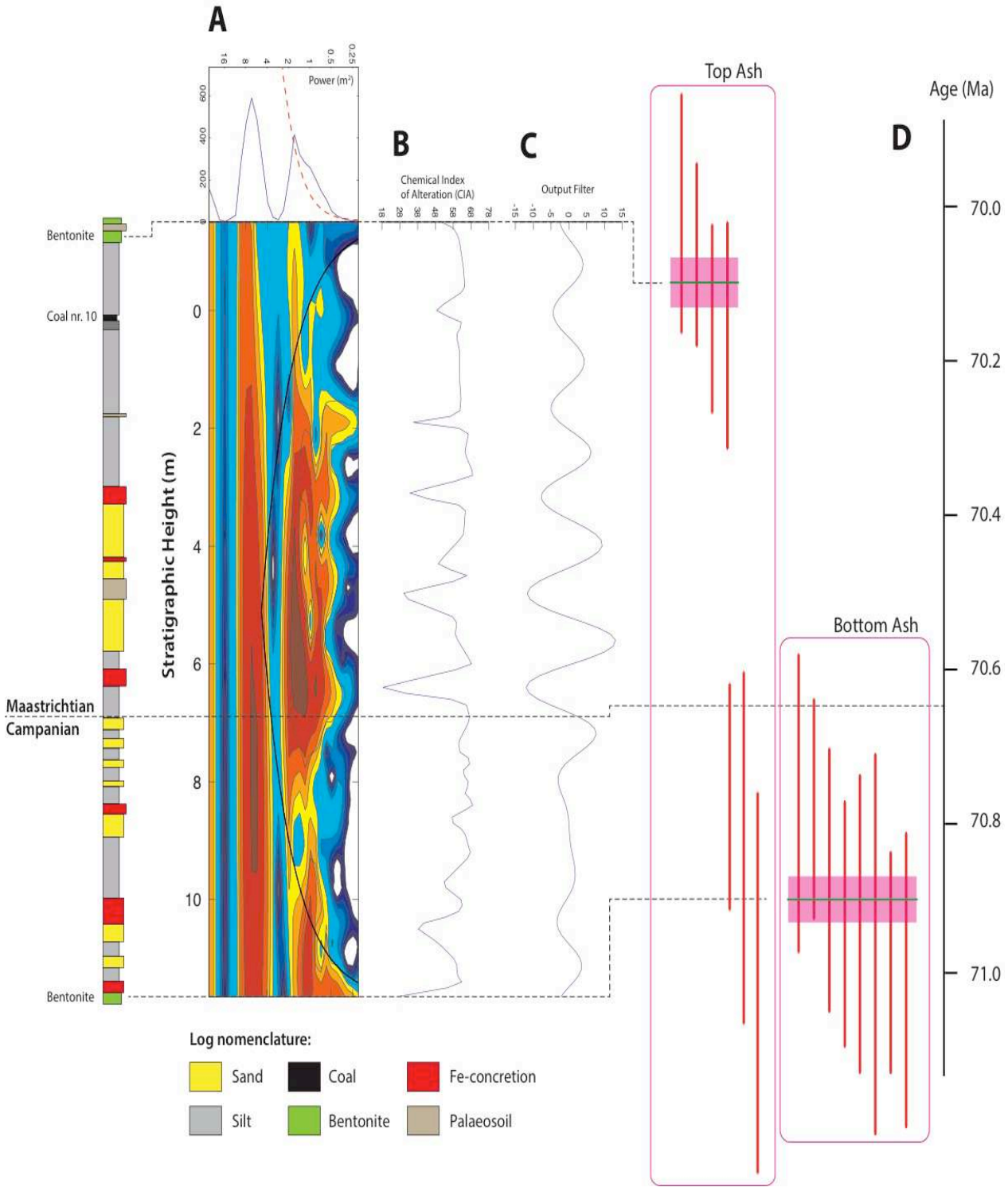

Fig. 4. (page précédente) Cadre cyclostratigraphique intégré avec nos âges U/Pb. L'analyse en ondelettes de l'indice chimique de l'altération (CIA ; %) permet d'identifier une périodicité à ~ 1,67 m, ce qui se traduit par 8 cycles d'excentricité du haut vers le bas de la section. Les âges U/Pb obtenus sur des cristaux isolés et fragments de cristaux de zircon des deux niveaux de cendres volcaniques datés ici montrent une durée de ~ 800 kyr entre les 2, ce qui est en accord avec le nombre de cycles. Les incertitudes sur les âges des grains isolés et les valeurs moyennes pondérées sont toutes présentées avec des intervalles de confiance à 2 σ .

Limite Turonien / Coniacien (T/C)

Les courbes des isotopes du carbone, telles que celles développées par Gale et al. (1996), Nishi et al. (2004) et Takashima et al. (2010) se sont révélées être de puissants outils pour corréler les sections sédimentaires provenant de diverses localités (Gale et al., 1996).

En utilisant les avancées obtenus grâce aux isotopes du carbone terrestre $\delta^{13}C$ et les enregistrements de foraminifères planctoniques dans la région centrale d'Hokkaido (Japon), dans le nord-ouest Pacifique, des sections du groupe Yezo du Crétacé ont été corrélées à celle de leurs homologues européens et nord-américains (Takashima et al., 2010, 2011). Cependant les âges des téphra dans la section de la rivière Kotanbetsu (Hokkaido) se sont révélés difficiles à évaluer et seuls quelques âges radiométriques sont actuellement disponibles (Obradvitch et al., 2002; Quidelleur et al., 2011). Les spectres $^{40}Ar/^{39}Ar$ d'âges apparents présentent souvent des évidences d'excès d'argon avec seulement quelques spectres d'âges utilisables avec un âge plateau défini suffisamment bien. De même, les zircons ont été difficiles à extraire et à analyser rendant ces minéraux souvent inappropriés pour la méthode de datation radiométrique U/Pb. Cependant, nous avons pu dater avec succès deux niveaux de téphra situés de part et d'autre de la limite Turonien / Coniacien, produisant une gamme d'âge pour cette limite comprise entre 89.31 ± 0.11 Ma et 89.57 ± 0.11 Ma, ou, si on considère ces deux valeurs, un âge moyen pour cette limite à 89.44 ± 0.24 Ma (Fig. 5).

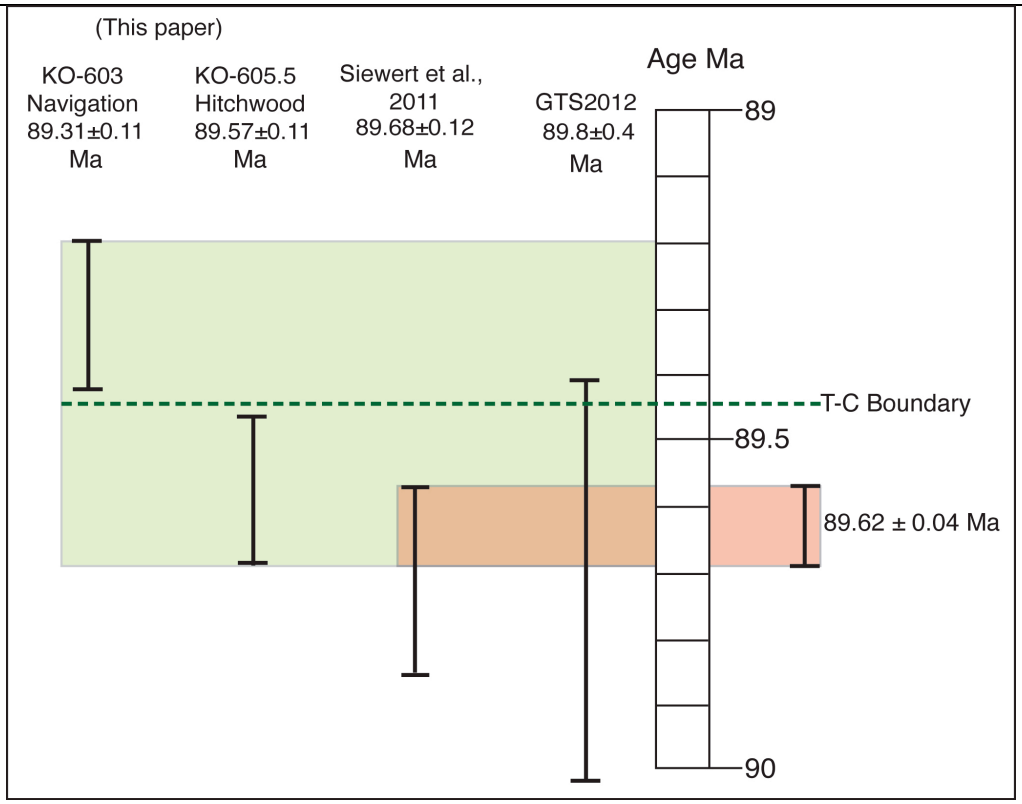

Fig. 5 Age de la limite Turonien-Coniacien (T/C), calculé à partir de deux téphra volcaniques (KO-603 et KO-605.5) datés par U/Pb dans le cadre de ce projet. Ces niveaux correspondent aux excursions des isotopes du carbone Navigation et Hitchwood identifiés de part et d'autre de la limite T/C (Takashima et al., 2010). A partir de ces deux seuls âges la limite peut être calculée à 89.44 ± 0.24 Ma. Cependant, l'utilisation des âges publiés par Siewert et al., (2011) combinés aux nôtres permet de proposer un âge très bien contraint de 89.62 ± 0.04 Ma pour la limite Turonien / Coniacien.

Cet âge est en accord avec l'âge de 89.8 ± 0.4 Ma proposé dans l'échelle GTS2012 (Gradstein et al., 2012). En outre, en combinant les âges U-Pb publiées par Siewert et al. (2011), nous sommes en mesure d'affiner l'âge de la limite et de proposer un âge pour la limite T /C de 89.62 ± 0.04 Ma (Fig. 5). Cet âge couplé avec la courbe des isotopes du carbone nous permet de proposer un âge très bien contraint pour la limite Turonien/Coniacien.

Enfin, l'utilisation des âges obtenus dans ce projet, nous a permis de calculer de nouveaux âges pour les limites. Ces âges pourraient être utilisés et contribuer à la révision de l'échelle des temps géologiques, et pourraient être inclus dans les échelles des temps géologiques de future génération (Fig. 6).

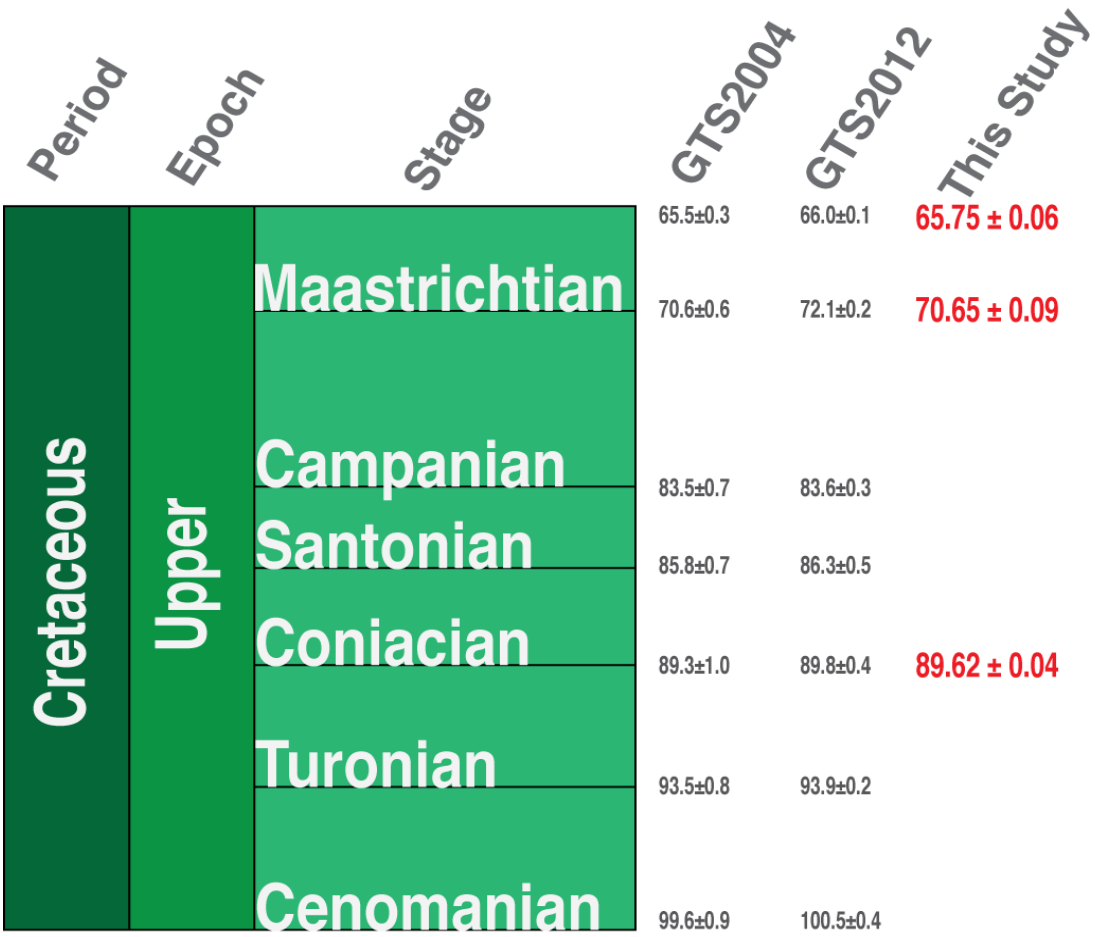

Fig. 6 Ages (en Ma) des limites d'étages du Crétacé Supérieur obtenus dans le cadre de ce projet GTS-Next, comparés aux âges publiés précédemment dans le cadre des échelles de temps GTS2004 et GTS 2012 (Gradstein et al., 2004; 2012).

I. Introduction

I.1. Project Aim

GTS Next project (www.gtsnext.eu)

GTSnext -Towards the next generation of the Geological Time Scale for the last 100 million years - the European contribution to EARTHTIME- is a Marie Curie Initial Training Network funded under the 7th Research Framework Programme.

The principal scientific objective of the network is to establish the next generation standard Geological Time Scale with unprecedented accuracy, precision and resolution through integration and intercalibration of state-of-the-art numerical dating techniques. Such time scales underlie all fields in the Earth Sciences and their application will significantly contribute to a much-enhanced understanding of Earth System evolution.

I.1.2 GTS Next

Time is a fundamental parameter in the Earth Sciences, essential for the integration of disparate datasets, unravelling cause and effect relationships, and for the quantification of rates and durations of geological processes. Temporal relationships are often the key to causality arguments in Earth Sciences, for example between environmental and biological change during mass extinction events. The Geological Time Scale (GTS) is instrumental for the quantification of geological time; however, published time scales are commonly based upon a limited number of geochronological tie-points and derivative age models that are different and of widely variable quality. The accuracy and resolution of such time scales are also variable, generally in the order of 1 to 0.5% at best. Large uncertainties - on the order of several millions of years - still exist in the age and duration of key geological intervals. Furthermore, it is increasingly clear that different techniques are yielding different ages for the same horizon suggesting that systematic bias may exist between the various techniques applied. This situation hampers full exploitation of the GTS for understanding Earth System evolution.

Recent developments in astronomical tuning and improvements in radio-isotopic dating bear the exciting prospect of a major breakthrough in the absolute calibration

of the GTS: direct intercalibration of astronomical and radio-isotopic dating and time scales. This breakthrough will inevitably lead to a greatly enhanced understanding of many fundamental processes underlying Earth's evolution through the application of the new integrated time scale with its unprecedented accuracy, precision and resolution. The principal objective of GTSnext, our Initial Training Network (ITN), is the training of a new generation of scientists with the skills and understanding of time scale chronometry and the application of various techniques in order to facilitate an enhanced understanding of Earth System evolution. GTSnext will focus on the specific strengths of the European research teams in time scale development: astronomical dating of the Cenozoic through Cretaceous, direct intercalibration with radio-isotopic dating, $^{40}Ar/^{39}Ar$ tephrachronology, U/Pb dating, and intercalibration between key isotope systems used in high resolution geochronology (www.gtsnext.eu).

GTS Next is split up into 12 sub projects (Fig.I.1) consisting of 9 PhD projects and 3 Postdocs. The Neogene, Paleogene and Cretaceous will be dated with the 3 individual dating techniques and then compared to obtain the most accurate dating tool possible.

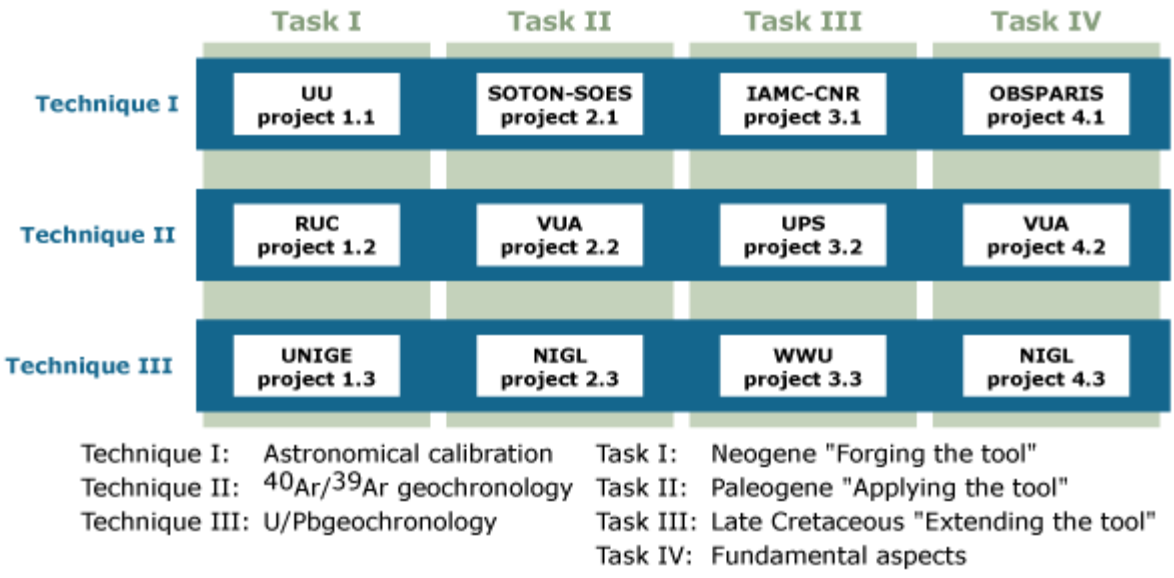

Fig.I.1 GTS next project outline.

Project 3.2 Constraining the Upper Cretaceous Period: $^{40}Ar/^{39}Ar$ Dating method.
University Paris Sud 11

I.1.3. Aim

Here we propose to calibrate the upper Cretaceous (66-100 Myr) time scale using $^{40}Ar/^{39}Ar$ dating of high temperature minerals (sanidine) extracted from volcanic ashes with the aim of constraining the tuning of cyclic successions in Europe to the nearest 405 kyr eccentricity cycle in the astronomical solution. The highest potential to attain the required very high-resolution and high-quality dates for Late Cretaceous time lie within the abundant silicic ashes found in the Western Interior Basin (WIB), which occur intercalated in dominantly shallow marine successions. These projects require a multi-disciplinary approach with radio-isotope dating techniques integrated with magnetostratigraphic, chemostratigraphic and cyclostratigraphic methods.

Well constrained marine records in Europe has made it possible to determine accurate cyclostratigraphic interpretations for the last 125 Ma, numerous works such as (Obradovitch. 1993; Gradstein et al, 2004; 2012; Kuiper et al, 2008), have worked to create a high resolution timescale. However, parts of the timescale are not fixed but instead relative "floating" timescales that need to be pinned down to an absolute datum to accurately determine the age and climatic history of that era.

One main problem is the lack of ash beds surrounding some of the major boundary or important paleo-magnetic horizons within Europe. The stratigraphic sections where the best cyclostratigraphy is available are located in Italy, southeast France and England. Unfortunately, no volcanic tuff layers without severe weathering can be found and only low temperature minerals (glauconite) provide useful radiometric dating of the Lower Cretaceous stage durations (Fiet et al, 2006), but with uncertainties no smaller than about 1% and puzzling ages of each stage boundary.

Without fixed points in time the results are just relative dates, to overcome this problem, project 3.2 and 3.3 were created to locate possible boundary ash beds in alternate sections in North America to date using absolute techniques. The combination the North American and European sections together we are to ensure that

the same horizon markers can be found. We will attempt this by using a multi-disciplinary geochronological approach to fully quantifiy an absolute age to use in the formation of the next geological timescale.

Recent improvements of the $^{40}Ar/^{39}Ar$ dating technique have lowered the analytical uncertainties down to 0.1% for best suitable minerals, such as sanidine. On the other hand, systematic uncertainties as high as 1 - 2% remain. This is due to the lack of definitive agreement on the age of flux monitor standards, even for the FCT sanidine, one of most analyzed. One of the objectives of this project will be to compare U/Pb and $^{40}Ar/^{39}Ar$ ages within the late Cretaceous time interval, where both techniques are optimized in terms of radiogenic production.

I.1.4 The geological timescale

"A system of chronological measurements that relate to stratigraphy and time, utilised to describe timings and relationships between events."

Dates have always played an important role in geology; determining evolutionary chains, paleoclimatic changes and paleogeography history, however when discussing said results it is increasingly important to correlate events to a specific time in history, making the geological timescale an important tool. The final aim of this project is to update, improve and utilise all possible geochronological methods to accurately acquire possible datums for the new geological timescale.

Since the first published geological timescale, which included absolute dates in 1913 (Holmes, 1913) there have been considerable improvements over the years to fully integrate numerous geological fields to form one geological timescale.

- In 1977 the International commission on stratigraphy (ICS) was established and has greatly refined the international chrono-stratigraphic scale.

- Continued improvements in the chronometric scale by geochronology allow a precise calibration to chrono-stratigraphic markers thus ensuring an improved geological timescale that can be updated.

Over time the geological timescale has evolved to the internationally calibrated editions of the GTS2004 (Gradstein et al, 2004) and GTS2012 (Gradstein et al, 2012). Previous examples such as Homes (1937, 1960) and Kulp (1961) relied heavily on radiometric datums or stratigraphical statistics while the most recently updated timescales incorporate numerous scientific fields to ratify and quantify suitable ages and GSSP's for each Periods, Eons and Stages. Previously stated, not all geochronological methods are suitable for each time, therefore we can group the timescale into different divisions that showcase the various evolutions in time scale work.

Pre-Cambrian Scales: Changing considerably from the original Holmes (1937) timescale, the most recent estimates of GTS 2012 put the age back as far as ~4600 Ma. This part of the timescale is entirely made up of radio-isotopic ages derived from the U-Pb ages of samples such as the Jack Hills formation, Australia (Wilde et al, 2001).

Paleozoic Scales- Spanning 291 Myr between 541.0 and 252.2 Ma the GTS2012 timescale varies differently from that of Holmes (1960) and Kulp (1961) mainly due to updates in geochronology methods such as the high precision U-Pb and $^{40}Ar/^{39}Ar$ radio isotopic ages (Williams et al, 2000) coupled with narrow bio-stratigraphic horizons just like the graptolite (Cooper and Sadler, 2010) horizons in the Ordovician. Due to the scarcity of reliable datums but reliable stratigraphic precision, a straight fit biostratigraphic scaling was used to adjust stage boundary ages in GTS2012 (Gradstein et al, 2012).

Mesozoic Scales. Spanning an interval of 186 Myr (251 - 66.0 Ma), this part of the timescale has improved dramatically and encompasses statistical approaches alongside various geochronological methods such as radioisotopic data, bio-

stratigraphic horizons, magnetostratigraphy and also cyclostratigraphy. Particular improvements in the Late Cretaceous timescale were mainly due to Obradovitch's (1993) $^{40}Ar/^{39}Ar$ ages obtained from the Western Interior, while orbitally tuned beds (Fiet et al, 2001) in the Early Cretaceous have helped pin ages on certain boundaries through the Cenomanian and Albian.

Cenozoic Scales: Dating from 66.0 Ma to present, this scale encompasses a multitude of geochronological methods. However, unlike previous timescales, orbitally tuned dates in the Cenozoic have an unprecedented accuracy, pinned down with an accurate geomagnetic polarity timescale (Cande and Kent, 1992; 1995) through the Neogene and Paleogene.

I.2 Introduction to the Cretaceous Period

Derived from the Latin 'Creta' meaning chalk, this geological period spanned from ~145 – 66 Ma GTS2012 (Gradstein et al, 2012) and is characterised by high eustatic sea levels, warm climates, inland seas and oceanic anoxic events (Skinner et al, 1995). The Cretaceous period followed on from the Jurassic, ending abruptly as a mass extinction event into the Paleogene (Hildebrand et al, 1991). It is the last period found of the Mesozoic and forms part of the Phanerozoic timescale.

Throughout the Cretaceous, the supercontinent Pangea fractured into the modern day continents indicating a surge in undersea volcanism and sea floor spreading enhancing CO_2 and the greenhouse climate in the middle to late Cretaceous (Seller, 2005). Rich in both marine, land and vertebrae life, dinosaurs continued to dominate the land while new groups of mammals and birds started to spread throughout Pangea (Stanley et al, 1999).

I.2.2 Evolution of the Cretaceous timescale

Previously in 1937 (Holmes) the Cretaceous was subdivided into three series; Neocomian, Gallic and Senonian created from evidence in the lithology obtained from outctrops in Neuchatel, Switzerland. The term Neocomian was introduced into the literature in the revised geological timescale of Holmes (1937) until Kulp (1961)

whereby the term was abolished for smaller subdivisions that were applicable in other global areas rather than definitions devised for areas around the Parisian basin. Overall, twelve main revisions of the Cretaceous have been utilised in the past (Fig. I.2.), beginning with a simple period orientated of 1937 (Holmes) to the highly tuned stage orientated timescale of GTS2012 (Fig.I.2&3). Since GTS82, nomenclature of the periods has stayed constant and defines a Europe centric approach in terms of the definitions of each sub division. On occasions such as the EX88 timescale (Haq et al, 1987) smaller subdivisions were introduced, however did not stand up to scientific criticism and were abolished in favor of the current system.

Improvements in the $^{40}Ar/^{39}Ar$ dating method have helped create the modern day Cretaceous timescale, with the most significant revison published by Obradovitch (1993) using radiometric ages of bentonites in local ammonite zones found in the Western Interior seaway. Correlations of the North America ammonite zonations were achieved through rare occurrences found within the European stages and zones (Cobban et al, 1993) combined with strontium isotope curves (McArthur et al, 1993, 1994) of the Campanian-Maastrichtian.

The base of the majority of the GTS2012 ages were calculated using revised $^{40}Ar/^{39}Ar$ ages of Obradovitch (1993), utilising a cubic spline fit to refine the boundaries, however, portions of the data were soon updated as Obradovitch (1993) ammonite horizons were unable to correlate with the European GSSP sections. The latest revision of the Cretaceous timescale incorporates cyclostratigraphic tuning of orbitally tuned outcrops in Europe (Herbert, 1995; Fiet et al, 2001; Grippo et al, 2004; Kuiper et al, 2008) but these are usually relative floating timescales and an absolute radiometric age is usually necessary to pin down the cycle series.

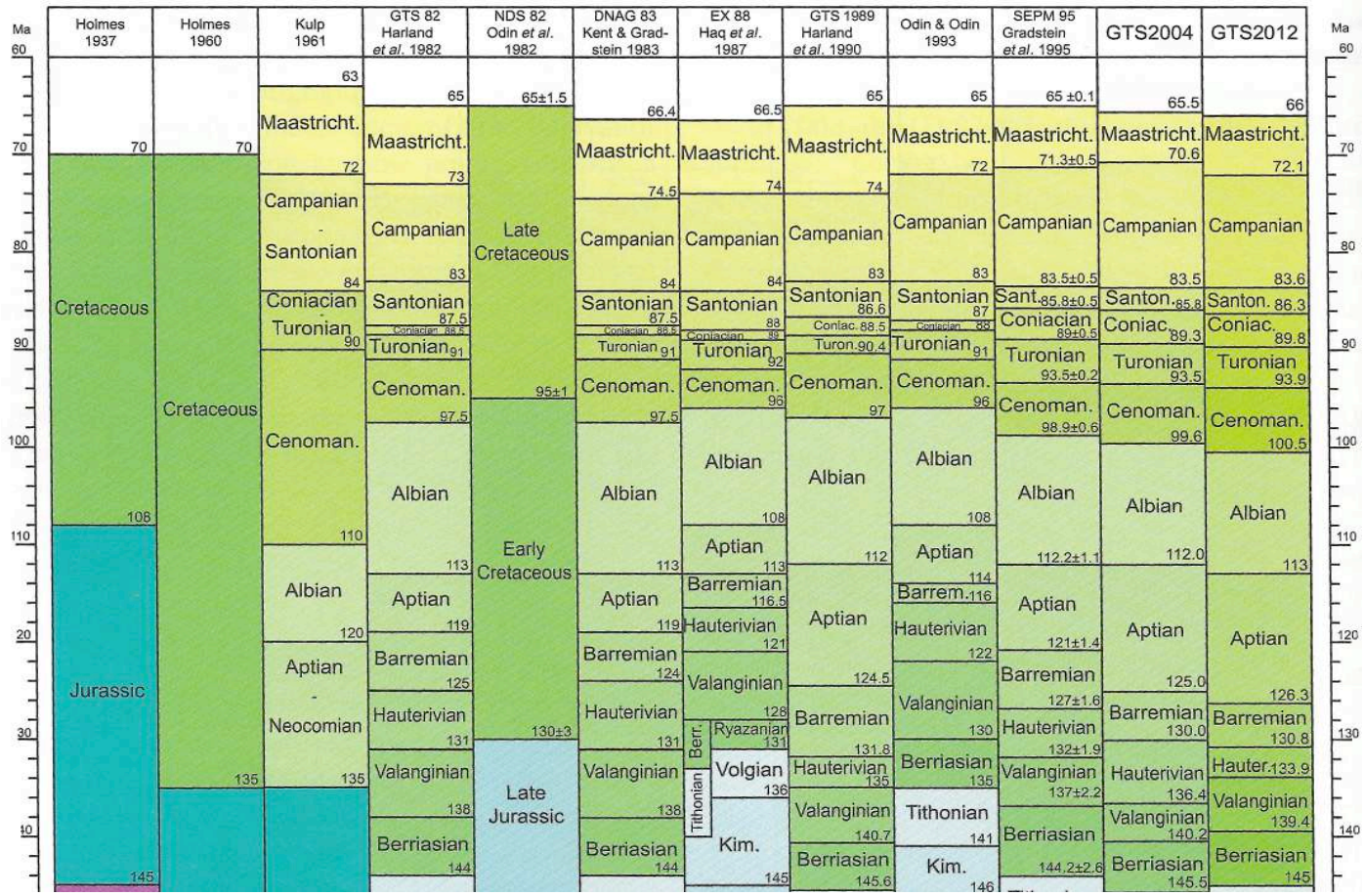

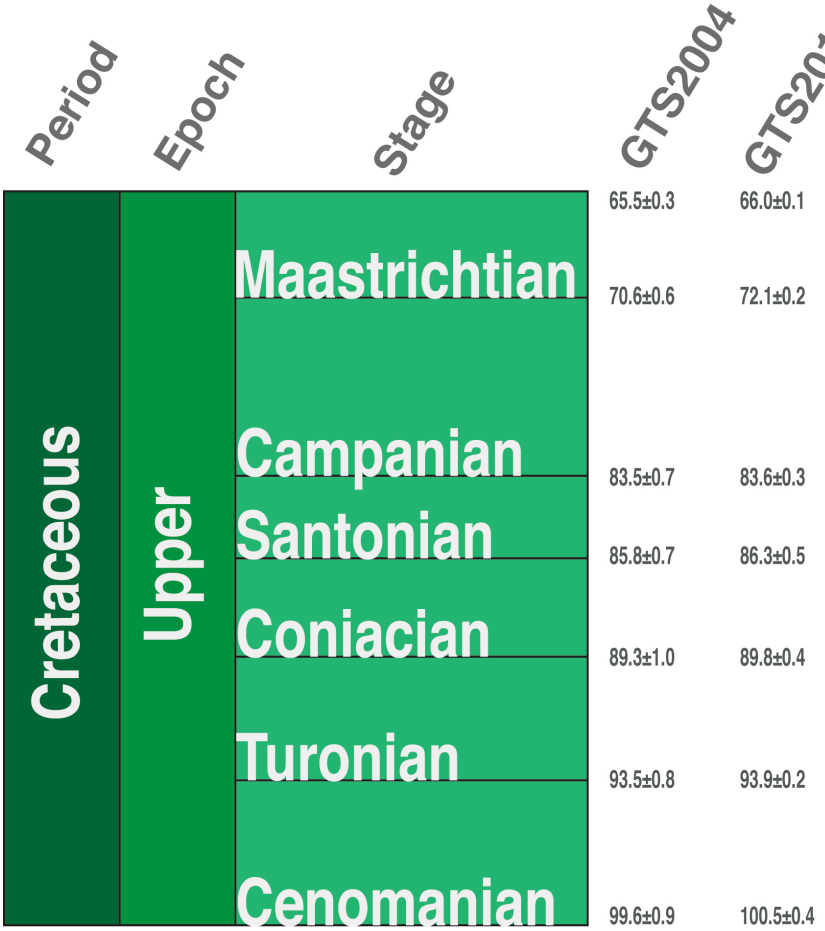

Fig.I.2. (Above) Historical evolution of the Cretaceous time scale, includes the most updated GTS 2012 ages (Gradstein et al., 2012).

Fig.I.3 (Left) Ages for the Upper Cretaceous (Ma) comparing the published ages from the two most recent revisions of the geologic timescale GTS2012 and GTS2004 (Gradstein et al., 2004; 2012).

I.2.3 Cretaceous Time Scale Stages.

Lower Cretaceous

Stretching from ~146-100 Ma it encompasses a total of six stages, Berriasian, Valanginian, Hautervian, Barremian, Aptian and the Albian. All of which were defined by exposures of limestone marl ammonite assemblages found in SE France and NW Switzerland.

- ***Berriasian**:* Base of the Cretaceous succeeding the Jurassic, currently there is no defined GSSP, however the base is defined on the primary appearance of *Berriasella Jacobi* in the Berrias region SE France (Coquand, 1871; Rawson, 1983; Zakharov et al, 1996).

- ***Valanginian**:* Overlying the Berriasian, it spans 145.5 ± 4 Ma to 140.2 ± 3.0 Ma (GTS2012). First described by Edouard Desor in 1853, this period is named after the type cast in Valangin (Switzerland). The base of the Valanginian marks the first appearance of the Calionellid species *Calionellites darderi* and ends at the first appearance of the ammonite *Acanthodiscus* (Ogg et al, 1988; Blanc et al, 1994; Aguado et al, 2000).

- ***Hauterivian**:* Overlying the Valanginian it spans the time of 136.4 ± 2.0 to 130.0 ± 1.5 Ma (GTS2012). Introduced by Eugen Renevier in 1873, termed after the town Hauterive in Switzerland the base is defined as the initial appearance of *Acanthodiscu*s, no GSSP has yet been established. (Renevier. 1874; Rawson et al, 1983; Channell et al, 1995; Reboulet et al, 1999; Gradstien et al, 2004).

- ***Barremian**:* Overlying the Hauterivian it spans the time of 130.0 ± 1.5 to 125.0 ± 1.0 Ma (GTS2012). Named from the type locality of Barreme in the Alpes-de-Haute-Provence (France) and discovered by Henry Coquand this stage starts as the principle instance of the ammonites *Spitidscus hugii* and *Spitidiscus vandeckii* ending with the geomagnetic reversals at the start of the M0r chronozone (Channell et al, 1995; Rawson et al, 1996).

- ***Aptian**:* Overlying the Barremian, the Aptian dates from 125.0 ± 1.0 to 112.0 ± 1.0 Ma (GTS2012). Stemming from the locality area of Apt in Provence (France), it was introduced by Alcide d'Orbigny in 1840. Its base is laid at the M0r magnetic anomaly ending at the first exposure of the Coccolithophore *Praediscosphaera columnata* (Herbert et al, 1992; Channell et al, 1995; Erba et al, 1996).

- ***Albian:*** Overlying the Aptian it forms the final stage of the Lower Cretaceous, aged from 112.0 ± 1.0 - 99.6 ± 0.9 Ma (GTS2012). Specified from the locality Alba, (from the river Aube in France) it was introduced again in 1842 by Alcide d'Orbigny. It forms the last stage of the Lower Cretaceous and is defined by the earliest appearance of *Rotalipora globotruncanoides* first appears (Hart et al, 1996).

Upper Cretaceous

The upper Cretaceous dates from 100.5 ± 0.4 to 66.0 ± 0.1 Ma (GTS2012). Starting at the base of the Cenomanian to the top of the Maastrichtian boundary ending in a global extinction event into the Paleogene. Climatically, generally warmer than present day, there was a general cooling trend throughout this time (Skinner et al, 1995). The tropics began to restrict equatorial regions while the northern latitudes experienced more seasonal climates (Seller, 2005).

- ***Cenomanian***: Marking the start of the upper Cretaceous dating from 100.5 ± 0.4 to 93.9 ± 0.2 Ma (GTS2012). Introduced by Alcide d'Orbigny in 1847 and named from the French city of Le Mans. It forms the base of the upper Cretaceous and is placed as the earliest appearance of *Rotalipora globotruncanoides*. The boundary has an official GSSP at the base located in Mont Risou, Rosans in the French Alps (Gale et al, 1996).

- ***Turonian*****:** Dating from 93.9 ± 0.2 to 88.8 ± 0.4 Ma (GTS2012). The start of the Turonian marks a global oceanic anoxic event called the Bonarelli horizon and was defined by the French paleontologist Alcide d'Orbigny in 1842. Orbigny named it after the French city of Tours in the region of Touraine,

which is the original type locality. The base of the Turonian stage is defined as the place where the ammonite *Watinoceras devonese* first appears. This boundary has an official GSSP type locality in Rock Canyon anticline, Pueblo, Colorado, USA (Cobban et al, 1991; Gale et al, 1996; Kennedy et al, 2000).

- ***Coniacian***: Extending from 89.3 ± 1 Ma to 85.8 ± 0.7 Ma (GTS2012) it precedes the Turonian. Named after the French region and city of Cognac, it was discovered by Henri Coquand in 1857 and is defined as the first presence of the indoceramid bivalve *Cremnoceramus rotundatus*. It forms as part of the magnetic chronozone C34 inside the Cretaceous magnetic quiet zone of normal polarity (Wood et al, 1994; Kauffman et al, 1996).

- ***Santonian***: Stretching from 86.3 ± 0.5 to 83.6 ± 0.3 Ma (GTS2012). Defined in 1857 by Henri Coquand it is named after the town of Saintes in France. Its base is disclosed due to the appearance of the bivalve *Cladoceramu unilatopicatus* (Hanncock et al, 1996).

- ***Campanian*****:** 83.6 ± 0.3 Ma to 72.1 ± 0.2 Ma (GTS2012). Introduced again in 1857 after the village of Champagne in Charentes Maritimes, France, its current status is now actually within the Maastrichtian but the name of the period is kept. Currently the base of the Campanian is defined at the extinction of the crinoid *Marsupites testudinarius* species (Gale et al, 1996).

- ***Maastrichtian****:* Sustaining from 72.1 ± 0.2 Ma to 66.0 ± 0.1 Ma (GTS2012) overlying the Campanian boundary this marks the end of the Cretaceous Period with the global K-Pg mass extinction event. Introduced by Andre Huber Dumont in 1849, it was defined as the Maastrich formation in the Netherlands. Its base is defined as the appearance of ammonite *Pachydiscus neubergicus*. A GSSP was ratified 2001 as the Grande carrier section France. This GSSP is actually a mean of several bio-events rather than a single ammonite occurrence. (Odin et al, 1996; Odin et al, 2001).

The top of the Maastrichtian boundary is easily identifiable due to the presences of the global iridium anomaly marking the famous K-Pg boundary (Alvarez et al, 1980), which identifies the extinction of many groups of life and species such as foraminifera, ammonites and belemnites.

I.2.3 Characteristics of the Cretaceous period

Paleogeography.

The geographical positions of the landmasses throughout the Cretaceous changed considerably through time; amid the onset of this period two super continents Gondwana and Laurasia existed. Meanwhile, South America, Australia and Antarctica rifted away from Africa forming the South Atlantic Ocean and continued to widen (Kauffman et al, 1995; Seller, 2005). As active rifting in the Atlantic ridge, and Africa continued to move away from South America, both the North and south Atlantic seas joined together (Palmer et al, 1999). India had eventually separated from Australia and Antarctica migrating northwards colliding with Asia in the Cenozoic era (Palmer et al, 1998; Seller, 2005).

Major influences of the paleogeography of this time come from both the increase in rifting coupled with sea level rise (Wicander et al, 2000). Sea levels in the Early Cretaceous marked a sea level rise of ~100-200m peaking in the Late Cretaceous sea at 250m higher than present day levels, marking the highest sea level rise in Earth's history (Kauffman et al, 1995; Wicander et al, 2000). Thought to have occurred due to displacement of water by the enlarged mid-oceanic ridges and higher ocean volume due to warm climates (Seller, 2005). High sea levels inundated the various continents forming shallow epicontinental seas most notable in North America (Western Interior Seaway), Europe and Africa. At this time, land consisted of only 18% of the global surface 2/3 of the present day value (Kauffman et al, 1995).

Non-synchronous transgressions arose in the Late Cretaceous formed by geo-tidal eustasy whereby differential masses on earth's surface caused bulges, allowing differential sea level heights in the various worldwide seas and basins (Wicander et al, 2000; Seller, 2005). Due to constriction of oceanic circulations and low differential

temperatures in the equator and polar-regions, a number of oceanic anoxic events occurred (mainly during the mid-Cretaceous) depositing characteristic black shales such as the Bonerelli event (Selby et al, 2009).

Oceanic anoxic events conceptualised by Sclanger and Jenkyns (1967) characterised the Cretaceous period and occur on a number of occasions within varying geographical and temporal scales. They defined periods of time where much of the world's oceans were severely depleted of oxygen, depositing large carbon rich sediments. Two main OAE events are observed for this period; OAE1 comprised of several events during the Apitan-Albian and OAE2, which coincided with the end of the Cenomanian. OAE1a is the most studied of all the sub OAE1 events and is known as the Selli event (Menegatti et al, 1998), occurring within the early Aptian ~119 Ma.

The OAE2 Cenomanian-Turonian boundary event is commonly refered to as the Bonarelli event (Arthur et al, 1988; Tsikos et al, 2004; Karakitsios et al, 2007) and is type-casted from the Marche Umbria (Italy) locality, measuring as a thin (30-35cm) highly enriched carbon rich black shale (44.5 WT% TOC) located close to the Cenomanian-Turonian Boundary (93.9 ± 0.2 Ma). It bought on the extinction of many species including 27% of all marine, invertebrates (Karakitsios et al, 2007). How OAE events occur is a controversial and debatable topic and is thought to be a process of a multitude of factors. Large-scale volcanism (Jenkyns et al, 1993), dissociation of gas hydrates (Larson et al, 1999) and increased biological production (Pancost et al, 2004) have been studied to determine the cause of such events. Primarily, OAE2 is thought to occur due to the sub-oceanic volcanism coinciding with peak crustal productivity (Jenkyns et al, 1999).

Paleo-magnetically the majority of the Cretaceous occurred during a quiescence of activity compared to other periods, especially from the Early Aptian to the late Santonian whereby a period of 42 Myr was devoid of geomagnetic reversals, forming the Cretaceous Normal-Polarity super-chron (Lerbekmo et al, 1997; 2004).

Concerning the Cretaceous, three distinct realm sub-divisions existed: Northern Boreal, the Southern Boreal and the Tethyan Region.

- ***Northern Boreal***: Consisting of North America, Europe, Russia and Japan this area indicates several temperature changes during the late Cretaceous indicating that the Nothern Boreal and Tethyan regions were non linear (Skinner et al, 1995).

- ***Southern Boreal***: This area is located south of the Tethyan Region, composed of Australia and Antarctica. Bad preservation and lack of climatic indicators lack the detail for interpreting various climatic behaviors (Skinner et al, 1995).

- ***Tethyan Region***: Separating the two Boreal regions by the presence of fossilised reefs containing mainly rudist bivalves, foraminifera and certain ammonites habitable in this warmer water. The separation of North and South America deepened the marine connection between the Tethys Sea and Pacific, allowing for a strong westward current inferred from fossilized faunal patterns (Skinner et al, 1995; MacLeod et al, 1997; Seller, 2005).

Towards the end of the Cretaceous close to the K-Pg boundary the paleo-geography resembled present day positions (Fig.I.3.) of global seas and continents with exceptions such as the separation of North and South America, and the connection of Antarctica to various landmasses (MacLeod et al, 1997).

Cretaceous lithologies

High sea levels coupled with warm climates formed an abundance of cooclithophores (Skinner et al, 1995; Stanley et al, 1999) leading to the creation of huge worldwide deposits of Chalk (e.g. English Chalk section). High sea levels increased accommodation space allowing thick sedimentations of various lithologies such as limestone beds and terrestrial brackish lithologies such as those in the Western Interior Basin (Lerbekmo et al, 1997; Eberth. 2005). The severe lack of oceanic circulation and warm climates dominated the Mid-Cretaceous time, causing multiple anoxic events forming organic rich shales, typical source rocks for oil and gas such as those in the North Sea (Selby et al, 2009).

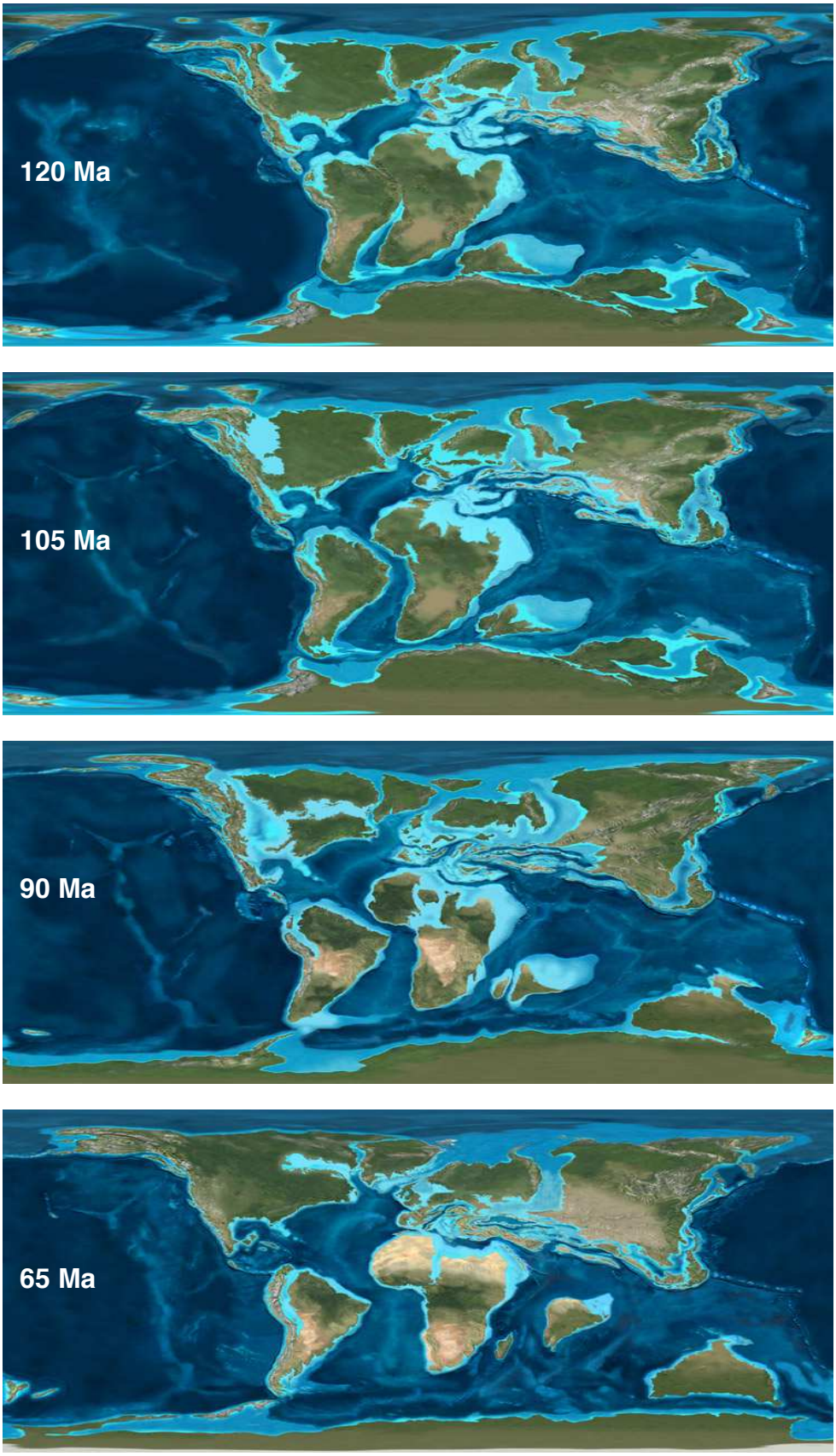

Fig.I.3. Evolution of the continents throughout the cretaceous. Note that throughout the majority of the late cretaceous a large inlet sea (Western Interior Seaway) is present in North America. (Ron Blakey, NAU Geology)

Climate

Average surface temperature of the Cretaceous ranged around ~18^{o}C (4^{o}C above present day levels), it was also characterised by a high CO_2 levels six times the present measuring 1700ppm giving way to the characteristic greenhouse world (Frakes et al, 1988; Seller, 2005).

The late Cenomanian represents the highest mean sea-level observed in the (Phanerozoic eon), past 504 million years (Seller, 2005) approximately one hundred and fifty meters above present day sea-levels. A corollary is that the highlands were at all time lows, so the landscape on Earth was one of warm broad shallow seas inundating low lying land areas on the precursors to today's continents (Wicannder et al, 2000; Seller, 2005).

Fossilised faunal assemblages show tropical to subtropical conditions as far as 45^{o}N with temperate conditions extending to the poles. In addition, many evaporate successions around 10-30^{o}N can be found in early Cretaceous sediments, indicating an arid climate (Stanley et al, 1999; Taylor et al, 2003) coupled with closed oceanic current while the presence of coals around 30^{o} pole-wards indicate humid mid-latitudes also supported by the presence of a highly weathered deposits: Laterite and Bauxite (Taylor et al, 1997).

A temperature curve throughout the Cretaceous (Fig. I.5&6.) represents a bell curve, with lower temperature in the onset of the Cretaceous rising to the mid then falling slightly toward the Paleogene (Eberth and Currie, 2005). Data from oxygen isotope ratios of marine calcitc organisms show a surface water temperature of ~30^{o}C at the equator to around 14-17 ^{o}C at the poles (Stanley et al, 1999; Wicannder et al, 2000; Taylor et al, 2003).

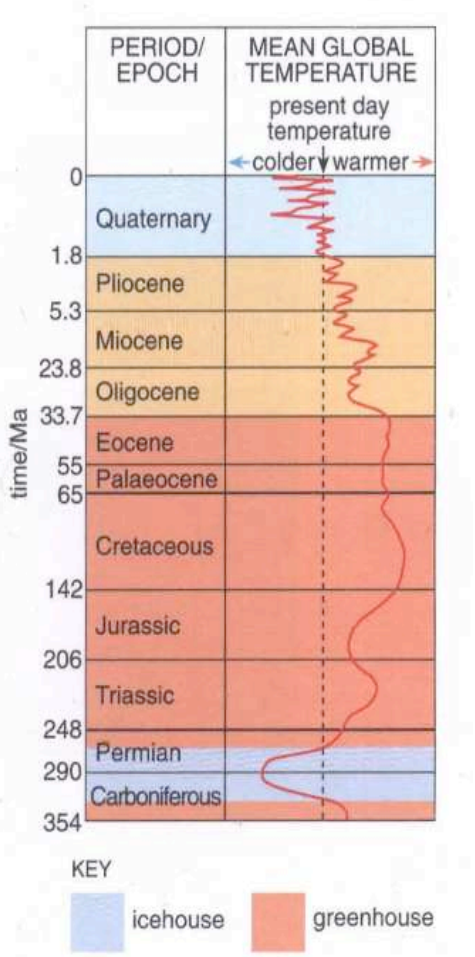

Fig.I.5. Temperature gradient for the Quaternary-Carboniferous age, Showing that the warmest temperatures were recorded in the Cretaceous period, cooling slowly to current day values. (Figure by Seller, 1995)

Oceanic currents developed from fossilized marine records show evidence of warmer water life-forms around Argentina and Africa suggesting a counterclockwise gyre in the South Atlantic ocean (Ovenchikina et al, 2005). Larger foraminifera in Ireland and the East Coast of Canada indicate the development of a proto gulf stream current in the mid Cretaceous (Stanley et al, 1999).

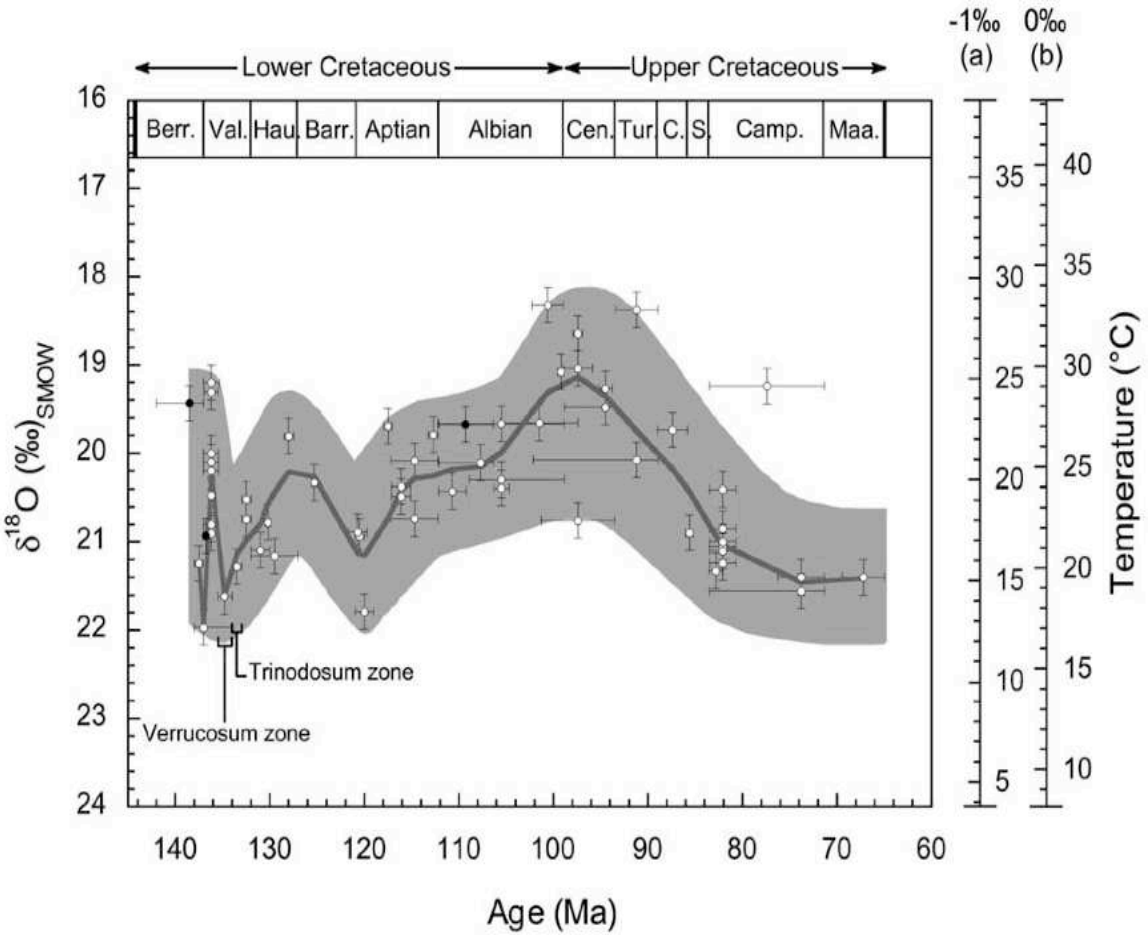

Fig.I.6 Evolution of ^{18}O values derived from fish teeth of the western Tethys during the Cretaceous. Isotopic temperatures are calculated using equations determined by Kolodny et al. (1983). The curve represents the bell shaped curve of the mean temperature rise towards the middle of the Cretaceous. Figure Taken from (Ovechikina et al., 2005)

Life

The Cretaceous period marks a bridge from early life forms from the Paleozoic to the Cenozoic era. Dinosaurs were prevalent since the Triassic and Jurassic, however angiosperms, placental mammals and most fishes developed modern day characteristics (Seller, 2005).

- ***Fauna***: Angiosperms spread throughout the Cretaceous, expanding considerably into the Campanian, prevalent due to the presence of pollination aided by insects such as bees. First representation of leafy trees and grasses developed, however ferns and conifers such as *Arucaria* (Ovechkina et al, 2005) still predominantly covered the landscape.

- ***Marine*:** Throughout the Cretaceous the marine realm mirrored closely to the division of the Tethyan and Boreal realms. Within the Tethyan region large reef forming Rudists assemblages dominated (Taylor et al, 2003), along with some less dominant reef forming corals. This is the base from the large oil/gas reservoir rocks of the Cretaceous. Other marine life commonly found in the Tethyan region are: Calcareous algae, benthic foraminifera, actaeonelid and nerineid snails. Within the Boreal regions belemnites and inoceramids prevailed in the cooler waters (Taylor et al, 2003; Ogg et al, 2004), ideal for distinguishable bio-stratigraphic markers utilised in geological timescale work. An abundance of chalk forming coccolithophores were present throughout the Cretaceous giving way to the period's name. Additionally, radiolarians, dinoflagellates and diatoms although present were less abundant (Seller, 2005; Stanley et al, 1999). Ammonites were also abundant during this time, with many species present allowing for the majority of boundaries to be defined. (Obradovitch et al, 1993; Ogg et al, 2004)

- ***Land***: Predominantly ruled by dinosaurs in the early Cretaceous, it became more diverse in North America and Asia (Eberth and Currie, 2005). Although small mammals did exist through the Jurassic-Triassic periods, the rise of Placental, and Marsupials extended its reach overtaking the dinosaurs after K-Pg Mass extinction (Seller, 2005).

I.3.1 Geochronology

Is the basis of determining ages of rocks, fossils and sediments using multiple scientific methods of varying precision. While biostratigraphy determines strata of similar ages or periods of coexistence, it creates a rough floating scale in time. The application of geochronology allows us to pin precise time.

Various geochronological methods exist that can be applied to a realm of scientific problems. In most scenarios not all dating methods (Fig.I.7) are suitable or applicable, therefore care should be taken when considering a particular method that conveys reliable results that are both accurate and precise. In some tasks, numerous methods can be utilised to create a highly tuned a geochronological history.

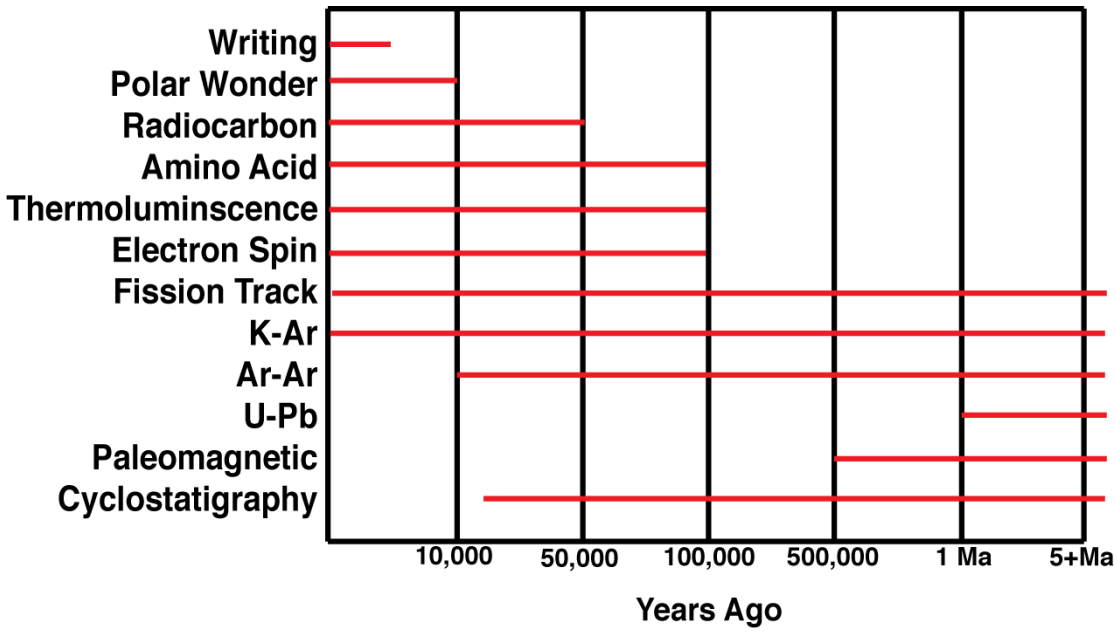

Fig.I.7 Age ranges and applications for various geochronoligcal methods. How far back in time we can use these methods.

Results and errors in geochronology exist within a magnitude of orders, datums can be well constrained in order of a particular year such as the 79AD Vesuvius eruption, (recorded in letters by Pliny) with uncertainties in millions of years such as the Jack Hills Zircons, Western Australia (Wilde et al, 2001). Errors can be extremely large but normally proportional to the amount of time that has passed. Below are some of

the most widely known/used methods in geochronology with the main emphasis to quantify ages for the geological timescale.

I.3.2 Radiometric dating.

A key method utilised in the formation of the geological timescales and used in samples of varying ages in orders of magnitude. Core principals rely on the ability to measure the amount of radioactive decay of a radioactive isotope with a known half-life allowing us to determine absolute age. Various radioactive isotopes exist in the world with suitability and practicality issued dependent on known geological times. The main radiometric isotopes currently used in timescale work are outlined below (Fig.I.8.).

Parent Isotope	Daughter	Half-Life
Uranium (U)-235	Lead (Pb)-207	704 Ma
Potassium (K)-40	Argon (Ar)-40	1.3 Ga
Uranium (U)-238	Lead (Pb)-206	4.5 Ga
Thorium (Th)-232	Lead (Pb)-208	14 Ga
Rubidium (Rb)-87	Strontium (Sr)-87	49 Ga

Fig.I.8. Common isotopes utilised in radiometric. In use, those of a closer half life to the sample of unknown are utilised.

These methods are applied to date both natural and manmade materials allowing information from evolutionary changes, man made historical changes and ages of major events such as the K-Pg Mass extinction. Coupled with geological stratigraphy, this method provides significant results on evolutionary/climate change over Earth's history and under certain conditions can be also used to date ancient artifacts.

The majority of ages derived by radio-isotopic timescale work utilise the U-Pb, K-Ar and $^{40}Ar/^{39}Ar$ dating methods. Recent advances in these methods has limited precisions to within 1% error allowing datums to correlate beds and identify certain cyclostratigraphic horizons necessary to fix relative floating timescales from orbitally forced tuning (Kuiper et al, 2008).

Alternate pieces of information can also be gathered from radioisotopic analysis such as thermochronology, allowing the extraction of closure temperatures and thermal history of the sample, thus lending information to orogenic history and possible basinal uplift rates (McDougall and Harrison, 1999). Currently the Cretaceous timescale is influenced mainly from radioisotopic ages (In particular $^{40}Ar/^{39}Ar$ dating) derived from ash horizons correlated by bio-statigraphy in the Western Interior basin (Obradovitch, 1993). The various radiometric dating methods and Cretaceous ages will be discussed in detail further in the chapter II ($^{40}Ar/^{39}Ar$) and chapter IV and V (U-Pb & $^{40}Ar/^{39}Ar$).

I.3.3 Magnetostatigraphy

A chronological correlation technique used to date relatively both volcanic and sedimentary sequences. The basic principles consist of Earth's episodic magnetic field reversals and the correlation of reversals in geological time (Fig.I.9.). Both volcanic and sedimentary sequences hold magnetic minerals reflecting the direction by primary remnant magnetism (Thermoremanent and depositional remanent magnetization) of the earth's magnetic field at Time 0.

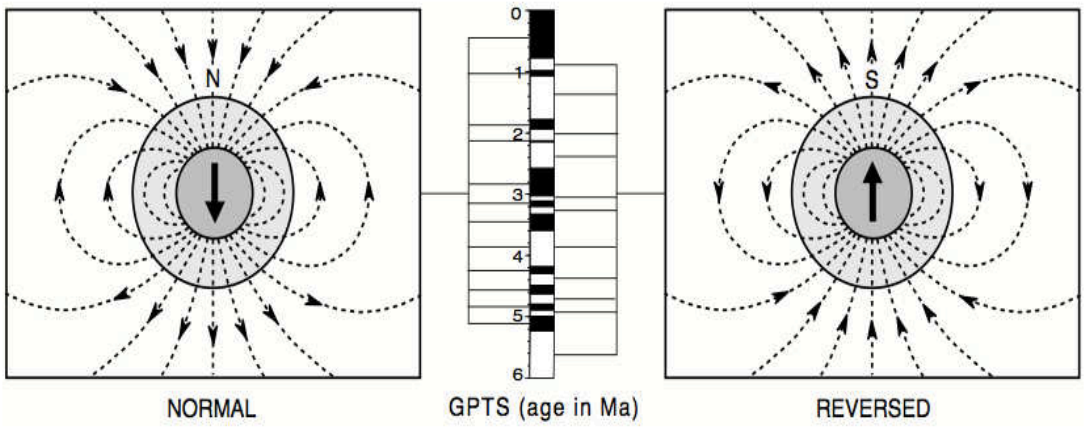

Fig.I9. Representation of Earth's magnetic field in a typical geological record.

Correlation of the observed polarity sequence can be matched to the radiometrically calibrated geomagnetic polarity time scale (GPTS) developed from well established ocean floor spreading magnetic anomalies (Berggren et al, 1995; Cande and Kent, 1995). Magnetostratigraphy is termed as a relative dating method, it requires an anchor point to match the exact magnetozone in time. Mainly radiometric ages, bio-

stratigraphic horizons or orbital tuning are utilised allow us to pinpoint the exact time and fix the polarity sequence.

Problems with this method can arise from magnetic overprinting of samples acquired through chemical and thermal change, periods of long-term reversals such as those within the Cretaceous that lead to a lack of magnetic information in that period. The magnetostratigraphic record is applied to help correlate problems between different environments especially between terrestrial and deep-sea sequences (Lerbekmo, 1995). Chapter III-V will discuss this method in detail, explaining the data acquisition technique and the process of correlating sections from the Western Interior Basin to well defined astronomically tuned European sections.

I.3.3 Astronomical tuning

Presently, one of the most accurate dating methods for the last 35 Ma, whereby astronomers provide valid orbital solutions in Earth's orbital parameters (Laskar et al, 1999; 2008). Changes in climate due to Milankovitch cyclicity is recorded in the lithology, thus matching patterns of cyclic variations in climate records with patterns of changes in solar radiation.

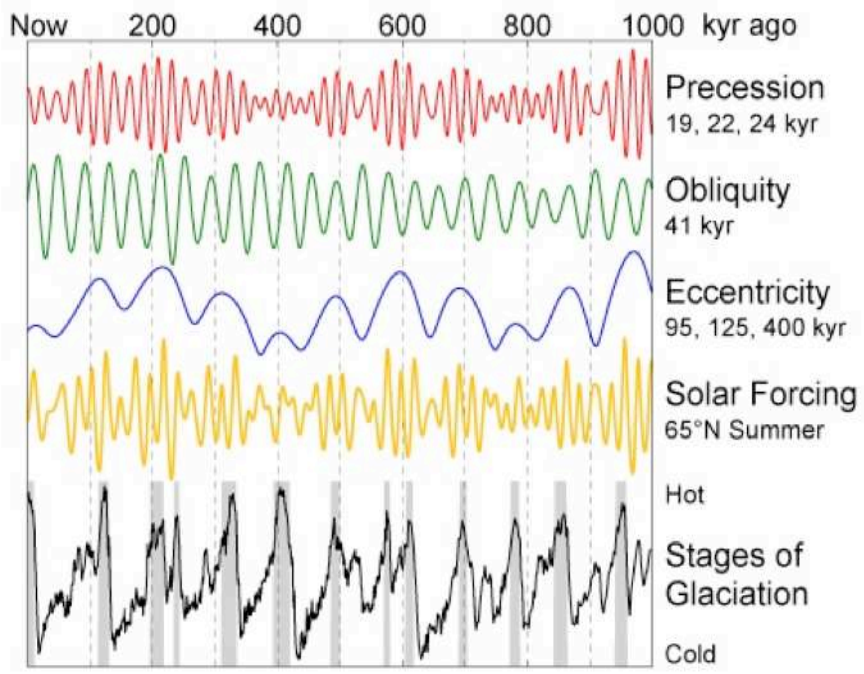

Fig.I.10, How Milankovitch cycles affect solar forcing (insulation). The precession of the equinoxes, Obliquity (Variation in earth Axis) and changes in Earth's orbit (Eccentricity) and responsible for causing changes in Earth's Climate such as the 100kyr cycle observed in the Neogene period (Quinn et al., 1991).

It is based on cyclical changes in climate proxy records mirroring variations in insolation, which can applied to a particular outcrop allowing high precision time constraints. Currently, orbital solutions by Berger and Loutre (1992) and Laskar et al. (1999) show a concise stable tuning pattern up to ~100M (Laskar et al, 1999), this method has difficulties in older Paleozoic strata due to limitations in tidal dissipation and chaotic diffusion in the inner solar system for precession and obliquity, however the more stable 404 ka eccentricity cycle which is reliant by gravitational interaction between Earth, Jupiter and Venus are recognised as stable through the Phanerozoic (Berger and Loutre, 1992; Laskar et al, 1999). Currently, many GSSP's in the Neogene have been accurately dated and recorded using this dating method.

Most astronomical dating work has been compiled on deep marine sections as they show the most stable controlled records, however work is now being compiled on fluvial sections in the Western Interior Basin such as the Hell Creek formation in Wyoming USA (Hilgen et al, 2010) and will be discussed further about the possibilities in Canada. Although accurate up to the Cretaceous period, cyclicity can be found in sediments of older age, (Herbert et al, 1999; Olsen and Kent, 1999) thus being utilised as a floating timescale, pinned down by various radiometric ages. Work is also being compiled to use cyclic controlled lithologies +100 Ma to help correct and create possible astronomical tunings for early Earth. Errors for astronomical tuning are hard to infer and climatic feedback is not an instant occurrence, and is thought to have a lag-time of around a few thousand years, still however much more accurate than radiometric methods (Kuiper et al, 2008; Hilgen et al, 2013).

I.3.4 Incremental dating

A precise annual dating technique utilising cyclical changes in the sedimentary record producing both relative and actual datums depending on the method and wherever there is an exact time 0. Such incremental dating techniques are as follows.

-Dendrochronology
-Ice Cores
-Lichenometry
-Varves
-Spleothems.

These techniques produce highly accurate ages as far back as 10 ka before present. Another main benefit adapted from these methods, allow us to deduce precise climatic variation, resulting as great paleoclimatic indicators. Other techniques within this field also include tephrachronolgy using geochemical fingerprinting to determine the unknown volcanic ash into dated tephra.

II. Standards

II.1 Introduction to $^{40}Ar/^{39}Ar$ Dating

The $^{40}Ar/^{39}Ar$ radiometric dating method was invented (Merrihue and Grenville Turner; 1966) to supersede the K-Ar dating method developed by Nier (1940), it utilises analysis of the decay ratio of isotope $^{40}K \rightarrow {}^{40}Ar^*$ with the stable form of ^{39}K, irradiated into ^{39}Ar by bombardment of neutrons in the nuclear reactor. Using these defined ratios of the decay ratio of ^{40}K to stable $^{40}Ar^*$, we are able to calculate radiometric age.

Primary uses for the $^{40}Ar/^{39}Ar$ technique allow the dating of both igneous and metamorphic minerals, reflecting the time when the mineral passed through its closure temperature, dependent on the mineral measured (~300^{o}C biotite, ~550^{o}C muscovite, McDougall and Harrison, 1999). The variable closure temperatures and abundance and occurrence of potassium in the various minerals allow us to determine eruption and thermal evolution of the mineral.

Comparing this method to previous radiometric techniques, slight age discrepancies occur within the literature (Renne et al, 1998; Kuiper et al, 2008), for instance, comparison of U-Pb and $^{40}Ar/^{39}Ar$ ages can differ due to fractionation and residence in the magma chamber, closure temperatures of the recorded minerals and values of decay constants used.

This chapter is divided into three parts, the first part describes the history, theoretical basis of the technique and fluence monitors utilised and how these factors determine the dominant values in the absolute error. Part two will discuss methodology of the Paris Sud 11 $^{40}Ar/^{39}Ar$ dating method followed by results of the incremental heating ages of the San Juan volcanic field samples and J factor uncertainty determination. It will also discuss analytical reproducibility. Part three will revolve around the repercussions on the FCT age value on geological timescales including the K-Pg boundary.

1.1 History of $^{40}Ar/^{39}Ar$ dating technique

Developed from the K-Ar technique, it started from the discovery of the individual isotopes from the two different elements. It forms one of the earliest dating techniques discovered, improving overtime immensely to the current analytical standards of today. Individually the two elements were discovered at different times with Potassium isolated in 1808 by Humphrey Davy and Argon discovered later in 1895 by Rayleigh and Ramsay. The discovery that ^{40}K decays into ^{40}Ar by Aldrich and Nier, (1948) really initiated this as a plausible decay series for radiometric dating. The first K-Ar radiometric ages were published and recognized in 1950 from analysed Sylvite Oligocene evaporate deposits (Smits and Gentner, 1950) developed from using improvements in decay and atmospheric corrections, static vacuum techniques and improved sensitivity in K% quantity.

$^{40}Ar/^{39}Ar$ dating originated from principles first developed by John Reynolds in Berkeley, while working on neutron irradiated meteorite samples, recording ^{39}Ar signal derived from neutron bombardment. Primary $^{40}Ar/^{39}Ar$ ages were obtained by Merrihue and Turner, (1966) and exponentially grew to become one of the most utilised current radiometric dating methods. The concept grew due to the unpopularity of having to measure precise concentrations of K% and the ability to simultaneously measure Argon isotope ratios, increasing the accuracy and precision of ages, thus overtaking K-Ar as the main radioisotope dating method.

Since 1966, improvements within the $^{40}Ar/^{39}Ar$ system are evolving to include a wide variety of geological problems such as basinal evolution and thermochronology. Currently, work is focused on the age of the standard used as a fluence monitor, decay constants and improvements in mass spectrometer measurements, while J factor determination is constantly pushing the boundary and accuracy of this technique.

II.1.2 Concepts the of $^{40}Ar/^{39}Ar$ dating technique

Decay channels

Potassium naturally occurs in 3 isotopes, ^{39}K (93.2581%), ^{40}K (0.0117%) and ^{41}K (6.7302%). ^{40}K is radioactive (Neir, 1935), decaying with a half life of 1.248×10^{-9} years to both stable ground state ^{40}Ca and ^{40}Ar constituents (Table.II.1). ^{40}Ar derives from in-situ decay of ^{40}K present in most minerals, being inert it does not easily bind with other atoms in the crystal lattice only incorporating once the lattice becomes a closed structure (i.e. when the temperature becomes lower than the closure temperature) entrained through radioactive decay.

Both $^{40}Ar/^{39}Ar$ and K-Ar dating techniques assume that relative abundances (Fig.II.2) of the isotopes of K are constant in rocks and minerals, essential as ^{40}K is not measured directly and is inferred from isotopic ratios. Constant ratios have been proven throughout, showing change in decay constants no greater than 0.15% (Garner et al, 1975), only in some extra terrestrial samples altered by cosmic radiation (Kendall et al, 1960; Burnett et al, 1966; Verbeek and Schreiner, 1967). Humayun and Clayton, (1994) isotopically analysed K from rocks using secondary ionization mass spectrometry and found variations of just ± 0.5‰ in $^{39}K/^{41}K$. thus considered as constant.

Isotope	Abundance (%)
^{40}Ar	99.600
^{38}Ar	0.632
^{36}Ar	0.336
^{39}K	93.2581
^{40}K	0.01167
^{41}K	6.7302

Table.II.1 Relative abundances of K and Ar isotopes.

Based upon the decay of naturally occurring isotope of $^{40}K \rightarrow {}^{40}Ar$. Decay of this isotope decays non linearly into a branching pattern (Fig.II.2):-

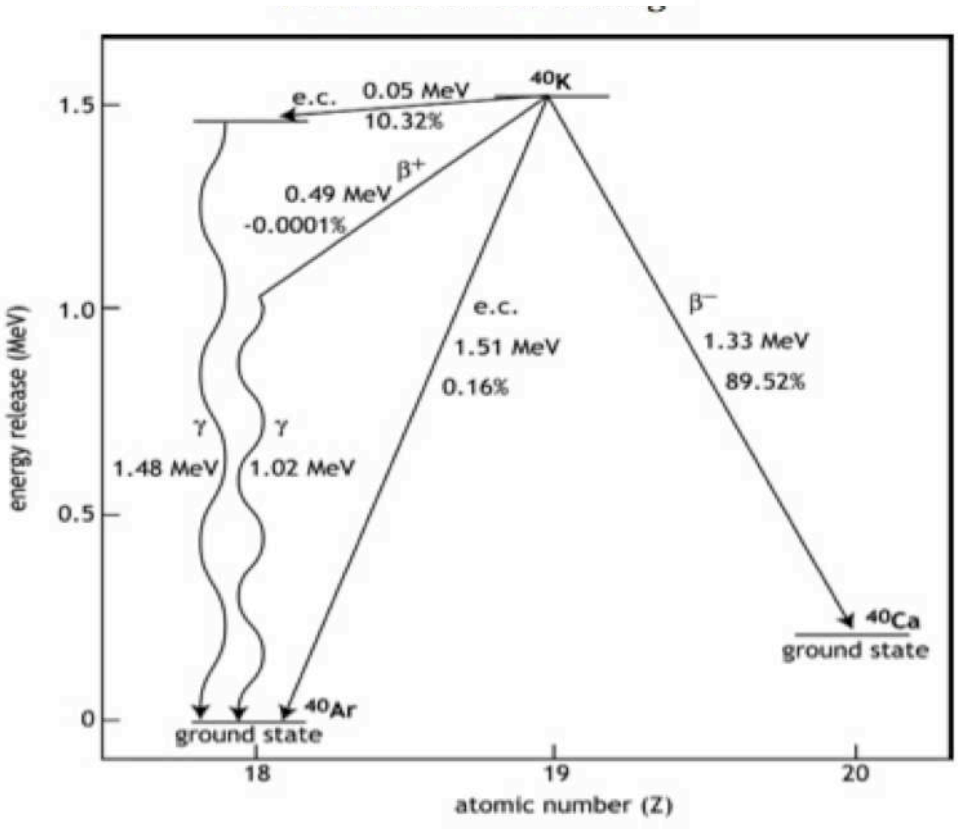

Decay	Decay Factor	Value
$^{40}K \rightarrow 40Ca$	λ_{β^-}	$4.692 \times 10^{-10}\ a^{-1}$
$^{40}K \rightarrow {}^{40}Ar$	λ_e	$0.572 \times 10^{-10}\ a^{-1}$
$^{40}K \rightarrow {}^{40}Ar$	λ'_e	$0.0088 \times 10^{-10}\ a^{-1}$
Combined	$\lambda = \lambda_{\beta^-} + \lambda_{ec} + \lambda'_{ec}$	$5.543 \times 10^{-10}\ a^{-1}$

Fig.II.1 Taken from McDougall and Harrison (1996). Decay scheme for ^{40}K illustrating the dual decay to ^{40}Ca (89.5%) and ^{40}Ar (10.5%) . Note that the ^{40}K to ^{40}Ar branch is dominated by electron capture. The table beneath shows each decay scheme along with the route in which the particular element decays. (Dalrymple and Lanphere, 1969). It should be noted that the ^{40}Ca is the dominant ^{40}K decay branch, however its common attribute in nature hinders the ability to detect enrichments in ^{40}K ,makes it not an ideal attribute in the dating decay scheme.

$^{40}K \rightarrow {}^{40}Ar$ predominantly decays by orbital electron capture with a net release of 1.51MeV and occurs by capture of an extra nuclear electron by a proton, converting it to a neutron with emission of neutron, thus producing an isobaric daughter nuclide.

II.1.2.2 Age equation

When utilising this dating method a few rules and assumptions must be considered before a reliable age datum can be extracted from the ^{40}Ar-^{39}Ar:

- ^{40}K nuclide decays independently of external influences such as pressure and temperature and must be constant.
- $^{40}K/K$ ratio is constant at any given time (Variations of only 0.015% have been measured by Garner et al, 1975).
- That all radiogenic ^{40}Ar measured results from the in-situ decay of ^{40}K.
- Corrections for any non-radiogenic argon such as atmospheric contamination can easily be calculated and deducted.
- The sample must have remained a closed system since the event being dated, including gain or loss of either argon or potassium. This assumption varies with samples of complex geological and thermal histories, thus a step heating technique is utilised to extract information from partially opened systems.

II.1.2.3 Calculating ages

The K-Ar age equation is simply given as

Eq.2.1
$$t = \frac{1}{\lambda} \ln \left[1 + \frac{\lambda}{\lambda_e + \lambda'_e} \frac{^{40}Ar^*}{^{40}K} \right]$$

Whereby t is the time since closure, λ is the total decay of ^{40}K and (λe + λ'e) is the partial decay constants of ^{40}Ar.

In conventional K-Ar dating, a K-bearing sample is split into two fractions: one is analyzed for its potassium content, while the other is fused in vacuum to release the argon gas. After purification has been completed, a spike enriched in ^{38}Ar is mixed in and the atomic abundance of the daughter product ^{40}Ar is measured relative to the ^{38}Ar added. In the Cassignol-Gillot technique the stability of the analytical conditions prevent the use of ^{39}Ar tracer.

Similar to K-Ar the $^{40}Ar/^{39}Ar$ dating method is based on the same decay scheme, however unlike previous techniques, measurements are dealt in the same sample, thus eliminating the need for separate aliquot experiments. For the $^{40}Ar/^{39}Ar$ method the ^{39}Ar generated from ^{39}K during irradiation with fast neutrons is proportional to the present ^{40}K as $^{40}K/^{39}K$ ratio is essentially constant in nature therefore the $^{40}Ar/^{39}Ar$ ratio is proportional to age.

The $^{40}Ar/^{39}Ar$ date equation is noted as the following:

Eq 2.2
$$t = \frac{1}{\lambda} \ln\left[1 + J\frac{^{40}Ar^*}{^{39}Ar_K}\right]$$

Whereby the age of the sample is exactly proportional to the ratio of the two argon isotopes. To obtain the $^{40}Ar^*/^{39}Ar$ ratio the following must be calculated:-

Eq.2.3
$$^{39}\mathrm{Ar_k} = {}^{39}\mathrm{K}\,\Delta\int \varphi(\varepsilon)\sigma(\varepsilon)\mathrm{d}(\varepsilon).$$

Δ representing the duration of irradiation

$\varphi(\varepsilon)$ neutron flux energy

$\sigma(\varepsilon)$ nutron capture cross section of ^{39}K

^{39}Ar is formed during the irradiation of the sample in a fast-neutron nuclear reactor. $^{40}Ar^*$ is formed naturally from the decay of ^{40}K over time, from equation 2.1 it can be obtained as follows:

Eq 2.4
$$^{40}\mathrm{Ar}^* = {}^{40}K\ \frac{\lambda_e + \lambda'_e}{\lambda}\left[(e^{\lambda t}) - 1\right]$$

Combining the equations 2.3 and 2.4 together for the number of atoms formed from neutron bombardment and $^{40}Ar^*$, we get the ratio of $^{40}Ar^*/^{39}Ar$:

Eq 2.5
$$\frac{^{40}Ar^*}{^{39}Ar_K} = \frac{^{40}K}{^{39}K}\frac{\lambda_e + \lambda'_e}{\lambda}\frac{1}{\Delta T}\frac{\left[(e^{\lambda t}) - 1\right]}{\int \varphi(\varepsilon)\sigma(\varepsilon)d(\varepsilon)}$$

This can be easily simplified by defining it as a dimensionless irradiation number related as parameter J

Eq 2.6
$$J = \frac{^{39}K}{^{40}K}\frac{\lambda}{\lambda_e + \lambda'_e}\Delta T \int \varphi(\varepsilon)\sigma(\varepsilon)d(\varepsilon)$$

The J-value is discussed further in this chapter, but is essentially calculated using flux monitor standard minerals of know age intermittent between samples of unknown age to deduce the neutron flux across its axis. From equation 2.1, it can be calculating using.

Eq 2.7
$$J = \frac{e^{\lambda Ts}}{\frac{^{40}Ar*}{^{39}Ar_k}}$$

Whereby Ts is the age of the standard, and the $^{40}Ar^*/^{39}Ar_k$ is the measured ratio.

This technique has evolved and its errors involved are lower than in K-Ar dating as exact determination of K is not needed, however the $^{40}Ar/^{39}Ar$ results are based on relative dates, and in order to calculate actual datums it must be compared to a standard of known age herein lying the main problem

II.1.2.4 J-Value.

$^{40}Ar/^{39}Ar$ dating has huge potential for age determination in geological realms, however limitations in its decay constant and age calibrations of its sample has limited its accuracy to ~2% error. While very well constrained and deemed in some areas the more reliable of the two methods, the U-Pb dating method has some limitations such as sample residence time in the upper crust magmatic chamber and accuracy dating younger samples. Therefore to accurately utilise the $^{40}Ar/^{39}Ar$ dating method to its full benefit, much work has to be done to figure out the discrepancies.

J-value is determined as the quantity of $^{39}Ar_k$ formed during neutron bombardment and is proportional to ^{40}K, to the irradiation duration and efficiency (Eq 2.6). To calculate the neutron bombardment on unknown age samples (Eq 2.7), a flux monitor

standard of known age is added to the irradiation. Using the comparison of know ages it is possible to determine the J curve along the irradiated tube, Thus allowing us to effectively date the unknowns.

To accurately measure the J-value of the "unknown" sample it is necessary to have a well established "age known" sample called standards. The problem lies in the fact that even for "age known" standards the proposed age of the sample varies considerably between published studies (e.g. Renne et al, 1998; 2010; Kuiper et al, 2008; Channell et al, 2010). It should also be noted that neutron fluence gradients vary in a 3 dimensional array, and is significant in the Y and X axis varying up to 1.0% cm (Renne et al, 1998), thus important to quantify. Throughout this chapter we will discuss how we calculate the J-factor neutron flux and how we can determine the J-parameter uncertainty on our ages.

II.1.2.5 Correction Factors

To calculate the final age of the sample, McDougall and Harrison, (1999) explain in detail the corrections and assumptions needed when finalizing ages for such a method and the following are outlining the main basic principles taken into account.

Atmospheric Argon

Measurements and composition of atmospheric argon must be taken into account when using this method (also applicable to the K-Ar technique) to discriminate any contaminating atmospheric argon contained within the sample and vacuum system where the gas from the sample is released into. To determine the mass discrimination of atmospheric argon in the mass spectrometer a derived value 295.5 Steiger and Jager (1977) is used, this correction is assuming that all of the ^{36}Ar is of atmospheric origin, after all other corrections (see below) have been accounted for.

Nuclear interference

Calcium

Calcium derived isotopes can be corrected by measuring the ratio of the different isotopes relative to ^{37}Ar in a CaF_2 salt as it is determined that the ^{37}Ar measured is in direct agreement with the proportionality of Ca in the system. As the decay of ^{37}Ar

has a half-life of 35.1 days it is important to date and correct samples 6-8 months since irradiation. This measurement allows the determination of the $[^{36}Ar/^{37}Ar]_{Ca}$ and $[^{39}Ar/^{37}Ar]_{Ca}$ ratio involved in the $^{40}Ar^*/^{39}Ar_K$ calculation.

Potassium

The reaction of ^{40}K->^{40}Ar by neutron bombardment is corrected similar to that of the calcium derived interference. To calculate this a K rich salt is irradiated and the ^{36}Ar is assumed atmospheric, then utilising a salt such as K_2SO_4 the $[^{38}Ar/^{39}Ar]_K$ correction is derived.

II.1.2.6 Decay Constants

Decay rates of ^{40}K are continuously up for debate with most utilising the constants derived from Steiger and Jager, (1977). Evolving accuracy and the need for precise datums within the community has made it important to fully quantify such numbers. Recent publications of Renne et al. (2010), and Min et al. (2000) have helped draw attention in these decay rates (Table.II.2). A more detailed study has recently proposed new values (Renne et al, 2010) however it should be noted that the decay constants of Steiger and Jager are statistically indistinguishable from these new values. For sake of comparison with other studies, we will use throughout this study the widely used Steiger and Jager, (1977) values.

Decay Factor	Steiger and Jager (1977)	Renne et al (2010)
λ_{β^-}	4.692×10^{-10} a^{-1}	$(4.9737 \pm 0.0093) \times 10^{-10}$ a^{-1}
λ_e	0.572×10^{-10} a^{-1}	$(0.5755 \pm 0.0016) \times 10^{-10}$ a^{-1}
λ'_e	0.0088×10^{-10} a^{-1}	0.0088×10^{-10} a^{-1}
$\lambda = \lambda_{\beta^-} + \lambda_{ec} + \lambda'_{ec}$	5.543×10^{-10} a^{-1}	$(5.5492 \pm 0.0093) \times 10^{-10}$ a^{-1}
$\lambda_e + \lambda'_e / \lambda_{\beta^-}$	0.117 ± 0.001	0.117
$.\lambda / \lambda_e + \lambda'_e$	9.540	9.497
$T_{1/2} = \ln 2 / \lambda$	$1.250 (\pm 0.002) \times 10^9$ a	1.491×10^9 a

Table.II.2. Comparison of decay constants for ^{40}K derived from Steiger and Jager (1977) & Renne et al. (2010)

II.1.2.7 Error propagation.

Data acquistions, signal regression and ages are calculated using an in-house program developed by Xavier Quidelleur (using a labview software), following protocol from McDougall and Harrison, (1999). Error propagation is based on the variance contribution from each parameter and is determined by the weighted squared partial derivative of the age function.

Error propagation has simply been calculated by the formula derived from Dalrymple et al. (1981):

$$\sigma_t^2 = \frac{J^2\sigma_F^2 + F^2\sigma_J^2}{\lambda^2(1+FJ)^2}$$

Whereby: σt is the age error

J is error on equation J equation

F is the $^{40}Ar^*/^{39}Ar_K$ ratio

λ is the combined decay constant

σr is the error on the $^{40}Ar^*/^{39}Ar$ ratio

σj is the error on the J value.

The collection of all parameters can be assessed as the numerical error (Scaillet et al, 2000), however when dealing with J you need to combine not only the analytical error but also the systematic error determining the standard uncertainty and the neutron flux based on the developed J-curve. Later in this chapter I will discuss how we are able to fully quantify the uncertainty surround the J-value and how this is used to determine total age uncertainty.

II.2. Fluence monitors.

In this chapter I will discuss the relative uses of some of the major monitor flux standards, how they were dated and any issues affecting their reliability.

Certain qualifications must be met when using a sample as a flux monitor, the following is an outline of such aspects:

- *Uniform $^{40}Ar/^{40}K$ ratio.*
- *Potassium and radiogenic argon should be homogeneously distributed within the crystal lattice.*
- *Should be of similar age to an order of magnitude to the sample of unknown age.*
- *The ideal crystal size, to eliminate effects such as recoil in the smaller grains or inclusions in larger sized crystals.*
- *Sufficient quantity to provide collaboration and continuity.*
- *Simple cooling history.*

Once these have successfully been determined, calibration and inter-laboratory measurements are usually carried out to determine its uses within the dating community (Dalrymple et al, 1981; Roddick et al, 1983; Lanphere et al, 1990).

II.2.1 The major flux monitors.

Most $^{40}Ar/^{39}Ar$ laboratories utilise a variety of standards in their work from own laboratory standards, inter-laboratory and inter-project standards. The following standards are the most currently utilised and the evolution of the flux monitor ages will be discussed.

-Fish Canyon Tuff sanidine (FCs)
-Taylor Creek Rhyolite sanidine (TCRs)
-HD-B1 biotite
-MMhb-1 Hornblende

A brief geological background will be given for the FCT and TCR as these are widely used in both this thesis and current work, however discussions will also include HD-B1 and MMhb-1 fluence monitor ages.

II.2.2 Fish Canyon Tuff.

San Juan Volcanic Field

The most well known and utilised of the present $^{40}Ar/^{40}K$ dating community standards; Fish Canyon Tuff (FCT) is the largest pyroclastic (Lipman et al, 1970) intermediate to silicic volcanic ash flow (5000km^3) deposit found in the San Juan volcanic field centered at La Garita Caldera (Fig.II.2.), Colorado, USA. Stretching to an area the size of 25000km^2, the tuff is assured to belong to single stage eruption, based on its geochemical signature of high chemical consistency SiO_2, matrix and consistent phenocryst content and composition (Bachmann et al, 2007).

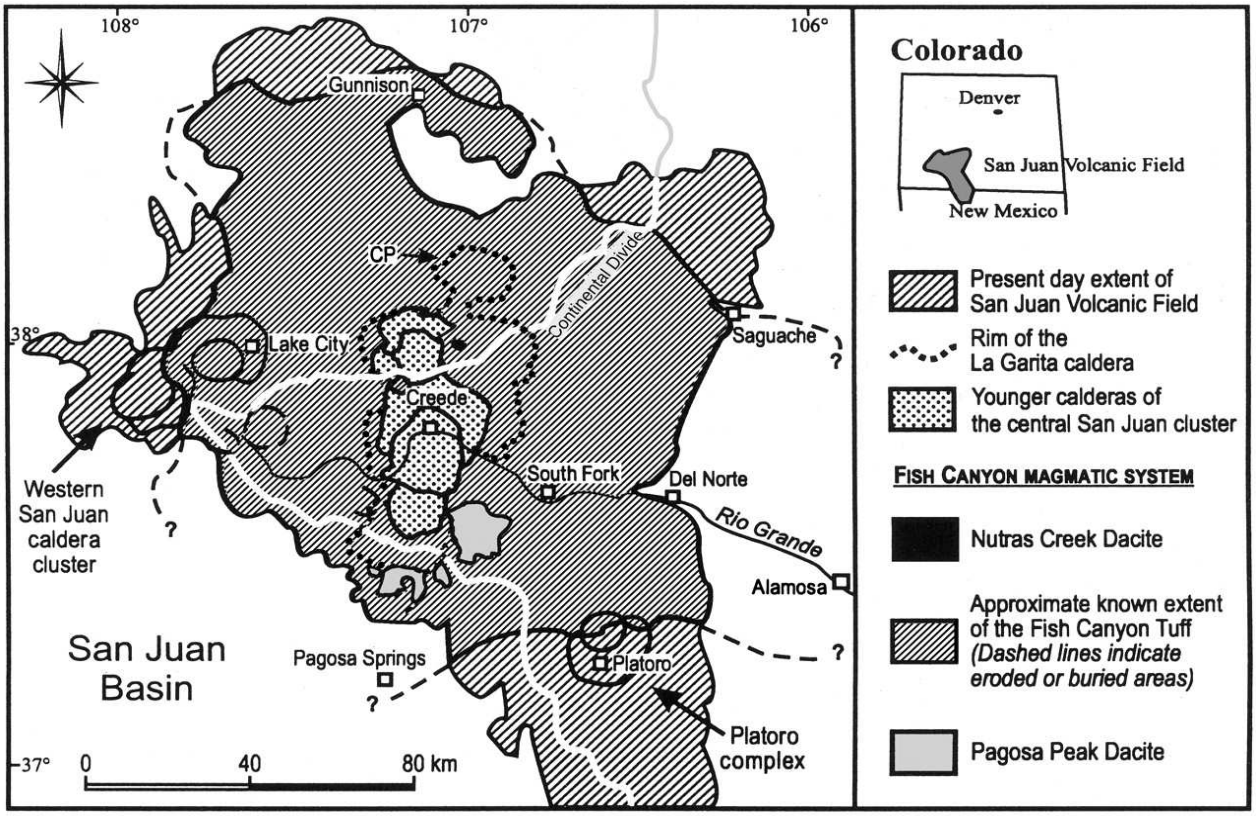

Fig.II.2. Schematic geological map of the San Juan Volcanic field, Colorado, USA (Bachmann, et al, 2007).

The San Juan volcanic complex has a volume of ~40,000km^3 primarily formed from andesitic magnetism during 35-30 Ma with large explosive eruptions ageing from ~29 Ma, it records numerous (~18) large silicic ash flow sheets (Bachmann et al, 2007). Around the FCT eruption a series of 9 major ash flows dominated the central San Juan cluster and forms one of the largest deposits within this field. During the Miocene and the opening of the Rio Grande rift, volcanism changed to a basaltic and high siliclastic alkali rhyolite (Bachmann et al, 2007).

Throughout the short cluster of events surrounding and including the FCT, three rapid placement events occur:

- Pre caldera Pagosa Peak Dacite (PPD)
- Syn collapse Fish Canyon Tuff (FCT)
- The post collapse Nutras Creek Dacite (NCD)

Individual characteristics:

PPD

Immediately predating the eruption of FCT, a 200 km^3 low energy pyroclastic deposit petrologically identical to FCT (Bachman et al, 1999). However, structurally entirely different to the FCT, it contains 90% high proportion of poorly vesculated magmatic fragments developed in a fine-grained matrix.

FCT

A medium to silicic volcanic body with high K Calc-Alkaline chemistry it gives a key recognizable geochemical signature. Erupted in short succession from the collapse of the La Garita caldera, un-zoned crystal rich dacite with solidus mineral assemblages of zircon, feldspars, quartz, in a silicic matrix glass (Whitney et al, 1985). It is characterised as a phenocryst rich crystal vitric tuff with no sorting and minor gradational variations. Emplacement was rapid shown by absence of welding breaks in the outflow facies and is presumed to be within the order of days (Bachman et al, 2007).

Geochemical and textural displays show evidence for simultaneous dissolution of feldspar + quartz of hydrous phases reheating form 720-760^oC (Bachman et al, 2002; 2005), coupled with high crystallinity FCT cooled to a near solid crystal mush before partial re-melting suggested to of occurred by upward percolation of hot water rich fluid phases through the crystal rich mush, rather than a significant re-heating event (Bachmann et al, 2007). Fish Canyon Tuff, is ideal for a flux monitor standard due to its homogenous composition, high crystal contents and lack of compositional zoning in pre-eruptive magma chamber (Silva et al, 1991).

NCD

Nutras Creek Dacite is a small post eruption lava flow following the FCT eruption. It is characterised by exposures of devitrified flow banded Fish Canyon magma and outcrops on the northern flank of the resurgent dome of the La Garita caldera (Bachmann et al, 2007).

The three individual flows (PPD, FCT and NCD) that create the San Juan Volcanic field are indistinguishable in age and are the main focus of this Chapter.

2.3 Previous Literature of FCT

Currently the main emphasis of the $^{40}Ar/^{39}Ar$ community seems to focus on the age of the FCT as its main standard whereby Cebula et al. (1986) initially proposed the use of FCT as a possible flux monitor. Since the primary age developed from Steven et al. (1967) there has been vasts amount of published literature (Fig. II.3, Table II.3) attaining ages from a array of methods such as U/Pb and $^{40}Ar/^{39}Ar$ alongside astronomically tuned ages. Some ages were calculated by fission track dating, but with such large uncertainties they will not be included in this chapter, additionally ages derived from the Rb/Sr method should be cautionally examined due to the relatively large uncertainty of the ^{87}Rb decay constant.

The bulk of ages were derived from inter-calibration with a primary standard (such as MMHB-1 Hornblende, and GA1550 Biotite) whose age was previously determined by K-Ar dating. Over time, aspects of each primary standard such as K content were re-measured against the original ages reported in such articles as Beckinsale and Gale, (1969) and updated to represent the total error. U/Pb ages derived from Oberli. (1990), Lanphere and Baasgaard, (2001) and Schmitz and Bowring, (2001) show varying ages of older and younger age estimates of FCT due to a variety of factors. Lanphere and Baasgard, (2001) achieved a younger age but was inferred due to possible lead loss and inheritance. While ages derived from Orberli et al, (2002) and Schmitz and Bowring, (2001), exhibit older ages than any other method partly due to prolonged residence time in the magma chamber.

Other FCT ages have utilised individual well constrained events such as Vesuvius or astronomical tuning to develop a strong age model, (Hilgen et al, 1997; Renne et al, 1998b), these however run into problems such as high errors in young samples on the $^{40}Ar/^{39}Ar$ method. Moreover, combining the astronomical tuning methods towards tephras of known age to acquire the FCT age has become the tool to define standard age irrelative from K-Ar.

Currently the two main ages of Renne et al. (2012) and Kuiper et al. (2008) are currently the most utilised and will be discussed further .

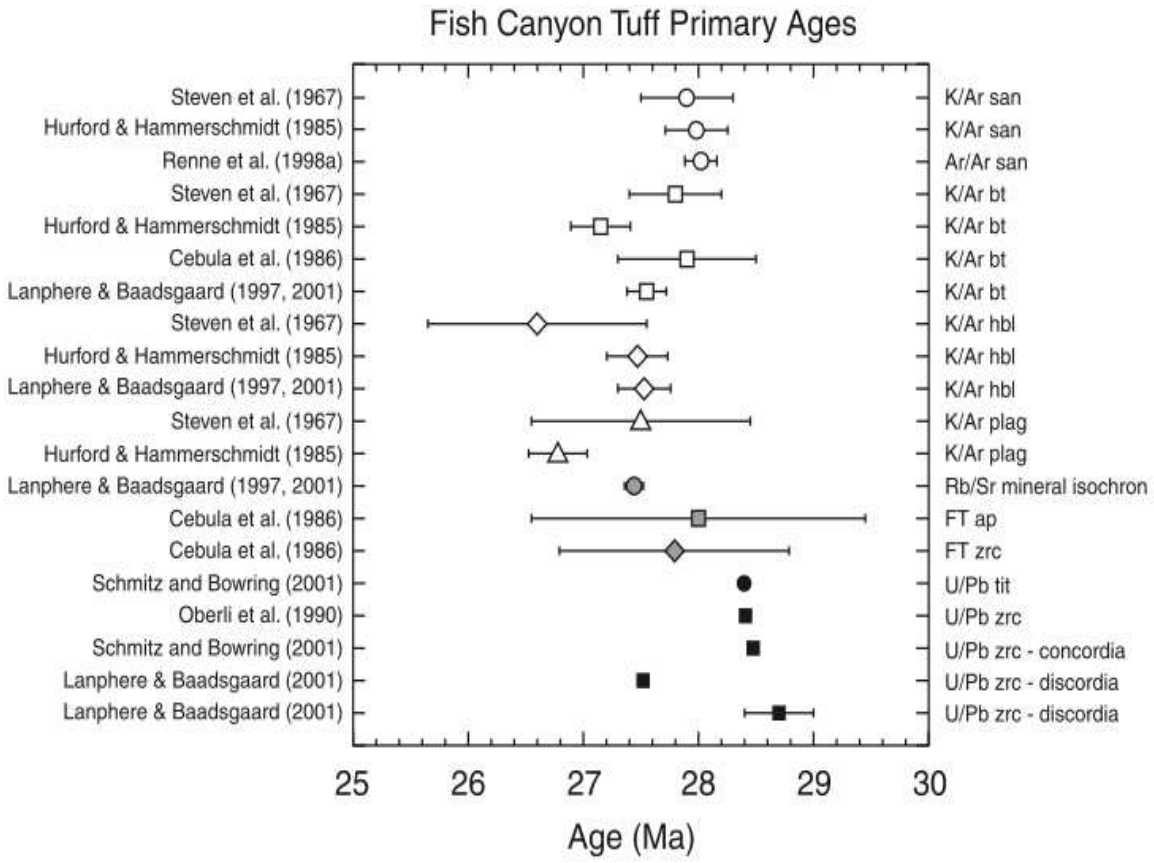

Fig.II.3 Part 1. Fish canyon primary tuff ages from Fig.II.5, against the various geochronological methods utilised.

Table of main ages

Analytical method	Age (Ma±1σ)	Study
K/Ar	27.9 ± 0.4	Steven et al. (1967)
K/Ar	27.4 ± 0.4	Hurford and Hammerschmidt, (1985)
K/Ar	27.9 ± 0.6	Cebula. (1986)
U/Pb	28.4 ± 0.1	Oberli et al. (1990)
Ar/Ar	28.09 ± 0.10	Wijbrans et al. (1995)
Astronomical	28.15 ± 0.19	Hilgen et al. (1997)
U/Th-He	30.1±0.5	Reiners and Farley. (1999)
Ar/Ar	28.02 ± 0.16	Renne et al. (1998)
Ar/Ar	27.98 ± 0.075	Villenueve et al. (2000)
U/Pb	28.48 ± 0.03	Schmitz and Bowring. (2001)
U/Pb	27.52 ± 0.05	Lanphere and Baadsgaard. (2001)
U/Pb	28.36 ± 0.03	Oberli et al. (2002)
Ar/Ar + Astronomical	28.201 ± 0.023	Kuiper et al. (2008)
Ar/Ar	28.305 ± 0.036	Renne et al. (2010)

Table.II.3 Fish canyon primary tuff ages from the previous table, against the various geochronological methods utilised. Note that the Rb/Sr age do not include the uncertainties in its decay constant.

II.2.4 Kuiper et al. (2008):

28.201 ± 0.046 Ma

A FCTs age derived from cyclostratigraphy and synchronization to astronomically calibrated tephras form the Melilla section Morocco. Although attempted previously to calibrate the $^{40}Ar/^{39}Ar$ dating method to the astronomical solution, no suitable section could be found. This required a section able to indentify magnetostratigraphic boundaries, relative constant sedimentation rate and suitable mineralogy such as sanidine (suitable size minerals for decreased recoil and open-system alteration).

The Melilla section was astronomically tuned and correlated against a well tuned Mediterranean reference section that is utilised in the Neogene time scale GTS2004, matching the number of sedimentary cycles with that of the reference core. Advancements in sensitivities of mass spectrometers have allowed single sanidine

crystal measurements thus diminishing the error associated with bulk mass age distributions. Several ash levels were sampled and extracted from various tephra layers in the section.

The known tephra ages obtained from the Melilla horizons were used as the flux monitor and dated the FCT as the unknown. The samples were then dated at the Vrije University (VU) Amsterdam (Fig.II.4) and at the Berkley Geochronology Centre (BGC) using the decay constants of 5.463 ± 0.214x10^{-10} (Min et al, 2000) they obtained an age of 28.201 ± 0.046 Ma (Fig.II.6).

The comparisons of the FCT standard ages against U/Pb also show a constant 1% bias between ages. However with the revised Kuiper et al. (2008) age the U/Pb and $^{40}Ar/^{39}Ar$ approached concordance.

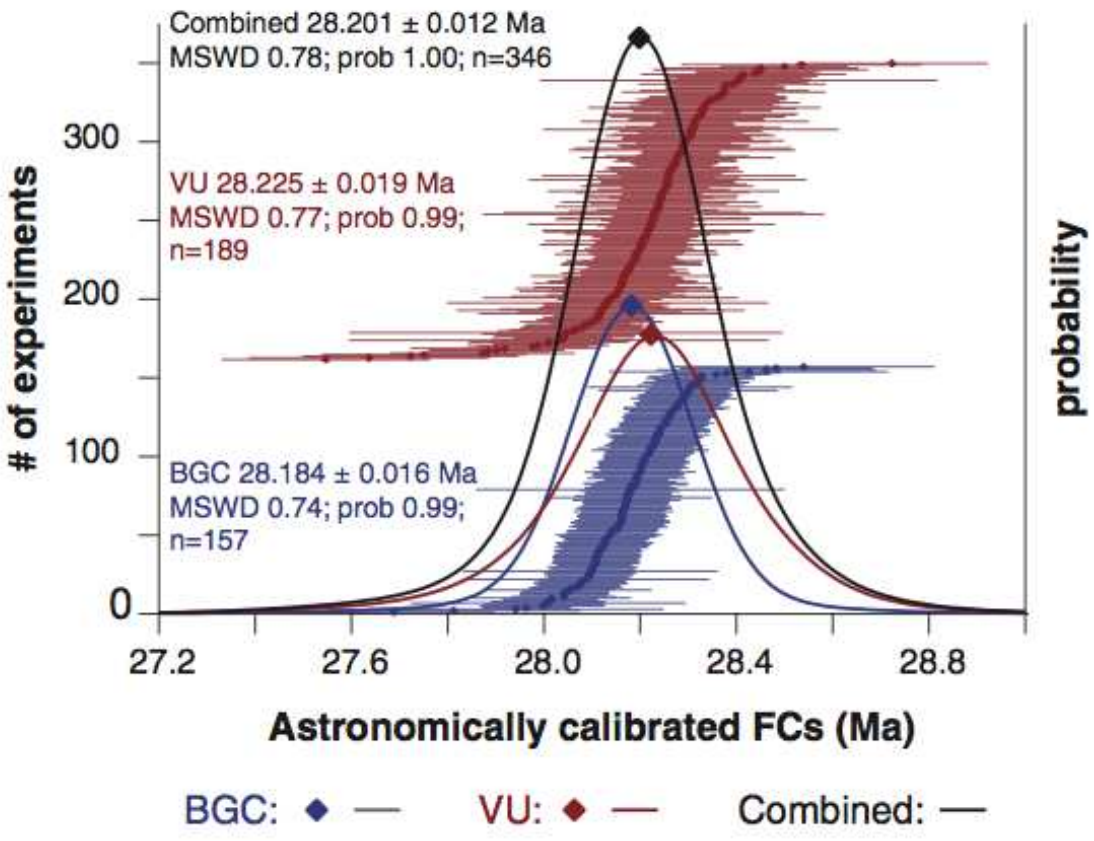

Fig.II.4 from Kuiper et al. (2008). Astronomically calibrated FCT ages, using astronomically tuned Tephras, FCT was dated as unknonhwns. These results are of single crystal fusion dates only displayed at 1sigma erorr. Using the uncetainity in astronomical age of ± 10ky and FCT age of 28.201 ± 0.012 Ma a final age of 28.201 ± 0.046 Ma is deduced. Note that each single measurment is obtained with a typical uncertainty of 0.1 to 0.2 Ma.

II.2.5 Renne et al. (2010)

28.305 ± 0.036 Ma

This is the most recent published standard age of the FCT flux monitor and is established from the past Renne et al. (1998) determinations, however the updated 2010 version combined information on new calculated decay constant (Beckinsale and Gale, 1969; Steiger and Jager, 1977; Renne et al, 2012).

The primary Renne et al. (1998) age of FCT 28.02 ± 0.28 Ma derived from mass calculations of numerous irradiations and single crystal laser fusion $^{40}Ar/^{39}Ar$ geochronology. Using both primary MMHB-1 and GA-1550 standards to second principle Alder Creek, FCT and TCR, inter-calibrations between the same samples as Karner and Renne, (1998) were able to demonstrate an age based on a primary standard dated by K-Ar and can be utilised to calibrate various secondary standards.

Samples were irradiated in eleven separate batches, and measured in the BGC laboratory using singles crystal total fusion with relative analysis error ~0.3%, FCTs ages were found to be highly reproducible. However the large systematic errors are caused by incoherences in the imprecise K and Ar decay systems i.e decay of ^{40}K by electron capture. Improvements of the decay constant and the age of FCT were calculated by comparing $^{40}Ar/^{39}Ar$ ages of volcanic rocks with ages determined by other methods such as U-Pb dating. Renne et al. (2010) addressed the older utilised decay constants (Steiger and Jager, 1977) by statistical optimization and constraints from ^{40}K activity, K-Ar isotopic data, U-Pb ages alongside $^{40}Ar/^{39}Ar$ results, comparing them to estimate the partial decay constants of FCT at :

FCs $^{40}Ar^*/^{40}K$ ratio $(1.6418 \pm 0.0045) \times 10^{-3}$

$\lambda e -$ $(0.5755 \pm 0.0016) \times 10^{-2}$

$\lambda \beta -$ $(4.9737 \pm 0.0093) \times 10^{-10}$

This older age attained by Renne et al. (2010) approaches the youngest zircon ages reported by Schmits and Bowring, (2001). It should be noted that when using this FCT age for the flux monitor standard, their new decay constants must be utilised.

II.2.6 Taylor Creek Rhyolite Sanidine

Formed in the Mogollon Datil volcanic field, Craton County, (New Mexico, USA) the TCR is formed of ~20 lava flows / domes over an area of 100km^2. The rhyolite contains 15-35% rounded eu-hedral and sub-heudral quartz, sanidine plagioclase with traces of biotite and hornblende phenocrysts (Duffield et al, 1990). Chemically it is composed of 77.5 ± 0.3% SiO_2 content with little varying composition and near constant feldspar phenocryst species, it is homogeneous in its $^{40}Ar^*/^{39}Ar_k$ ratio. $^{40}Ar/^{39}Ar$ ages obtained for products of this volcanic field show a growth period of no more than 100,000 years (Duffield and Dalrymple, 1990) making it a relatively instantaneous exposure, erupting from a single magma chamber.

Apparent ages of TCR (Table.II.4) are determined independently from primary standards derived from K-Ar ages (Inter-calibrated to primary GA1550), additionally, ages are calculated relative to FCTs ages. Although similar in composition and age to FCT, a non-uniform distribution is occurent (Renne et al, 2010).

Analytical method	Age (Ma±1σ)	Study
K-Ar	24.0 ± 0.5	Elston. (1973)
K-Ar	27.7 ± 0.9	Ratte et al. (1984)
Ar/Ar	27.92 ± 0.08	Duffield and Dalrymple. (1990)
Ar/Ar	28.34 ± 0.12	Baksi et al. (1996)
Ar/Ar	28.34 ± 0.16	Renne et al. (1998)
Ar/Ar, Cyclo	28.53 ± 0.02	Kuiper et al. (2008)

Table.II.4 TCR ages acquired from the various analytical techniques.

Again the two commonly used TCR ages are Kuiper et al. (2008) and Renne et al. (1998). The age of 28.34 ± 0.32 Ma acquired from Renne et al. (1998) is based on inter-calibration from FCT which itself is based on the K-Ar primary standard age of GA1550, while the Kuiper et al. (2008) age of 28.53 ± 0.02 Ma is based on the inter-calibration of FCT derived from astronomical tuning, thus eliminating the K-Ar uncertainties. The relationship between the FCT and Taylor creek for Kuiper et al. (2008) is derived as 1.0112 ± 0.0010 with a correction of 0.65%

II.2.7 Primary standards

Previously, there was an abundance of varying own laboratory and inter-laboratory standards. Over the years, more are turning to FCTs or TCRs as the main fluence monitors, however primary standards calibrated to $^{40}Ar/^{39}Ar$ ages are still utilised and still deemed as important fluence monitors.

HD-B1

A primary Biotite standard from the Bergell granodiorite (Italy) with a grain size of 200-500μm. The age of the standard is of 24.21 ± 0.32 Ma (Hess and Lippolt, 1993; Wijbrans et al, 1995; Schwarz and Trieloff, 2007). The age is determined from multiple K and Ar analysis determined from several laboratories with $^{40}Ar/^{39}Ar$ step heating showing homogenous distribution of K and Ar inside the crystal lattice alongside no evidence of excess argon (Hess and Lippolt, 1993).

GA1550

Biotite standard from a Monzonite in New South Wales (Australia) introduced by McDougall and Roksanic, (1974). Its age was first determined by K/Ar measurements using the classic approach based on ^{38}Ar isotopic dilution giving an age of 97.9 ± 0.7 Ma. An age of 97.8 ± 0.2 Ma, and 98.5 ± 0.8 Ma (Baksi et al, 1996, Spell and McDougall, 2003) respectively, was measured and recalculated based on a different $^{40}Ar^*$ and K% content. Renne et al. (1998) re-calculated an age of 98.79 ± 0.54 Ma with a K content of 7.626 ± 0.0016% and is currently the most widely used.

MMhb-1

Hornblende from a syenitic body McClure mountain Complex of southern Colorado, USA (Alexander et al, 1978), its age was calculated primarily as 519.4 ± 2.5 Ma, then from 17 independent laboratories an age of 520.4 ± 1.7 Ma (Samson and Alexander, 1987) with a inter-laboratory precision of 1.89% was established. While $^{40}Ar/^{39}Ar$ ages show minor impurities reproducible to a precision of 0.1%. Previous ages inter-calibrated with new $^{40}Ar/^{39}Ar$ ages give an age of 523.1 ± 2.6 Ma (Renne et al, 1998), 521.1 ± 2.6 Ma (Baksi et al, 1996) and 523.8 ± 2.1 Ma (Spell and McDougall, 2003).

II.3.1 Methodology

Three of the San Juan Volcanic field products erupted from the La Garita caldera (Lipman et al, 1997) PPD, FCT and NCD were prepared firstly by crushing samples in a cyclic rock crusher, followed by sieving to various sized fractions. These fractions were microscopically inspected to deduce the best size fractions necessary for this experiment. Large crystals (1-0.5mm) tend to have multiple inclusions while the small fraction <40μm could pose stronger problems from recoil effect during irradiation (e.g. Onstott et al, 1995). Two batches from each sample 125-250μm and 250-500μm were primarily washed with de-ionized water in an ultrasonic bath then separated using heavy density liquid separation (Bromoform, 2.55-2.58 g/cm^3). The remaining density fraction passed through a second cleaning process, followed by magnetic separation through a Franz isodynamic magnetic separator, leaving sanidine as the major constituent. The sample is again cleaned by ultrasonic bath with ground mass removed by a series of diluted nitric acid and hydroflouric acid washes. These aliquots were then weighed and packed tightly into 1cm diameter copper discs, ready for irradiation. FCs and TCs flux monitors were packaged into 20mg copper discs and placed at the required intervals, tightly packed within the vacuumed sealed quartz tubes to prevent movement thus allowing a better constrain of the J-value.

Irradiation

Irradiation conditions are determined by the subject matter, whereby a rough age and K content are assumed to determine the length of irradiation so that $^{39}Ar_k$ produced is sufficient compared to the $^{40}Ar^*$ measured. This again is important when dealing with the sensitivity of the mass spectrometer as too low ^{39}Ar production could impede the accuracy of the results. In total 6 ~0.2g packages of unknowns were created and stacked linearly up to 7cm in height in a 1cm diameter quartz tube, each placed between two flux monitor standards either side (Fig.II.8).

Samples were sent to a cadmium shielded CLICIT facility fast neutron nuclear reactor in Oregon (USA), undergoing a 40h irradiation cycle. Cadmium shielding is particularly important as it minimizes the occurrence of alternate reactions such as

$^{40}K(n,p)^{40}Ar$ due to the reduction of thermal neutrons required for this reaction (Mcdougall and Harrison, 1999).

Half way through irradiation, quartz tubes are turned 180^{o} to minimize nuclear flux across the Z-axis. All fluence monitor J-values were calculated using the Steiger and Jager, (1997) decay constants. Vertical variations in the J-value varies 4% along its length, more of which will be discussed in the results.

Fig.II.8. Four vacumed sealed quartz tubes packed ready for irradiation. The larger copper discs represents samples of unknown age, packaged between two sets of fluence monitors either side.

II.3.2 Measurements

Measurements were completed on the $^{40}Ar/^{39}Ar$ multi-collector instrument (Fig.II.9) devolved in University Paris Sud laboratory and fully described in Coulié et al, (2004). Previous work compiled on the age of MMhb-1, FCT, TCR and HD-B1 show good reproducibility (e.g. Renne et al, 1998; Spell and McDougall, 2003; Schwarz and Trieloff, 2007) and show an analytical error of lower than 0.1% for well behaved samples, ideal for this study.

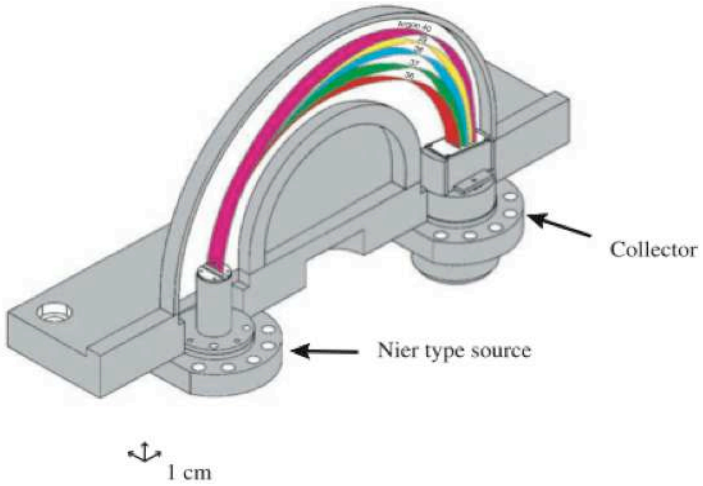

Fig.II.9 Schematic view of multicollecter nier type source mass spectrometer (Coulié et al., 2004)

Potassium interfering reactions were calculated using the values proposed by Renne et al. (1998): 7.0 x 10^{-4}, 1.2 x 10^{-2}, 7.2 x 10^{-4} and 2.68 x 10^{-4} for $[^{40}Ar/^{39}Ar]_K$, $[^{38}Ar/^{39}Ar]_K$, $[^{39}Ar/^{37}Ar]_{Ca}$ and $[^{36}Ar/^{37}Ar]_{Ca.}$ Age uncertainties and calculations follow McDougall and Harrison, (1999), with ^{40}K decay constants and isotopic ratios of Steiger and Jager, (1977). Signal stability of this particular mass spectrometer was measured by 500 data acquisitions with a $^{40}Ar/^{39}Ar$ ratio stability of 0.015%, cup calibration was continuously measured throughout the whole experiment and showed indistinguishable variability along with daily peak monitoring. Mass discrimination was calculated from $^{40}Ar/^{39}Ar$ atmospheric pipette using the value of 295.5 (Steiger

and Jager, 1977) and with a signal similar to that of $^{40}Ar^*$ expected peak of each standard. This ^{40}Ar signal was then passed onto each faraday cup to determine the $^{40}Ar/^{39}Ar$, $^{38}Ar/^{39}Ar$, $^{37}Ar/^{39}Ar$ and $^{36}Ar/^{39}Ar$ ratio used for cup calibration to the final calculations of air and unknown measurements. Atmospheric argon was determined before each sample and throughout the day, aliquots with typical ^{40}Ar signals of 1.5 x 10^{-11}A were measured, giving an average $^{40}Ar/^{36}Ar$ atmospheric ratios of 304 ± 1 over the course of the two sets of irradiations. Such value, which is significantly from the admitted atmospheric ratio, is explained by the mass discrimination operating within the nier source where heavy nucleus is more easily ionized than lighter ones. On the other hand, no mass fractionation is induced by the faraday cups (McDougall and Harrison, 1999).

Fluence monitor samples were unwrapped from copper pellets and loaded into a clean copper tray into predetermined holes then covered by a quartz cover to prevent mixing of the samples under utilisation of the high energy laser. This was connected back to the extraction line and baked over night at roughly ~120^{o}C. Similarly, age unknown samples were loaded into a quartz tube glass within the original copper pellet, the molybdenum crucible at the base of this quartz tube was then heated up high temperatures (~1500^{o}C) under vacuum to be purified. Finally, the sample was loaded into the base of the crucible and heated up to a low temperature (~400^{o}C) for ~20 minutes while pumping to release any volatiles present. The vacuum is monitored during this degassing step so that the volatiles have successfully been removed from the sample, before analysis can be initiated.

Fluence monitors were fused using a Nd-YAG infra-red laser at 0.8A, while the samples were step heated using a high frequency (HF) furnace. After heating the gas, it is first purified by 700^{o}C Ti foam following by 15 minutes on an AP10Gp SAES getter heated to 400^{o}C. The sample is then transferred to an additional coal trap undergoing a second purification under a SAES Al-Zr getter, before measurement in the mass spectrometer. Unknowns were typically measured on average ~13 incremental steps set with the HF furnace and determined by the total argon released.

Blanks were introduced periodically into the mass spectrometer undergoing the same method as step heated samples and total laser fusion. Maximum laser power yielded

undetectable readings for the blanks while the RF fusion maximum blank heating up to 1100°C obtained a typical reading of 7.7 x 10^{-14} and 1.4 x 10^{-16} A for ^{40}Ar and ^{36}Ar signal, respectively. Such low ^{40}Ar value corresponds to ~0.5‰ of a typical signal and, since they define a ratio with atmospheric value within uncertainties, no correction was applied. Similar to Coulié et al, (2004), the ^{39}Ar, ^{38}Ar and ^{37}Ar blanks were undetectable.

Before measurement of each sample, a zero is taken while the mass spectrometer remains pumping. After five sets of one hundred measurements are taken (which takes about 5mn), the mass spectrometer is closed and the sample is introduced. Once again the sample is measured in five sets of one hundred measurements, continuously for all five Ar isotopes. Age reproducibility of the ^{40}Ar/^{39}Ar method derived from Ethiopian and Siberian samples and standards (Coulié et al, 2003; Ricci et al, 2013), show analytical errors of lower than 0.1% with total error of ~1% dominated by errors in the J-values and fluence monitor ages (e.g. Renne et al, 1998). Due to the low Ca content, $[^{39}Ar/^{37}Ar]_{Ca}$ and $[^{39}Ar/^{36}Ar]_{Ca}$ corrections did not affect the age of the sample. Mass discrimination were determined from an air pipette system, while blanks were determined on the same conditions as samples.

To determine the J-value curve we utilised the FCs and TCs ages developed from Kuiper et al. (2008) 28.201 ± 0.046 and 28.53 ± 0.02 Ma, respectively, again this decision will be discussed later within the results and discussion. Uncertainty in the J value dominates the total error estimate and will be propagated into the final error of mean, plateau and isochron ages of future samples. It is common practice to assign a conservative arbitrary uncertainty of 0.2% to J (Renne et al, 1998; 2010). This will be discussed later and an alternative approach will be preposed.

In this study, no particular outliers were measured on all samples, therefore all steps will be considered within the results. Weighted mean ages were calculated if more than one sample were measured, with uncertainties herein are quoted at 1-sigma level. Ages themselves have been heavily scrutinized and all intercepts and mean squared weighted deviation (MSWD) have been calculated and inspected regarding statistical significancy (e.g. Mahon et al, 1996; McDougall and Harrison, 1996) while the plateau ages and analytical uncertainties were calculated by inverse variance

weighting from a minimum of 3 steps accounting to at least 50% of the total ^{39}Ar yielded. All dated samples commonly use mean square weighted derivatives as a statistical test to validate the both the plateau and weighted mean age. An MSWD of >1 show scatter that cannot be attributed to error alone while a value of <1 shows too large a analytical error which all samples fall into.

II.4. Chosen monitor age.

In this part I will highlight the main arguments for the particular FCT properties and standard ages and why I will utilise the FCT age achieved by Kuiper et al. (2008).

Pre-residence time of the siliclistic magma is a fiercely debated subject when dealing with standard materials (Schoene and Bowring, 2006), i.e is the silicic magma formed by crystal fractionation or pre existing crustal melting, (Keller et al, 1970: Mahood et al, 1990; Bachmann et al, 2000; Couch et al, 2001) explain and prove using geochemical features that the various silicic magmatic bodies such as that of the FCT, PPD, NCD magmatic body were partially re-heated by a vast injection of mafic magma, and indicate re-heated rejuvenation of near solidus upper crustal magmatic bodies (Bachmann et al, 2002). Problems arise in using sanidine as a primary standard due to difficulties in quantitative extraction $^{40}Ar^*$ from viscous melts.

II.4.2 Recent determination of FCT age

As discussed previously, many studies involving different dating techniques have been devoted to the FCT. The age of 28.02 Ma (Renne et al, 1998) have been used extensively for the last decade, but it was recently challenged by two recent studies proposing a significantly older value. From $^{40}Ar/^{39}Ar$ analyses performed at Vrije Universiteit Amsterdam (VU) and Berkeley Geochronology center (BGC) of tuffs intercalated within well constrained sedimentary sections using cyclostratigraphy, an

age of 28.201 ± 0.023 Ma was proposed by Kuiper et al. (2008). More recently, from an approach based on comparison with $^{238}U/^{206}Pb$ dating of zircon and newly proposed decay ^{40}K decay constant values, Renne et al. (2010) proposed an even older age of 28.305 ± 0.036 Ma.

These two recent FCT standard ages differ slightly from each-other. Inter-laboratory experiments show both the BCG and the VU laboratories are within 2σ analytical error, therefore demonstrate that the difference is not due to analytical systematics. In addition, both laboratories utilise the same error propagation technique and programs, and similar MAP mass spectrometers. The only noticeable difference between the two laboratories comes down the packing of samples for irradiation and the calculation of the J-factor.

While the VU uses a similar set up as University Paris Sud (see previous section), the BGC laboratory irradiates samples using a cylindrical vessel that places standards around the unknowns, the J value is then calculated as an 3D array, determining the neutron flux change both along the Y and X axis.

II.4.3 Uncertainties in Kuiper et al. (2008) age.

To obtain this FCT age of 28.201 ± 0.023 Ma (Kuiper et al, 2008), it was assumed that the orbital forcing and sedimentary expression develops no lag time and is determined as zero in the calculation. Work is now in place to determine this by monitoring sapropel layers in the Mediterranean basin (Hilgen et al, 2008; Kuiper et al, 2008), with, currently, a proposed value of ± 10 kyr. This approach also requires that the sedimentation rate for the astronomically tuned section is constant for the whole succession and that no hiatus occurred. Astronomical tuning is also dependent on the accuracy of the solution presented (Laskar et al, 2004), and is calculated with variables such as tidal dissipation. Presently, these uncertainties are not accounted for and might significantly increase the FCT age proposed with an uncertainty of only 0.023 Ma (1σ).

II. 4.4 Uncertainties in Renne et al. (2010) age.

To utilise the new Renne et al. (2010) age of 28.305 ± 0.036 Ma, one must also include the new decay constants published in the Renne et al (2010) paper. These new

decay constants pushed the $^{40}Ar/^{39}Ar$ ages for several major events significantly older than either U-Pb or astronomical estimates. For example, newly re-calculated Bishop Tuff (BT) age of 778 ± 4 ka using this FCT age leads to an age of 793 ± 4 ka for the Matuama-Brunhes reverse to normal polarity geomagnetic transition (MBT), when the 15 kyr well-constrained stratigraphic offset between BT and MBT is considered (Sarna-Wojcicki et al, 2000). Such MBT age is significantly older than ages derived from orbital tuning, which lies between 773 and 781 ka (Bassinot et al, 1993; Channell et al, 2004; Lourens et al, 2004). Finally, it should be noticed that the new ^{40}K decay values proposed here have been challenged by Schwarz et al. (2011), who suggest that important issues remain to be clarified before they can be used in $^{40}Ar/^{39}Ar$ or K-Ar age calculations.

II. 4.5 Chosen flux monitor age

Inter-calibration factors between the various flux monitor standards (FCs, ACs, TCs MMhb-1) are precise enough that they offer little in error uncertainty in the age calculation (Renne et al, 1998), however there still lie some discrepancies when using primary standards to date secondary. Recent astronomical calibrated $^{40}Ar/^{39}Ar$ multi-collector noble gas single crystal ages of FCT (Rivera et al, 2011) with orbitally tuned A1 tephra Sanidines from Faneromeni (Crete) sections show an age of 28.172 ± 0.028 Ma in ± 0.10% uncertainty with the age given by Kuiper et al. (2008).

Using astronomically tuned $^{40}Ar/^{39}Ar$ ages for the age FCT we can reach a ±0.1% level of accuracy, as the total uncertainty on the astronomical age (including interactions and applied orbital solution) can serve as an alternative to multi disciplinary (K-Ar, $^{40}Ar/^{39}Ar$ and U/Pb) combined ages, whereby we avoid uncertainties in cross calibration of the radiometric ages, and effects such as magma chamber residence times, spike calibration and Pb loss in zircons. It is for these reasons we choose to utilise the age published by Kuiper et al. (2008) throughout this project.

II.5. Results

II.5.1 J-Value determination

We combine these two standards using the ages given by Kuiper et al. (2008), with TCR age based on the R^{FCT}_{TCR} ratio of 1.0112 ± 0.001 ±1σ (Renne et al, 1998). A curvi-linear regression was applied for each standard height resulting in a third polynomial fit curve for all irradiation vials. All samples correlate easily with each other backing up the claims of the reported ratios of Renne et al. (1998). The maximum J value variance was measured as 4%. Fig.II.10 shown below additionally compares all J values attributed to the individual quartz tubes, from the 40h irradiation.

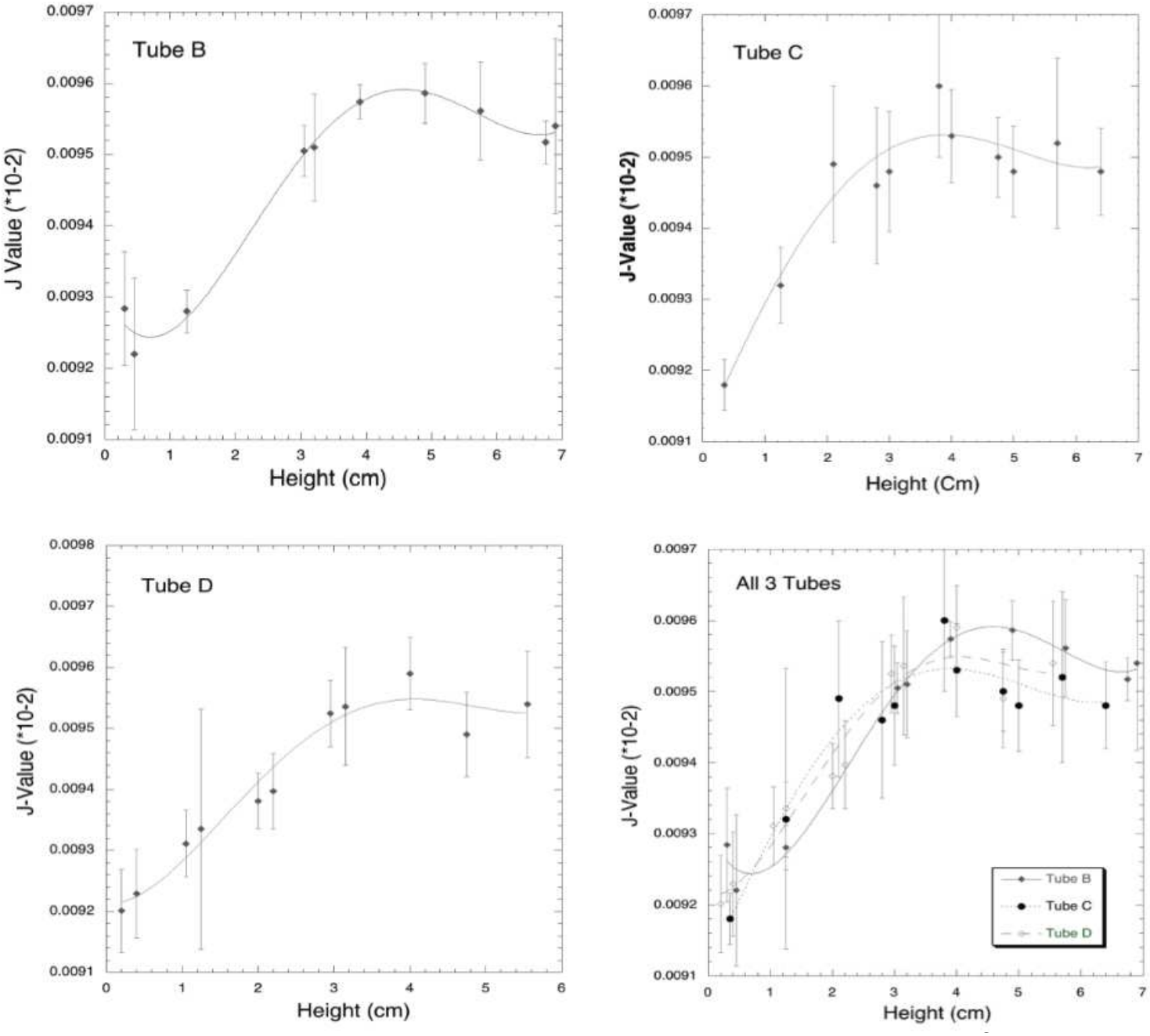

Fig. II.10. (Previous page). J-curves calculated for each individual quartz tube. The fourth graph represents all tubes combined. Each of the fluence monitors fall within the calculated 3rd polynomial fit curve and show a maximum variation of ~ 4% over height (cm).

As there were only small pertubations in the J-Value between the three tubes (expected since they were irradiated tightly together), they were compiled into one final curve that represents all of the fluence monitors measured (Fig.II.11).

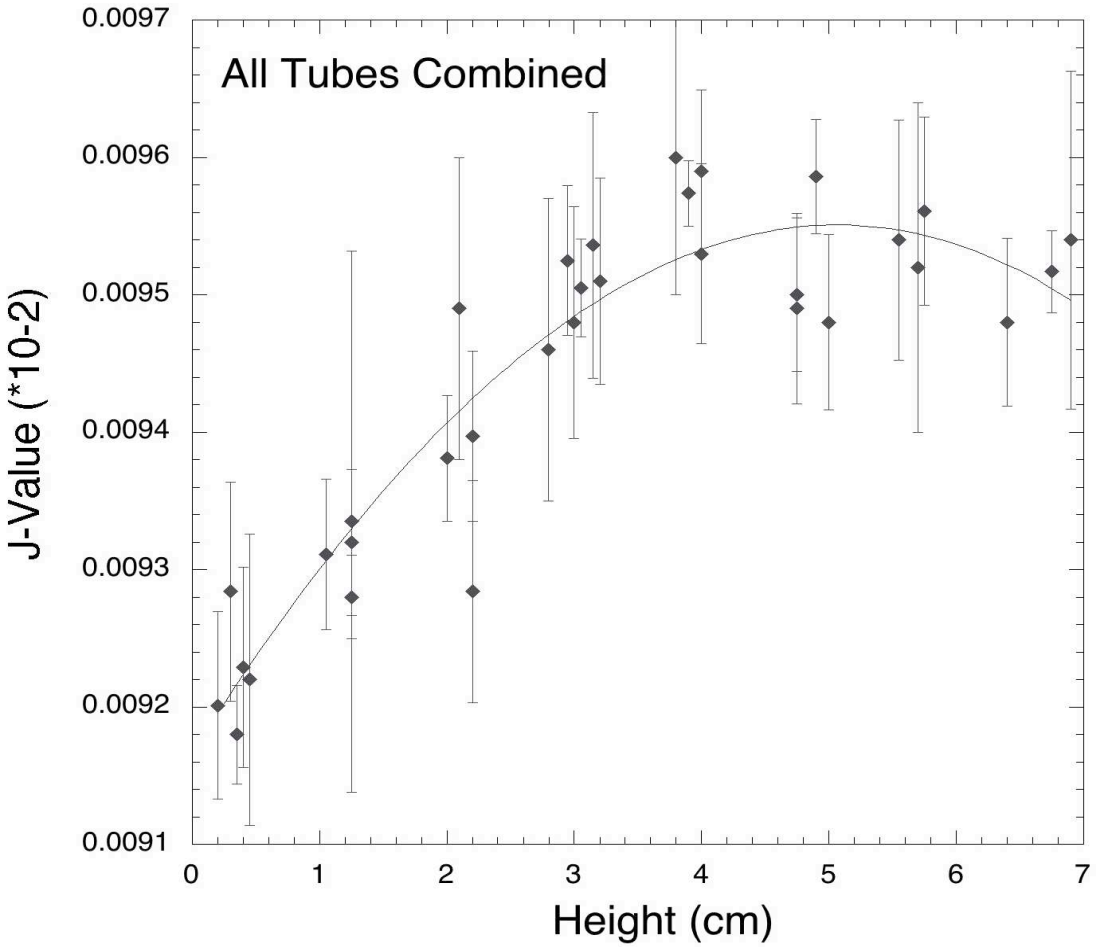

Fig II.11. Demonstrates clearly the small pertubations in J-value across all fluence monitor values. As we want to determine both the most accurate age and to quantify the J value systematic error, the J Values were calculated on unknowns depending in which tube they were irradiated rather than the group varying J-Value.

The inter-calibration between the two standards show that our results match with the ratios achieved both at the Vrije Univeristy (VU) and Berkley Geochronolgy Centre (BGC), thus showing that inter laboratory bias error is small, but also that the applied mass discrimination used in the two programs ArArCalc and IPHYGENE is also systematic.

II 5.2 New $^{40}Ar/^{39}Ar$ Ages.

Due to high potassium concentrations, sanidine crystals were easily measured on the three unknown ages of NCD, FCT and PPD. Most steps were utilised when quantifying the plateau ages, however some small steps that represent a diminishable amount of $^{39}Ar_K$ released especially at the very start and towards then end were not taken into account. These low temperature steps yielded improper ages due to incomplete radiogenic argon retention near the grain surfaces (Albarede, 1978).

A) Fish Canyon Tuff (FCT) Ages (Fig.II.12; Table II.5).

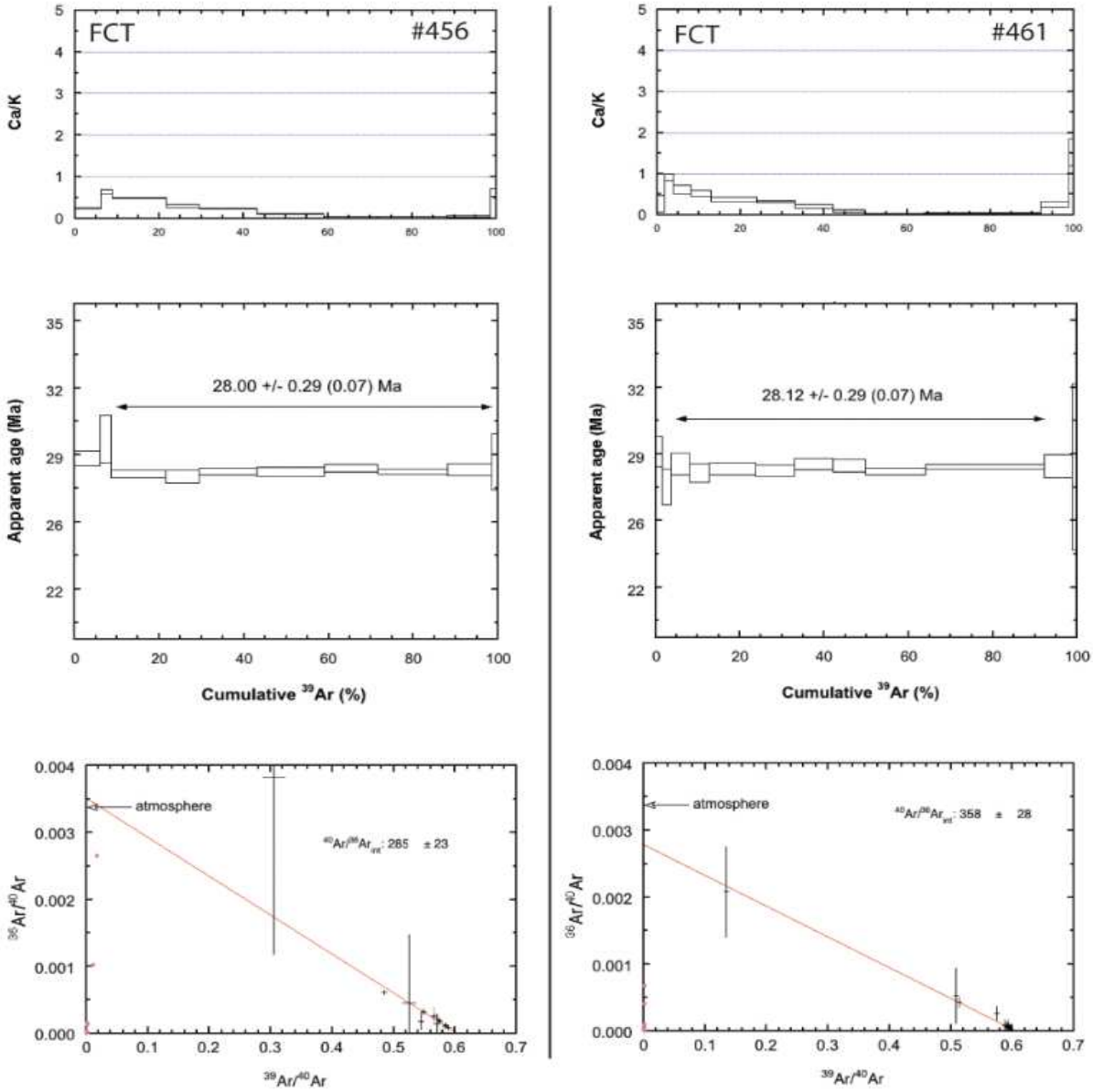

Analysis	J-Factor	Total Gas Age (Ma)	P. Age (Ma)	Analy. Un (Ma)	Total Un (Ma)	Iso Age (Ma)	(40/36)i	MSWD
#456	9.486E-3	28.07 ± 0.42	28.00	0.07	0.29	28.06 ± 0.31	285±23	0.37
#461	9.504E-3	28.14 ± 0.47	28.12	0.07	0.29	28.02 ± 0.68	358 ± 128	0.46

(Fig.II.12) In both cases age plateaus were calculated using ~90% of the ^{39}Ar released over an average of 8 steps for each sample with each step featuring more than 90% in radiogenic $^{40}Ar^*$. The weighted mean age of the two FCT plateau is calculated as 28.06 ± 0.1 Ma. Within error, both inverse isochron plots exhibit atmospheric $^{40}Ar/^{39}Ar$ intercepts.

B) Nutras Creek Dacite (NCD) Ages (Fig.II.13, Table II.6.

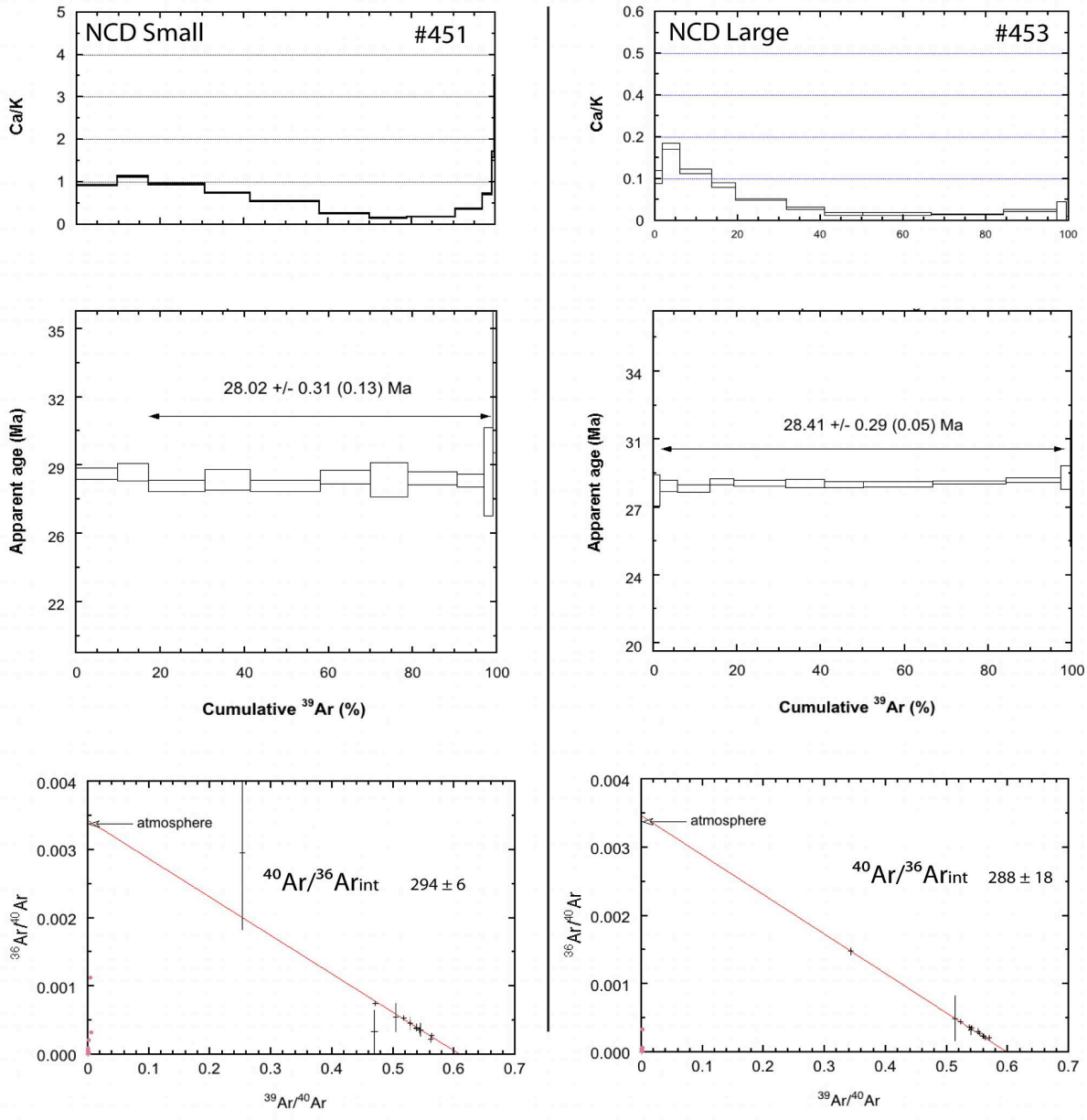

Analysis	J-Factor	Total Gas Age (Ma)	P. Age (Ma)	Analy. Un (Ma)	Total Un (Ma)	Iso Age (Ma)	(40/36)i	MSWD
#451	9.550E-3	28.108±0.568	28.02	0.13	0.31	28.061±0.549	291.3±36.0	0.42
#453	9.544E-3	28.392±0.349	28.41	0.05	0.29	28.743±0.322	288.2±18.0	0.63

(Fig II.13) In both cases show well defined age plateaus were calculated using ~80 - 95% of the ^{39}Ar released over average of 8 steps each sample. Each step picked show ^{40}Ar* radiogenic percentage of over 90% as so were included in the final plateau age. The weighted mean of the two samples give an age of 28.21 ± 0.13 Ma with both isochrons falling within error to atmospheric values. Two sized fractions have been analysed here. PPD ages for 125-250µm and 250-500µm, corresponding to PPD small and PPD large, respectively.

C) Pagosa Peak Dacite PPD (Fig.II.14, II.15; Table II.7, II.8).

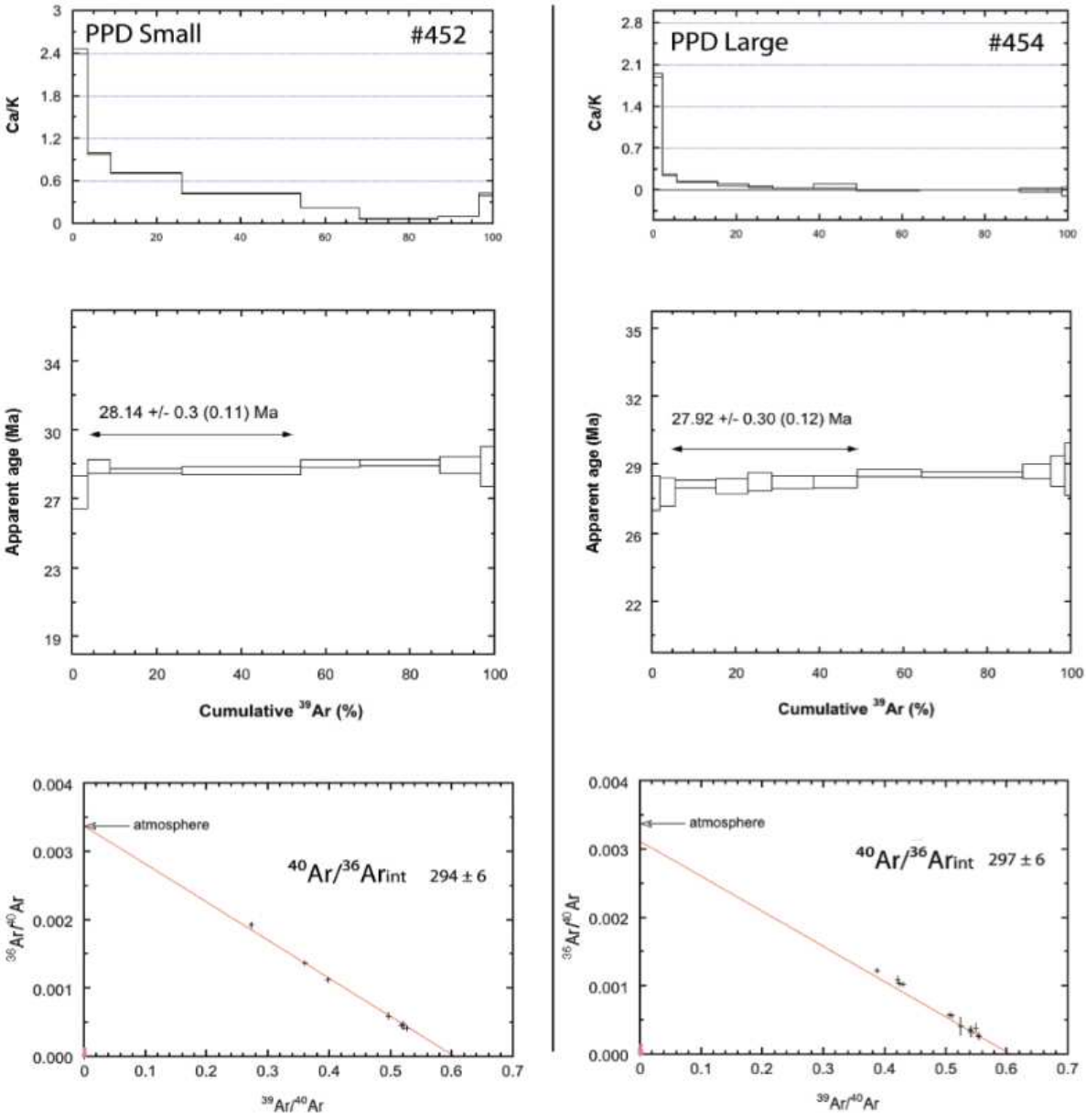

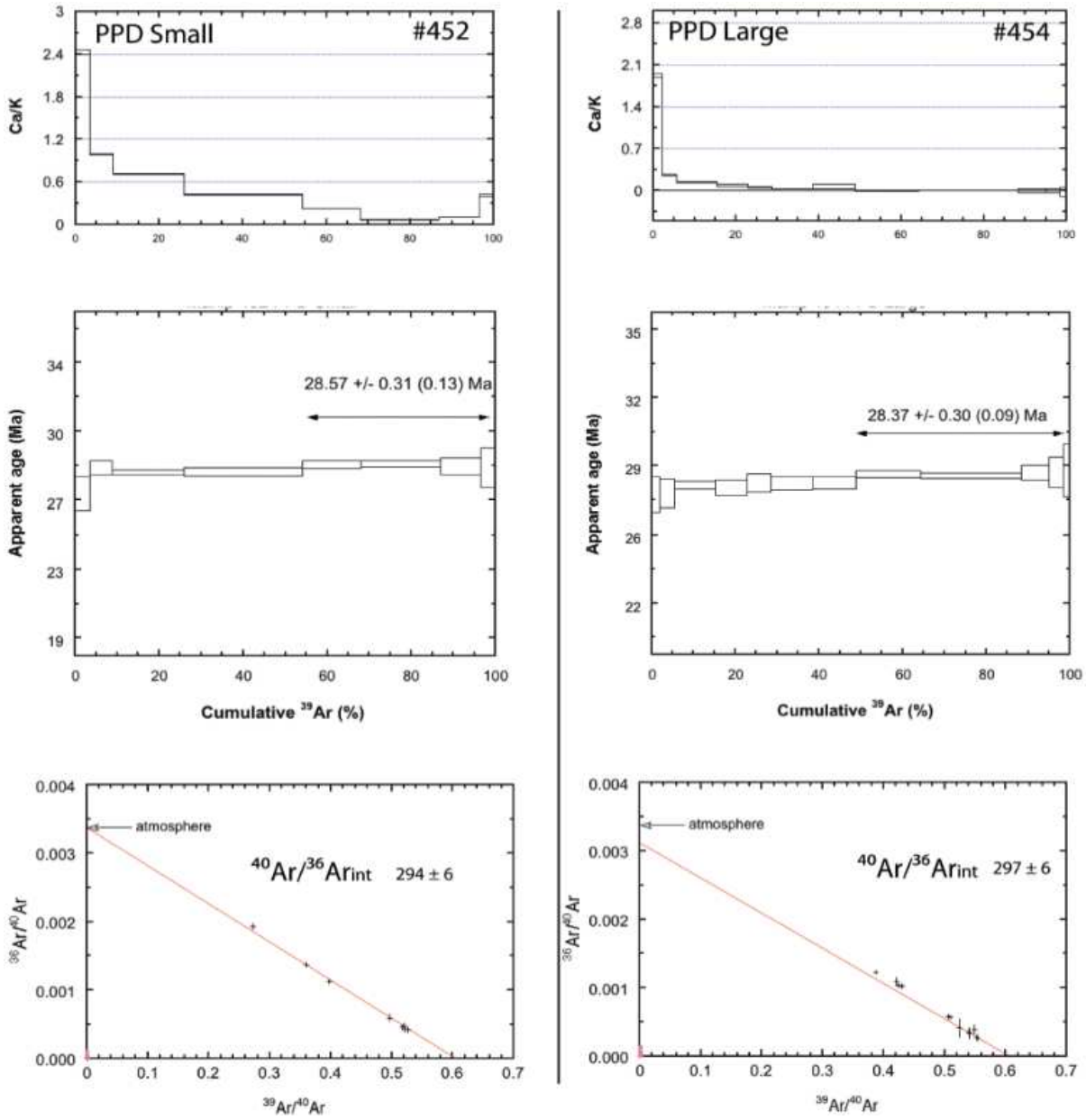

Two size fractions have been analysed here, of 125-250µm and 250-500µm respectively

Table below represents both high (HT) and low (LT) temperature steps.

Analysis (LT)	J-Factor	Total Gas Age (Ma)	P. Age (Ma)	Analy. Un (Ma)	Total Un (Ma)	Iso Age (Ma)	(40/36)i	MSWD
452	9.572E-3	28.295±0.417	28.14	0.11	0.3	28.132±0.313	295.8±3.0	0.51
454	9.543E-3	28.138±0.419	27.92	0.12	0.30	27.887±0.343	296.7±6.0	0.21

Analysis (HT)	J-Factor	Total Gas Age (Ma)	P. Age (Ma)	Analy. Un (Ma)	Total Un (Ma)	Iso Age (Ma)	(40/36)i	MSWD
452	9.572E-3	28.295±0.417	28.57	0.13	0.31	28.590±0.363	294.8±6.0	0.06
454	9.543E-3	28.138±0.419	28.37	0.09	0.3	28.135±0.659	320.2±67	0.06

(Fig.II.14; II.15) PPD proved slightly more problematic in defining an age plateau, with two distinct ages both releasing around 50% of the ^{39}Ar. The low temperature steps give a mean age of 28.03 ± 0.16 Ma while the higher temperature steps give a significantly older mean age of 28.47 ± 0.16 Ma. Such discrepancy between low and high temperature ages could be explained by mixing of two sanidine populations with the oldest being more argon retentive, hence releasing its radiogenic ^{40}Ar to higher temperatures. The Ca/K diagrams somehow support this hypothesis where two contrasting ranges of values are observed for low and high temperatures. All isochrones from these samples trend towards atmospheric at the 95% confidence level and support the hypothesis that excess ^{40}Ar is not a concern here.

II.5.3 Calculating J factor uncertainty.

For uncertainty calculations an arbitrary percentage is usually enforced for the analytical determination of the J-factor and is of ~0.02% (Kuiper et al, 2008; Renne et al, 2010), however using the samples of known age as "unknown", we were able to fully quantify the perceived error. Stated previously, we can separate the J-Factor error into both the analytical uncertainty of the standard and secondly into the uncertainty in the standard age. From this determination, we are able to use these calculations effectively to all of the ages presented here as the same fluence monitor is utilised in the entire thesis.

We can ascertain through previous highly reproducible measurements that the, mass discrimination and error corrections are highly accurate, therefore the age difference between the unknown the fluence monitor ages must be caused wholly by the large J variance and its uncertainty.

As we measured FCT as a fluence monitor and as unknown we were able to calculate the uncertainty. Calculating our unknown age of FCT we determined a weighted mean age of 28.19 Ma correcting this and using as Kuiper et al. (2008) FCT age of 28.201 Ma we obtain an age difference of 11 ka, The standard determination of J is written as a percentage and is calculated as 0.44%, this will be applied to all future age determinations throughout this thesis to correct the final uncertainties.

II.6 Discussion of Ar/Ar ages

II.6.1 Analytical reproducibility

Comparison of age specta, total gas ages and J-value calculations from the above samples will be used to support the analytical reproducibility for our $^{40}Ar/^{39}Ar$ data. These results will be compared to previous literature to highlight and show that the ages throughout my thesis would be comparable with those dated in other laboratories.

A previous compiled report on the analytical dating on all three of the San Juan volcanic field samples was published by Bachmann et al. (2007). The published ages were acquired using high precision U/Pb and $^{40}Ar/^{39}Ar$ dating of various minerals. For this comparison, I will focus on the high temperature sanidine $^{40}Ar/^{39}Ar$ ages as other minerals such as the large feldspar phenocrysts and horneblende were not dated in Paris Sud. Bachmann et al. (2007) ages were determined from step-heating and single crystal analyses and are based on an age of 28.34 Ma for the TCR standard, which is equilivant to FCT with an age of 28.02 (Renne et al, 2008) used as the flux monitor. Table II.9 below shows the comparison between Bachmann et al. (2007) ages recalculated to FCT=28.201 Ma (Kuiper et al, 2008) and our ages.

Experiment	PPD	NCD	FCT
Bachmann et al. (2007) Plateau ages (Relative to FCT=28.201 Ma)	28.12 ± 0.09 Ma	28.25 ± 0.09 Ma	28.22±0.09 Ma
Incremental Heating This study (Relative to FCT=28.201Ma)	28.03 ± 0.11 Ma	28.22 ± 0.07 Ma	28.06 ± 0.07 Ma

Table II.9. Ages obtained from this study compared to Bachmann et al. (2007) incremental ages. All ages are relative to FCT 28.201 Ma (Kuiper et al, 2008)

FCT

Individually, age spectrums show reliable plateaus with sample #461 achieving an age of 28.12 ± 0.07 Ma which is in great agreement with the recalibrated age of 28.22 ±

0.09 Ma (Bachmann et al, 2007). However sample #456 (28.00 ± 0.07 Ma) does not fall into agreement, and is too young compared with Bachmann et al. (2007) age. Therefore, this younger age produces an overall younger mean FCT age of 28.06 ± 0.07 thus falling only in agreement with Bachmann et al. (2007) age when the age is utlised with maximum age uncertainity in use. All errors reported do not including the J value uncertainty as this was not utilised in Bachmann et al. (2007) ages.

NCD

All NCD step heating techniques shows strong reliable plateau ages, the youngest NCD sample (Sample #451) age 28.02 ± 0.13 Ma falls outside error for NCD recalibrated ages in Bachmann et al. (2007). Additionally, sample #453 also falls outside uncertainty, however this could possibly be due to inclusions commonly associated with larger crystals size increasing the age slightly. Calculating a mean age of the two samples we obtain an age of 28.22 ± 0.07 Ma which falls in complete agreement and is indistinguishable compared to the recalibrated Bachmann et al. (2007) proposed ages of 28.25 ± 0.09 Ma.

PPD

Both ages acquired from the two samples show similar plateau age spectrums as Bachmann et al. (2007), whereby we see a familiar two stepped spectrum. To calculate the final ages, Bachmann et al. (2007) utilised the whole plateau whereby we chose to separate the two distinct steps as a high temperature and low temperature age (As each plateau falls outside 2 sigma error thus not able to propose one reliable plateau age). As we suspect the incorporation of older sanidine grains with higher retentvity we prefer to rely on the low temperature ages, when comparing to ages published in Bachmann et al. (2007).

Using the low temperature steps we achieve ages of 28.14 ± 0.11 and 27.92 ± 0.12 Ma for samples #452 and #454 respectively. Sample #452 falls in good agreement with the proposed age of 28.12 ± 0.09 Ma published by Bachmann et al. (2007) and would be indistinguishable in age. However using sample #454 we achieve a much younger age, which again brings down the mean age of the two samples, still however in agreement.

Total gas ages compared to total fusion ages acquired by Bachmann et al (2007), show no relationship and fall outside of error, this could be partly due to the amount of experiments reproduced in the single crystal dating technique, as few total gas age leads to a higher spread of ages rather than a smaller age spread calculated by a mean average.

II.6.2 Total gas age

Analyses of standards are measured using total fusion, thereby releasing ~100% of the radiogenic $^{40}Ar^*$. In this case to compare results we can use total gas ages calculated with our incremental heating techniques. As the various assemblages found in the San Juan volcanic field are with uncertainties determined as instantaneous from one another (Bachmann et al, 2007), we can compare all the total gas ages from the samples presented above.

The combined total gas age of all three units from La Garita caldera Table II.10 and Fig.II.15 gives a weighted mean age of **28.19 ± 0.125** Ma. The discrepancy with the Kuiper et al. (2008) FCT age of 28.201 ± 0.046 Ma from which our J-values have been calculated is only of 0.04%, which highlights the accuracy of the approach followed here. Regarding the precision, we can use the standard deviation of our mean age of 28.190 ± 0.125 Ma to apply this uncertainty of 0.44% to the J-factor of all future age determinations throughout this thesis.

Effectively since all three FCT, NCD and PPD volcanics can be considered a synchroneous within error, and behave nicely with regards to $^{40}Ar/^{39}Ar$ analyses (Bachmann et al, 2007) , the spread in total gas ages observed here in Fig.II.15 and Table.II.10 can only be due to the uncertainty in calculating J from the 3rd polynomiacl curve used in this study (Fig.II.11).

Sample	Province	T. Age (Ma)	Un. (J-error = 0%)
456	FCT	28.07	0.28
461	FCT	28.14	0.33
451	NCD	28.11	0.47
453	NCD	28.39	0.18
452	PPD	28.29	0.28
454	PPD	28.14	0.29

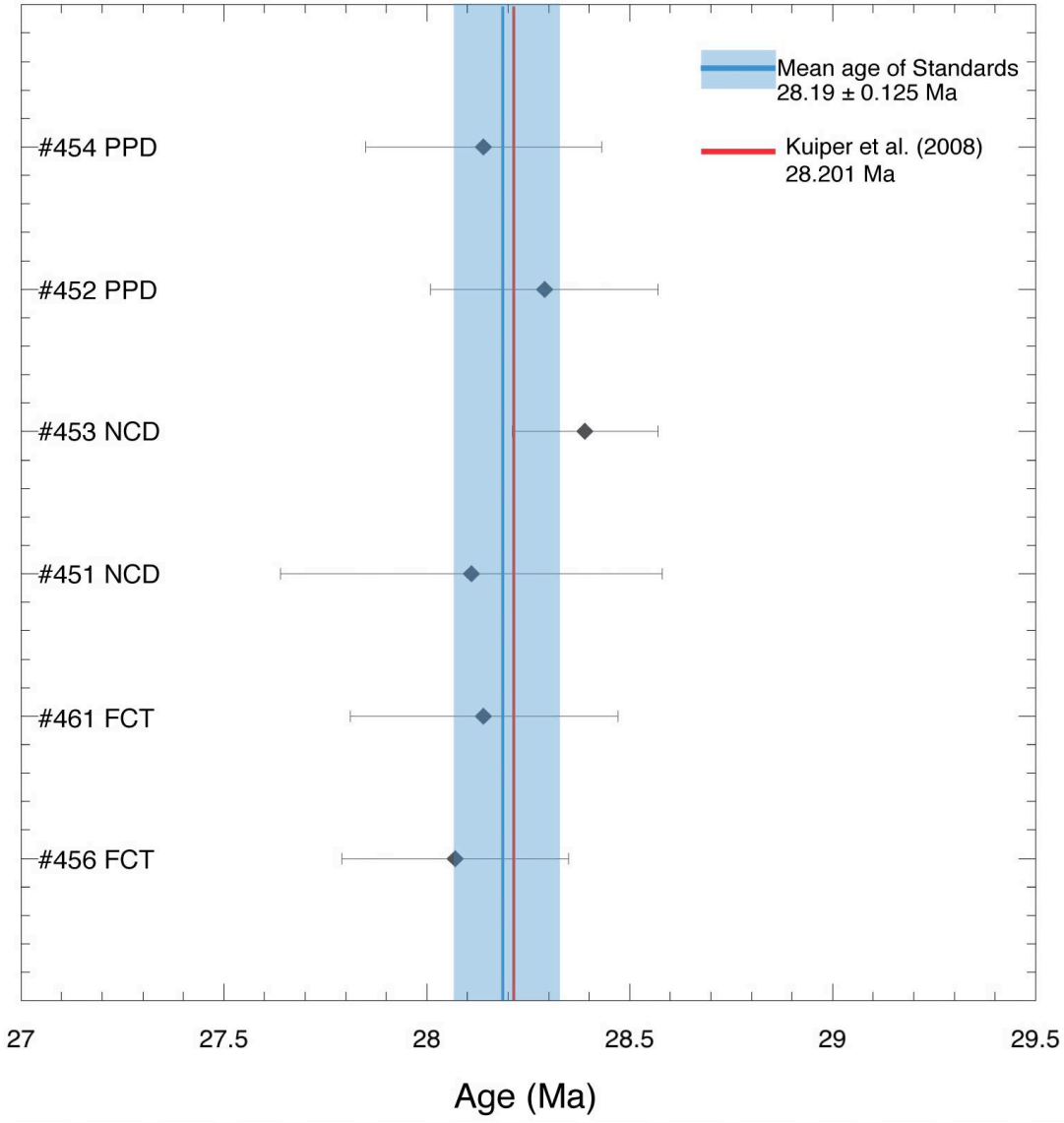

Table. II.10. (Above) Total gas ages from each sample. **Fig. II.15** Graph showing mean total gas ages for all three units from La Garita caldera (Table II.10). The blue line and shaded area represents the weighted mean age of **28.19 ± 0.125** Ma calculated from this study. While the reference red line represents the 28.201 Ma FCT age of Kuiper et al. (2008).

II.6.3 Changes to the standard age

Calculating ages on standards is an ongoing important process in the evolution and progression of the $^{40}Ar/^{39}Ar$ dating and geological timescale community, although changes are now on a much smaller scale (see previous section), they still prove many problems in quantifying high precision ages in the geochronology domain (Renne et al, 2012, 2013). Now, the main issue might be the determination of realistic and well determined uncertainties associated with the age of the FCT and other standards used as flux monitors for the $^{40}Ar/^{39}Ar$ dating technique.

Commonly utilised, preventing that the sedimentary succession is suitable, astronomical solutions can be very accurate chronometers (e.g, Laskar et al, 2011). However solutions are relative in time and require a fixed anchor point to determine the age. Seemingly small changes in the standard age has a knock-on effect in determining the age of this anchor point, down the particular 20,000 yr precession cycles in some cases. Therefore, it is important that we try to fully quantify this as far as possible.

The main geological time scale boundaries that seems to be effected by the age of the Fish Canyon Tuff standard are the Cretaceous/Paleocene (K/Pg) and Paleocene/ Eocene (P/E) boundaries. They are global well-defined boundaries found in a multitude of geological environments and can be used as good example on how seemingly small changes can affect a major event. Table II.X highlights the evolution of ages between key geological boundaries and the age of the standard used. The evolution of the K-Pg boundary will be discussed in much more detail in chapter IV when we discuss a multi-disciplinary experiment dating the K-Pg boundary.

Event	Gradstein et al, 1994	GTS 2004	Hilgen et al, 2006	Swisher et al, 2006	Kuiper et al, 2008	GTS 2012	Renne et al, 2013
FCT	27.84	28.02	28.2	28.12	28.201	28.201	28.305
K/PG	65.0	65.5	65.8	65.84	65.95	66.0	66.043
P/E	---	55.0	55.70	55.59	55.75	56.0	…

Table II.11. .Evolution of global timescale event boundaries and their chosen FCT monitor age (Ma).

III. Canada

III.1. Overview.

The aim of GTS Next project reflects the ability to use all three methods of dating to compile a precise age for each boundary, here lies the problem. Currently the majority of cyclostratigraphy is focused within the marine realm. Large continuous sedimentation ensures the most reliable results, however ash layers within the boundaries are seriously lacking.

While European sections such as Zumai, Soplana, Gubbio would be the ideal study areas, we are forced to look elsewhere. Localities with greater ash layer preservation, numerous past volcanic episodes and sediments that retain cyclostratigraphic proxies are required to relate this to the European counterparts. One way we can relate two distinct outcrops is to compare the known marker horizons or paleomagnetic interpretations. The combination of the two independent analyses will allow us to combine the results to form larger Trans-Atlantic geochronological history.

Late Cretaceous sediments can be found throughout the world such as the North Pacific (Hokkaido sections), North America (Western Interior Basin) and European sections (Gubbio). One particular area continuously investigated is the North American counterparts; due to the abundance of fossils, preserved ash beds and semi continuous stratigraphy (Eberth and Currie, 2005), the Western Interior Basin is a great area to study thus able to link towards the European cyclo-stratigraphically controlled counterparts.

III.2. Western Interior basin.

Introduction

Stretching from the base of the gulf of Mexico and meeting with the arctic ocean in the north, a 3000km long large inland sea formed dating from the mid to late Cretaceous. Splitting the North American landmass in two, a large cordilleran type foreland basin formed. The main process of which caused by the subduction of the Farallon plate underneath the North American plate during the Early Cretaceous time (Hay et al, 1993).

Fig.III.1. Western Interior Seaway, North America, during the Late Cretaceous

The Western Interior basin (WIB) (Fig III.1.) is defined as a near textbook example of a foreland basin system (Jordan et al, 1981). Formed as a depression, adjacent and parallel to the local orogeny (Beaumont et al, 1993). In this case the Laramide orogeny. At its largest, the basin stretched 760m deep and 970km wide.

During this time, two seaway landmasses existed, Laramidia to the west and Appalachia to the east. Existing throughout the Upper Cretaceous separated by a large inlet seaway, both landmasses show distinct changes and varied faunas; Tyrannosaur and Ceratopsian dominated faunas in the Laramdia section while the eastern Applachia region was dominated by Dryptosarus, and Hadrosaurs (Srivastava et al, 1970; Brinkman et al, 2003). Laramidia exhibits one of the most varied dinosaur fossil assemblages in the world, due to the preservation rates of such fossils, however such fossiliferous evidence in Appalachia were destroyed in the Pleistocene ice age (Eberth, 2005).

III.2.2 Location

Geographically the Western Interior Basin stretched from the Gulf of Mexico up to the most northern parts of Canada / Alaska with a secondary limb stretching (at maximum flooding level) to the most northern parts of Hudson bay. During the basins 35 Myr life, tectonic and sedimentoloigcal process changed and shaped the foreland basin, migrating, expanding the seaway over time joining with the Tethyan sea (Beaumont et al,1993; Catuneanu et al, 2008).

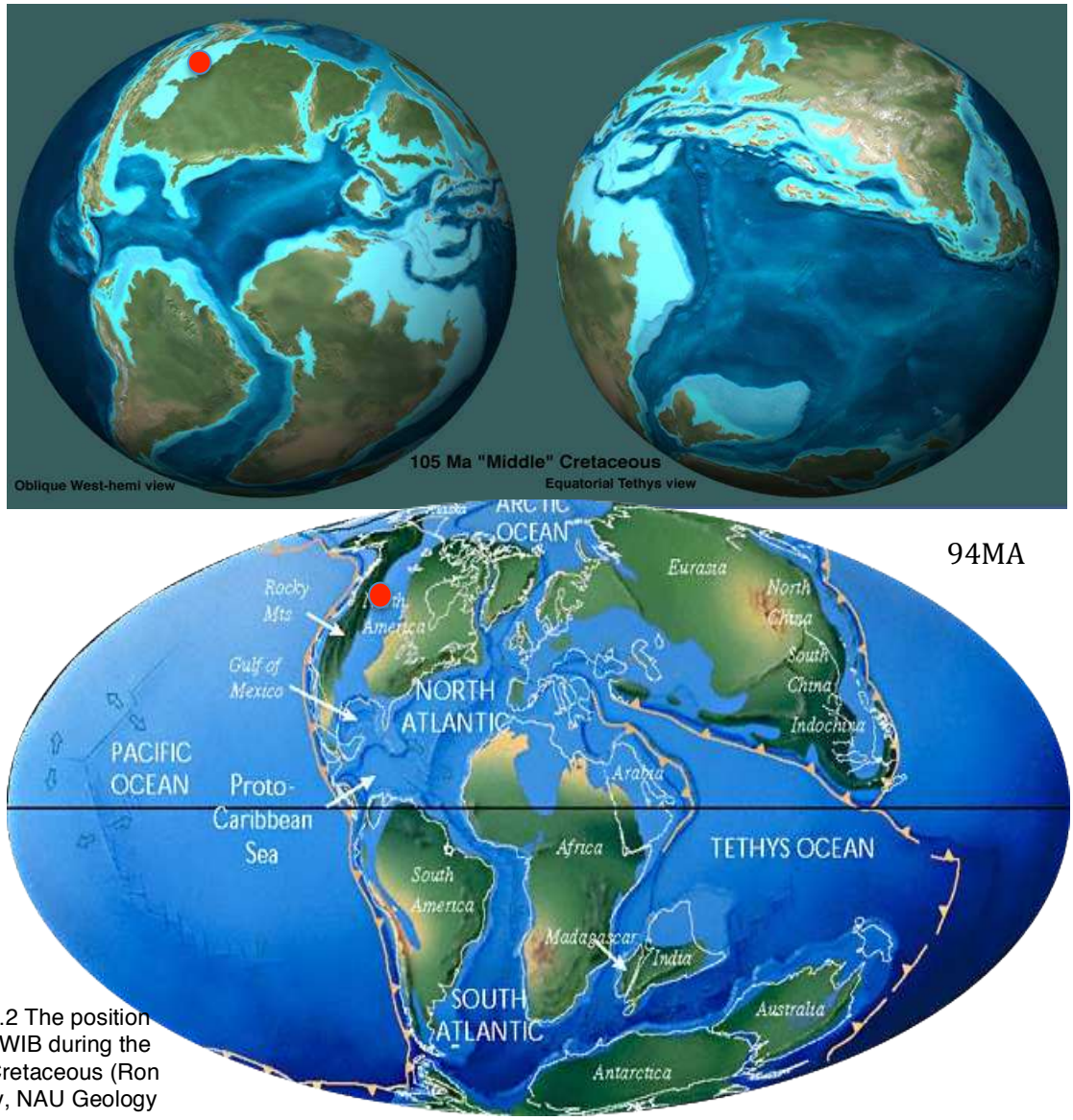

Fig. III.2 The position of the WIB during the Late Cretaceous (Ron Blakey, NAU Geology

III.3. Foreland Basins

The Western Interior basin is a stereotypical retro-arc foreland basin, related to oceanic-continental collision (Flemings, 1989; DeCelles et al, 1996; Catuneanu et al, 2004). The basin formed on top of the lithospheric flexure point of the overriding plate (Fig.III.3.). Other notable retro-arc basins examples are the Andean Basin and the Aquitaine basin, France (Sinclair et al, 2002).

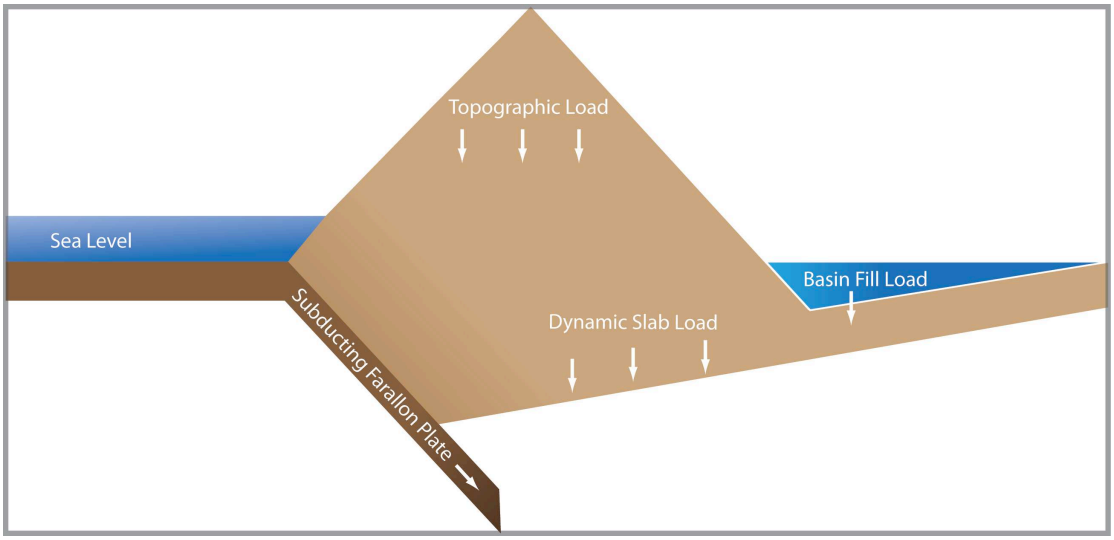

Fig.III.3. Schematic diagram of the Western Interior basin Retro-Arc foreland basin.

The WIB retro-arc formation represents an end-member type basin whereby sediment in-fills accommodation space from flexure loading rather than space generated by lithospheric extension (Rift basins) (DeCelles et al, 1996; Sinclair et al, 2005). Generally retro-arc basins are associated with regions of compressional tectonics, formed due to crustal thickening and changes in mass on the lithosphere, thus causing a change in lithospheric buoyancy (Cantuneanu et al, 2000). The change in mass produces a lithospheric flexure, causing a variable void in accommodation space. This acquired space is in-filled by transported eroded material from the topographic load, causing a continuous layered stratigraphy that spreads and wedges away from the mountain belt. This particular basin formed due to lithospheric flexure and tectonic loading in the convergent Laramide orogeny (DeCelles et al, 1996; Cantuneanu et al, 2000, Sinclair et al, 2005,).

III.3.1 Evolution of a foreland basin.

A foreland basin is defined as an elongate region of potential sediment accommodation that forms on continental crust between a contractional orogenic belt and the adjacent craton, mainly in response to geodynamic processes related to subduction the resulting peripheral or retro-arc fold thrust belt (Bourrouih et al, 1995; Sinclair et al, 2005; Naylor et al, 2008).

It consists of four discrete depozones referred to as the wedge top, foredeep, forebulge and back bulge depozones (Decelles and Giles, 1996) (Fig.III.4.). Which of these depozones a sediment particle occupies depends on its location at the time of deposition rather than its ultimate geometric relationship with the thrust belt.

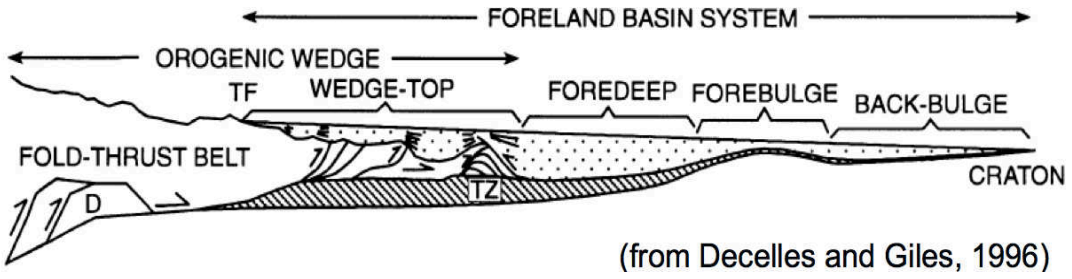

Fig.III.4. Foreland Basin System (Decelles and Giles, 1996).

The longitudinal dimension of the foreland basin system is roughly equal to the length of the fold thrust belt and does not include sediment that spills into remnant ocean basins or continental rifts (Decelles and Giles, 1996).

In general the oldest deposits found in foreland basins are dominated by fine-grained turbiditic sediments associated with the initial stages of mountain formations where both sediment supply and topography are low (Naylor and Sinclair, 2008). Over time, later deposits are dominantly continental or shallow marine characterising a maturing mountain belt with enhanced topography erosion and increased sediment supply. The main body of the WIB filled during the initial flooding event from the north during the early to late Albian stages (William and Steck, 1975).

III.4. Formation of the Western Interior basin.

Tectonic setting

The Precambrian to the early Jurassic represents the formation of a depo-centre formed on the passive edge of the continental margin, forming the cratonic platform seen today in the Rockies and Northern parts of Canada (Beaumont et al, 1993). Eventually the onset of lithospheric flexure due to tectonic loading on the pacific side of the Rockies began to form a new basin alongside the ancient Rockies (Beaumont et al, 1993; Cantantuneanu et al, 2000). The onset of the subduction of the Carillon plate underneath the North American plate during the Early Cretaceous time, controlled the onset of the Laramide orogeny (Jerzykiewicz et al, 1985). Compressional tectonics controlled crustal shortening and thickening on the cordilleran orogeny while crustal loading caused variable subsidence changes within the fore-deep basin, thus affecting the sedimentation patterns and rates over time (Beaumont et al, 1993).

Sedimentological evidence throughout the WIB show patterns of loading and unloading simultaneously in differing areas causing subsidence changes along the strike and dip of the foreland basin, (Beaumont et al, 1993) thus forming a semi-elliptical foredeep basin (Fig.III.5), evidence of which shows a variable changing hinge line along strike and dip in the varying lithologies (Cantuneanu et al, 2000).

Both current and previous works have attempted to correlate sections through the entire WIB basin using CCDP core holes (Langenberg et al, 2006; Eberth, 2011), however disconformities in the eastern flank caused by flexural, subsidence and migration of the hinge-line showed differing lithologies to that of the western side (Cantuneaunu et al, 2000). Therefore, the WIB can be described by its sediments in the distal and proximal sectors and not as the same unit (Heller et al, 1988, Catuneanu et al, 1997). Both proximal and distal movements can be responsible for the correlative system tracts either side of the Bearpaw marine hingeline (Fig.III.5). Greater crustal shortening of 150km in the south of the basin, caused a southward trend in sediment transportation regime determining the area to be a subsidence dominated foredeep proximal setting (Cantuneaunu et al, 1989).

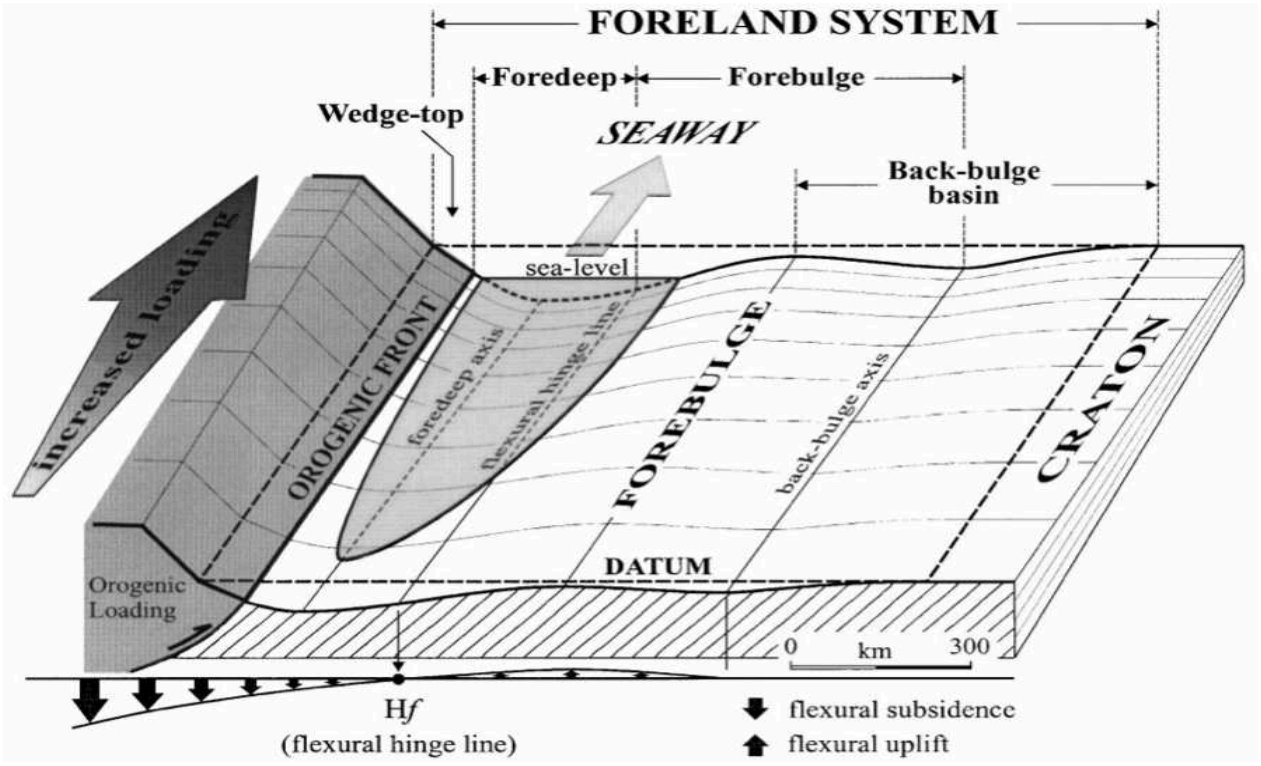

Fig.III.5 (Cantuneanu et al., 2000) Flexural loading along the foreland system during orogenic loading with strike variability. Differential loading and subsidence patterns in the WIB lead to a semielliptical loading pattern.

During the development of the WIB, high levels of volcanism was present throughout much of the Cretaceous, in total over 600 volcanic eruptions have been noted through the presence of ash or rework ash layers during the mid - late Cretaceous (Catuneanu et al, 2000). Water depth in the Western interior basin varied throughout the period and was dependant upon eustatic sea level rise coupled with tectonic subsidence (Fig.III.5).

The depositional environment of the WIB coupled with the increase of volcanism of the Laramide orogeny ensured great preservation of strata, thus making it an ideal area to locate datable ash beds, extensively used in previous and current Cretaceous timescale work (Lerbekmo et al, 1985, 1992; Obradovitch. 1993).

III.4.2 Evolution of the WIB

Stated previously, typical stratigraphy of the WIB consists of periods of seaward interbedded traipsed clastic divisions with marine mudstone and limestone beds (Kauffman et al, 1969; Sweet et al, 1996). Campanian-Maastrichtian basinwide progradational assemblages are present, however irregularities in the strata and

maximal flooding surfaces make it difficult for regional correlation (Jerzykiewicz et al, 1986; 1988). Both central and southern regions of the WIB exhibit major discontinuities and erosional patterns during the time of maximum flooding events, thus indicating variability in tectonic activity from the Laramide orogeny typical of foreland basin (Cantuneanu et al, 2000).

Northwards of the WIB around Montana and southern Alberta, reduced tectonic activity has established a more continuous section with stratigraphy consisting of series of inter-fingering clastic wedges within the marine sections, typical of the horseshoe canyon (explained in detail in chapter IV) formation (Jerzykiewicz et al, 1988; Cantuneanu et al, 2000). Focusing our field site within Central / Southern Alberta lets us establish greater detailed continuous stratigraphy and aims to reduce hiatuses within our section.

III.5. Sequence stratigraphy.

Primary deposited sediments (Mescocoridlle Geanticline, Nevada) were dated back to the Late Jurassic, they represent a series of clastic wedges deposited onto the western margin as successive terranes by crustal loading of contractional tectonism, caused by the subduction of the Panthalassa plate (Kauffman et al, 1969; Embry et al, 1993). The first major onset of sediments formed the flagship stratigraphy of the WIB, commonly associated with the Morrison and Kooteney formations, USA and Canada respectively. It arrived as the first major clastic wedge onset at the same occurrence as a magmatic quiescence in the cordillera (Berriasian age). Additionally, this lull in magmatic phase is thought to be the cause behind the large regional unconformity noted during this time. (Jerzykiewicz et al, 1986; 1988; Stockmal et al, 1987).

The start of the Cretaceous period is marked by a coarse fluvial conglomerate spreading throughout the base of the WIB in both the Canadian and North American counterparts. The lower Cretaceous shows evidence in Canada of at least two transgressive cycles, with marine waters extending in North America into the Albian. Mannville and Kootenai sediments show evidence of fluvial and estuarine systems during this time (Catuneanu et al, 2000; Eberth. 2005). Towards the mid Cretaceous,

episodes of tectonic quiescence, syn-depositional magmatic rocks and an increase in erosion show a change to a constructive building stage of the WIB (Quinney. 2011; Leckie et al, 2012).

The upper Cretaceous continues to represent a period of constructive sediment inflow forming the present day basin fill stratigraphy. Successions start to trend to a more regional scale with larger hiatuses and unconformities some representing millions of years pocketed throughout the basin, caused partly by several major marine transgressions and eustatic sea level changes and secondly the elliptical subsidence pattern caused by differential loading and subsidence by local tectonic processes. (Cauneanu et al, 2000; Eberth. 2005)

The highest marine transgression is recorded during the Turonian (Fig.III.6.) with a relative 300m sea level rise, this was the largest extent of water within the WIB, exhibiting evidence showing possibility of shallow seas extending on the distal Canadian shield, connecting with the Hudson Bay and Atlantic Ocean (Kauffman et al, 1984; Dawson et al, 2009).

The upper Cretaceous continues to represent locally controlled sedimentations with at least 6 various transgressive stages again contributing to a more localized stratigraphy then before. Low erosional rates in the northern proximal parts of the WIB show high frequency cyclicity (Hell Creek, Wyoming. Horseshoe Canyon Formation, Alberta) in sediments in the order of 10-125 ka suggesting possibility of orbitally forced eustasy (Jerzykiewicz et al,1986; Catuneanu et al, 2000; Dawson et al, 2009).

Regional and basin wide infill continued until the Late Campanian-Maastrichtian where the Western Interior Seaway began to wane (Fig.III.6.) especially throughout the United States. Shallow subduction of the Farallon Plate continued to drive the Laramide Orogeny causing the break up of the basin and the increase in volcanism. Eventually the seaway began to diminish into the early Paleocene leaving behind a classic retro-arc basin fill (Dawson et al, 2009). From the onset of the tectonics forming the Cordilleran Orogenic belt ~155 Ma accretion and contractile deformation continued for the next 100 Ma forming the present day Laramide Rocky Mountains range.

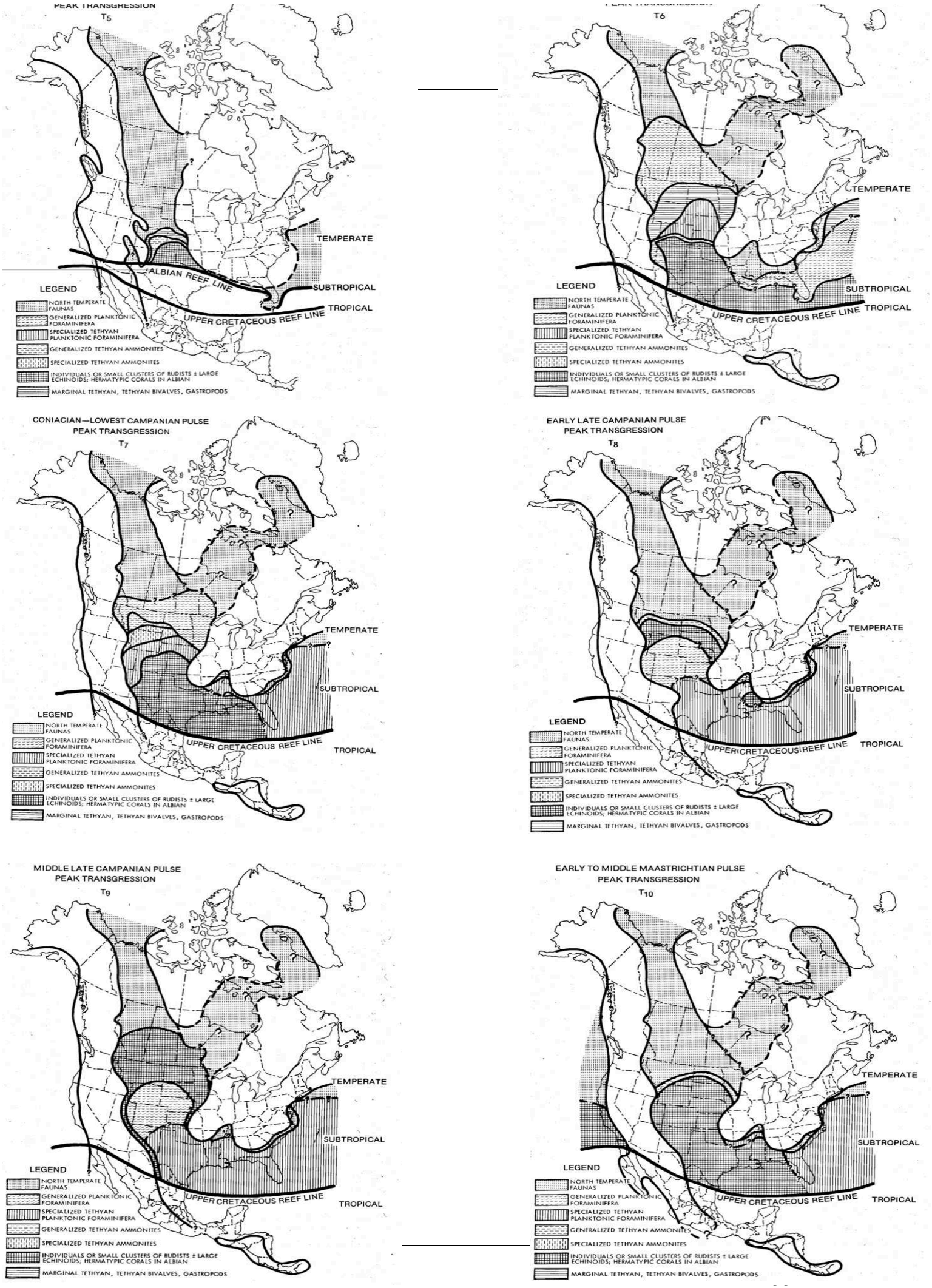

Fig. 6 (Kauffman et al, 1984) Schematic evolution of the western Interior basin. Showing the main transgressive states . Not the largest onset dated around the early Turonian .

III.6. Previous Work on the Western Interior Basin.

The extent and time spanning sections of the WIB has made the successions famous in numerous geological fields. The rich fossiliferous beds of macro and micro-fossils has created an ideal section to study evolutional history throughout the Cretaceous (Eberth. 2007). Great preservation rates especially on the proximal side of the foreland basin have generated numerous vertebrae finds of large Cretaceous species (Sweets et al, 1996).

Large volcanic episodes, great preservation rates and relatively consistent sedimentation rates over a large period of time have made the area ideal to study geochronology throughout the Cretaceous period. Regular occurrences of both fossils and bentonitic beds have allowed us to accurately acquire numerous datums linking sections basin wards but also to that of the marine realm (Lerbekmo et al, 1985,1992,1995; Obradovitch. 1993).

Extensive amounts of work are now focusing on various successions to interpret and improve the quality of the modern day Cretaceous timescale. Notably most recent work comes from analytical improvements of the radiometric and cyclostratigraphic interpretations from samples located by Obradovich (1993). These key sections have been utilised throughout the literature whereby ages are still being disputed. Data is available on other localities throughout the WIB and can be utilised to extend the reaches of (e.g. Eberth. 2005) the timescale, improve on current datums and to regionally correlate areas of interest.

III.6.2 Obradovitch. (1993)

Taken as a signature step in the formation of the current Cretaceous timescale, this database successfully dated a variety of boundary ash tuff layers (e.g Lohali Point, Four Corners, Pueblo, USA) using $^{40}Ar/^{39}Ar$ radiometric dating around the WIB. Stratigraphy was assigned by ash layers interbedded with re-evaluated bio-stratigraphic markers in particular to ammonite zonations (assumed as equal duration) by W.A Cobban and W.J Kennedy. This work also helped assign correlation between the heavily euro-centric Cretaceous era with ammonitic bio-zones of North America,

eventually leading to the correlation on a global scale (Such as the Yezo basin Japan, e.g Quidelleur et al, 2011).

Boundary	Obradovitch (1993) Age (Ma)	GTS2012 Age (Ma)
Maastrichtian-Paleocene	65.4 ± 0.1	66.0 ± 0.1
Campanian-Maastrichtian	71.3 ± 0.5	72.1 ± 0.2
Santonian-Campanian	83.5 ± 0.5	83.6 ± 0.3
Coniacian-Santonian	86.3 ± 0.5	86.3 ± 0.5
Turonian-Coniacian	88.7 ± 0.5	89.8 ± 0.4
Cenomanian-Turonian	93.3 ± 0.2	93.9 ± 0.2
Albian-Cenomanian	98.5 ± 0.5	100.5 ± 0.4

Table III.1. Cretaceous boundary ages.

Ages published (Table III.1, above) focus heavily on the Upper Cretaceous with determination of reliable Lower Cretaceous ages problematic due to the location of suitable ash layers and troubling biostatigrpahy. Ages for the Lower Cretaceous were estimated using sea floor spreading rates used in similar studies such as Kent and Gradstein, (1985) and determined against the Hawaiian M-sequence lineations by Larsen and Hilde, (1975). Estimations in sea floor spreading were considered constant, not coincinding with many nano-fossil events thus not providing the most reliable ages.

Since 1993, the Upper Cretaceous ages have changed with the exception of the Coniacian-Santonian boundary. Recent improvements in radiometric dating, fluence monitors and the introduction on new geochronology techniques such as cyclostratigraphy, have shifted much emphasis in recalibrating these ages. Work by Meyers et al. (2012); Siewert et al. (2011); Quidelleur et al. (2011), coupled with newly researched biostratigraphic horizons (Cobban et al, 2006) in the WIB has helped develop the current GTS2012 timescale. In this project, I will discuss further assessment of these revised ages in later chapters.

III.7. Canada.

Previously stated, the WIB stretched from the central part of Canada downwards proximal to the volcanic edifices in the Laramide orogeny. Near constant sedimentation rates (Eberth. 2011) and great preservation of ashes within the WIB, make Canada an ideal location for fieldwork. Much emphasis has been made within the North American key sections noted by Obradovitch (1993) signature paper, however relatively lacking in published ages by the northern counterparts in Canada.

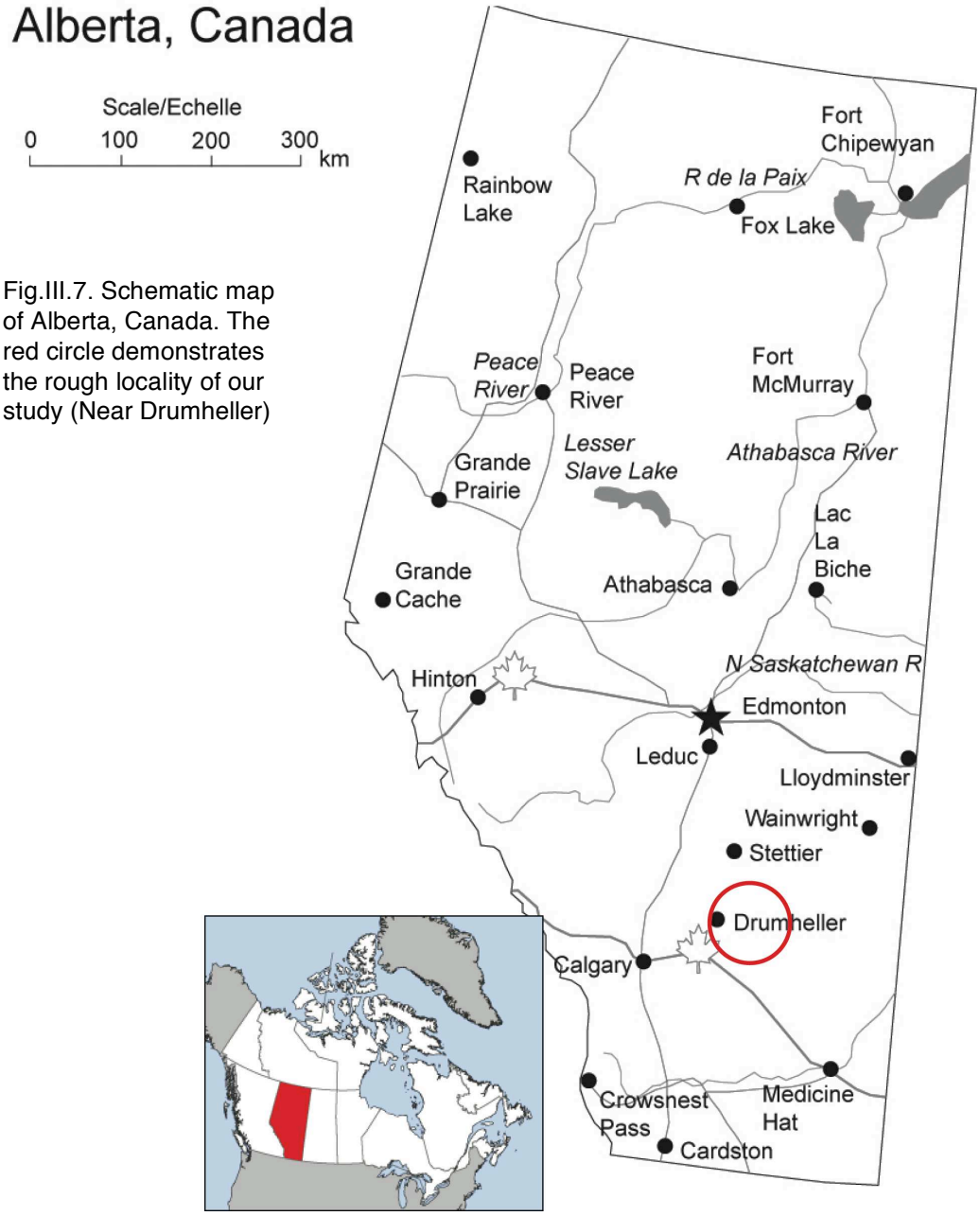

Fig.III.7. Schematic map of Alberta, Canada. The red circle demonstrates the rough locality of our study (Near Drumheller)

During the Cretaceous the most western edge of Canada formed the Laramide orogeny while the foreland basin stretched towards the east (Kauffman et al, 1984). To find the most suitable area for ideal mineralogy (+100µm) needed for $^{40}Ar/^{39}Ar$ analysis, the closer the succession to the source of material is needed. Studies have shown that in Canada the best preservations can be found in both Alberta and Saskatchewan (Lerbekmo et al, 1985, 1992, 1995; Eberth. 2011). For this particular study we mainly focused within Alberta in particular the southern and central sections (Fig.III.7.).

III.7.2 Geological history of Alberta.

Alberta is largely covered with glacial deposits of recent age, but beneath its blanket of sediment are a variety of rocks ranging in age from Archean, some 3 billion years old, to the late Tertiary (Caldwell et al, 1984; Leckie et al, 2000). The ancient, deep crustal rocks of the Canadian Shield are exposed in the northeast corner of the province, but they are everywhere beneath the relatively thin layers of younger sedimentary rocks, which date from three separate time periods: the Devonian, the Cretaceous–Paleocene, and the Oligocene–Miocene (Kauffman et al, 1977). The oldest rocks tend to be marine, laid down in the shallow continental seas typical during this time, while the youngest sediments tend to be non-marine, made of river-washed gravel and sand from the rise and erosion of the Rockies to the west. Compressive forces from continental collisions have pushed parts of the Rockies eastward onto the plains in thrust sheets extending its reach into the distal parts of the WIB (Stott et al, 1963; Kaufmann et al, 1977; Mcneil et al, 1981).

The basement lithology of Alberta formed approximately 3 billion years ago during the Precambrian era by the Tethyan sea transgression and regression of the super continent Pangea (Kauffman et al, 1977). The Canadian Shield formed while Alberta faced towards the equator; it is composed of a variety of Precambrian rocks that includes granite gneisses and quartzites (Stott et al, 1963; Leckie et al, 2000). The visible portion of this lithology makes up approximately three per cent of Alberta's current land cover, while the remainder underlies all of Alberta's plains and mountains, forming a sloping foundation for the province, at its deepest point six km below the surface (Caldwell et al, 1984; Leckie et al, 2000).

After the basement Precambrian rocks, the Western Canadian sedimentary basin can be subdivided into two reflection sedimentation patterns (Kauffman et al, 1977; Caldwell et al, 1984; Leckie et al, 2000).

- The Paleozoic to Jurassic platformal succession, dominated by carbonate type lithologies deposited within the stable craton adjacent to the ancient parallel Laramide orogeny.

- The overlying mid Jurassic to Paleocene foreland basin succession, dominated by clastic rocks formed during the evolution of the leaside of the passive margin.

During the Cretaceous and Paleocene the WIB sequence stretched through the Claggett, Bearpaw and Cannonball transgressive-regressive cycles. Since the Paleocene era there has not been net erosion and sediment bypass within the region (Jerzykiewicz et al, 1986; Catuneanu et al, 2000; Dawson et al, 2009).

Rocks immediately underlying the interior plains form a wedge decreasing eastwards where it meets with the only part of the exposed Canadian shield. The bedrock wedge is otherwise only exposed along deeply eroded river valleys (Leckie et al, 2000). In most cases it is covered by a surface layer of sediment deposited during glaciation, overlying a rock wedge containing much of Alberta's petroleum coal and oil sand resources. Bedrock of the interior Plains consists of older Devonian limestones located near the Canadian Shield and the younger Cretaceous-Paleogene shale and sandstone that extends eastwards from the foothills (Catuneanu et al, 2000; Leckie et al, 2000).

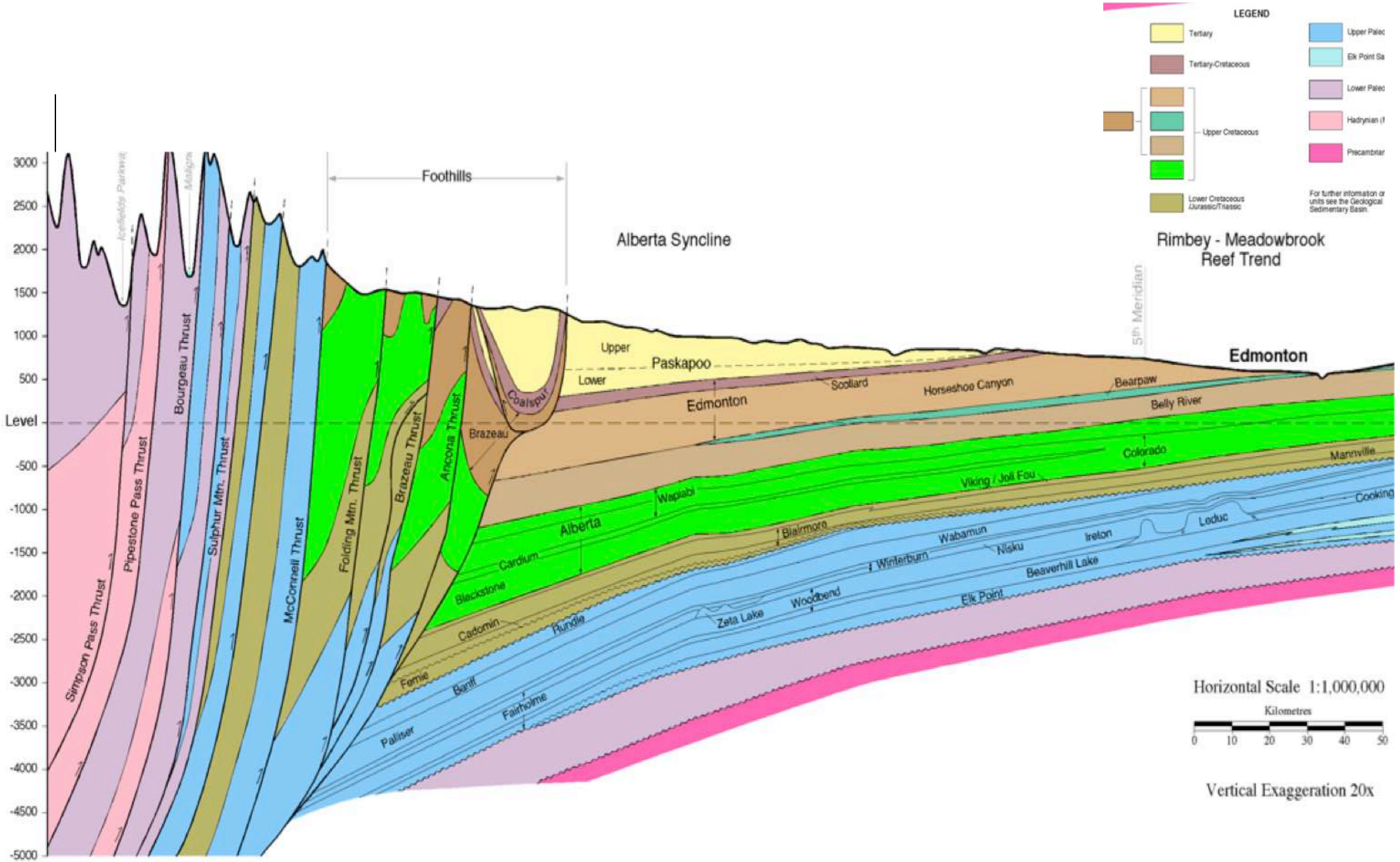

Fig.III.8 Cross section of Alberta Syncline. Note the position of the Edmonton Sequence including the Horseshoe Canyon Formation (ERCB Canada).

Fig.III.9. Geological Map of Alberta, and work section. The work area is around the township Drumheller

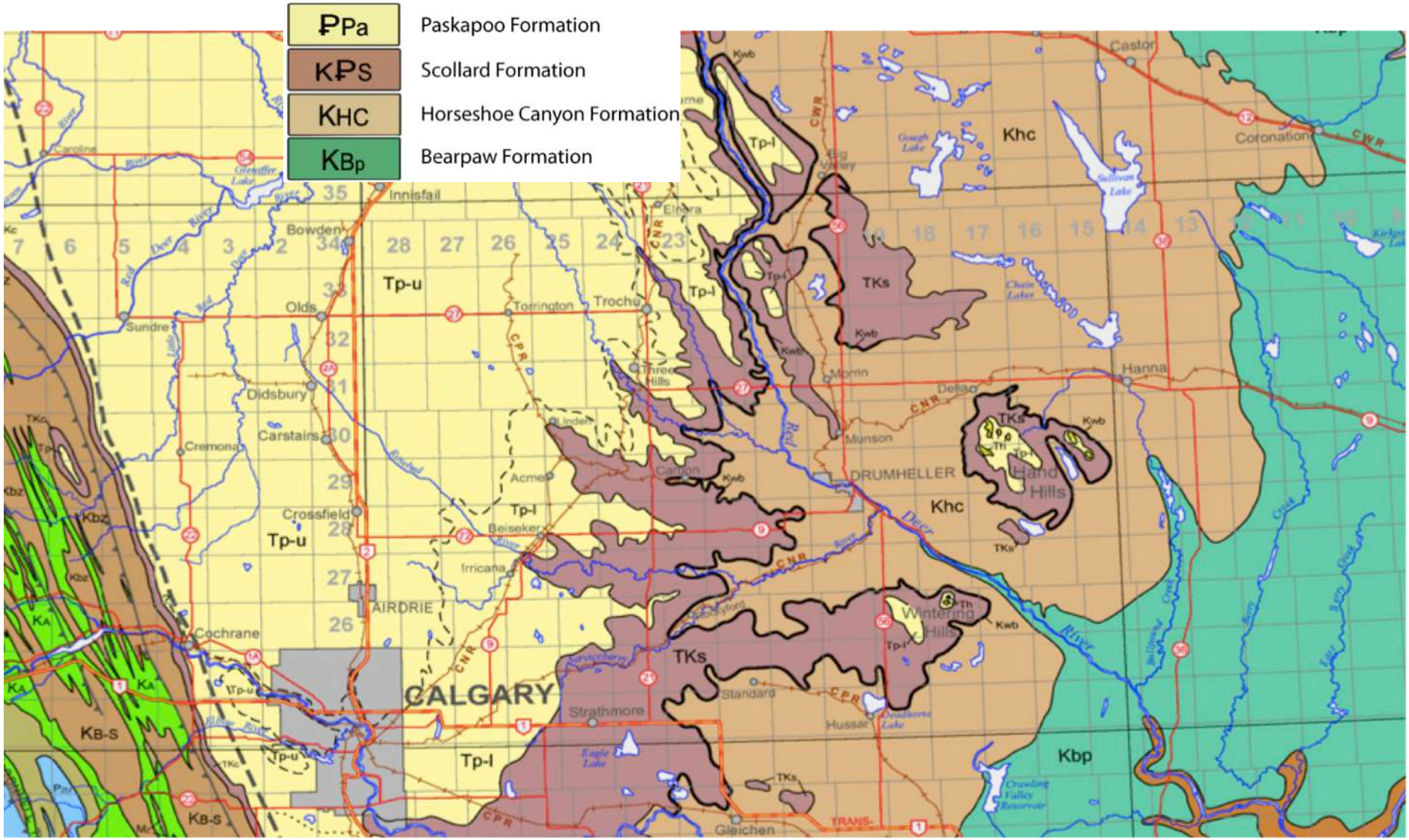

III.7.3 Interior Plains

The region covers almost 87 per cent of Alberta between the Canadian shield and Cordilleran, encompassing mainly the Boreal Plains, the Prairies and the Taifa plains in northwestern Alberta. The area contains numerous geological features such as high-level plateaus (Cyprus Hills), Badlands (Red Deer River Valley) and deeply eroded river valleys (Lerbekmo et al, 1995; Eberth. 2011). Combined together the Rocky Mountains front, main ranges and foothills accommodates approximately 10 per cent of Alberta landmass (Fig.III.8; III.9). Major valleys usually run from southeast to northwest in these particular areas such as the Blackstone river (Jerzykiewicz et al, 1986). The main geological characteristics of this area are the following:

- Foothills: Transition zone between Rocky Mountains and Interior Plains, characterised by low shale and sandstone ridges/hills that run parallel to the mountain ranges.

- Front Ranges: West of the Foothills, their eastern edge forms a distinct boundary where older dolomite and limestone rock have been exposed.

- Main Ranges: West of the Front Ranges and along the Alberta and British Columbia border, they form Alberta's highest mountains, capped by permanent snowfields and glaciers (Jerzykiewicz et al, 1986; Catuneanu et al, 2000).

For this particular study we focus mainly on the Interior plains of Alberta, East of the Rocky Mountains forming the typical badland and prairie type cast relief systems characterized by gently dipping interbedded silts, mudstone, sandstones and rich coal layers (Catuneanu et al, 2000; Eberth. 2011). The majority of the Interior basin is separated into different counterparts of the same lithology i.e nomenclature of beds is different however the lithology stays the same throughout Alberta. Previously stated in this project we will focus on the Edmonton group succession located near Drumheller.

III.7.4 Edmonton Group

The Edmonton group is a stratigraphic unit of late Cretaceous to Paleocene age, found within the Western Canadian Sedimentary basin. It is comprised of multiple lithologies such as fine grained sandstone, organic rich shales (Coal), bentonitic sandstone and shales, and ironstone concretions deposited in fresh to brackish environment (Allan. 1945; Lerbekmo et al, 1995; Langenberg. 2007; Eberth. 2011). This unit comprises of three separate sub-units: Scollard formation, Battle and Horseshoe Canyon Formation (Fig.III.10).

Thicknesses of the entire Edmonton group unit measures 763m (Allan.- 1945) in the Canadian Rockies foothills diminishing to an average 350m in the great plains (Eberth. 2011). It forms the erosional surface topography typical in central Alberta, giving way to the typical badlands relief. The Edmonton group overlays the marine Bearpaw transgression unconformably (in some cases conformably overlaying the Belly River Formation, Fig. III.10). and ends disconformably with the overlaying Paskapoo.

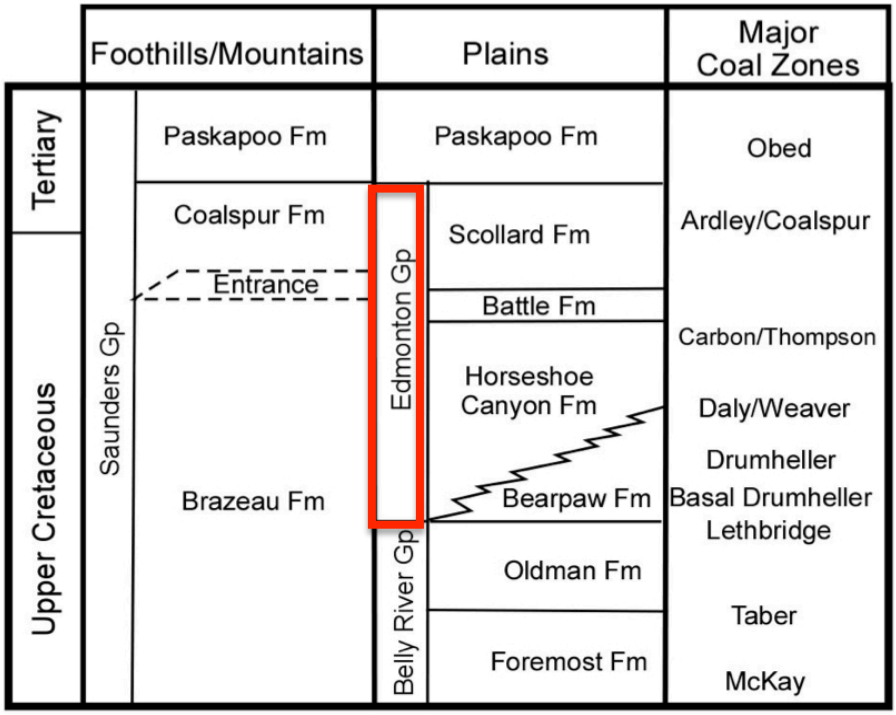

Fig. III.10 (Langenberg. 2007) Geological units in the Alberta Plains. The Edmonton group is comprised of 3 smaller sub units.

The Edmonton group clastic wedge can be regarded as the result of the late stage accretion of the insular superterrane with the intermontane terrace (Catuneanu et al,

2000; Eberth. 2011). Stated before, the WIB consits of similar successions under varying nomenclature, therefore the Edmonton group is similar to the:

-Fox Hills formation, Saskatchewan,
-St Marys river formation, Southern Alberta,
-Horsethief formation, Montana,
-Frenchman formation in Cypress hills, Alberta/Saskatchewan,
-Wapiti group and Brazeau group,
-Coalspur formation, Alberta foothills (Lerbekmo et al, 1995, Langenberg. 2007) .

III.7.5 Scollard formation

Exposed in the central and southern regions of Alberta along the Red Deer river near Trochu, this stratigraphic unit is aged from the Upper Cretaceous to Lower Paleocene and measures up to ~85-88m in thickness (Jerzykiewicz et al, 1985; Langenberg. 2007). Unconformably overlying the Whitemud/Battle formation (Fig.III.8; Fig.III.10.) and the Campanian-Maastrichtian aged Horseshoe Canyon Formation. It forms the uppermost part of the Edmonton formation finishing abruptly at the Paskapoo unconformity (Jerzykiewicz et al, 1985).

Containing the marker Cretaceous-Paleogene boundary (Fig.III.11), this unit can be located basin wide, identical to that of the Frenchman river (Saskatchewan), Hell Creek Formation (Montana, USA) and Lance Formation (Wyoming) and Coalspur (Central Alberta). The boundary itself is located in between the first coal seam (Nevis coal seam #13) present in the Scollard (Jerzykiewicz et al, 1985; Lerbekmo et al, 1995; Langenberg. 2007).

The formation consists of non-marine strata stacks deposited in the foredeep of the WIB (Khidir et al, 2010) split into two parts: the upper and lower part. The upper section comprises of coal rich beds containing two largest coal seams (Fig.III.8) found within the whole sequence:

-Nevis Coal bed: Located at the base of the upper section forming the transition from the lower, marking the K-Pg boundary.

-Ardley coal seam towards the top end of the Scollard, deposited in the Paleocene (Langenberg. 2007).

Both the upper and lower Scollard units mark two distinct unconformities, the lower boundary represents an unconformity within the lacustrine mudstones of the Battle formation (Gibson et al, 1977) while the upper section lies unconformably under the Paskapoo (Lerbekmo et al, 1990; Catuneanu et al, 2000) represented by a resurgence of large clastic deposits caused by an resurgence of tectonic activity in the basin (Khidir et al, 2010).

The sequence consists of siltstone units interbedded with thin olive-green mudstones, sandstones and relatively thick coal layers, deposited in as a series on the eastwards thinning wedge of the WIB, controlled by tectonic processes (Jerzykiewicz et al, 1985). This period of deposition represents a thrust phase of orogenic activity developing into a tectonic quiescence represented by the Scollard formation (Jerzykiewicz et al, 1985; Catuneanu et al, 2000).

Deposition of this unit occurs at a paleo-latitude of 60^{o}N in a variety of climatic conditions (Eberth. 2011). The dark organic rich coal bearing upper portion, represents warm humid conditions while the mudstone rich section of the lower part represents a low sinuosity meandering fluvial system in warm semi-arid conditions (Jerzykiewicz et al, 1985; Khidir et al, 2010). Within the lower and upper sections small laminar bentonitic horizons are present, increasing in number towards the base of the Paskapoo.

III.7.6 Battle formation.

A relatively thin succession of varying thickness (3-10m); easily identifiable by a characteristic purplish grey weathering pattern and petro-physical signature (Catuneanu et al, 2000; Eberth. 2011). This sub unit immediately overlies the siltstone/sandstone beds of the Horseshoe Canyon formation and primarily formed of dark purple brown mudstone/siltstone mix with a distinct lack of sandstone beds. The

mudstones are typically volcanic rich with pedogenic characteristics indicating paleosoil horizons (Catuneanu et al, 1998, 2000; Eberth. 2011)

The relatively small sized succession with limited sedimentation infill represents a period of basin stability (Hamblin, 2004). Several chemically altered orange coloured weathered beds lie within the formation, easily identifying this change from bordering formations. Towards the north, the Battle formation becomes discontinuous and sometimes non-existent with the Scollard preceding the HCFm (Hamblin. 2004).

The boundary between the Battle and the Scollard formation is debated with recent analysis from Catuneanu et al. (2000) suggesting no regional disconformity, thus agreeing with past studies complied by Lerbekmo and Gibson, (1990). However, palynological studies by Koppelhus and Braman, (2010) suggest a possible mixed palynomorph assemblage in the lowest most portion, supporting evidence of an unconformity below the Scollard. For this purpose it should be stated that the work of Lerbekmo, Gibson and Catuneanu were complied on the Red Deer section of this lithology, coinciding with our area and thus will be the chosen interpretation in our study.

Whitemud formation

Previously thought as a separate formation lying between the HCFm and Battle, it has now been downgraded to a unit of informally pedogenically altered horizon within the HCFm and not of that of a separate unit. (Hamblin. 2004; Eberth. 2010).

III.8. Horseshoe Canyon Formation.

Overview

Located along the Red Deer river, Drumheller Alberta, the Horseshoe Canyon Formation (HCFm), is part of the larger Edmonton group and measures up to ~227m in vertical thickness, with an average sedimentation rate of 4.5cm/ka (Hamblin. 2004). As part of the Edmonton group the HCFm, is overlain by the Battle, and Scollard formation and forms the base of the Edmonton group.

Spanning a period of ~6 Myrs, the succession formed during the late Campanian (Magnetochron 32r) to early Maastrichtian age (Magnetochron 30n) and is primarily exposed along the Red Deer river section. The acute dipping strata was deposited in a semi low-brackish environment (Eberth. 2011) and is mainly composed of mudstone, siltstone, sandstone and carbonaceous shales. Environmentally, the sequence represents deltaic environments, estuarine channels, coal-swamps and point-bar systems (Hamblin. 2004; Eberth. 2011). Brackish water trace fossil assemblages occur within these bar deposits and demonstrate periodic incursions of marine water into the estuaries (Hamblin. 2004).

The Horseshoe canyon formations includes numerous beds of sub-bituminous coal within the lowermost 120 to 15 metres. Deep industrial heritage created from the coal bed formations is evident around the local area, with coal bed formations measuring up to 70-120m in thicknesses (Lerbekmo et al, 1998; Leckie et al, 2000). Each coal seam is individually smaller around 10-20m thick but culminates to combine a coal bed mining target for drilling companies.

The HCFm is extremely fossiliferous and famous for its classic finds as Albertosaurus, Edmontonia, Parksosaurus and Trondon (Eberth. 2011). Surface exposures of strata of the Edmonton group extend in an arcuate band along the eastern margin of the Alberta syncline. The southern limit of the group occurs where the Edmonton strata below the Battle formation inter-finger with beds of the St-Mary River formation (Hamblin. 2004).

III.8.2 Location

The HCF is located around the area of Drumheller (Fig.III.11), Alberta. Continuing from the village of Dorothy (Base of HCFm, Bearpaw intersection) to Dry island Buffalo Jump provincial park. The shallow dipping strata is best viewed along the outcrops along the red deer river section near Trochu named from the horseshoe shape approximately 3km long (Hamblin. 2004; Eberth. 2011).

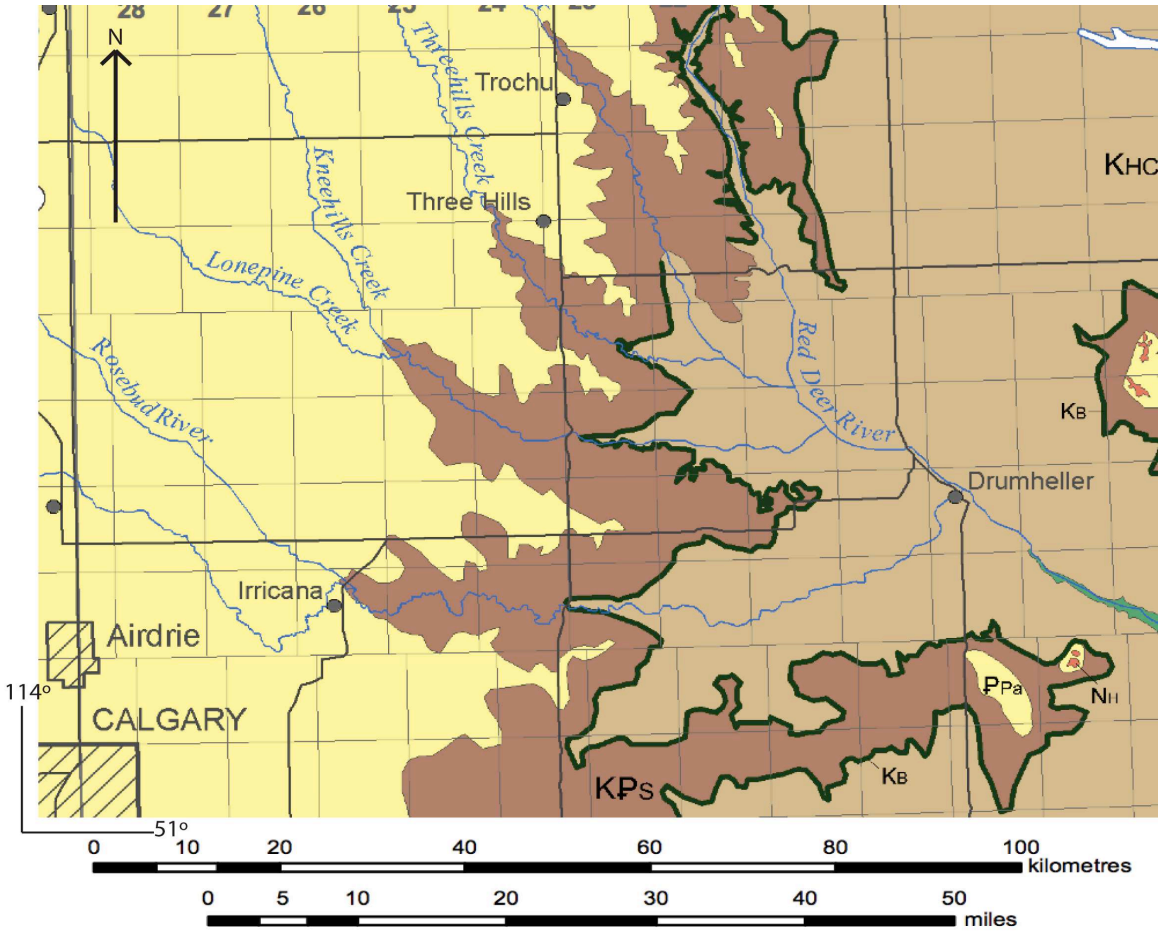

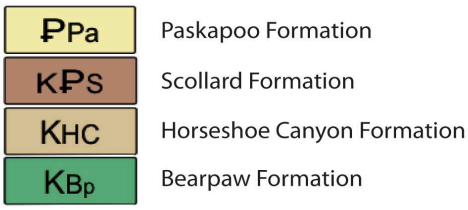

Fig.III.11. Location and geology of Drumheller and the regional unit. Note the presence of Horshoe canyon formation along the Red Deer river.

Exposure of the successions transcends along the Red Deer River section, easily visible over a large length due to the shallow dipping of the beds, additionally, lateral beds can be both continuous and diachronitas (Eberth. 2011) exposing in certain areas, thus making it a challenging area to log in complete sequence. However, certain marker horizons such as coal zones, allow the whole section to be correlate

both sides of the valley thus being able to create a fully composite log (Lerbekmo et al, 1995; Langenberg. 2007). However it should also be noted that throughout the entire succession these coal seams marker beds are also irregular and it is therefore we use the bounded coal swarm nomencular utilised from the Gibson. (1977), Straight and Eberth, (2002).

III.8.3 Units

Continental deposits that inter-finger and overlie the maximum northwards and westerwards extent of the marine Bearpaw formation define the base of the HCFm. Previous work has been attempted to define each succession just by the presence and absence of coaly beds, however recent work by Hamblin. (2004) and Eberth. (2011) were able to define five individual units that can be characterised to various complexities in

Upstream Influences:	-Indirect tectonics
	-Related climatic influences
Downstream Influences:	-Sea level change

Upstream influences can affect grain size, sedimentation rate supply and subsidence while the downstream can affect sedimentation thickness and lithology. Combinations of upstream and downstream complexities determine patterns of sediment accommodation and rates (Hamblin. 2004; Eberth. 2011).

III8.3.1 Unit 1

Overview:-

Unit 1 meaures a thickness of ~160m and forms the base of the HCFm. This unit is intermediately interfingered with the upper part of the Bearpaw formation and marks the start of non-marine strata, representing the top of the maximum flooding surface. The base is characterised by fine grained sandstones that represent a combination of shore-face and estuarine channel deposits (Leckie et al, 2000; Eberth. 2011).

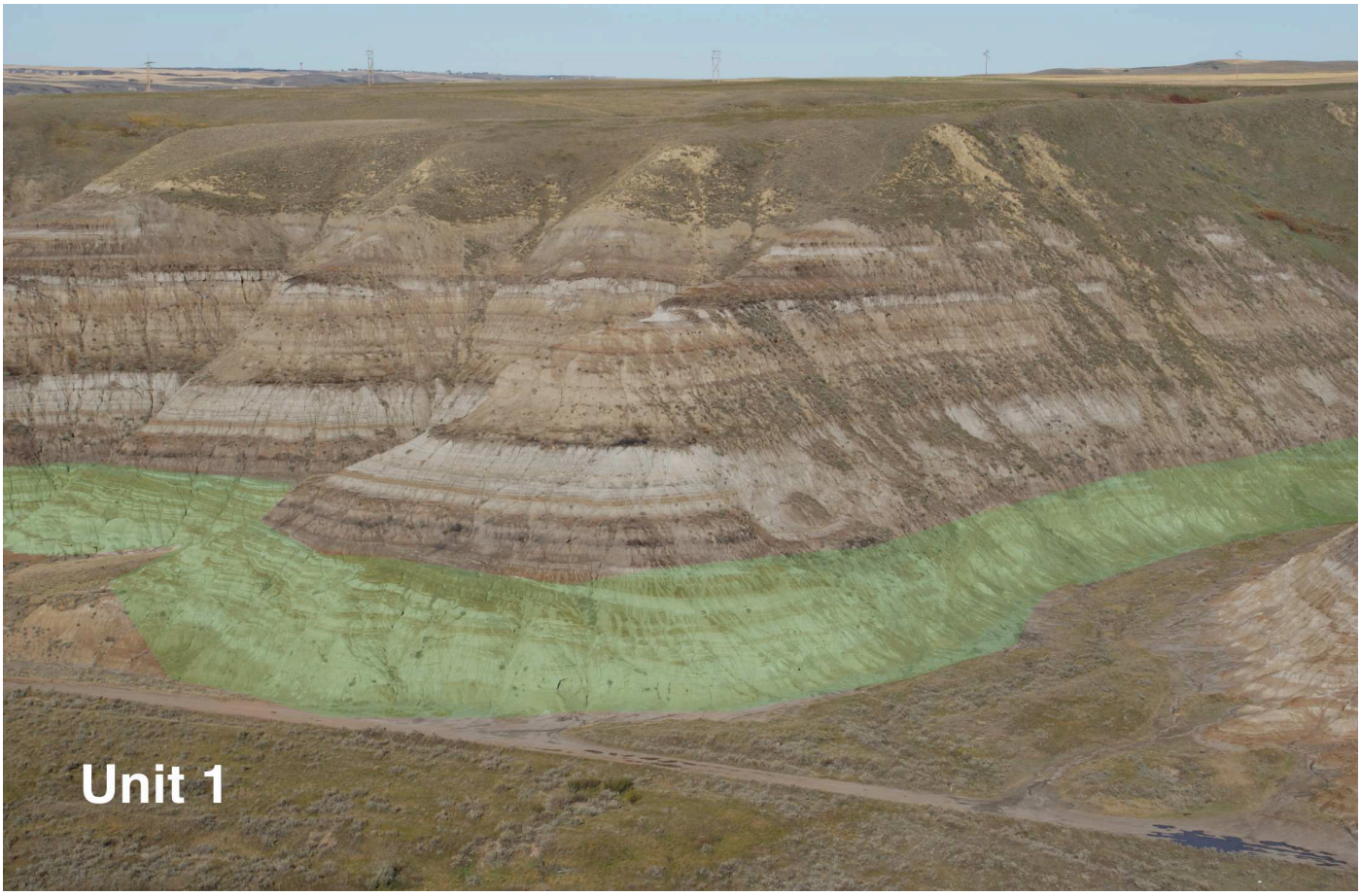

Fig.III.12 Typical type unit 1 section, located east of Dorothy township. Picture shows the base of the Bearpaw marine formation (shaded green) with the overlying horizontal stratified HCFm unit 1.

Stratigraphy:-

This sub-unit consists of thin coals (Fig.III.12), and coal swarms with lenticular paleochannel sandstones, tabular shallow marine sandstones and a variety of non-marine, brackish and mudstone facies. It consists of a variety of coaly to sandy coastal plain facies that make up a progradational succession (Hamblin. 2004; Quinney. 2011).

Regional Coal Correlations

This particular unit holds 0-9 numbered coal swarms:

- #0-5 - Exposed from east Coulee until the town of Drumheller, this particular package is known as the Drumheller Coal Zone (Chen et al, 2005).

- #6-7 - Exposed from the Horse-thief canyon until Rosedale. Named the Garden Plain-Daily Zone.

- #8-9 - Midland provincial park to Morrin and Tolman bridges. Named the Weaver Coal Zone.

Bentonites

Present between coal zones 6-7, is a relatively thick ~15m intermitted bentonite. Mineralogy studies allows this package to be traced basinwards using both mapping and gamma-ray logging (Langenberg. 2007). The presence of this iconic stratum allows regional successions to be easily linked and stratified. The large presence of bentonitic beds show a large increase in volcanism, possibly representing an increase in tectonic activity in the Laramide orogeny (Eberth. 2011).

Formation

Unit 1 presents a large drop in relative sea level and decrease in subsidence causing a stacking of sediments from the coal #6 level. The Drumheller bentonite zone also suggests an increase in volcanism and tectonic changes. (Leckie et al, 2000; Hamblin. 2004; Eberth. 2011).

Dorothy bentonite

A 13.5m thick benotic bed located in the Bearpaw formation at the base of the HCFm, this horizon outcrops at the Red Deer Valley section near a small hamlet called Dorothy, 12 km from Drumheller. The resulting bed was formed from reworked ash, geochemically constrained as a Plinian type short eruption with a rhyolitic compostion (Lerbekmo et al, 2002).

Early ages by Gordy and Edwards, (1962) date the intrusion by K-Ar Sanidine as 85 ± 3 – 72 ± 3 Ma with whole rock ages of an older 112 ± 3 Ma. However, the most recent ages of the Dorothy bentonite by Rb-Sr ages give an age of 73.5 ± 0.4 Ma (Baadsgard et al, 1999). Although sampled, we were unable to obtain any Sanidine or Zircons for radiometric dating.

III.8.3.2 Unit 2

Overview

Compared to the unit 1, this slightly thinner unit of ~40m, is charecterised by a lack of coaly horizons. In particular, the lower half of this sub unit contains the basinwide Drumheller Marine Tongue, (DMT) and rests between coal #9 + #10 swarm. Normal lithology includes fine to medium coarse-grained sandstones with fine laminated beds, and an increase in grey green vertisol paleosols (Hamblin. 2004). Somewhat fossiliferous, the unit also contains shards of reworked vertebrae fossils (Eberth. 2011; Quinney. 2011).

Stratigraphy

The top of unit 2 is marked by the presence of a laterally extensive 15m thick zone of stacked tabular beds of fine grained planar to ripple laminated sandstonse with minor and highly localized cross-bedding (Quinne, 2011). Unit 2 records significant upstream and downstream influences; the relatively low sedimentation rate, vertisols and absence of organic rich coal suggest a comparatively dry climate with palynology suggesting a more northern cooler climate. In addition the presence of the DMT insists a relative sea level rise during this time (Leckie et al, 2000; Hamblin. 2004; Eberth. 2011; Quinney. 2011).

Regional Coal Correlations

#10- Poorly sub-bitumous “coal” layer interbedded into the Drumheller Marine Tongue.

Bentonites.

Morrin Bridge: Key locality for the Campanian-Maastrichtian boundary. Two thin bentonites beds are located close to the two thin coal #9 + #10 beds. The lack of bentonites in this particular unit, suggests a possible lull in the volcanic activity (Eberth. 2011).

Formation

Mostly non-coaly representing a drier climate, the upstream tectonic and climatic influences reduced the sediment supply and subsidence while a eustatic sea level rise maintained a modest degree of accommodation. Evidence of upstream influences

causing the rising level of tectonics and seasonal dryness could of formed a rain shadow effecting during this time (Eberth,. 2011; Quinney. 2011).

III.8.3.3 Unit 3

Overview

Unit 3 is relatively small thin ~15m succession. Forming the top of the Morrin bridge section, holding the upper half of the DMT, the sub unit consists of large iron concretion beds, and small scale stacked bedded sandstone (Eberth. 2011).

Stratigraphy

Small-scale sandstone shows evidence of laterally continuous laminations, and ripple marks, characteristic of shallow estuarine environments (Eberth. 2011). Fossil assemblages are still present, with mainly dinosaur teeth and small fish vertebrae, common for a shallow estuarine environment (Leckie et al, 2000; Hamblin. 2004; Eberth. 2011; Quinney. 2011).

Formation

High volcanic content within the sandstones suggest an possible increase in tectonic activity. While the stacked sandstones reflect late stage high stand and marine turn-around consistent of the downstream influences.

Fig.III.13 Morrin Bridge section containing the Campanian-Maastrichtian boundary (Estimated to be around halfway up the succession). This section contains both Unit 2 and Unit 3 (Note the car for scale)

III.8.3.4 Unit 4

Overview

A 25m thick succession that lies conformably over the previous unit, notable for its complete lack of coaly beds (Fig.III.14). Formed totally in a non-marine, deltaic brackish environment. This unit is abundant in verterbrate fossils (i.e. Albertasaurus), found mostly at the base of paleochannel sandstones (Eberth, 2011).

Stratigraphy

Consisting of a combination of mudstone, fine-grained sandstone with iron concretions, complete with fine laminations and mesoscale cross-bedding (Quinney. 2011). This unit incorporates the upper half of the Tolmann marine tongue and bares resemblance to the stratigraphy found in Unit 2. Fine-grained sandstone, coupled with siltstone and small paleochannels relay a relatively dry climate (Hamblin. 2004; Quinney. 2011).

Fig.III.14 Panoramic view from Knudsen's farm section; The bottom half in the distance represents unit 4 with a total lack of coaly beds. Unit 5 can be seen overlying this unit with the Coal bed in the foreground and the presence of darker beds in the distance.

Formation

The bottom half of this unit defines an increase in mudstone to sandstone ratio, while the top half indicates the first occurrence of organic rich sandstones. This unit records evidence for both upstream and downstream influences, recording increasing rates of subsidence and eustatic lowering (Eberth. 2011; Quinney. 2011). However, the low ratio of mudstone / sandstone mix and lack of stacked paleochannels possibly suggest an increase in subsidence rate and accommodation rate at the same time (Eberth, 2011).

8.3.5 Unit 5

Overview

A ~25-40m thick succession that gradually overlays unit 4 (Fig.III.14). The top ~10m of this succession forms a layer called the Whitemud; a pedogenic and weathered interval that has been declassified as a formation to be a part of a subunit of unit 5 (Eberth, 2011). The end of the HCFm lies unconformably under the Battle formation. (Hamblin, 2004; Quinney, 2011)

Stratigraphy

Unit 5 consists of fine-medium grained sandstone, with gradual changes evident throughout the section from mudstone to sandstone, alongside small scale paleo-environmental markers such as ripple marks and low angled laminations. Mineralogical studies of the unit show a more mature matrix including quartz, potassium and feldspars (Leckie et al, 2000; Hamblin, 2004; Eberth, 2011; Quinney, 2011).

Coal Swarm

Dark organic rich horizons return in this particular unit after a notable absence from the previous. With two rich coal zone swarms included. #11- Carbon + #12 – Thompson (Discussed further in chapter IV).

Formation

Reflecting mainly upstream influences such as climatic wetter conditions, the thicker unit indicates an increase in sediment supply. Additionally, the unit also indicates an

increase in subsidence rate, however during the Whitemud formation, the unit records a time of reworking and weathering, offering a reversal of the upstream and downstream influences and indicated the change to a cooler climate (Leckie et al, 2000; Hamblin, 2004; Eberth, 2011; Quinney, 2011).

Utilising the presence of datable bentotic beds alongside analysed geochemical proxies extracted within these sections, it is possible to deduce reliable ages which are useful for both timescale and stratigraphical correlation of the WIB. In chapter IV we will use a multi-discplinary approach to calculate the age of the K/Pg boundary from the same sections described above. Additionally, we will use the same approach in chapter V to calculate the age of the Campanian Maastrichtian boundary found within Units 2 + 3.

IV. The Cretaceous / Palaeogene Boundary

Multidisciplinary Approach for Resolving the Age of the Cretaceous / Palaeogene Boundary: Cyclostratigraphy, $^{40}Ar/^{39}Ar$ and U-Pb Geochronology.

Benjamin D. Heredia	(University of Bern, Switzerland)
Jonathan R. Gaylor	(University Paris Sud XI, France)
Frits Hilgen	(University of Utrecht, The Netherlands)
Klaus Mezger	(University of Bern, Switzerland)
Xavier Quidelleur	(University Paris Sud XI, France)
Jan Wijbrans	(Vrije University Amsterdam, The Netherlands)
Silja Huesing	(University of Utrecht, The Netherlands)
Willem Langenberg	(University of Alberta, Canada)
Klaudia Kuiper	(Vrije University Amsterdam, The Netherlands)

IV.1. Introduction

The stratigraphic record contains a wealth of information about gradual processes and catastrophic events on the Earth's surface including changes in oceanic and atmospheric chemistry, climate change, eustatic and relative sea-level changes, mountain building and erosion, basin subsidence, and strong evidence of biological evolution. Understanding these processes and relating them to causalities in Earth's history requires precise and accurate quantification of geological time.

Scientists working on timescales and timescale calibration have aimed to extend the orbital calibration from the Eocene to the Cretaceous, building upon an astronomical time scale independent of radio-isotopic dating (e.g. Laskar et al, 2004; 2011), thus filling the gaps in the Cenozoic timescale and reducing the age uncertainties on the K/Pg boundary (e.g. Hilgen et al, 2008; Hilgen et al, 2010, Westerhold et al, 2008; 2012; Min et al, 2000; Renne et al, 2010; EARTHTIME and GTSnext initiatives). However, both approaches have their limitations and problems. Most of the astronomical ages depend upon the applied astronomical solution, interpolation between two astronomically tuned calibration points, and lags between orbital forcing and sedimentary expressions (e.g. Laskar et al, 2004; 2011; Hilgen et al, 2008; Westerhold et al, 2008). Furthermore, uncertainties in the computation of Earth's

orbital parameters beyond 50 Ma (e.g. Laskar et al, 1990; 2004; 2011; Pälike et al, 2004) and radio-isotopic age constraints from $^{40}Ar/^{39}Ar$ dating (e.g. Min et al, 2000) challenge the correct tuning of such an important event in Earth's history.

For more than 30 years, the Cretaceous/Palaeogene (K/Pg) boundary probably has been the most investigated boundary in chemical, biological and geological terms. Almost simultaneously, Alvarez et al. (1980) and Smit and Hertogen (1980) showed that platinum group elements, which are severely depleted in the Earth's crust relative to cosmic abundances, occur in anomalously high concentrations in deep-sea sediments at the K/Pg boundary and concluded that they may be indicative of a potential extraterrestrial source impacting Earth, and causing the end-Cretaceous mass extinction. The impact crater was later found at Chicxulub, Mexico (e.g. Hildebrand et al, 1991). The occurrence of a single impact is globally supported by the recognition of a single impact ejecta layer, which includes spherules, shocked minerals and Ni-rich spinels found in most of the outcropping K/Pg sections either very proximal, proximal, intermediate or distal to the impact crater (e.g. Schulte et al, 2010). Notwithstanding the global evidence, there has been controversy about the causes of this mass-extinction event. Alternative interpretations for the mass extinction include multiple meteorite impacts (e.g. Keller et al, 2002; 2003) and massive lava emissions in the Deccan Traps flood basalt province (e.g. McLean, 1985; Courtillot et al, 1986; 1988; Duncan and Pyle, 1988; Chenet et al, 2007, Keller et al, 2009). The multiple meteorite impact idea is supported by paleontological and stratigraphic data from diverse very proximal through proximal sections relative to the crater (e.g. Keller et al, 2004; 2012), implying that all intermediate and distal sites lack resolution and completeness to firmly establish a correlation to the main crater found in the Yucatan peninsula (e.g. Keller et al, 2003; 2004).

The second major phase of the Deccan volcanism has been suggested to encompass 80% of the total lava pile erupted on a very short timescale (~1 Ma) and has been related to occur synchronously with the mass extinction (e.g. Chenet et al, 2007; 2008). Environmental consequences have been thought to be devastating due to gas release in relative short time interval (e.g. Chenet et al, 2007; Self et al, 2008). However, uncertainties in the age estimations in the Deccan Traps volcanism may hamper proving its synchronicity with the mass extinction. It is thus clear that a better

understanding and detailed chronology of the volcanic activity at the Deccan Traps and a precise and accurate age estimate for the boundary clay is crucial for determining the cause-and-effect relationship for this important event in Earth's biological evolution.

The $^{40}Ar/^{39}Ar$ method is the most widely used radio-isotopic dating technique for calibrating floating astrochronologies in the late Cenozoic time, and the possibility to synchronise astronomical and radio-isotopic dating techniques for this time interval has been proven (e.g. Kuiper et al, 2008). However, the absolute accuracy in the $^{40}Ar/^{39}Ar$ system is still limited to ~2.5% (Min et al, 2000; Renne et al, 2010), mainly due to uncertainties in the age of standards (or age monitors), the absolute abundance of ^{40}K and radioactive decay (e.g. Begemann et al, 2001). U-Pb zircon geochronology, has become a concise tool for calibrating geologic timescales due to precisely determined U decay constants, high-precision measurement methods, and an internal check for open-system behavior provided by the dual decay of ^{235}U and ^{238}U to ^{207}Pb and ^{206}Pb, respectively. Precise and accurate determinations of U/Pb ratios by isotope dilution thermal ionisation mass spectrometry (ID-TIMS) yield high-precision U-Pb dates (0.1% or better), currently becoming widely used for high-resolution geochronology in Earth sciences. Furthermore, Earth's orbital parameters have been used to correlate climatic variations and to generate astronomically calibrated geological time scales of high accuracy (e.g. Gradstein et al, 2004). However, on long time scales the inner Solar System is chaotic, limiting the accuracy of such astronomical models with increasing age (e.g. Laskar et al, 1990, 2011; Pälike et al, 2004). Geological and geochemical data is thus needed for sediments older than 40 Ma to determine whether or not the climate controlled sedimentary deposits are linked to orbital parameters.

In the present study, a multi-disciplinary approach is applied to constrain the age of the K/Pg boundary. The approach is based on the development of a cyclostratigraphic framework in land-based sedimentary successions and the application of high precision-high accuracy U-Pb zircon and $^{40}Ar/^{39}Ar$ geochronology for a section containing the K/Pg boundary and a volcanic ash as close as ~30 cm to the "boundary clay" in the Horseshoe Canyon Formation in western Canada.

IV.2. Geological Setting

The "boundary clay" at El Kef, Tunisia, at the base of the Danian and the top of the Maastrichtian defines the K/Pg boundary (e.g. Molina et al, 2006). There are, however, more than 350 sites worldwide where the boundary is exposed, showing distinct ejecta distribution features with respect to the distance to the Chicxulub crater (e.g. Schulte et al, 2010). The boundary is defined at El Kef by a lithological break, an oxidised red-layer at the base of the boundary clay, the presence of chemical anomalies (e.g. the Ir-anomaly), spherules (e.g. Ni-rich spinels), shocked quartz, a negative $\delta^{13}C$ shift (Molina et al, 2006) and is considered to be isochronous in marine and continental sections (e.g. Molina et al, 2006; Schulte et al, 2010). However, since the discovery of this impact crater under a thick sedimentary cover, several attempts have been made to constrain the time of its formation using cyclostratigraphic and radio-isotopic techniques (e.g. Izett et al, 1991; Obradovich, 1993; Swisher et al, 1992; 1993; Kuiper et al, 2008; Renne et al, 2010; 2013).

The Horseshoe Canyon Formation in the Western Canada Sedimentary Basin is particularly well suited to determine the time of the K/Pg boundary because it consists of a thick package of alternating sediments that includes volcanic ash beds, and is well exposed along the Red Deer River in southern Alberta (Fig.IV.I). On the basis of the Ir-anomaly and the presence of the boundary clay, the K/Pg boundary in the area has been placed at the bottom of Coal nr.13 (Lerbekmo and St.Louis, 1986; Therrien et al, 2007). No evidence for multiple impact related sedimentary layers was found within the coal or underlying and overlying units. Thus the observations from this section indicate that one event caused the Ir-anomaly and the deposition of the boundary clay, a conclusion that is also observed in the studies of Lerbekmo and St. Louis (1986) and Therrien et al, (2007).

The uppermost part of the Horseshoe Canyon Formation shows a relatively well-preserved cyclic alternation of organic-rich material, silt and sandy horizons (i.e. a cyclothem, which defines here the basic bundle), in which altered volcanic ash layers are abundant (Fig.IV.2). Rationale is that if the deposition of each alternation, during sea-level fluctuations, is controlled by changes in the astronomical parameters, it

should be possible to "pin-down" the respective periodicities (precession, obliquity or eccentricity) from the stratigraphic record. Furthermore, volcanic ash layers containing sanidine and zircon crystals may help to determine the absolute time elapsed during the deposition of a certain number of alternations (or cyclothems), thus resolving the dilemma of whether or not these periodicities do exist in this particular sedimentary environment.

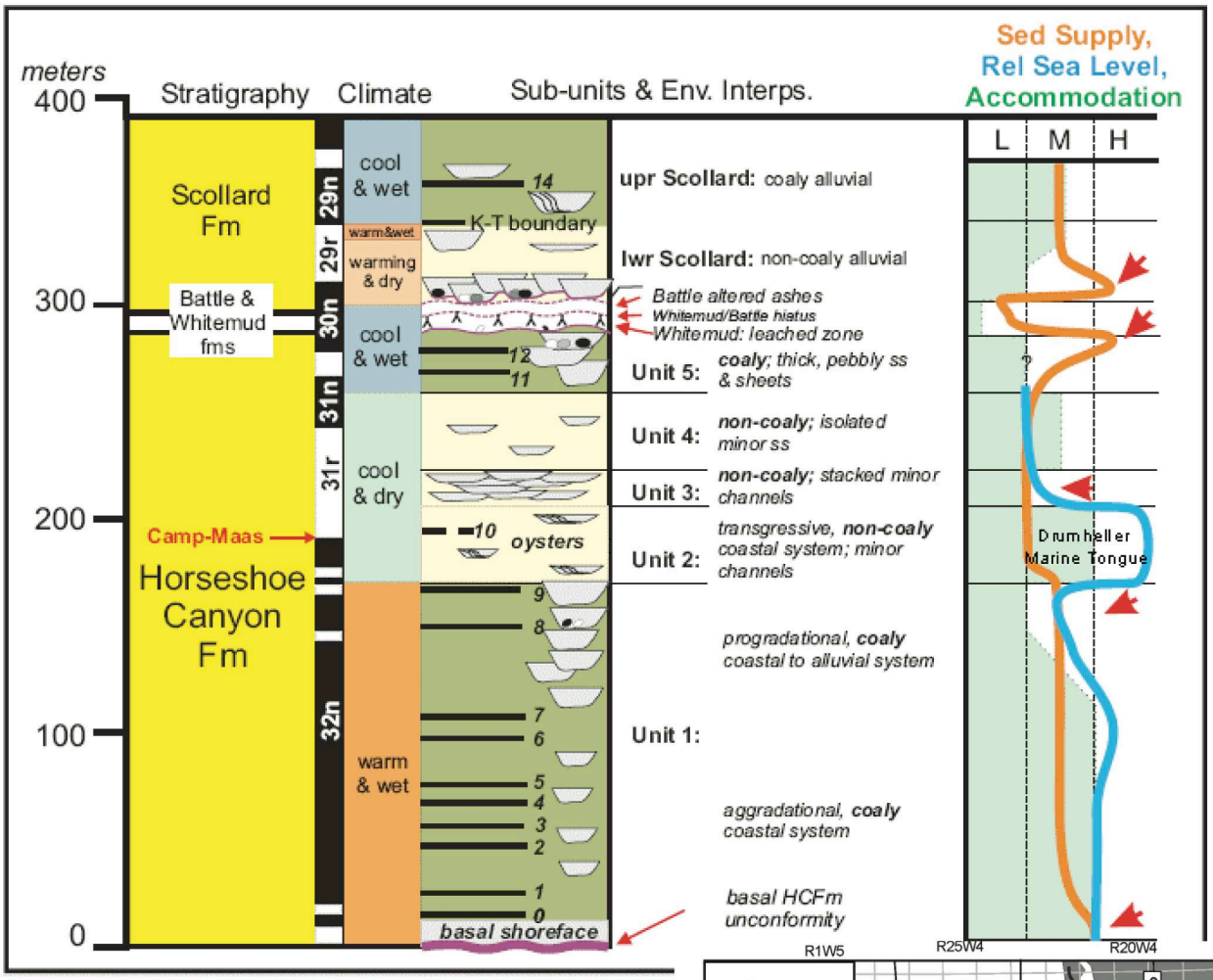

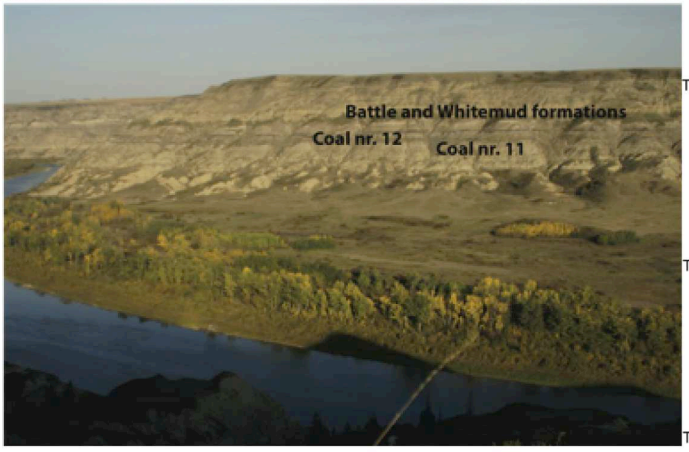

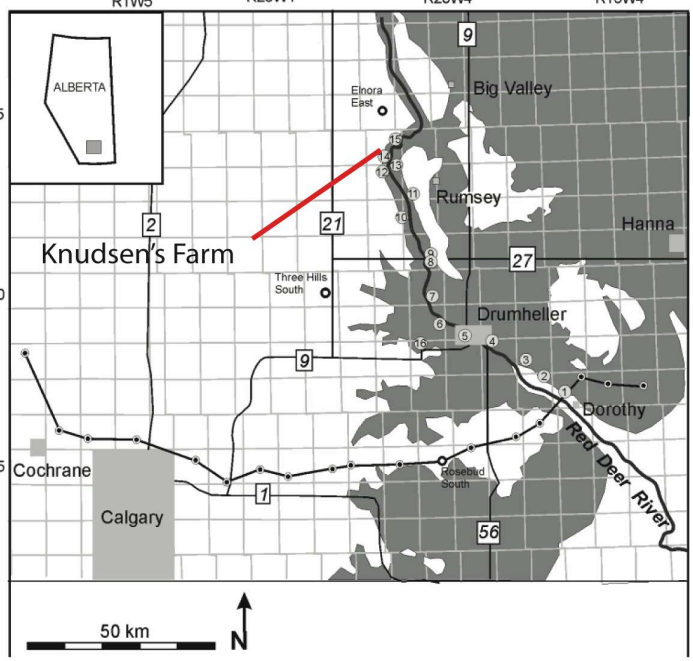

Fig.IV.1. (Previous page) Location map, lithostratigraphic divisions showing the inferred climatic and palaeoenvironmental conditions, and the panoramic view of the sediments exposed along the Red Deer River. The K/Pg boundary is located at the bottom of Coal nr. 13. Modified from Eberth. (2010).

Parts of the Upper Cretaceous Horseshoe Canyon Formation are well exposed in the Knudsen's Family Farm section along the Red Deer River (Fig.IV.1 and Fig.IV.2). At this locality the sedimentary sequence exposes a continuous section whose uppermost part comprises Unit 5. According to Eberth (2010), Unit 5 represents a setting mainly consisting of bench forming, stacked, alluvial channel sand-silt successions with minor paludal-lacustrine deposits. The Knudsen's Family Farm section is dominated by sand at the base, but the uppermost part is dominated by regular cyclic alternations of organic rich-silt-sand horizons from the Scollard tuff up to Coal nr. 14 (or Ardley Coal; Fig.IV.2). According to Eberth and Currie (2005), Unit 5 lacks vertebrate fossils, although the presence of remains of dinosaurs and other vertebrates has been observed in the area. The lack of vertebrate fossils suggests that there was a shift to cooler climate, having a negative impact on temperature sensitive vertebrates (Larson et al, 2010). However, there is no precise information available so far about the timescales on which climate was shifting in the area or the causes of the change on climate.

Fig.IV.2 (Next Page). Composite photograph and detailed log of the Knudsen's Family Farm section at the uppermost part of the Horseshoe Canyon Formation in Alberta, Canada. The precession-related cycles are indicated, following the main alternation of organic rich-silt- sand. The section is composed of at least 22 alternations from the Scollard tuff to Coal nr. 14 (or Ardley Coal). However, the thickness of the main alternations is variable throughout the entire section, increasing the amount of sand above the K/Pg boundary and decreasing the thickness of the organic-rich layers. Below Coal nr. 14 a thick package of sand is observed in the entire area suggesting a main unconformity, thus hampering the extension of the cyclostratigraphic framework.

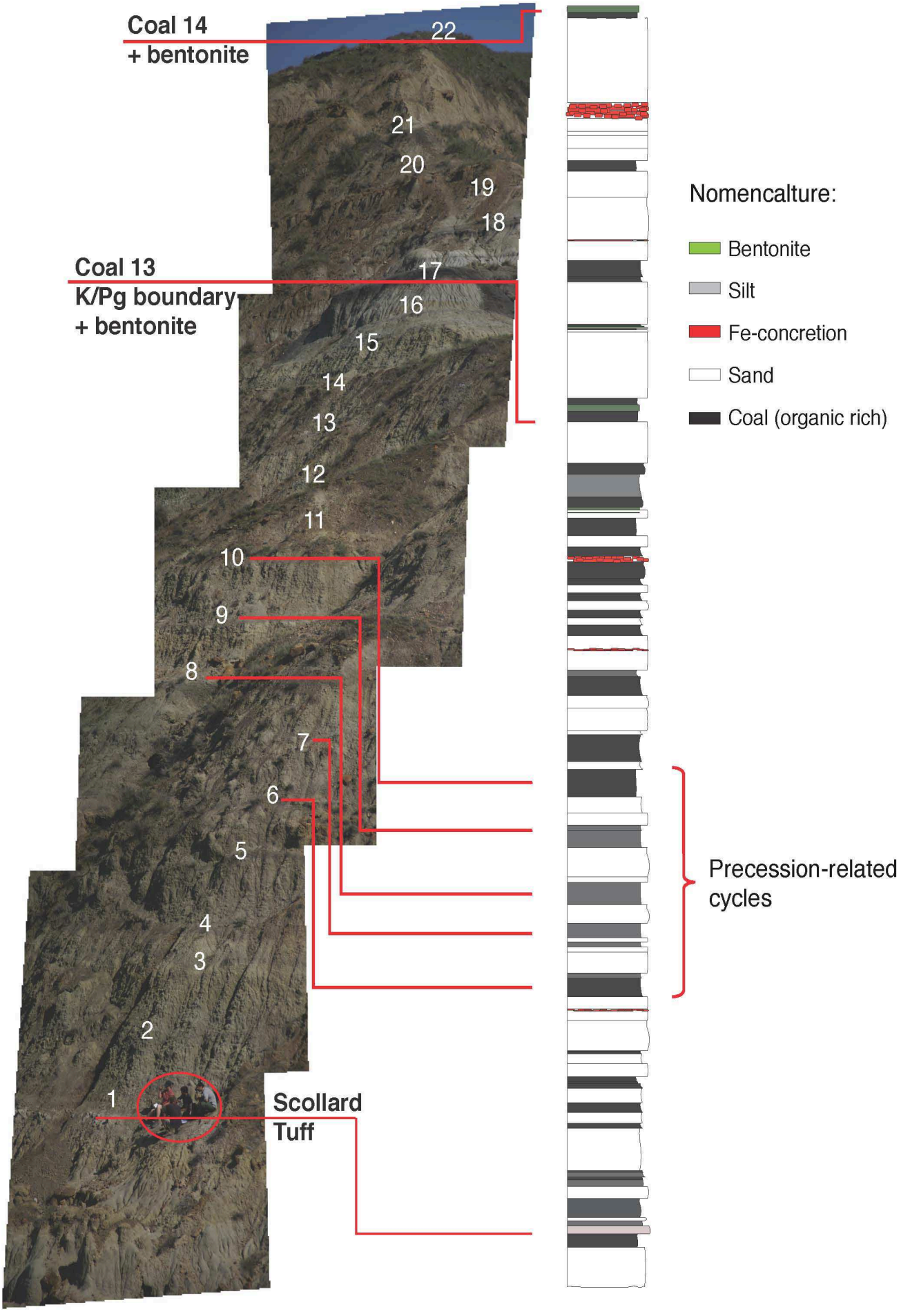
Coal 14
+ bentonite
22
21
20
19
18
Coal 13
K/Pg boundary
+ bentonite
17
16
15
14
13
12
11
10
9
8
7
6
5
4
3
2
1
Scollard
Tuff
Nomencalture:
Bentonite
Silt
Fe-concretion
Sand
Coal (organic rich)
Precession-related
cycles

IV.3 Samples and Methods

In order to obtain proxy records, samples from each single lithology of the ~45 m thick Knudsen's Family Farm section at the uppermost part of the Horseshoe Canyon Formation were taken, trying to cover each bundle at a resolution distance of ~40 cm per sample. Lithological proxies, such as colour and magnetic susceptibility were taken by using a spectrophotometer and susceptometer, respectively. The colour of all samples were analysed at least 3 times and averaged. The colour spectrum includes the L*(D65), a*(D65), b*(D65) and the spectrum from 400 to 700 nm with increases of 10 nm. Major and trace elements on whole rock powders were determined with a Thermo XRF instrument. All the analyses for lithological and chemical proxies were performed at the Fort Hoofddijk palaeomagnetic laboratory at the University of Utrecht. Furthermore, several samples from well-preserved altered volcanic ashes within the coal layers were taken for mineral separation, targeting the separation of sanidine and zircon grains.

IV.3.2 Cyclostratigraphy

For developing the cyclostratigraphy, all samples were normalised to a very homogeneous coal layer (Coal nr. 13 or Nevis Coal) in order to redefine the relation between layers. Although an intrinsic parameter that can be influenced by changes in sedimentation rates, the colour proxy (especially the blueness or b*(D65)NORM =(b*(D65)Sample/b*(D65)Coal13); Fig.IV.3) was observed to be the main sedimentary parameter responsive to climate- controlled periodicities, as colour is directly linked to lithology. The normalization enhanced contrast between sedimentary layers (i.e. dark layers are the most organic rich, as they are closest to unity), matching the observations made in the field. Similar patterns were observed for the Fe# (i.e. $Fe\#_{NORM}$= (Fe_{tot}/(Fe_{tot}+Mg)) Sample / (Fe_{tot}/(Fe_{tot}+Mg)) Coal13; Fig. IV.3), when normalised to the coal.

Weathering indices have been widely used in studies of both modern and ancient profiles for providing a better understanding of elemental mobility, for evaluating soil fertility and development, for characterizing alterations associated with neo-tectonics, and for demonstrating the impact of climate on the bedrock (e.g. Price and Velbel,

2003; Bahlburg and Dobrzinski, 2009).The chemical index of alteration (CIA_{NORM}= (Al/(Al+Ca+Na+K) Sample / (Al/(Al+Ca+Na+K)Coal13); Nesbitt and Young, 1982) is a commonly used weathering index applied to siliciclastic sedimentary rocks, as it measures the amount of chemical weathering of silicate minerals, particularly K-feldspar, through hydrolysis and exchange of the cations Na+, K+ and Ca2+. In the Kundsen's Family Farm section the CIA shows no correlation with the colour or the Fe# most probably due to a combination of grain-size effects, incorporation of older weathered material, mobilisation of the cations during diagenesis or the presence of apatite in the layers. Thus, the cyclostratigraphic framework was developed exclusively using colour ($b^*(D65)_{NORM}$) and $Fe\#_{NORM}$.

The $b^*(D65)_{NORM}$ and the $Fe\#_{NORM}$ co-vary closely and in agreement with the observed alternations in the lithology. Field observations suggest that the thicknesses of the basic alternation fluctuates between ~1.8-2.2 m from the bottom at the Scollard Tuff to the K/Pg boundary. In the stratigraphically higher part of the section the thicknesses of the basic alternation show a decreasing amount of organic-rich layers and become dominated by thick sand layers all the way to the top of the section. Therefore the cyclostratigraphic framework was restricted to the lowermost part, where the alternations are observed to be more consistent.

For pinning-down the possible information linked to Earth's orbital parameters (or periodicities), a decomposition of the stratigraphy of the Knudsen's Family Farm section into depth-frequency space was performed by using the freeware AnalySeries program (Paillard et al, 1996). A strong periodicity is thus observed at ~1.8-2.2 m in the proxies data (Fig.IV.4). The wavelet analysis applied to the same datasets from the Scollard tuff to the K/Pg boundary also confirms the same periodicity for both $b^*(D65)_{NORM}$ and $Fe\#_{NORM}$. The periodicities larger than 8 m were removed by notch filtering. The wavelet analysis allowed a local decomposition of the stratigraphy into time series (Torrence and Compo, 1986). The Morlet wavelet of the $b^*(D65)_{NORM}$ and the $Fe\#_{NORM}$ show a reasonably large number of oscillations, ensuring good frequency resolution (Fig.IV.4). The Morlet wavelet is a complex wavelet function aimed to capturing oscillatory behaviour of the time series. This complex wavelet function returns information about both amplitude and phase (Torrence and Compo, 1986).

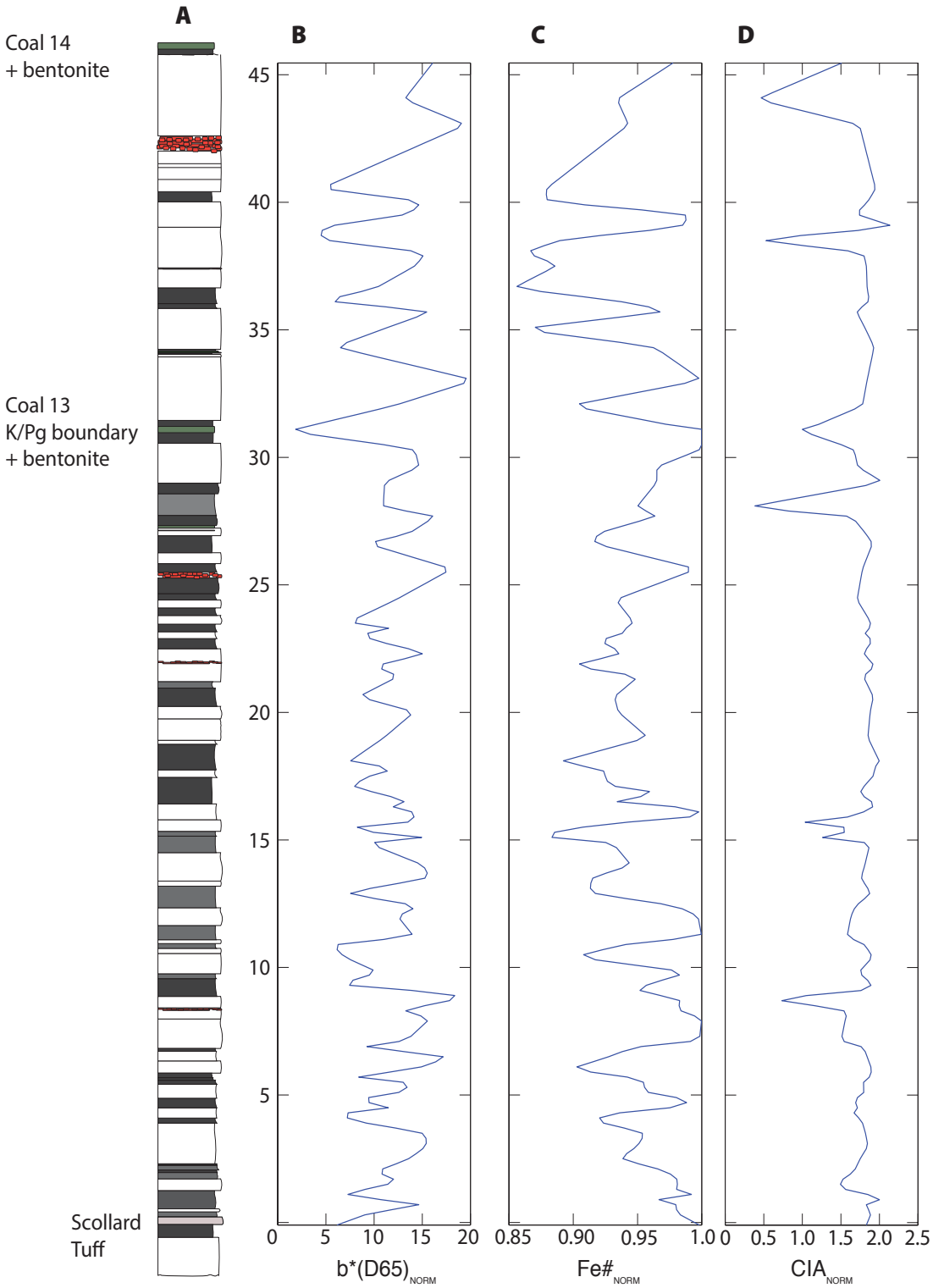

Fig.IV.3. A Detailed log of the Knudsen's Family Farm section, showing the main lithology. Intrinsic parameters are plotted against the lithology; **B.** Blueness or b*(D65)NORM; **C.** $Fe\#_{NORM}$; **D**. CIA_{NORM} . All the lihological and chemical proxies have been normalised to Coal nr. 13. Decreases in colour correlate with decreases in Fe#, possibly pinpointing to the deposition of organic rich layers. The CIA characterises the deposition of sand horizons better showing higher values compared to organic rich horizons.

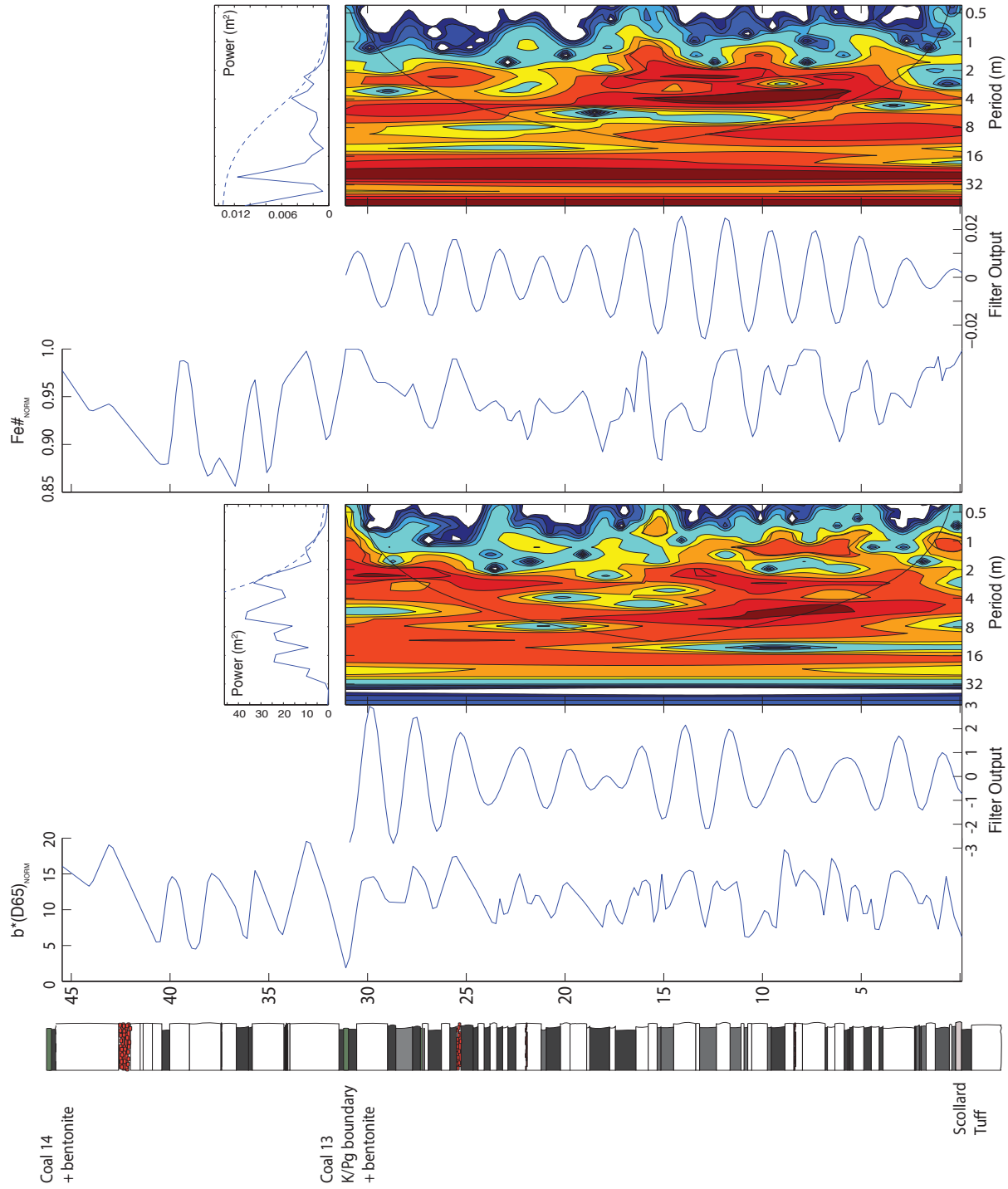

Fig.IV.4. Detailed log of the Knudsen's Family Farm Section plotted against the proxy records for the blueness ($b^*(D65)_{NORM}$) and the $Fe\#_{NORM}$. The filter output indicates that there are 13- 14 cycles related to the lithology and the proxy data. The wavelet analysis also confirms these periodicities observed in the field, varying between 1.8 and 2.1 meters. The cyclostratigraphic framework exclusively has been developed to the lower part of the section until the K/Pg boundary, as above the boundary, the section becomes dominated by the deposition of sands and the amount of organic rich horizons decreases.

IV.3.3 Magnetostratigraphy

The precise knowledge of the extension of magnetochrons has been crucial for the global correlation of Canadian sections to those of the Western Interior Basin in the US (e.g. Lerbekmo, 1985; Lerbekmo and Coultier, 1985; Lerbekmo et al, 1996). Paleomagnetic constraints from the Danian to the Maastrichtian in the Red Deer River section have been reported (e.g. Lerbekmo and Coultier, 1985), suggesting that the base of the C29r is ~13 m above the Scollard Tuff, whilst the top of the reversal is ~1-2 m above the K/Pg boundary. Oriented hand-samples were collected and thermally demagnetised in a magnetically shielded furnace using small temperature increments from 20 to 460°C. Some other samples were continued heated up to 550°C. The natural remanent magnetization was measure on a 2G Entreprise horizontal cryogenic magnetometer at the Paleomagnetic Laboratory at the Fort Hoofddijk, The Netherlands. The palaeomagnetic investigation presented here, suggests that the reversal is located at ~6 m above the Scollard Tuff (Fig.IV.5), whilst the top of the reversal could not be found in the section. Thus, independent time control is vital for the correct time constraints of the section and its global correlation.

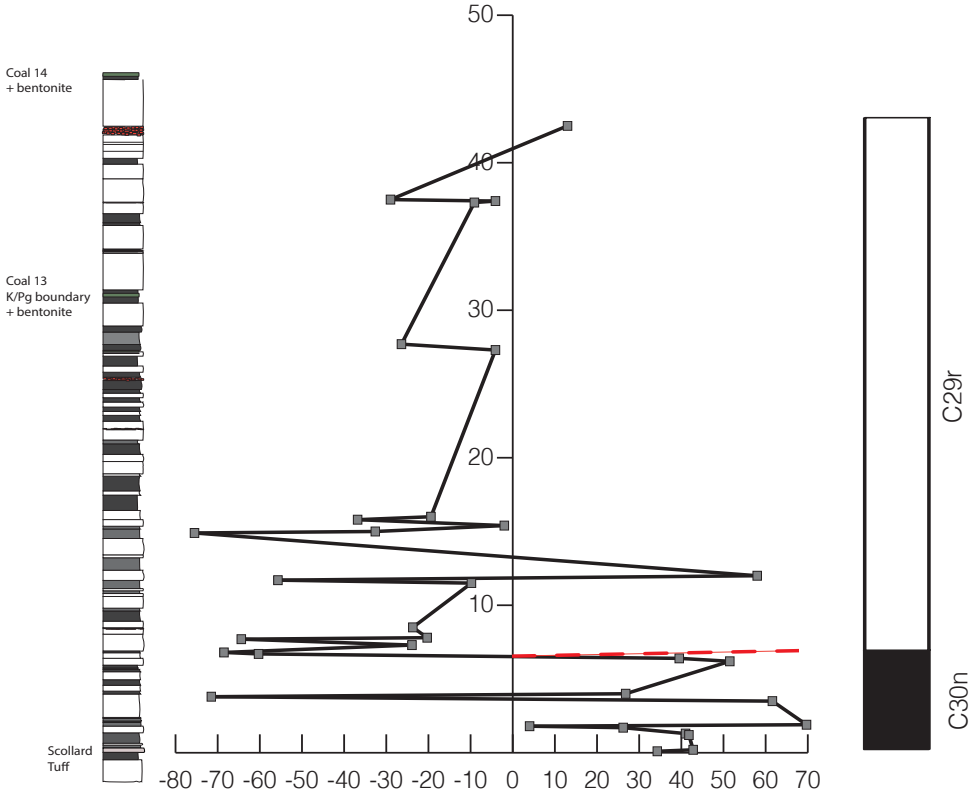

Fig.IV.5. Detailed stratigraphic log of the Knudsen's Family Farm section and the magnetostratigraphy from this study. The magnetostratigraphy has been performed on oriented hand-specimens.

IV.3.4 U-Pb zircon geochronology

Zircon crystals were separated from two well-preserved ash layers, one at the top of the section in the middle of Coal nr. 14 (or Ardley Coal; Fig.IV.2), and one at the middle of Coal nr. 13 (approx. 30 cm from the K/Pg boundary; Fig.IV.2), using standard techniques. Whole zircon grains, fragments and tips of individual crystals were selected for high-precision U-Pb analyses. All grains were annealed and dissolved in two steps, following the chemical abrasion method (Mattinson, 2005). U/Pb isotope ratios were determined by ID-TIMS using a Thermo Fisher Triton+, equipped with a discrete-dynode MasCom electronic multiplier in ion-counting mode. All analyses were performed at the Institute of Geological Sciences at University of Bern, Switzerland. Total procedural Pb blanks were 2.3 ± 0.8 - 0.50 ± 0.4 pg. Higher common Pb contents are attributed to an inherited component and corrected for using the common Pb composition from the two-stages model of Stacey and Kramers (1975). Mass fractionation factors in the electronic multiplier were constrained by using NBS982 for Pb and CRM-U500 for U. The tracer is enriched in ^{205}Pb and ^{235}U isotopes, and was calibrated using a certified gravimetrically mixed Pb-U solution (NBS982-IRMM056). Accuracy was performed by repeated analysis of the EARTHTIME 100, 500 and 2000 Ma synthetic solutions (Condon pers. comm.). All the U/Pb dates are reported with 2σ confidence levels. U/Pb isotopic data and dates are given in the supplementary data. All the age estimates plot on or near the Concordia line (Fig.IV.6).

$^{206}Pb/^{238}U$ age estimates for single grains and grain tips for the two samples range from 65.48 ± 0.10 to 66.26 ± 0.21 Ma (2σ) (Fig.IV.6). The youngest population is interpreted to represent the time of deposition of the tuff as these crystals are considered to have the closest relationship to the time of eruption (e.g. Crowley et al, 2007). Furthermore, weighted mean statistics are useful to analyse if the distribution of ages within individual volcanic ashes is due to analytical uncertainties or dispersion in zircon crystallisation. The mean square of weighted deviates (MSWD or reduced chi-square) is often used as a statistical test for the best fit of the calculated mean or regression line (e.g. Wendt and Carl, 1991). If MSWD is ~1, inhomogeneous samples will not contribute with additional scatter, meaning that the extent of the match between the observations and the estimates is purely analytical and thus in

accord with the uncertainty variance.

The volcanic ash sample in the Coal nr. 13 has at least five analyses that yield a weighted mean age of 65.746 ± 0.058 Ma (MSWD = 0.75), suggesting that the data are consistent with a null-hypothesis that all zircon grains crystallised synchronously. Zircon grains from Coal nr. 14 define more than two populations. The youngest population is interpreted to be the closest to eruption, yielding a mean age of 65.529 ± 0.056 Ma (MSWD = 0.95), whilst the second population yields a slightly older mean age of 65.844 ± 0.057 (MSWD = 0.88). Some of the older populations of zircon crystals from Coal nr. 14 also coincide with the older age estimate from the zircons at Coal nr. 13, suggesting that it may be the same magmatic reservoir depositing the two temporally distinct volcanic ashes. However there is no available isopach map for the area for determining the main locus of volcanism.

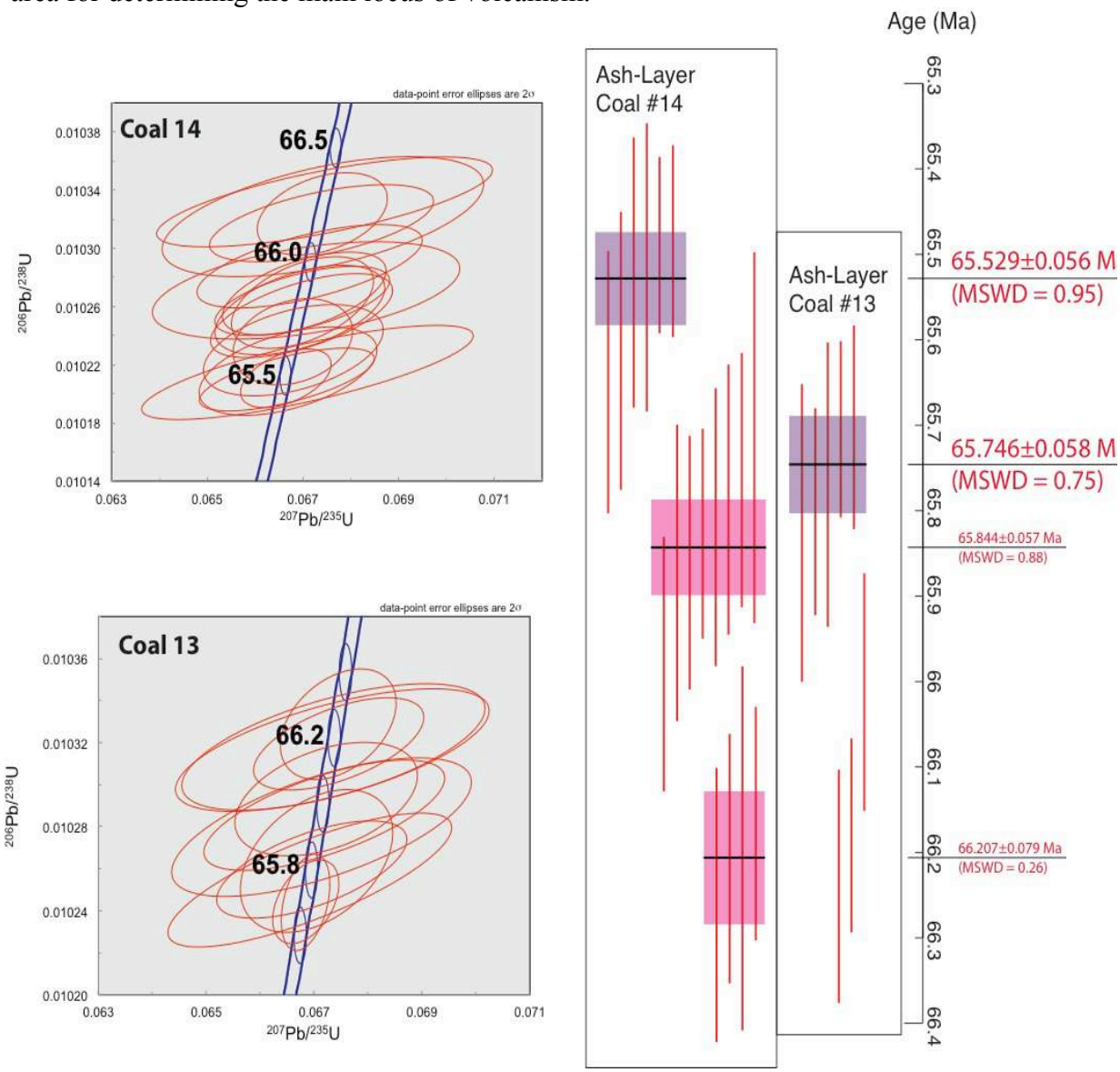

Fig.IV.6. (Previous Page) U-Pb concordia diagrams from the altered volcanic ashes preserved within the coal layers. Not all data is shown, as the eruption age was the prime objective in the U-Pb geochronology (i.e. youngest population or the autocrystic zircon). However, several other zircon populations have been observed and related to antecrystic zircon. Single grain and grain fragment $^{206}Pb/^{238}U$ zircon dates are also shown with their respective weighted means. Uncertainties in single analysis and weighted means are presented as 2σ intervals or 95% confidence levels. All data was plotted using the IsoPlot (Ludwig, 1991)

IV.3.5. $^{40}Ar/^{39}Ar$ Geochronology.

The $^{40}Ar/^{39}Ar$ dating method has been used widely to both accurately date and detect any perturbations since emplacement. The same two ash layers (Middle of Coal nr 14; Fig.IV.2 and Coal nr.13 30cm from K/Pg boundary) were disintegrated and sieved, while mineral isolation was performed by heavy liquid separation (Bromoform). The samples were stained and picked using a sodium colbaltinitrite solution to pick out sanidine crystals >7%wt K (Hynek et al, 2011). Finally the sanidine was cleaned using a 3 step acidic technique of HNO_{3conc}, followed by HF_{conc} then leached once more by HNO_{3conc}. About 0.2g of each sample was packaged into compact copper pellets and placed into 1cm vacuum sealed quartz tubes, tightly packed between two flux monitor samples for irradiation.

Samples were irradiated in the CLICIT position of the University of Oregon TRIGA fast neutron reactor, The first set for 40 hours while the second set sample was irradiated for 60 hours. Halfway through both irradiations the quartz tubes were flipped 180^{o} to reduce the neutron flux change across the z-axis. J-factor was determined using 20mg aliquots of Fish Canyon Tuff sanidine (FCT), Taylor Creek Rhyolite sanidine (TCR) on the first irradiation and HD-B1 biotite, FCT on the latter. Measurements were completed on the $^{40}Ar/^{39}Ar$ multi-collector instrument developed in our laboratory and described in Coulié et al, (2004).

Flux monitors were measured following total fusion and performed with a Nd-YAG infra-red laser at 0.8A, while samples were step heated with ~13 incremental steps using a high frequency furnace. After heating the gas, it is first purified by 700^{o}C Ti foam following by 15 minutes on an AP10Gp SAES getter heated to 400^{o}C. The

sample was then transferred to an additional coal trap undergoing a second purification under a SAES Al-Zr getter, before measured in the mass spectrometer.

Mass discrimination was determined from an air pipette system, while blanks were determined on the same condition as samples. Average $^{40}Ar/^{36}Ar$ atmospheric ratios of 304 ± 1 were measured over the course of the two studies. K interfering reactions were calculated using the values of Renne et al. (1998):7.0 x 10^{-4},1.2 x 10^{-2}, 7.2 x 10^{-4} and 2.68 x 10^{-4} for $[^{40}Ar/^{39}Ar]_K$, $[^{38}Ar/^{39}Ar]_K$, $[^{39}Ar/^{37}Ar]_{Ca}$ and $[^{36}Ar/^{37}Ar]_{Ca.}$ Age uncertainties and calculations follow McDougall and Harrison $^{40}Ar/^{39}Ar$ Techniques, with ^{40}K decay constants and isotopic ratios of Steiger and Jager, (1977). J Values were determined using the FCT and TCR ages of Kuiper et al. (2008) 28.201 ± 0.046 Ma and 28.53 ± 0.02 Ma respectively.

$^{40}Ar/^{39}Ar$ bulk mass sanidine plateau ages obtained for the two samples (Fig.IV.7) show an age range from 65.40 ± 0.30 to 65.88 ± 0.30 Ma. The ash from sample located inside Coal nr. 13 gives an age estimate for 65.88 ± 0.30 (MSWD 2.46) with 65% of the total ^{39}Ar released and 4 out of the 10 steps utilised. Each step contained more than 90% of radiogenic argon ($^{40}Ar^*$). Two step heated samples of Coal nr 14 were measured yielding ages of 65.621 ± 0.294 Ma (MSWD 1.31) and 65.40 ± 0.30 Ma (MSWD 0.13) giving a weighted mean age of 65.51 ± 0.21 Ma. Age plateaus for these two samples use both 61% and 90% of the total gas released with all steps measuring more than 90% of $^{40}Ar^*$.

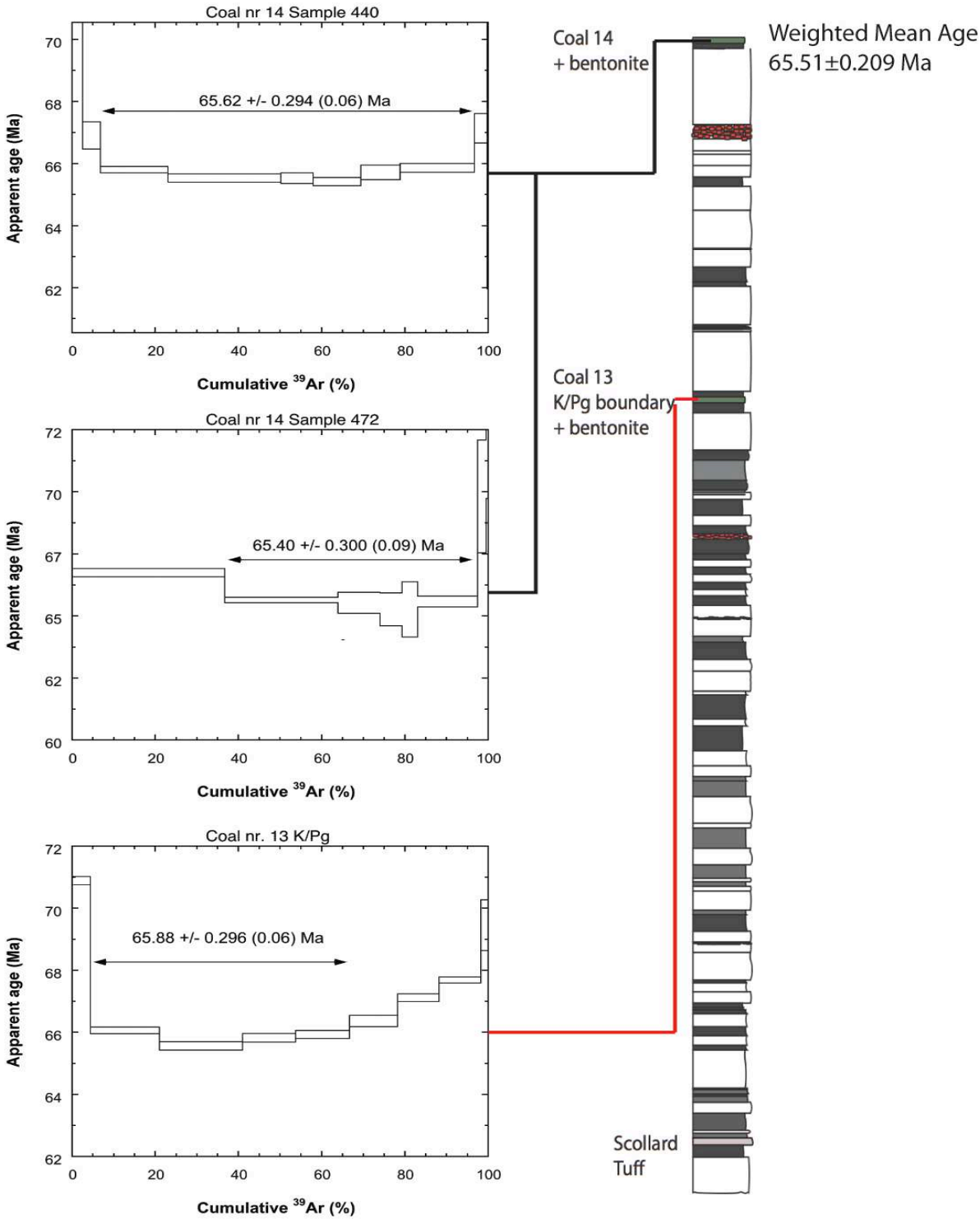

Fig.IV.7 ^{40}Ar/^{39}Ar step heated age spectrums for three samples acquired form Knudsen's farm section. All ages are given to 1σ error. Detailed analyses for each sample will be noted in the supplementary information

IV.4. Discussion

Although eccentricity modulates the amplitude of precession, the expression of eccentricity was not well developed in the field at the Knudsen's Family Farm sections, most probably because the section is too short and the possible interference of sandy horizons in the basic bundles, thus masking the cyclicity. A possibility is that the widespread coal layers may be related to eccentricity cycles, but this possibility is still to be tested. Parallel sections have been observed to preserve the same features (supplementary data). Therefore regional continuity along the Red Deer River can be assumed. Accordingly, the data from $b^*(D65)_{NORM}$ and the $Fe\#_{NORM}$ were filtered using the 1.8-2.1 m periodicities as registered in the time series and wavelet analysis, leading to the 13-14 precession cycles from the base of the section to the K/Pg boundary.

Compared with terrestrial marine successions and drill cores from the Atlantic and Pacific Oceans, cyclostratigraphic studies mainly have inferred that eccentricity minima can be observed as a poor expression of the marly part of the cycle, occurring at an interval of relatively thin carbonate-rich cycle at Zumaia (e.g. Dinarès-Turrell et al. 2003; Kuiper et al. 2008; Hilgen et al. 2010). Westerhold et al. (2008) have shown that marine successions and cores from the Atlantic and Pacific Oceans can be correlated even at precession scale level, making it possible to count 15-16 precession cycles from the base of the C29r to the K/Pg (Fig.IV.8). However, there is an apparent lack of full hierarchy of eccentricity cycles that mask the entire expression of the astronomical periods at Zumaia (e.g. Dinarès-Turrell et al, 2003). In several cyclostratigraphic studies the K/Pg boundary was tuned to eccentricity minima without any absolute age constraints but relying on derivative model ages from the cyclostratigraphic studies, target curves, and radio-isotope dating by $^{40}Ar/^{39}Ar$ (e.g. Dinarès-Turrell et al, 2003; Kuiper et al, 2008; Hilgen et al, 2010; Husson et al, 2011; Westerhold et al, 2012; Batenburg et al, 2012).

The identification of the 405-ka eccentricity minima (or maxima) linked to the hierarchy of the bundles is crucial for a chronostratigraphy that would allow for precise age estimations. At Zumaia, the K/Pg boundary lies at the base of a limestone-

dominated interval, which has been suggested to correspond to a 405-ka period o minimum eccentricity (e.g. Kuiper et al, 2008; Batenburg et al, 2012). In Zumaia, the 405-ka eccentricity minima coincides with the minimum value in the ~16 m band pass filter of the magnetic susceptibility, inversely correlating with the total reflectance (Batenburg et al, 2012). The intrinsic parameters thus correlate with the poorly expression of the marl horizons in the lithology at Zumaia. Consequently, the resulting tuning is made by placing the K/Pg boundary in the eccentricity minima as main phase relation (e.g. Dinarès-Turrell et al, 2003; Kuiper et al, 2008; Hilgen et al, 2010; Husson et al, 2011; Westerhold et al, 2012;). However, the U/Pb and $^{40}Ar/^{39}Ar$ ages can bring new insights in establishing the correct tuning of the K/Pg boundary, either in the eccentricity minima or maxima. If the age of the K/Pg is 65.746 Ma, then the phase relation has to change to eccentricity maxima by assuming that the astronomical solution for the 405 ka eccentricity cycle has been constant for the last 250 Ma.

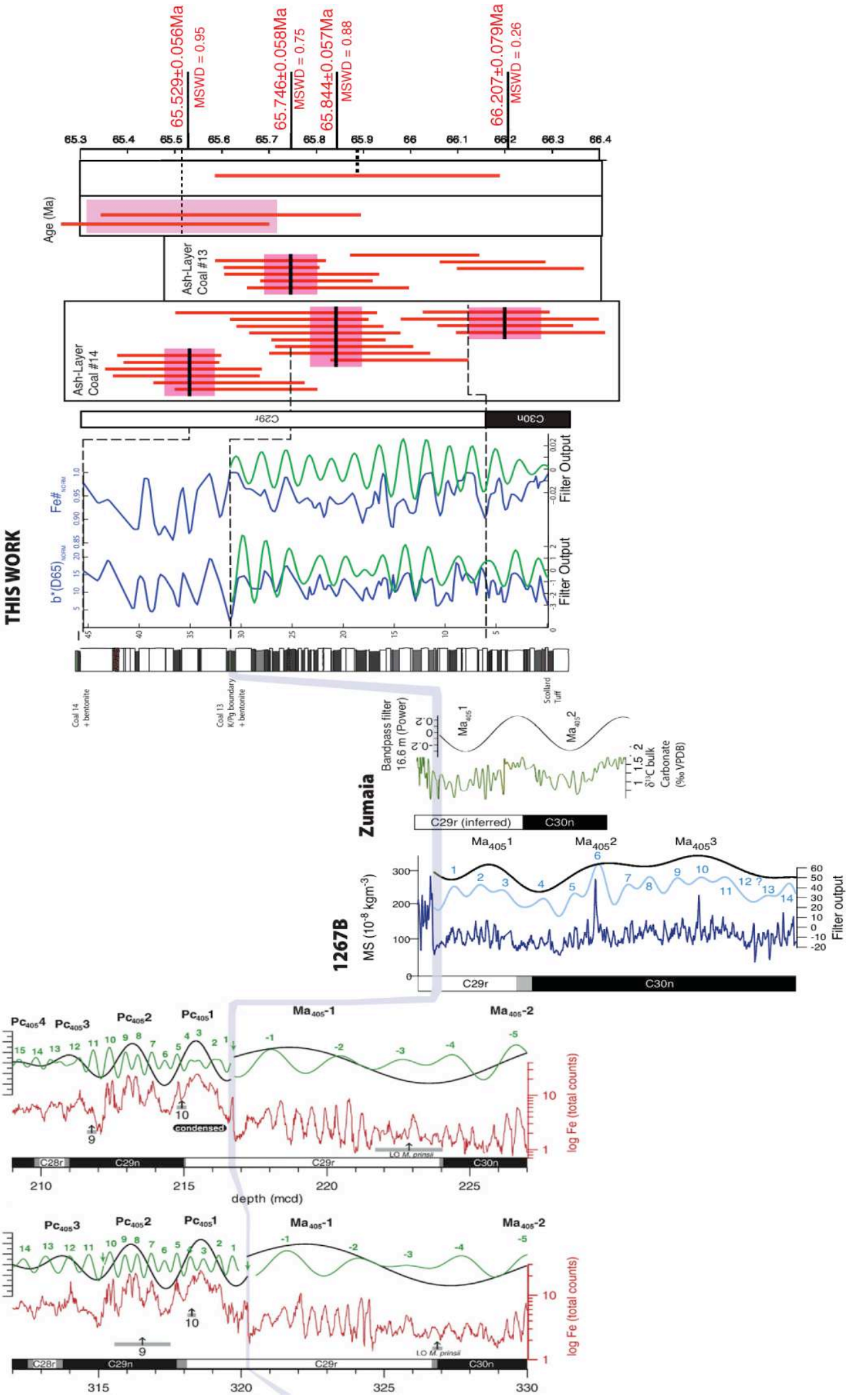
65.529±0.056Ma
MSWD = 0.95
65.746±0.058Ma
MSWD = 0.75
65.844±0.057Ma
MSWD = 0.88
66.207±0.079Ma
MSWD = 0.26
Age (Ma)
Ash-Layer Coal #13
Ash-Layer Coal #14
C29r
C30n
THIS WORK
Filter Output
Coal 14 + bentonite
Coal 13 K/Pg boundary + bentonite
Scollard Tuff
Zumaia
Bandpass filter 16.6 m (Power)
C29r (inferred)
C30n
1267B
MS (10-8 kgm-3)
C29r
C30n
1262
filter output
log Fe (total counts)
condensed
LO M. prinsii
C28r
C29n
C29r
C30n
depth (mcd)
1267

Fig.IV.8. (Previous Page) Comparison between Maastrichtian astrochronologies indicating the identified 405 ka eccentricity cycles from the K/Pg boundary and downwards in drill cores from the Atlantic Ocean and Zumaia (after Westerhold et al, 2008; Husson et al, 2011; Batenburg et al, 2012). Magnetostratigraphy linked to the intrinsic and extrinsic parameters. The K/Pg boundary is indicated at the different sections and directly linked to the development of the cyclostratigraphy in this study and the weighted mean $^{40}Ar/^{39}Ar$ and U/Pb dates.

Furthermore, the youngest zircon grains in each of the two ash layers above and below the K/Pg boundary (Fig.IV.6) are interpreted to be autocrysts that crystallised just prior to eruption. Older zircon grains in this volcanic ash are antecrysts that resided in the magma chamber and mixed with younger zircon grains just before eruption. These older grains show a wider age spread, and can be interpreted to record individual crystallisation pulses that lasted ~150 ka, and are probably related to new injections of magma into the magma chamber. Further generation of antecrystic zircon is suggested to have started as early as 65.879 ± 0.109 Ma (Supplementary Data).

U/Pb and $^{40}Ar/^{39}Ar$ ages are in concise agreement with each other at 2σ, large errors on the $^{40}Ar/^{39}Ar$ ages correspond to a lack of repeatable analysis , (thus lowering the weighted mean age error) and a conservative uncertainty assigned to the J-factor determination. $^{40}Ar/^{39}Ar$ age plateaus show a slight saddle effect which could suggest the presence of excess argon and possible different cation and anion vacancies whereby the ^{40}Ar is being held in two different lattice sites with constraining thermal degassing behavior. Due to these factors and the resolution of the ages needed to pin down cyclostratigraphy, the $^{40}Ar/^{39}Ar$ ages will only be used here as agreement to the ages proposed for U/Pb

The stratigraphic position of the boundary clay can thus be confined to the age between 65.746 ± 0.058 and 65.844 ± 0.057 Ma. The boundary cannot be younger than the youngest zircon age population at Coal nr. 13. Furthermore, if the bundles represent precession cycles, the boundary would be within the analytical uncertainty of the youngest population in Coal nr. 13. This work clearly contradicts the new age presented by Renne et al. (2013) for 14 tektites at Beloc, Haiti, and bentonites from Hell Creek, US, being both material directly deposited at the K/Pg boundary. The age for the boundary presented by Renne et al. (2013) is 66.043 ± 0.043 Ma, has been intrinsically calibrated with ^{40}K and ^{238}U decay constants. However, this age also

bears the uncertainty of the age monitor. When recalculating this age to the age of the astronomically tuned Fish Canyon tuff reported by Kuiper et al. (2008), the same age becomes ~0.3% younger, i.e. 65.836 ± 0.061 Ma. The situation becomes even more complicated when same age is recalculated to the age of the Fish Canyon tuff reported by Rivera et al. (2011). The age then becomes ~0.4% younger, i.e. 65.771 ± 0.060 Ma, which is in full agreement with our estimations. The U/Pb dates do not depend on such limitations from monitor ages and inherited uncertainties as the $^{40}Ar/^{39}Ar$ system does, but on the concordance of the data and the application of weighted mean statistics (Fig.IV.6).

The critical link between the Deccan volcanism and the K/Pg boundary has been thought to be resolved at Rajahmundry and Jhilmili due to palaeontologic, palaeomagnetic, geochemical and radio-isotopic age constraints (e.g. Keller 2008; 2012 and references therein). Deccan studies have suggested at least three major massive phases of volcanism, starting at 67.5 ± 1.0 Ma followed by the major phase at 64.9 ± 0.7 Ma and finishing at 62.2 ± 0.9 Ma. Gas release on timescales shorter than decades (e.g. Chenet et al, 2007; 2008) for the Deccan volcanism and its link to the severe mass extinction requires highly precise and accurate age estimates, which until now have not yet been generated. Until then the cause-and-effect relationship between volcanism and extinction cannot be resolved with confidence. Consequently the Deccan Trap volcanism will completely overlap with the K/Pg boundary with the low-resolution data currently available (Fig.IV.9).

IV.5. Conclusions

The location for the boundary in the Red Deer River area is related to the presence of shocked quartz (e.g. Grieve and Alexopoulos, 1988), an Ir- anomaly (e.g. Lerbekmo and St. Louis, 1986), and enrichment in microdiamonds, amino acids and heavy isotopes of extraterrestrial origin (e.g. ^{107}Ag, ^{236}U, ^{244}Pu; Carlisle, 1995). All these studies found the boundary near the base of Coal nr. 13, represented by the 1-2 cm thick boundary clay (e.g. Sweet et al, 1999). The altered volcanic ash-layer in Coal nr. 13 was found ~30 cm above the boundary clay (Therrien et al, 2007; this work). Therefore and assuming that the bundle containing the Coal nr. 13 represents a

precession cycle, the K/Pg boundary is within the analytical uncertainty in the youngest zircon population at 65.746 ± 0.058 Ma.

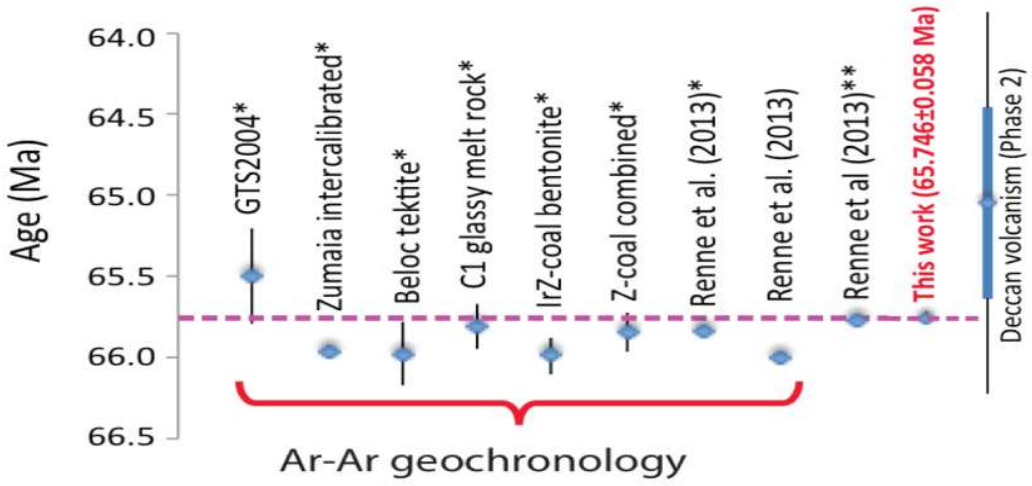

Fig.IV9. Summary of ages for the K/Pg boundary. * denotes the Ar-Ar dates have been recalculated using the astronomically calibrated Fish Canyon Tuff of Kuiper et al. (2008; 28.201 ± 0.046 Ma). ** denotes the $^{40}Ar/^{39}Ar$ dates have been recalculated using monitor age for the Fish Canyon Tuff of Rivera et al. (2011; 28.172 ± 0.028 Ma). The ^{40}Ar-^{39}Ar ages are taken form Obradovich (1993), Kuiper et al. (2008), Izett et al. (1991), Swisher et al. (1992) and Renne et al. (2013). Renne et al. (2013) age is calculated using 28.201 ± 0.060 Ma monitor age for the Fish Canyon Tuff. The Deccan Traps K-Ar age estimation of phase 2 has also been recalculated by Chenet et al, 2007 using the K-Ar Cassignol-Gillot technique suited for K poor Deccan Lavas on samples straddling the C29r/C29n reversal. Phase 2 of the Deccan Traps volcanism has been suggested to represent up to 80% of the total lava volume and directly associated to the end-Cretaceous mass extinction (e.g. Chenet et al, 2007). Recalculated ages are given with full error estimates in 2σ confidence level, although Chenet et al. (2007) only has been reported age estimates in 1σ level. The astronomical ages for the K/Pg boundary are mainly calculated by counting the number of precession or eccentricity cycles in marine successions and deep-sea cores (Dinarès-Turrell et al, 2003; Westerhold et al, 2008; 2012; Kuiper et al, 2008; Hilgen et al, 2010; Husson et al, 2011). The U-Pb age estimate here presented (65.746 ± 0.058 Ma) is a weighted mean of 5 zircon grains (2σ internal), taking into account uncertainties in tracer calibration. The dashed line marks the K/Pg boundary according to this work.

The cyclostratigraphy in the high-resolution proxy records from the land-based sedimentary succession at the Red Deer River section suggests that 11-12 precession-related cycles can be counted form the K/Pg boundary to the base of the C29r (i.e. ~231-252 ka, using the average precession period of 21 ka). However, there is space for improvements in the paleomagnetic constraints in the Horseshoe Canyon Formation.

On the basis of cyclostratigraphy and $^{40}Ar/^{39}Ar$ radio-isotopic dating, different studies (Fig.IV.9) have suggested different ages for the K/Pg boundary. Studies of sedimentary units in ODP hole 525A and 1267B (e.g. Husson et al, 2011) indicate that the K/Pg is very close to a ~400-kyr eccentricity minima giving a maximum and minimum age for the C29R between 65.89 ± 0.08 and 66.30 ± 0.08 Ma, assuming that the $^{40}Ar/^{39}Ar$ system and the cyclostratigraphy are intercalibrated. Our age estimates integrating the cyclostratigraphic framework, the magnetostratigraphy and the U/Pb dates give an age for the base of the C29r at 65.988 ± 0.031 Ma.

The age estimations presented in this work may have strong influence on the resulting interpretation of the amount of cycles form the K/Pg boundary to the base of the Eocene and to the C29r, and may help geoscientists in building a precise and accurate timescale around of most decisive events in Earth's history. A similar resolution as in this work is thus needed to say anything else about the synchronicity between the K/Pg boundary and the large volcanic activity at the Deccan Traps.

Acknowledgments.
Research team to the geology of the Western Canada Sedimentary Basin, A. Sweet, J. Lerbekmo (deceased), D. Eberth, and all the GTSnext (the next generation Geological Time Scale) staff and students are thanked for discussions on the field relations.

V. The Campanian / Maastrichtian Boundary

U-Pb, $^{40}Ar/^{39}Ar$ geochronology and cyclostratigraphy around the Campanian-Maastrichtian boundary in the Western Canada Sedimentary Basin: High precision ages in land-based sedimentary successions.

Jonathan R. Gaylor	(University Paris Sud XI, France)
Benjamin D. Heredia	(University of Bern, Switzerland)
Frits Hilgen	(University of Utrecht, The Netherlands)
Xavier Quidelleur	(University Paris Sud XI, France)
Klaus Mezger	(University of Bern, Switzerland)
Jan Wijbrans	(Vrije University Amsterdam, The Netherlands)
Silja Huesing	(University of Utrecht, The Netherlands)
Willem Langenberg	(University of Alberta, Canada)
Klaudia Kuiper	(Vrije University Amsterdam, The Netherlands)

V.1. Introduction

The late Cretaceous experienced a transition between a greenhouse-dominated environment to a cooler Cenozoic climate, accompanied by several perturbations in the carbon cycle (e.g. Sheldon et al, 2010). Reported changes in global foraminifera $\delta^{18}O$ and $\delta^{13}C$ records indicate deep water-cooling and reduced rates of organic carbon burial (e.g. Barrera et al, 1997; Li and Keller, 1998; Barrera and Savin, 1999). These periods of climatic variations led to first occurrences of localised late Cretaceous mass extinctions (e.g. Frank and Arthur, 1999; Keller, 2001; Bralower et al, 2002), and high amplitude sea level fall, which has been recognised in both hemispheres, arguing for very variable global environmental fluctuations (e.g. Kominz et al, 2004; Crampton et al, 2006, Simmons et al, 2007). However, the understanding of the causality and mechanisms for this important period of time is yet limited. Additionally, the spatial and temporal interaction between tectonics, climate and oceanic processes over large areas remains poorly constrained. The limitations are mostly due to the paucity of highly resolved absolute radio-isotopic age constraints for the upper Cretaceous.

The Campanian-Maastrichtian boundary is defined by the arithmetic mean of the thickness of sediments encompassing eight of nine-biostratigraphic datum levels at Tercis, near Dax in the département Landes, France (Odin and Lamaurelle, 2001,

Odin, 2001). The mean falls close to the initial appearance of the ammonite *Pachydiscus neubergicus*, which also marks the boundary effectively at the abandoned quarry section at Tercis (Odin and Lamaurelle, 2001). However correlation of the Camapanian-Maastrichtian boundary with other successions around the globe has proven to be a difficult task, partly due to insufficient preservation and inaccurate identification of microfossils, and partly due to endemism and diachroneity in marine faunas.

In the Western Canada Sedimentary Basin, the palynomorphic Campanian-Maastrichtian boundary is preserved in the sedimentary succession of the Horseshoe Canyon Formation and has been placed ~8 m below Coal nr. 10 (e.g. Lerbekmo and Braman, 2002, Hamblin, 2004; Eberth, 2010; Fig.V.1), based on magnetisratigraphic correlations with the Bottaccione section, Italy (e.g. Alvarez et al, 1977; Premili-Silva and Sliter, 1994), near the C31r-C32n polarity boundary. The boundary position at this level is supported by the placement of the Campanian-Maastrichtian boundary at the base of the Baculites baculus ammonite zone (e.g. Jeletzky, 1968; Gill et al, 1972; Hancock and Kauffman, 1989; Li et al, 1999).

In this work, highly precise and accurate U-Pb zircon age determinations are presented for two altered volcanic ashes alongside $^{40}Ar/^{39}Ar$ results, one at the bottom and one at the top of the Morrin Bridge Section along the Red Deer River (which contains the Campanian-Maastrichtian boundary). This section is also placed into a possible cyclostratigraphic framework; the aim is to contribute to the global correlation of the boundary and to evaluate to which degree the sedimentary successions in the Western Canada Sedimentary Basin records change in the astronomical parameters. This study will thus contribute to a reduction of the uncertainties generated by palynological definitions of the boundary in the Western Canada Sedimentary Basin.

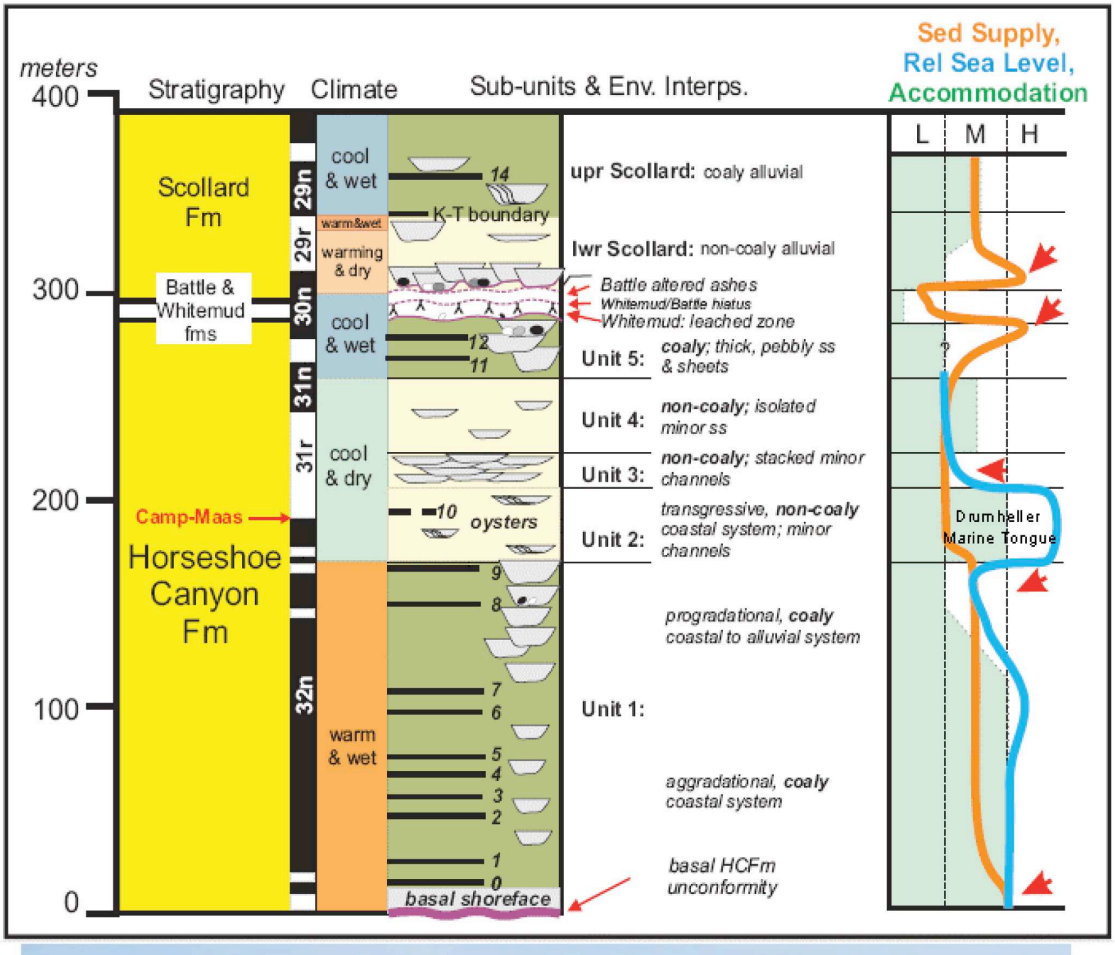

Fig.V.1. Location map, lithostratigraphic divisions showing the inferred climatic and palaeo- environmental conditions, and panoramic view of the sediments exposed along the Red Deer River containing the Campanian-Maastrichtian Boundary. The boundary is located ~8 meters below Coal nr.10. Modified from Eberth (2010).

V.2. Geology

The Western Canada Sedimentary Basin (WCSB) has been suggested to be mainly the result of the evolution of the Canadian Cordillera from the Jurassic to the Palaeocene (e.g. Porter et al, 1982). It is an asymmetrical sedimentary basin that developed between the deforming mountain belt of the Canadian Rocky Mountains and the adjacent craton, where large volumes of orogene derived sediments accumulated (e.g. Allen et al, 1986). The change from a mainly orthogonal to an oblique northward convergence regime in the mid- Cretaceous led to overthrusting of supracrustal rocks, resulting in rapid deposition of generally regressive wedges of marine and non-marine synorogenic molasse-like sediments from the Campanian to the Palaeocene (e.g. Jerzykiewicz et al, 1985). The Horseshoe Canyon Formation (HSCFm; Irish, 1970) belongs to the uppermost part of the WCSB, consists of interbedded sand, silt and organic rich layers and is exposed for more than 200 km along the Red Deer River (Fig.V.1). The depositional environment of the more than 550 m thick HSCFm varies from marginal marine to fluvial and lacustrine. The lower half of the HSCFm, mainly in the Campanian, was predominantly a paralic setting that lead to a widespread development of coal seams (e.g. Shepheard and Hills, 1990; Rahmani et al, 1988).

In western Canada, Jeletzky (1968) placed the Campanian-Maastrichtian Boundary at the base of the *Scaphites (Hoploscapites) constrictus – Inoceramus fibrosus* zone, which is equivalent to the base of the *Baculites baculus* zone in western US and with the *Belemnella lanceolata* zone in northern Europe at the base of the Maastrichtian (Jeletzky, 1968; Odin, 1996; Lewy and Odin, 2001). Lerbekmo and Coultier (1985) confidently reported the magnetostratigraphy of the HSCFm by taking samples along the Red Deer River and correlating it with the foraminifera-based polarity record from Gubbio, Italy (e.g. Alvarez et al, 1977). Lerbekmo and Coultier (1985) reported that the HSCFm strata include polarity chrons 33n to 30r, and the Campanian-Maastrichtian boundary.

This early work placed the Campanian-Maastrichtian boundary at about the level of Coal nr. 5. However, there was no regional isochronousity mainly between the

Bearpaw Formation (a marine shale with shore-line related facies in the magnetic zone C33n; e.g. Gibson, 1977) and the HSCFm in the Red Deer River and Cypress Hills areas. Later on and through a more detailed magnetostratigraphy and biostratigraphy, Lerbekmo and Braman (2002) placed the boundary near the level of Coal nr. 10, near the C31r and C32n polarity boundary (Fig.V.2). This new definition in western Canada basically agrees with the magnetostratigraphy of the Bottaccione section near Gubio, Italy, (Alvarez et al, 1977) which provides the nearest reliable magnetostratigraphy to that at Tercis, France.

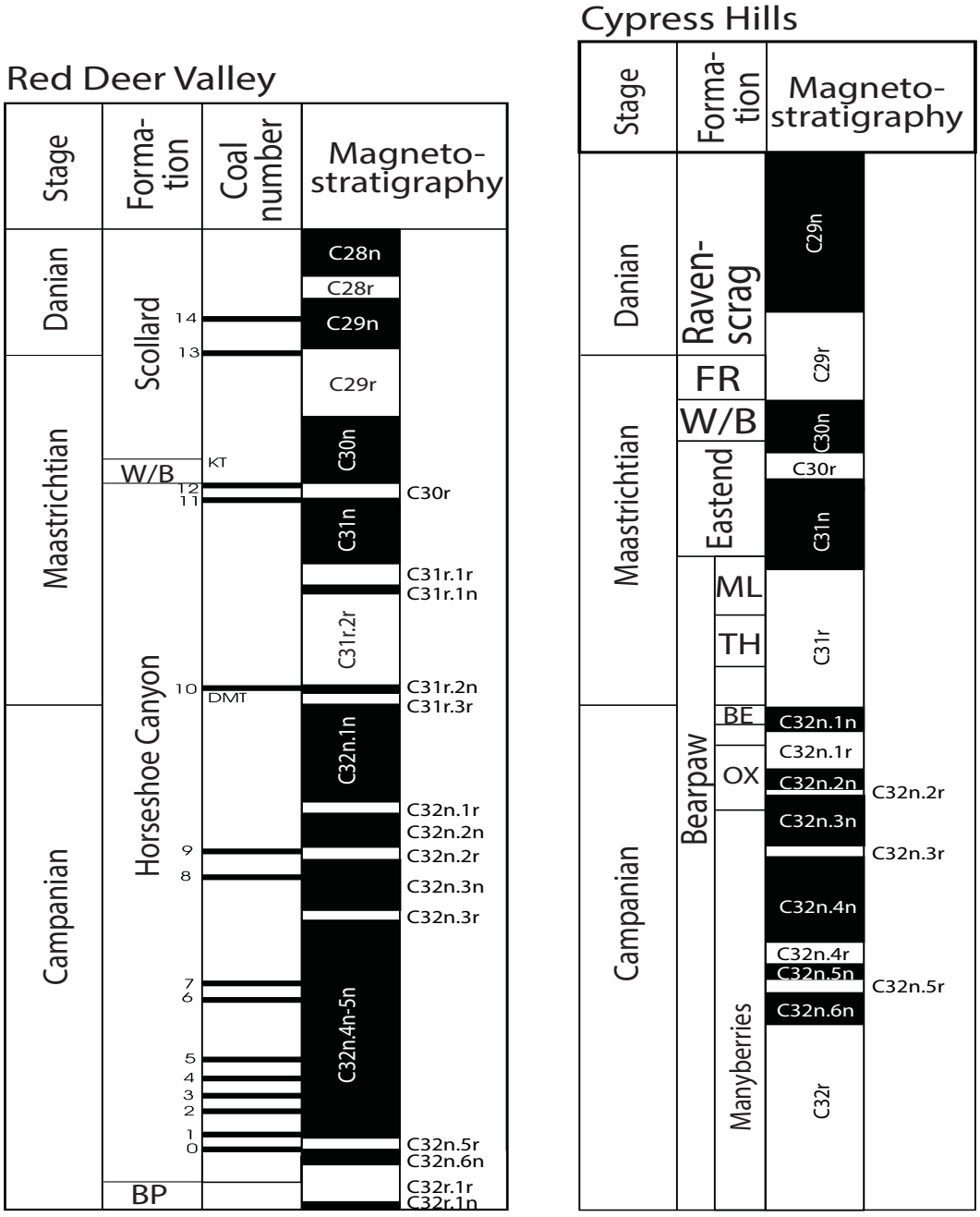

Fig.V.2. (Previous Page) Summary correlation of composite sections at the Red Deer River Valley and the Cypress Hills (modified from Lerbekmo and Braman, 2002). W/B, Whitemud/Battle Formations; BP, Bearpaw; KT, Kneehils Tuff; DMT, Drumheller Marine Toungue; FR, Frenchman Formation; ML, Medicine Lodge Member; TH, Thelma Member; BE, Berlanger Member; OX, Oxarart Member. The Cretaceous/Palaeogene boundary is at the bottom of Coal nr. 13 (e.g. Therrier et al, 2007) and the Campanian-Maastrichtian Boundary have been placed at the base of the C32n.1n (e.g. Lerbekmo and Braman, 2002).

V.3. Samples and Methods

Samples were collected from the ~13 m thick section at the Morrin Bridge that includes the Campanian-Maastrichtian boundary, trying to cover all the different lithologies (Fig.V.1&3). The colour proxy was taken using a spectrophotometer, whilst major and trace elements were determined with a Thermo XRF instrument. All the analyses were performed at the Fort Hoofddijk palaeomagnetic laboratory at the University of Utrecht (Supplementary Data, Table SIV-T1).

In general, sand layers are pale grey, well sorted and vary from very fine (50μm) to coarse grained (+150μm). Field observations and literature data (e.g. Hamblin, 2004; Eberth, 2010) show that some sands are fining upwards mainly due to channel filling. These fillings are mainly characterised by cross-bedding, ripple cross-lamination, low angle lamination and inclined stratification. These characteristics in the sand layers helped in avoiding channels during logging and sampling. The silt is generally green to grey, with intercalated sand mud deposits, typically with apparently randomly distributed thin sandy horizons (Hamlin, 2004; Eberth, 2010; this work). The organic rich layers are brownish, silt-rich and laminated, whilst coals are mainly black and some bituminous. Iron-concretions have been observed to be widespread and are concentrated in discrete horizons within the entire Red Deer River section. Iron concretions are mainly coarse-grained sands, reddish to greyish, with irregular bases and tops. Samples from well-preserved altered volcanic ashes above the coal layer at the top of the section (~15 cm thick) and one at the bottom (~40 cm thick) were taken for mineral separation, targeting the separation of sanidine and zircon grains.

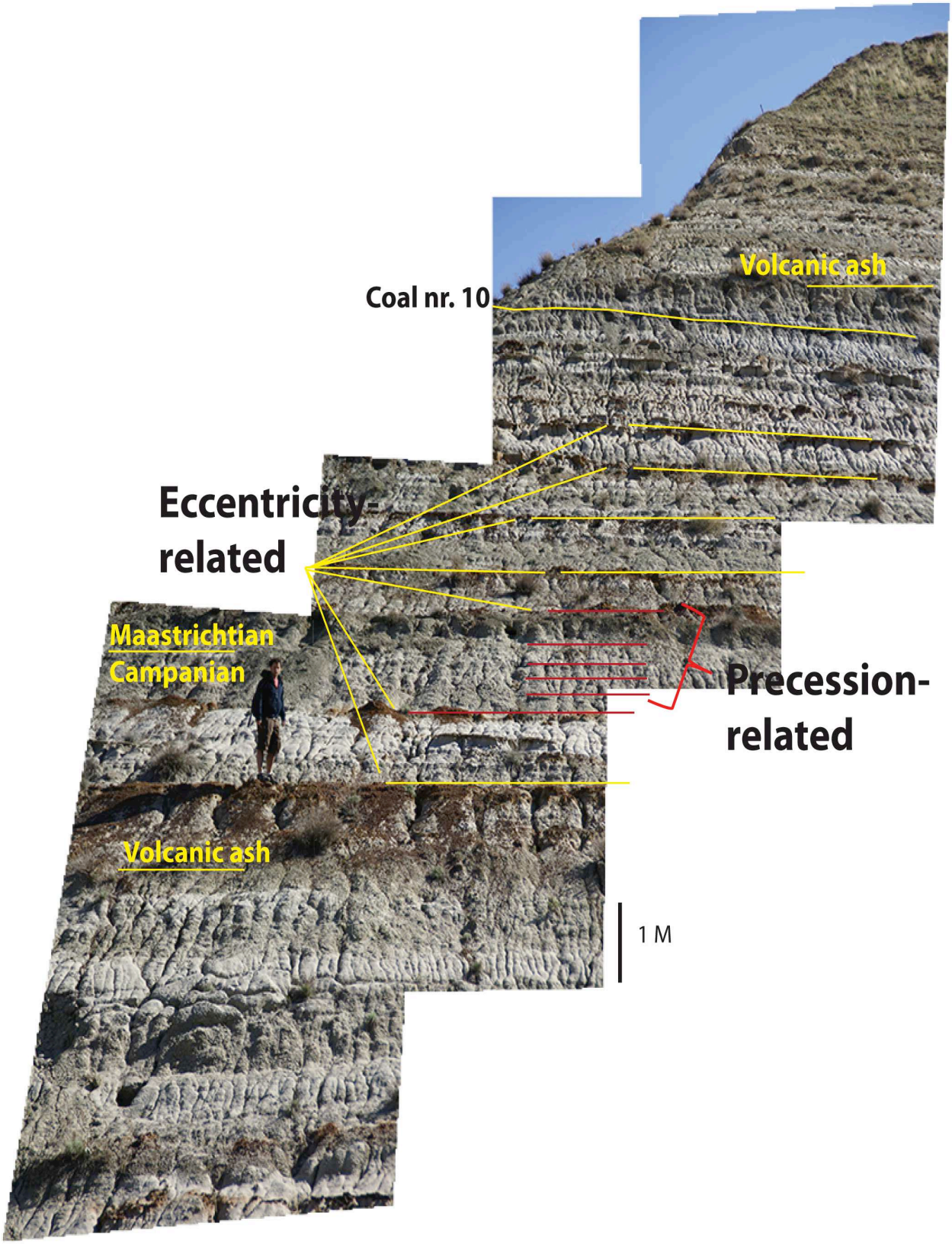

Fig.V.3 Overview of the Morrin Bridge Section containing the Campanian- Maastrichtian Boundary. The section is dominated by sand-rich layers. Fe-concretions and palaeosoils are regularly alternating with sands and silts that are deposited almost horizontally throughout the entire area. Marked is the palynological Campanian-Maastrichtian Boundary and at the top the Coal nr. 10. One altered volcanic ash layer containing zircon occurs at the base and the other at the top of the section.

V.3.1. Cyclostratigraphy

Chemical weathering indices (often referred to as indices of alteration) are commonly used in characterising modern and ancient weathering profiles (e.g. Taylor and McLennan, 1985; Price and Velbel, 2003), and in demonstrating the influence of climate on bedrock and alternations associated with neotectonics (e.g. Neall, 1977; Sharma and Rajamani, 2000). For "pinning-down" the climatic information from the alternations at the Morrin Bridge section, the Chemical Index of Alteration (CIA; Nesbitt and Young, 1982) was used, which measures the extent of alteration of feldspars to clays.

As shown in Fig.V.3, layers show no stratigraphic regularity in their thicknesses. It is therefore difficult to determine the thickness and associated cyclothem of a basic bundle. However, the approach used in this work was to perform a deconvolution of the stratigraphy into depth-frequency space by applying wavelet analysis (Fig.V.4). This procedure is ideal for analysing non-stationary time series where localised variations of power are expected (e.g. Torrence and Compo, 1997). For the stratigraphic column at Morrin Bridge, the wavelet transform was used to analyse the stratigraphic series that may contain non-stationary power at different frequencies. The Morlet wavelet of the CIA (Fig.V.4) shows a reasonably large number of oscillations, which ensures good frequency resolution. This is coincident with the troughs in the CIA plotted against the stratigraphy of the section (Fig.V.4b). The wavelet analysis thus suggests periodicities at ~1.67 m, which is coincident with the spacing in the deposition of Fe-concretions, palaeosoils and Coal nr. 10, at the uppermost part of the section. Filtering the CIA by using the ~1.67 m periodicities, a total of 8 eccentricity-related cycles were found (Fig.V.4c). It is suggested that these cycles are related to eccentricity because at one of the intervals, a very well preserved expression of the precession cycles was observed. According to Heredia et al. (in prep.) for a section containing the Cretaceous-Palaeogene (K/Pg) boundary, the expression of the precession in the area is composed of sand-silt-organic-rich material. This suggestion is based on an integrated approach between the development of a cyclostratigraphic framework and $^{40}Ar/^{39}Ar$, U-Pb zircon geochronology (Heredia et al. in prep).

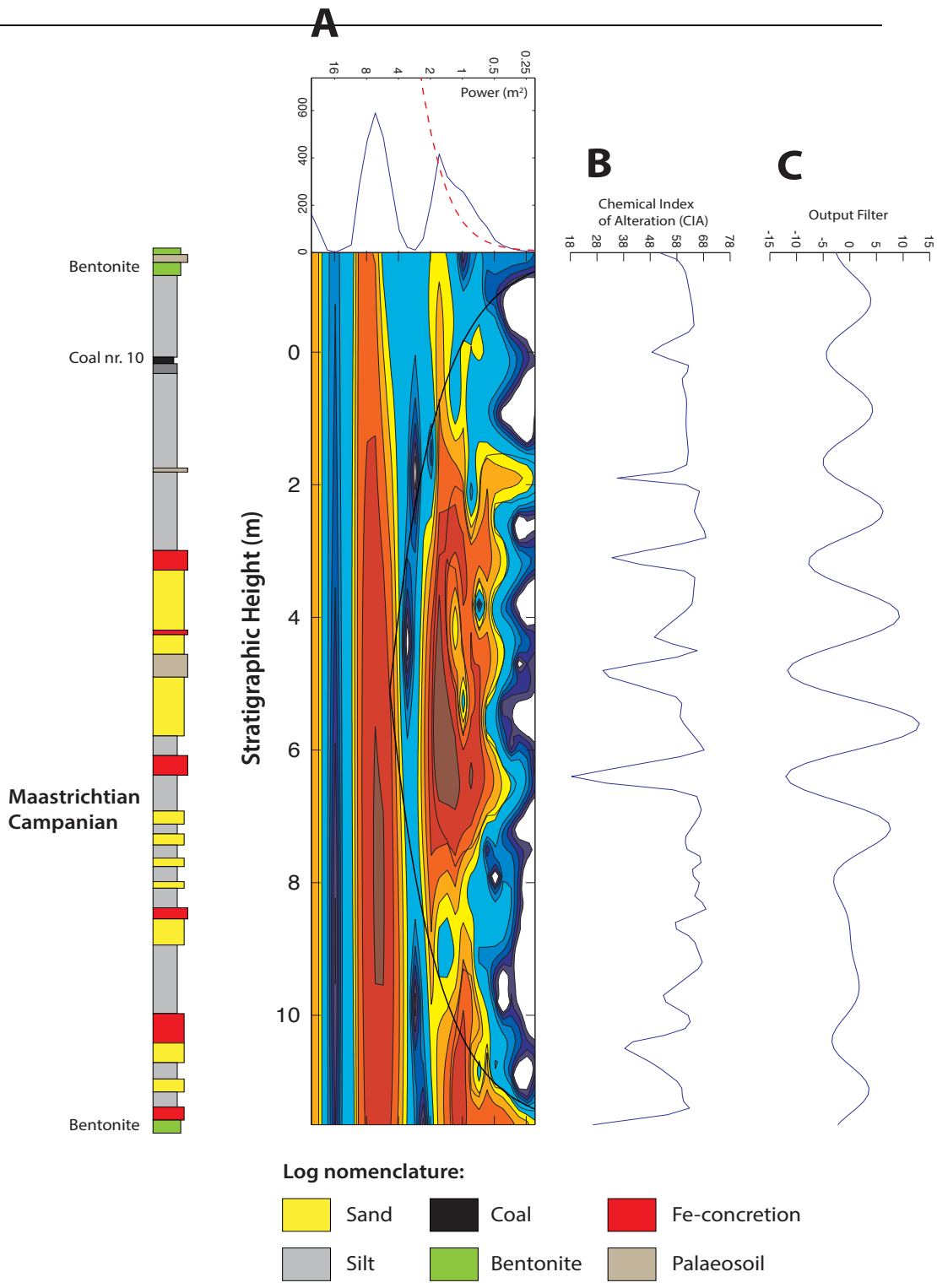

Fig.V.4. Detailed lithological log of the Morrin Bridge section showing the position of the altered volcanic ash layers at the top and bottom of the section. **A**. Wavelet analysis of the Chemical Index of Alteration (CIA=100*Al/(Al+Ca+Na+K)). For the wavelet analysis, a non- orthogonal wavelet function was used, aiming to determine continuous variations in the expected wavelet amplitude. The analysis clearly shows a periodicity of ~1.67 m. The dashed line in the power spectrum marks the 95% confidence level. **B.** Raw variations in the CIA.. The troughs are well correlating with the Fe-concretions, the palaeosoils and Coal nr. 10. **C.** Filter output modulated using the periodicities observed in the wavelet analysis. At least 8 eccentricity cycles are observed.

V.3.2. U-Pb geochronology

In order to "tie-in" the cyclostratigraphic framework at the Morrin Bridge section, high-precision U-Pb zircon analyses were performed on single grains, grain fragments and tips. All sample preparation and isotope analyses were performed at the Institute of Geological Sciences at University of Bern, Switzerland. Zircons were separated by standard procedures from the two volcanic ash layers. Grains and tips were annealed and dissolved in two steps, following the commonly used chemical abrasion method (Mattinson, 2005). U/Pb isotope ratios were determined by ID-TIMS using a Thermo Fisher Triton+, equipped with a discrete-dynode MasCom electronic multiplier in ion-counting mode. Total procedural blanks for Pb ranged from 2.3 ± 0.8 to 0.50 ± 0.4 ‰. Mass fractionation factors in the electronic multiplier were determined by using NBS982 for Pb and NBS-U500 for U. The tracer is enriched in ^{205}Pb and ^{235}U isotopes, and was calibrated using a certified gravimetrically mixed Pb-U solution (NBS982-IRMM056). Accuracy was performed by repeated analysis of the EARTHTIME 100, 500 and 2000 Ma synthetic solutions (Condon, pers. comm.). All the U/Pb dates are here reported at the 2σ confidence level. All the age estimates are shown to plot on or near the Concordia line (Fig.V.5). U/Pb isotope data and dates are given in the supplementary data file (Table SIV-T2). Inherited common-Pb was corrected by using the two-stage model for Pb evolution (Stacey and Kramers, 1975). Detailed chemical and lithological data, and U/Pb isotopic data are given in the supplementary data file.

Fig.V.5. Concordia diagrams for the zircon grains analysed from the volcanic ashes at the top and bottom of the section.

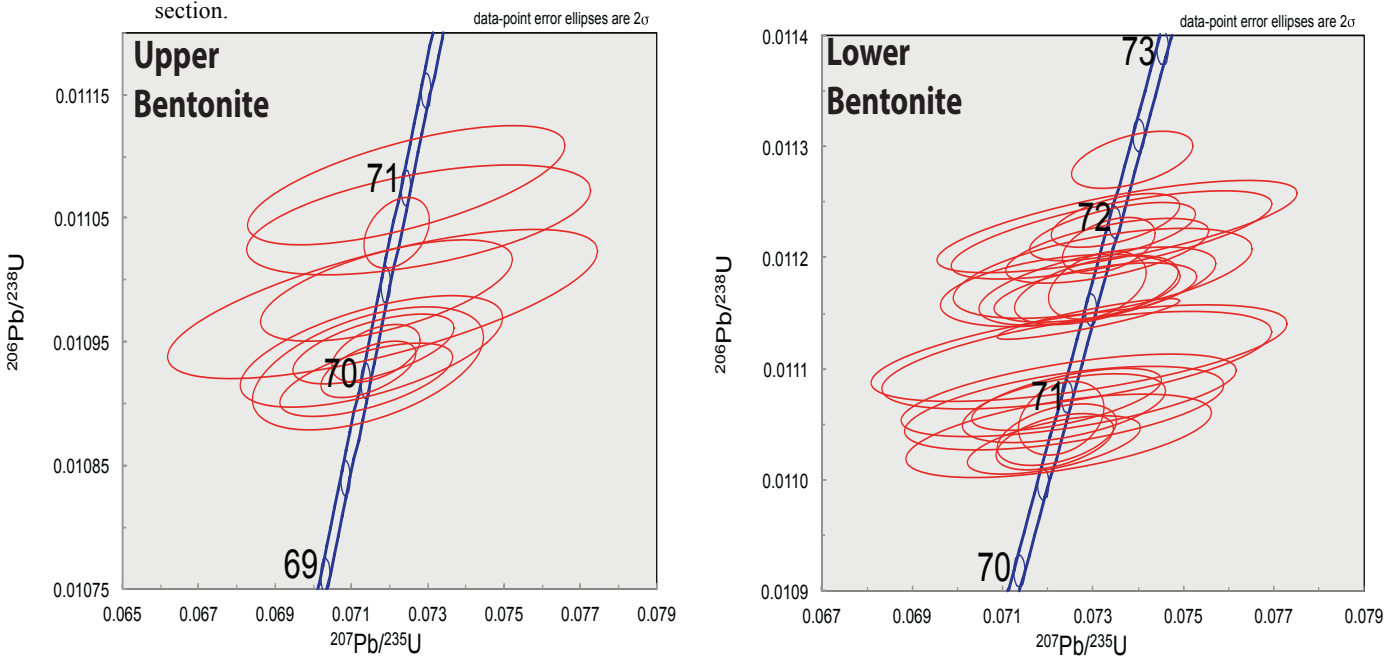

Ten individual grains (including tips and fragments) were analysed for the volcanic ash at the top of the section (sample MB-1.5), ~1 m above Coal nr.10. The three youngest grains yielded discordant ages and have high amounts of common-Pb and therefore were not included in the later statistical analysis. Four analyses from this sample yielded a weighted mean of 70.099 ± 0.065 Ma, with a mean square of weighted deviates (MSWD, or reduced Chi-square) of 1.06, suggesting that these zircons crystallised rapidly and within the uncertainty of the weighted mean (Fig.V.6). Three other grains (MB-1.5) yield a weighted mean of 70.83 ± 0.29 (MSWD=1.4), suggesting that these zircons resided in the magma chamber and grew over a longer time period (i.e. antecrystic zircons). Because of its better preservation, twenty-two zircons were analysed from the altered volcanic ash at the bottom of the section (sample MB32). Eight crystals yield a weighted mean of 70.902 ± 0.060 (MSWD=1.08), which it is here taken as the age of eruption (Fig.V.6). Furthermore two other population of ages were observed, one yielding a weighted mean age of 71.567 ± 0.089 and the other yielding a weighted mean age of 71.928 ± 0.060, suggesting that possible recharge of magma was occurring at sub-million year level.

Fig. V.6. ID-TIMS 206Pb/238U dates from the altered volcanic ash layers found at the top and bottom of the section. Youngest single grains and grain fragments $^{206}Pb/^{238}U$ zircon dates are also shown with their respective weighted means. Data were Th-corrected assuming a constant magma Th/U=3.0. Uncertainties in single analysis and weighted means are presented as 2σ intervals or 95% confidence levels. All data was plotted using the IsoPlot (Ludwig, 1991).

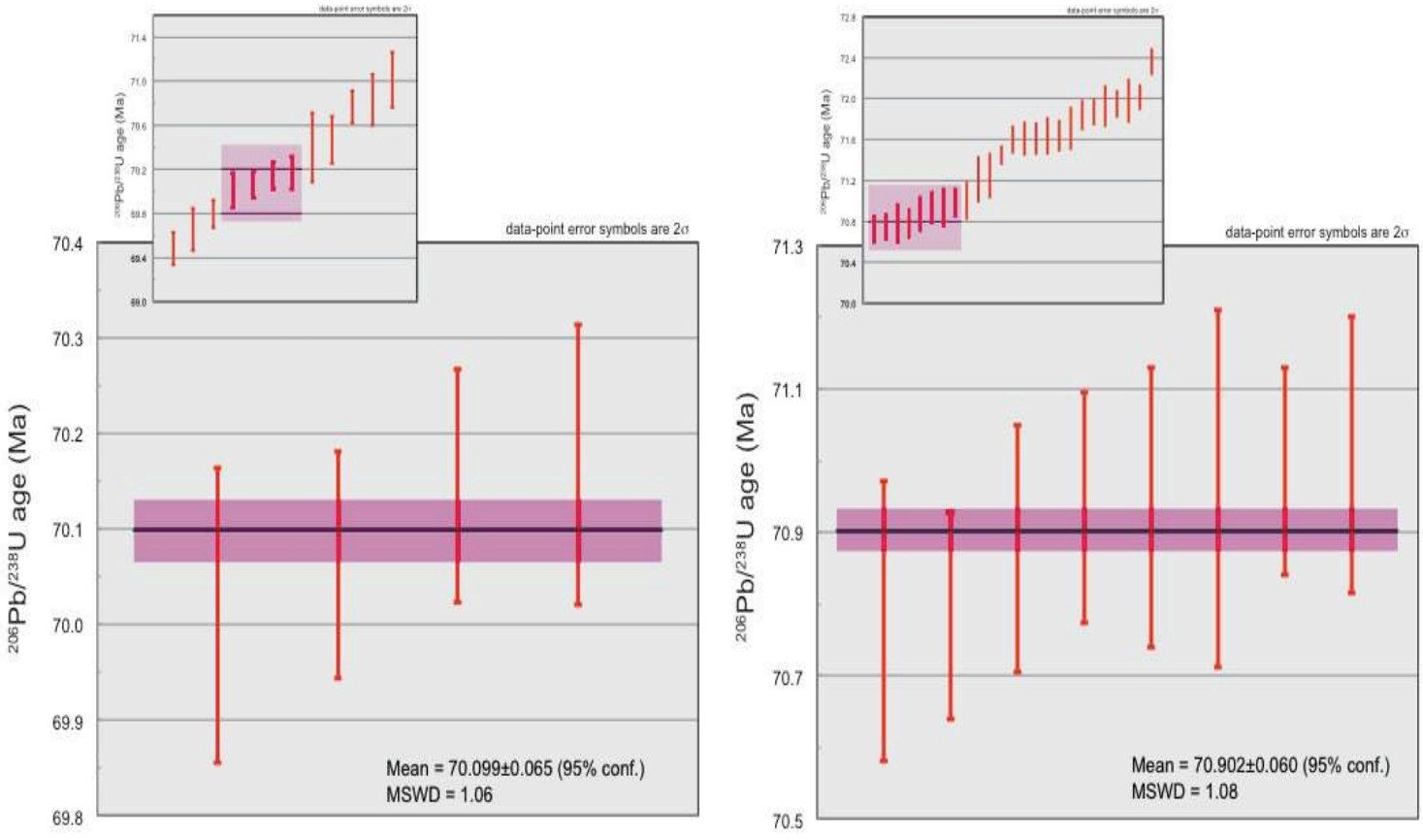

V.3.3 $^{40}Ar/^{39}Ar$ Dating

Similar to the U-Pb dating method, we utilised the same two ash layers within the section (Mb-1.5 & MB32). Samples were cleaned, sieved while mineral isolation was performed by heavy liquid separation (Bromoform). The samples were stained and picked using a sodium colbaltinitrite solution to pick out sanidine crystals <7%wt K (Hynek et al, 2011). Additionally, the sanidine minerals were cleaned using a 3 step acidic technique of HNO_{3conc}, followed by HF_{conc} then leached once more by HNO^{3}_{conc}. The first set of samples were packaged for both single crystal and step heating analysis while the later set was just packaged for step heating.

Both sets of samples followed similar irradiation patterns and were irradiated in the CLICIT University of Oregon TRIGA, The first set for 40 hours while the second set that included the replicable samples for 60 hours, halfway through both irradiations the quartz tubes were turned 180^{o} to reduce the neutron flux change across the z-axis. J-factor determination was determined using 20mg aliquots of Fish Canyon Tuff sanidine (FCT), Taylor Creek Rhyolite sanidine (TCR) on the first irradiation and HD-B1 biotite, FCT on the latter.

J-values were calculated using a weighted mean 3rd polynomial curve, flux monitors included all datasets whereby $^{40}Ar^{*}$ is higher than 95% radiogenic, with an uncertainty on the J value placed at 0.44% (1σ) for University Paris Sud (UPS) as calculated in the course of this study measurements of standards as unknowns. The Vrije University (VU) uses an arbitrarily value of between 0.2-0.3% (1σ). In total ~0.2g of each sample was packaged into compact copper pellets and placed into 1cm quartz tubes, tightly packed between two flux monitor samples for irradiation

Single Crystal analysis were attempted at the VU $^{40}Ar/^{39}Ar$ Laboratory, whereby the samples are fused with a 20W continuous Argon ion laser. The sample is then transported onto SAES getters for 300 seconds followed by argon isotope measurements on a Map 215-50 mass spectrometer. Measurements are performed on 10-12 scans in peak jumping in half mass intervals. System blanks are measured every 3-4 steps while the total system blank measured 1-10 x 10^{-17} moles of $^{40}Ar^{*}$.

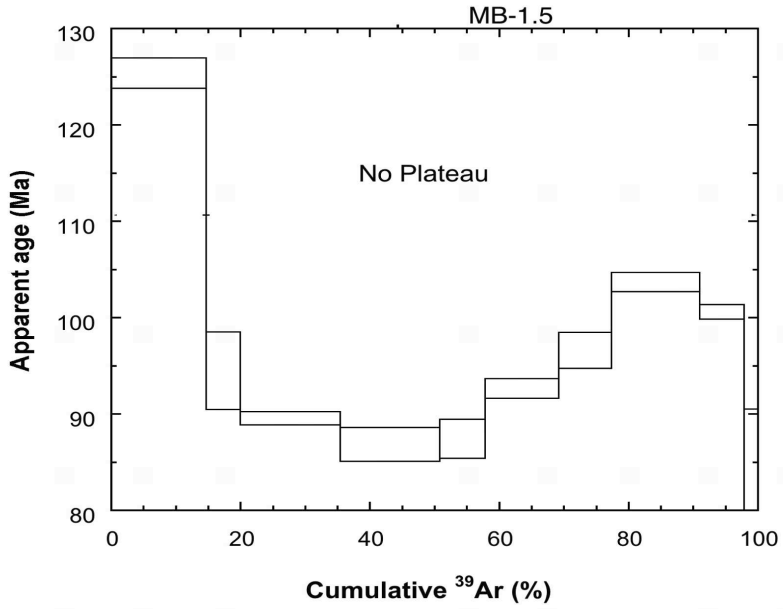

Fig.V.7. Typical $^{40}Ar/^{39}Ar$ age spectra exhibiting the charecterisitic saddle shape. Note that ages reach over 100 Ma.

Five replicates from each sample were analysed by total fusion single crystal, but did not give apparent reliable age. Results give low $^{40}Ar^*$ (50-60%), Ca/K ratios >1 and scattered ages above +100 Ma, thus not permissible for the scope of this study.

Total fusion step heating was carried out in UPS completed on the $^{40}Ar/^{39}Ar$ multi-collector instrument described in Coulié et al, (2004). Flux monitors and unknowns were measured using total fusion and step heating technique performed with a Nd-YAG infra-red laser at 0.8A and a high frequency furnace repectively. After heating the gas, it is first purified by 700°C Ti foam following by 15 minutes on an AP10Gp SAES getter heated to 400°C. The sample was then transferred to an additional coal trap undergoing a second purification under a another getter, before measured in the mass spectrometer. Unknowns were typically measured on average ~13 incremental steps set with the HF furnace.

Mass discrimination was determined from a air pipette system, while blanks were determined on the same conditions as samples. Average $^{40}Ar/^{36}Ar$ atmospheric ratios of 304±1 were measured over the course of this study. K interfering reactions were calculating using the values of Renne et al (1998). Age uncertainties and calculations follow McDougall and Harrison (1999), with ^{40}K decay constants and isotopic ratios of Steiger and Jaeger (1977). J Values were determined using the FCT and TCR ages 28.201 ± 0.046 Ma and 28.53 ± 0.02 Ma respectively (Kuiper et al, 2008) .

Total fusion ages compiled at Paris Sud show were duplicate and exhibit strongly disturbed ages, (Fig.V.7) with saddle shape spectra. Higher ages on the low and high temperature steps could suggest the presence of excess argon whereby the ^{40}Ar is being held in two different lattice sites with contrasting thermal degassing behavior. Alternatively such patterns coul be induced by a collective mix of various events, however feldspar crystals from this section appear to be euhedral thus not transported or reworked. Due to no reliable age constraints from either VU or UPS laboratory the $^{40}Ar/^{39}Ar$ results will not be considered further.

V.3.4 Magnetostratigraphy

In order to check the position of the magnetic reversals with the studied section and replace them in the framework defined by Lerbekmo and Braman, (2002) both hand orientated and 2.5 (cm) cored samples were extracted and analysed in two different attempts at Fort Hoofddijk, Netherlands.

Oriented hand-samples were collected and thermally demagnetised in a magnetically shielded furnace using small temperature increments from 20 to 360°C. Some samples were continued heated up to 550°C. The natural remnant magnetisation was measure on a 2G Entreprise horizontal cryogenic magnetometer. Due to their moderately indurated nature some samples were extracting using a special tool developed by Lerbekmo (1999), these samples were measured using both alternating field, and thermal demagnitisation, eventually combing both methods.

Results show poor signals and no reliable directions throughout all experiments, thermal demagnetisation proved problematic with temperature over 225^{o}C, thus making identification from strong field thermomagnetic results difficult to deduce. A Curie-balance experiment was attempted on five various samples (one of them shown in Fig.V.8) and show evidence of chemical changes of ferromagnetic minerals between 300-350^{o}C and 400-450^{o}C. Additionally AF demagnetization showed an anomalous overprint probably induced during sampling that prevented the use of magnetostratigraphy here.

V.4 Discussion

V.4.1. Cyclostratigraphy U-Pb zircon and $^{40}Ar/^{39}Ar$ geochronology

On a regional scale, tectonics, climate and sea-level changes are among the most important controlling factors during the deposition and distribution of coal and organic rich bearing layers in the Western Canada Sedimentary Basin (e.g. Dawson et al, 1994). Furthermore, the deposition of coal layers in North America generally has been interpreted as swamp and lacustrine deposits, accumulating next to river channels on an alluvial or deltaic floodplain, i.e. related to autocyclic processes in dynamic fluvial environments (e.g. Beerbower et al, 1964). According to Beerbower (1964), autocycles are produced by processes within sedimentary systems and can be characterised from local millimetre-scale ripple migration to changes in regional delta switching. Autocyclic processes may occur in aperiodic short time scales, randomly distributed in time and space, such as avulsion and meandering, and fluvial point-bar migration or lateral migration of such beach-barrier bars (Cecil, 2003 and references therein).

In contrast, allocycles result from processes occurring outside the sedimentary basin, possibly including tectonic activity, climate change, and eustatic sea-level changes (Beerbower, 1964). Tectonic subsidence and uplift due to changes in plate tectonic converging regimes and/or changes in spreading rates may have global implications. These processes together with changes in climate causing changes in fluvial sediment discharge are considered as allocycles (Beerbower, 1964). However, it is still obscure what the link between the secular changes in Earth's astronomical parameters and allocycles is. An integrated approach between sedimentary geochemistry, cyclostratigraphy and geochronology can help answering the question of whether or not dynamic land-based sedimentary deposits may record changes in Earth's orbital parameters (either precession, obliquity and/or eccentricity).

Some of the best-preserved exposures of oceanic- and climate-related events in epeiric-seas are those observed in the Western Interior Basin in the US and in the Western Canada Sedimentary Basin. In both areas, climate and tectonics have been

observed to control the formation of fine-grained, mixed siliciclastic deposits, particularly during the interaction between uplift and physical/chemical weathering. Climate conditions will determine weathering regimes whereas tectonic activity will drive the source area uplift, which at the end will create relief and influence eustasy. In basin analysis, seismic stratigraphy has traditionally defined first-, second- and third-order stratigraphic sequences in timespans of 200-300 Ma, 10-80 Ma and 1-10 Ma, respectively. However as resolution has increased, smaller-order stratigraphic sequences have been observed (e.g. Vail et al, 1991; Strasser et al, 2000).

In the Morrin Bridge section, the formation of these depositional sequences (alternations) of all scales are influenced directly by sea-level changes due to precession but more dominated by eccentricity cycles as shown in the cyclostratigraphic framework (Fig.V.9). These allocyclic units are identified by their regional and lateral correlation along the entire Red Deer River (this work; Hamblin, 2004; Eberth, 2010). The fact that the hierarchical stacking of these sequences (sand-silt-organic rich layers but also the distribution of Fe-concretions, palaeosoils and coal) and the wavelet analysis of the chemical variations may reflect the periodic changes in astronomical parameters (Fig.V.8), implying that Earth's insolation changes can be translated into sea-level fluctuations.

Furthermore, the time span between the two youngest populations in the, U-Pb zircon dates from the two volcanic ash layers clearly shows that the section is precisely coincident with eccentricity cycles, as the volcanic ashes are separated by ~800 kyr, i.e. eight-nine ~100 kyr eccentricity cycles as shown in Fig.V.8. However, care should be taken by using pure statistics for pinning-down astronomical parameter from the geological record. The overall sedimentation rate at the Red Deer River Valley at the Western Canada Sedimentary Basin has been suggested to be ~5cm/kyr, which means that the sedimentation rate as calculated here will be 1.7cm/kyr, i.e. a ~3 times lower sedimentation rate than the overall sedimentation rate. As the section is sand dominated, it is thus possible that some of the sand horizons would be related to uncorformities in the area.

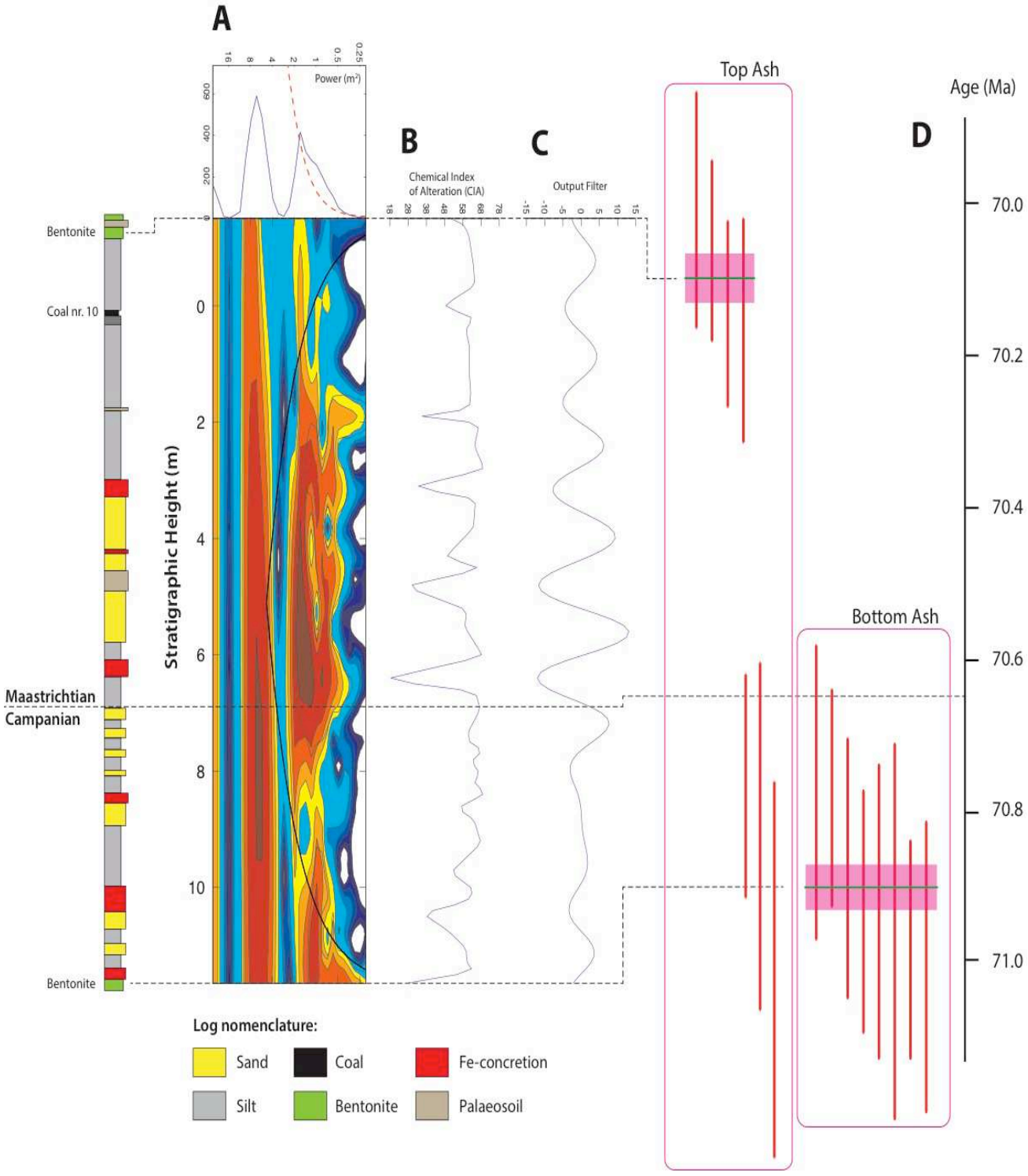

Fig.V.8. Integrated cyclostratigraphic framework with highly precise and accurate U/Pb zircon dates. It is shown that the Wavelet analysis of the CIA(%) pinpoints periodicities at ~1.67 m, which results in 8 cycles from the top to the bottom of the section. Highly precise and accurate single grain and grain fragment 206Pb/238U zircon dates from the two volcanic ashes show that there are ~800 ka between the 2 ashes correlating well with the amount of cycles. Uncertainties in single grain and weighted mean values are all presented as 2σ confidence intervals.

V.4.2. The age of the Campanian-Maastrictian Boundary

The age of the Campanian-Maastrichtian boundary has been defined in terms of the arithmetic mean of sediments enclosing first occurrences of ammonoid groups, where the mean is close to the first occurrence of *Pachydiscus neubergicus*, thus confirming correlation independent of diachronism (e.g. Odin, 2001). The boundary at Tercis lies in the middle of C32n2, in the upper part of the *Uniplanatius trifidus* zone at Gubbio with an age of 72.0 ± 0.5 Ma (mentioned in detail later, Barchi et al, 1997; Odin, 2001; Lewy and Odin, 2001; Odin et al, 2001a; 2001b). The GTS2004 proposed an age of 70.6 ± 0.6 Ma for the Campanian-Maastrichtian boundary on the basis of the last occurrence of *Uniplanatius trifidus*, which has been calibrated relative to the Sr-isotope curve of McArthur et al. (1994) and estimated to be ~750 ka younger than the boundary at Tercis. However the GTS2004 also suggests an age of 71.3 Ma on the basis of the first occurrence of *Belemnella lanceolata*, calibrated relative to the Sr-isotope curve of McArthur et al. (1994). Husson et al. (2011) precisely identified the *Uniplanatius trifidus* zone in ODP Hole 762C at the 15th long- term eccentricity cycle below the age of the K/Pg boundary (i.e. ~6.1 Ma from the K/Pg boundary).

They also assumed that the last occurrence of *Uniplanatius trifidus* in ODP Hole 762C is ~750 kyr older than at Tercis, thus suggesting an age for the boundary of 72.34 ± 0.07 or 72.75 ± 0.07 Ma. By directly comparing the work of Husson et al. (2011) and the cyclostratigraphy developed in the present study, it can be observed that the age proposed by Husson et al. (2011) is more than 1 Ma older than the age constraints from the Western Canada Sedimentary Basin (Fig.V.9). A particular drawback of the work presented by Husson et al. (2011) is that the entire 8.5 Ma astronomical calibration of the Maastrichtian, and consequently the Campanian, is based on the age of the K/Pg boundary as starting point, which has not been precisely defined but assumed to lie in the minimum of a long term eccentricity cycle, close to either 65.59 ± 0.07 Ma or 66.00 ± 0.07 Ma. On the basis of highly precise and accurate U/Pb and ^{40}Ar-^{39}Ar age constraints, Heredia et al. (in prep.) suggests an age for the K/Pg boundary of 65.746 ± 0.058 Ma, if so the eccentricity cycles here described will correlate with Ma40512 and Ma40513, when recalculating the Husson et al. (2011) cyclostratigraphic framework to the U-Pb and ^{40}Ar/^{39}Ar age of the K/Pg boundary (Fig.9).

Voigt et al. (2012) defined the Campanian-Maastrichtian boundary mainly on the basis of three independent methodologies: 1) Carbon isotope correlation between Tercis and Gubbio and adjusting the magnetic reversals to the recalculated Ar-Ar radio-isotope ages in the Western Interior Basin of North America (Obradovich, 1993). These results give an age of 72.14 Ma for the boundary; 2) Biostratigraphic correlation of inoceramid zones between Tercis and the Western Interior Basin and recalibrated ^{40}Ar-^{39}Ar ages (e.g. Obradovich, 1993, Cobban et al. 2006). In this model the Campanian-Maastrichtian boundary in the Western Interior Basin has an age of 72.2±0.2 Ma; 3) Astronomical calibration of the identified long-term eccentricity cycles in different core samples reported by Husson et al. (2011) in deep-sea sections, which already has been discussed.

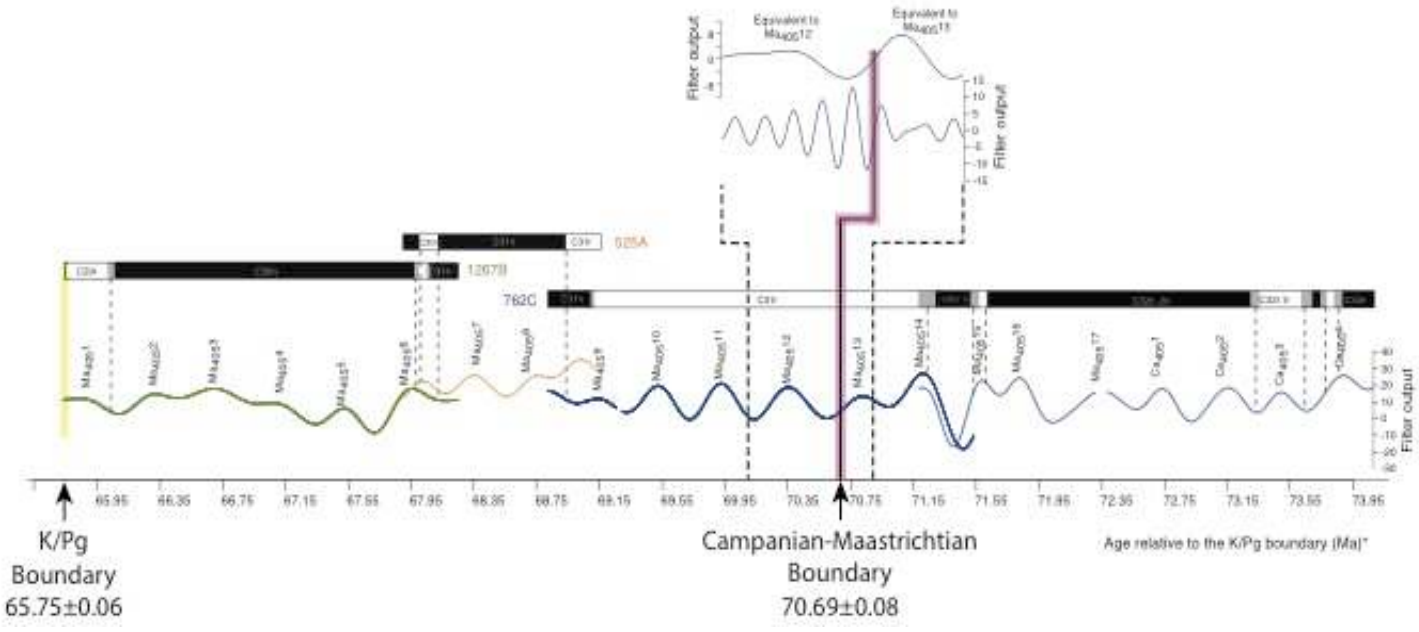

Fig.V.9. Comparison between the astronomical calibration of Husson et al, (2011) and the cyclostratigraphic framework developed in this study. By assuming continuity in this time scale, it can be suggested that the astrochronological framework developed in this study is correlative with the Ma40512 and Ma40513 of Husson et al, (2011). Dashed lines indicate the highly precise and accurate U/Pb zircon ages from the volcanic ashes at the Morrin Bridge section. The age of the Campanian-Maastrichtian boundary has been calculated using the cyclostratigraphic framework as it lies ~2.5 short eccentricity cycles above the lower volcanic ash. The timescale has been recalculated to the U/Pb and $^{40}Ar/^{39}Ar$ ages for the K/Pg boundary proposed by Heredia et al. (in prep.) at 65.746 ± 0.058 Ma.

Voigt et al, (2012) further presented a global correlation of carbon-isotope events and suggested that small discrepancies (of up to 700 ka) between ages are related to the uncertainties of radio-isotopic age estimations. Voigt et al, (2012) suggested that the "systematic" uncertainty in the $^{40}Ar/^{39}Ar$ age estimations can make it possible to average all the ages from the carbon isotope correlation between Tercis and Gubbio, the adjusted biostratigraphic correlation in the Western Interior Basin with the astronomical age of 72.75 ± 0.07 Ma of Husson et al, (2011), which result in an age of 72.1 ± 0.1 Ma. However taking into account all sources of uncertainty, including other systematic uncertainties (e.g. decay constant uncertainties in the $^{40}Ar/^{39}Ar$ system and monitor age uncertainties), a more strict error estimation will give an uncertainty of at least ~0.9 Ma and not 0.1Ma as proposed by Voigt et al, (2012).

Consequently, the tuning of astronomically floating time scales to debatable ages at the K/Pg boundary (as in the case of Husson et al, 2011) and diachronism between biohorizons increases the uncertainty in the definition of stage boundaries rather than reducing it (Fig.V.10).

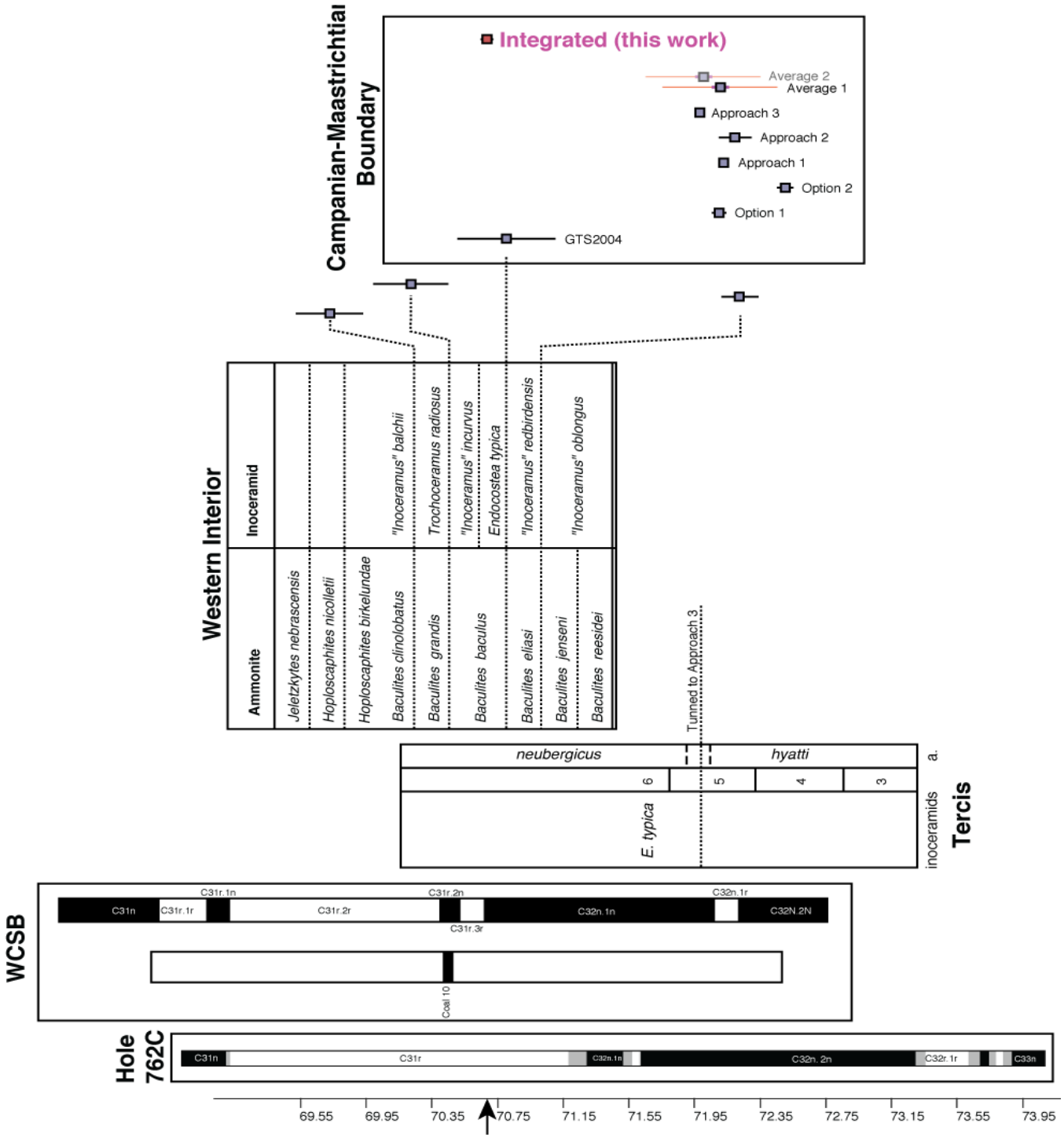

Fig. 10. Comparison between the magnetostratigraphy of ODP Hole 762C and the Western Canada Sedimentary Basin. Also shown are the inoceramid table from the Tercis section, which is the GSSP section, and the ammonites and inoceramids zonal table for the Western Interior Basin at the US. All Ar-Ar ages from the Western Interior Basin, including the GTS2004 (Gradstein et al, 2004), have been recalculated to the astronomically tuned age of the Fish Canyon sanidine (28.201 ± 0.046 Ma; Kuiper et al, 2008. Option1 and 2 of Husson et al, (2011) are recalculated to the U/Pb zircon ages of 65.75 ± 0.06 for the K/Pg boundary (Heredia et al, in prep). Approach 1, 2 and 3 and the average 1 are taken from Voigt et al, (2012). Average 2 is a recalculated age, taking 65.748 ± 0.058 Ma as the age for the K/Pg boundary.

V.4.3 Eruption age estimates

Eruption ages are commonly determined by $^{40}Ar/^{39}Ar$ dates from sanidine crystals, which usually record the time at which radiogenic Ar begins to accumulate following eruption and cooling below magmatic temperatures. This argument has been key for using the $^{40}Ar/^{39}Ar$ as the prime radio-isotope system for constraining biostratigraphic timescales (e.g. Obradovich, 1993; Cobban et al, 2006). In contrast to the $^{40}Ar/^{39}Ar$ dates, U-Pb age estimates in zircons from volcanic rocks have shown that zircon crystallisation can significantly predate eruption (e.g. Reid et al, 1997; Lowenstern et al, 2000; Charlier et al, 2005). Furthermore by directly comparing $^{40}Ar/^{39}Ar$ and U-Pb dates from the same samples, it has been shown that $^{40}Ar/^{39}Ar$ age estimates are ~1% younger than the $^{206}Pb/^{238}U$ dates (e.g. Min et al, 2000; Schoene et al, 2006).

Crowley et al, (2007) reported various precise and accurate $^{206}Pb/^{238}U$ zircon weighted mean ages for the Bishop Tuff, where the youngest weighted mean yielded an age that overlaps with reported $^{40}Ar/^{39}Ar$ sanidine ages, demonstrating that most zircon crystallised immediately prior to eruption. Thus, the classification of zircon with respect to age is used to avoid misinterpretation in the zircon data. The age estimates presented here, and tested with weighted mean statistics, have shown that the youngest populations can be related to the crystallisation of autocryst zircon, which is considered as a zircon that crystallised very late in the magmatic history of a sample, near the time of eruption. Older populations can be related to the crytallisation of antecrystic zircons or slightly older zircon inherited into the magma but that broadly originated in the same magmatic system and therefore shows similar chemical characteristics. Furthermore, when the mean square of weighted deviates is close to unity, inhomogeneous samples do not contribute with additional scatter, meaning that the data is consistent with the null-hypothesis that all zircons crystallised synchronously, i.e. the extent of the match between the observations and the estimates is in accord with the uncertainty variance (e.g. Wendt and Carl, 1991).

V.5. Conclusions

The Morrin Bridge section is mainly controlled by sand horizons, which have been related by autocyclicity in a dynamic sedimentary setting, and is thought to contain the Campanian-Maastrichtian boundary. In the work presented here, it is possible to reconstruct its cylcostratigraphic framework because the stacking of the smaller order sequences are astronomically controlled, mainly by short eccentricity cycles. Precession can be also recognised but only in some of the alternations. The horizons and individual layers can be followed along the Red Deer River, suggesting that their deposition is controlled by processes occurring outside the basin on a regional scale (i.e. allocyclicity). The reconstructed cyclicity with 8 intervals corresponding to the ~100 ka cycles are well supported by the highly precise U-Pb zircon age constraints. The zircon age population at the top (70.099 ± 0.065 Ma) and at the bottom (70.902 ± 0.060 Ma) of the section is directly coincident with the amount of cycles determined in the cyclostratigraphic framework.

The Campanian-Maastrichtian boundary in the Western Canada Sedimentary Basin coincides with ~2.5 eccentricity cycles above the youngest zircon age population at the bottom of the section and ~4.9 Myr before the Cretaceous- Palaeogene boundary (K/Pg) and thus corresponds to an absolute age of 70.65 ± 0.09 Ma. Although this age does not directly correlate with the age estimations proposed by other authors (e.g. Husson et al, 2011; Voigt et al, 2012 and references therein), it is an independent estimation regardless of the insufficient preservation and inaccurate identification of microfossils, endemism and diachroneity in marine faunas. The age presented here is ~1.4 Myr younger than earlier estimates (72.1 ± 0.2 GTS2012), which are chiefly based on microfossils, floating astronomical time scales and stable isotopes, but it correlates well with the age proposed by GTS2004 (recalculated from Gradstein et al, 2004).

However, as the boundary definition is complex and cannot be placed at a particular point but correlated on the basis of magnetostratigraphy and biostratigraphy with ammonites and inoceramids in the Western Interior Basin with those at the Western Canada Sedimentary Basin, the age for the Campanian-Maastrichtian boundary

presented here can be hampered by its misplacement in western Canada and therefore will not correlate with recent age constraints (e.g. Voigt et al, 2012). Nevertheless, the ages estimations presented in this work thus contribute important age constraints for the stratigraphy of late Cretaceous sediments in western Canada, and places the interdisciplinary work as the most powerful tool in timescale calibration.

Acknowledgments.

A. Sweet, J. Lerbekmo (deceased), D. Eberth, and the GTSnext (the next generation Geological Time Scale) staff and students are thanked for discussions on the field relations, and the developments of the cyclostratigraphy. The European Community's Seventh Framework Program (FP7/2007-2013) under Grant agreement no. [215458] has funded this research.

VI. Japan

VI.1 Overview

The Cretaceous period is characterised by numerous global oceanic anoxic events, rich ammonitic fossil assemblages and specialised foraminifera. However, lack of age diagnostic macro, micro-fossils in the North Pacific sections has made it difficult to link with global sections such as the western interior basin (North America). Using advances with terrestrial carbon isotope and planktonic foraminiferal records within central Hokkaido (Takashima et al, 2010), we are able to correlate these sections globally.

The Cretaceous Yezo group (Central Hokkaido, Japan) comprises of deep marine mudstones and turbidite sandstones interbedded with acidic volcanoclastic sediments deposited from late Aptian to the Paleocene (Nishi et al, 2004). Using various sections within the Yezo group we radiometrically date tuffs at the main stage boundaries in the Upper Cretaceous, located using previous carbon isotope and planktonic foraminiferal records (Takashima et al, 2010).

Samples from the present study have been derived from two main sections within the Yezo group region, Kotanbetsu and Shumarinai section. Together they span the time from the Albian-Cenomanian up until the Campanian-Santonian boundary. All sections are radiometrically dated here using $^{40}Ar/^{39}Ar$ and U-Pb techniques. Previous work (Obradovitch et al, 2002; Quidelleur et al, 2011) has successfully dated tuff beds within the Hokkaido sections using $^{40}Ar/^{39}Ar$, U-Pb and K-Ar techniques on the various Upper Cretaceous stage boundaries. They supply additional dates from different sections around the Hokkaido basin (Kotanbetsu sections) linked by the various faunal assemblages and carbon isotope curves, thus allowing us to link with the global counterparts, such as the English chalk record (Jarvis et al, 2002).

The combined radiometric ages achieved will contribute to previous global timescale attempts (such as those focused in the Western Interior basin) allowing synchronicity of events such as global oceanic anoxic events (e.g. OAE2, Bonarelli event). Achieved ages will also compliment the previous carbon isotope and planktonic foraminifera records allowing for a precise climatic history of the Northwest Pacific.

VI.2 Geological Setting

The geology of Japan is a complex array of successions resulting from multiple orogenies and various subduction related processes (Shigeta and Maeda, 2005). There is a clear absence or near absence of Pre-Cambrian to Lower Palaeozoic strata, initialising with the predominance of marine deposits formed during the Silurian (Shigeta and Maeda, 2005). Starting from the Mesozoic (Sugimura and Uyeda, 1973) the growth of Japanese arc systems has taken place along the continental margin of Asia since the Permian and dominated Japan's tectonic framework by a complex interaction of five plates: Eurasia, Amur, Okhotsk, Pacific and the Philippine Sea plate (Fig.VI.1), during which time there has been frequent land connections with east Asian continent from the Mesozoic to the Pleistocene (Taira et al, 2001). Bedrock of the Japanese islands were assembled as a result of westward subduction along the eastern margin of Asia (Okada and Sakai, 2000). Large accretionary prisms were constructed in the late Palaeozoic to early Jurassic that are composed mainly of deep ocean sediments and trench deposits. Active tectonics in Northeast Japan (Honshu and Hokkaido) are the manifestation of the interaction between the Amur and Okhotsk sub-plates (Okada and Sakai, 2000).

The Late Jurassic to Early Cretaceous marks an increase in subduction rate, (continued presently), generating vast volumes of arc magma, causing high temperature, low pressure metamorphism (Shigeta and Maeda, 2005). In the early Cretaceous, the Rebun Belt constitutes a magmatic front along the eastern margin of the Eurasian continent (Fig.VI.1b) which extended south to the Kitakami Massif (Okada and Sakai, 2000).

During the Cenozoic the Japanese island arc was under-thrusted by the Pacific plate (Taira et al, 2001) eventually changing direction ~45 Ma ago from a north-westerly to a simple westerly movement forming the creation of the Philippine sea plate. The change in direction is coeval with the initiation of the major northwest transform zone extending from New Zealand to the Equator, forming the Izu-Bonin Mariana and Tonga-Kermadec arc trench system. It is unsure which event initiated the change as the plate is surrounded by subduction zones therefore a void of movement history is recorded, and thus cannot be easily calculated (Okada et al, 1995).

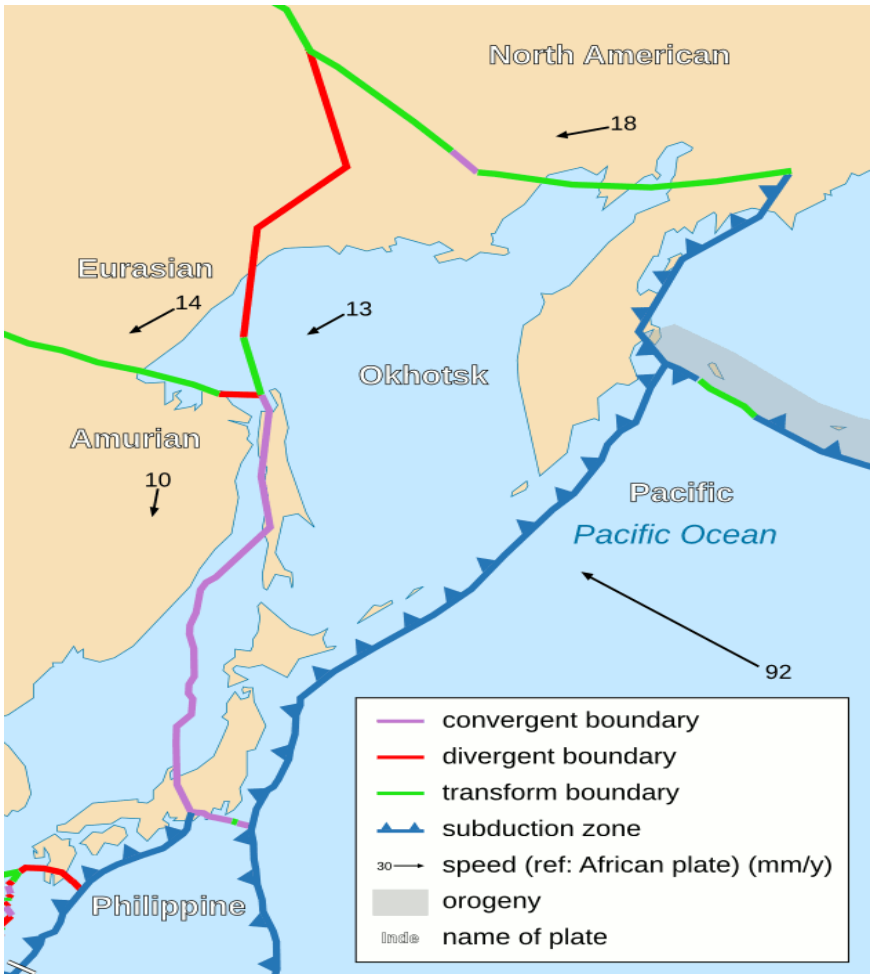

Figure VI.1. (A) Above. Schematic diagram of the current plate tectonics with attributed speed values of today. Plate boundaries are colour co-ordinated depending on the type of boundary involved. (B) Below, Paleogeographical reconstruction of the Earth 90 Myr agea alongside the position of the Yezo group.

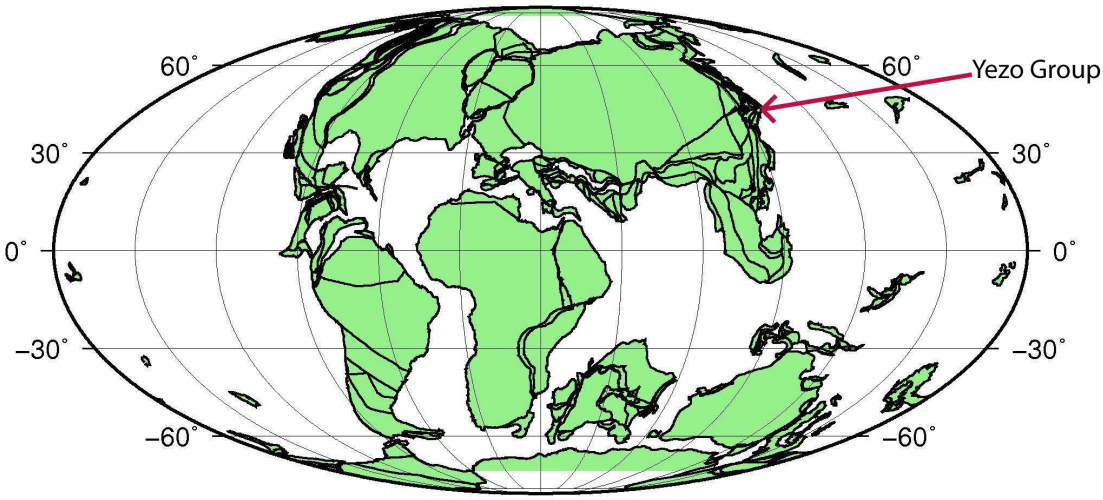

90.0 Ma Reconstruction

VI.2.2 Geology of Hokkaido

During the Cretaceous period, Hokkaido Island was separated into two tectonic masses, the Yezo Arc trench system in the west and the Okhotsk Block towards the east. Uplift and faulting exposed sequences in the central Hokkaido in a N-S orientation, and can be subdivided (Fig.VI.2) into six major accretionary sequences (Okada and Sakai, 2000). In the past, these islands formed an eastern marginal part of the Asian continent where violent igneous activity and tectonic movement took place from the late Palaeozoic to recent (Kumon and Kiminami, 1994). The next pages will descibe briefly the properties of each of the six major accretionary systems (Fig.VI.2).

Nemuro Belt: Located in the Eastern part of the island and representing the Campanian-Eocene time, the Nemuro Group is comprised of volcanic basaltic andesitic conglomerates, alongside clastic deposits (Okada and Sakai, 2000). It encompasses the Yubetsu group of which incorporates thick clastic sandstone and shale, formed in a trench fore-arc region where the Pacific plate subducted easterwards under the Okhotsk plate during the late Cretaceous to early Palaeogene (Kumon and Kiminami, 1994). This thrust belt is best known to encompass the K-Pg boundary in the Northwest Pacific.

Tokoro Belt: Built from a complex of three units of varying age: The upper Jurassic-Upper Cretaceous Nikoro Group consists of a large 4000m thick ophiolitic basaltic deposit accompanied by radiolarian chert and micritic limestone (Okada and Sakai, 2000). This unconformably underlies the Campanian to Palaeocene Saroma formation of terrigineous turbiditic deposits. Finally the Yubetsu Group (Campanian-Paleocene) is a large 10,000m thick deposit (Kumon and Kiminami, 1994) which is similar to the Saroma group and is composed of terrigenous and volcanic turbidites (additonally located within the Nemuro belt).

Hidaka Belt: Dating from the Valanginian to Palaeocene, the Hidaka supergroup is composed of turbiditic clastic sediments intermittent with chert and limestone successions (Okada and Sakai, 2000).

***Kamuikotan Belt*:** Deposited during the late Tithonian to the Albian, this belt is characterised by high pressure and temperature metamorphic rocks which correspond to the ophiolitic Sorachi group (Okada and Sakai, 2000).

Ishikari belt: This will be discussed in detail further, but summarised by deposits from the Aptian up to the Maastrichtian, forming the well studied Yezo Supergroup basin. Ishikari is broken up into four main groups, the Lower, Middle and Upper Yezo along with the Hako-Buchi groups. Aged from late Barremian-Late Albian the Lower Yezo group measures 1000-1300m thick and comprises turbidite facies of shallow marine carbonates that are extremely fosssiliferous (Okada and Sakai, 2000). The middle Yezo group demonstrates extensive Late Albian-Turonian 1800-2000m thick shallow marine coarse grained clastic deposits deposited towards the west, while the eastern side is dominated by muddy offshore facies. The Coniacian to Santonian aged upper Yezo deposits form a 400-1300m thick succession of artillaceous facies formed by the Urakwan transgression (Kumon and Kiminami, 1994).

Finally, the Hakobuchi group is a 400-900m coarse grained massive interbedded sandstone / deep marine deposit, aged between the Campanian to Maastrichtian (Okada and Sakai, 2000). Throughout this group numerous small coal swarms characteristic of the warm Cretaceous climate are present, allowing a detailed carbon isotope curve to be calculated (Okada and Sakai, 2000).

Rebun-Kabato belt

Dating from the Valanginian to the Berremian, this lower Cretaceous Kuanehrig group is composed of siliceous shales, pyroclastic flows of varying composition interbedded with clastic deposits. Within this belt, many ammonite bearing marine clastic layers and limestone layers present allowing correlation to basin wide systems (Okada and Sakai, 2000).

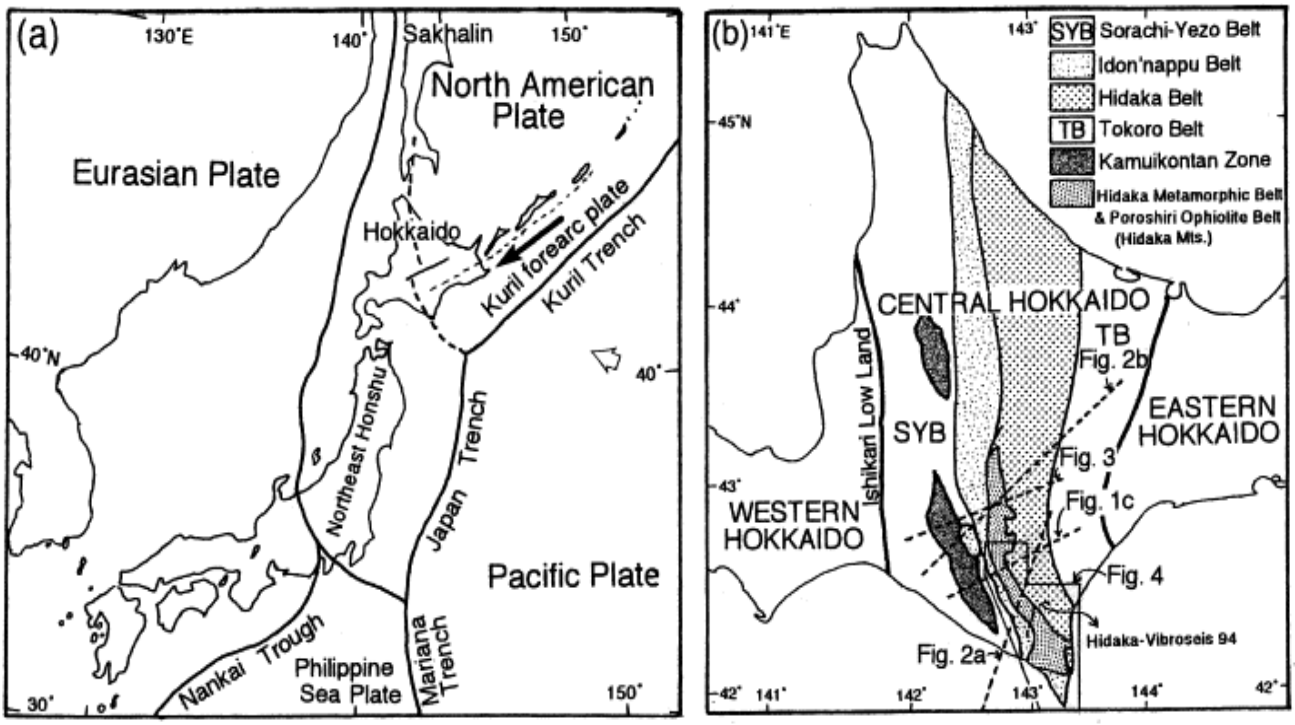

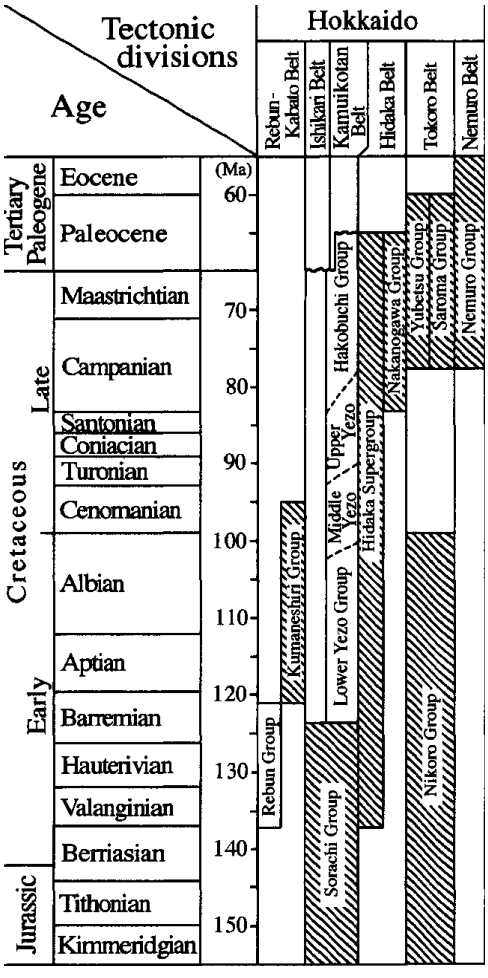

Fig.VI.2 (Right) Stratigraphy of major Cretaceous units in the Hokkaido region Japan. All six subunits described above are present indicating the associated ages for each group (Taken from Okada and Sakai, 2000).

(Above) Regional geology of the Central Hokkaido region and associated units. Figure (a) demonstrated the position of the described locality in relation to surrounding plate tectonics. Figure (b) represents the position and location of all N-S trending belts within the Hokkaido region, while figure (c) shows a E-W schematic cross section through the Hokkaido island.

VI.2.3 Yezo Supergroup

Separated into two tectonic masses, Hokkaido is represented as a Yezo Arc-Trench system to the west and the Okhotsk Block towards the east (Okada and Sakai, 2000). The yezo-supergroup along with smaller coastal basin in the Kitakami area were developed as the result of the development of a fore-arc basin formed by southward migration of the Rebun belt magmatic front along the margin of the Eurasian continent (Kuwabe et al, 2003).

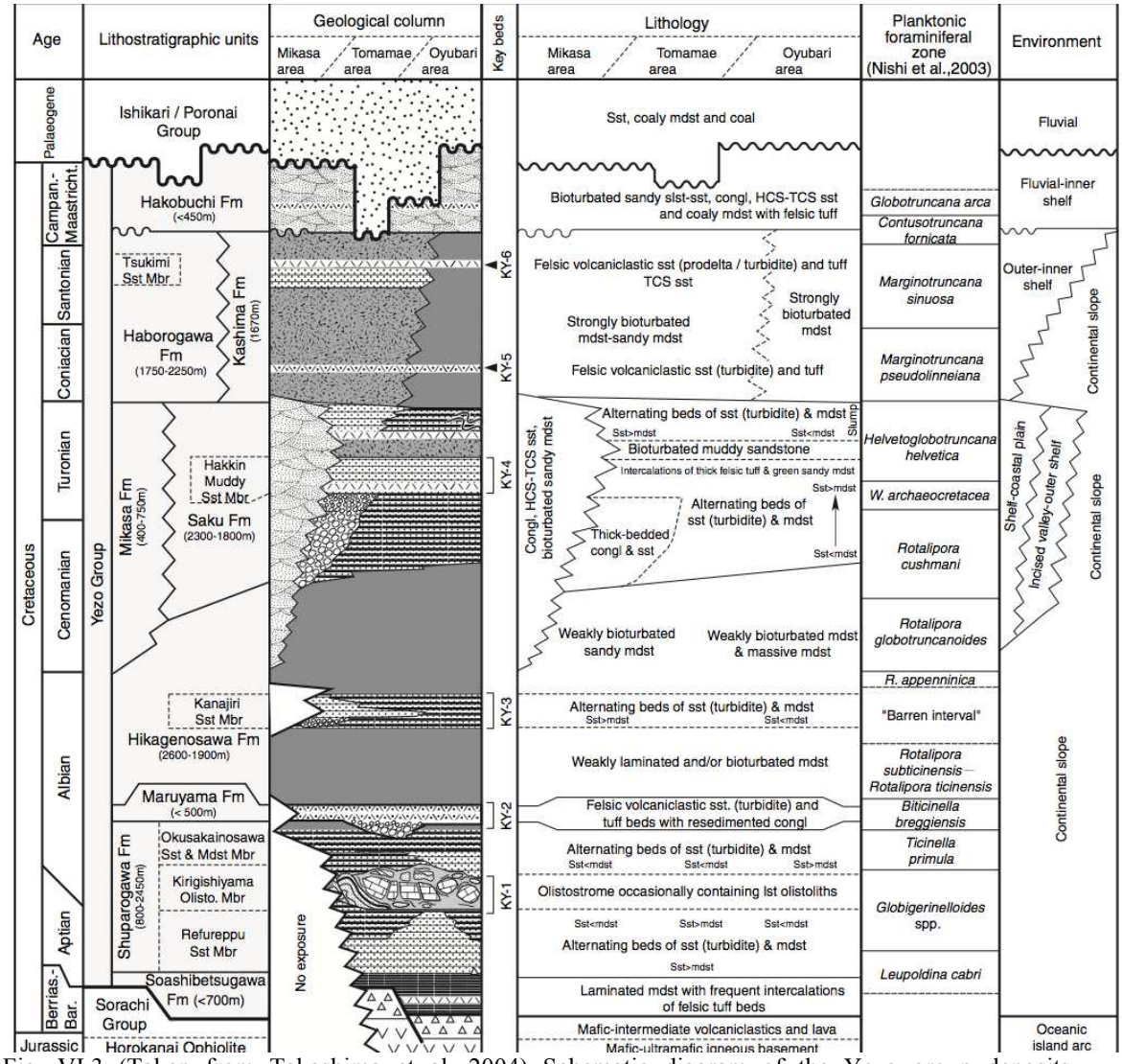

Fig. VI.3 (Taken from Takashima et al, 2004) Schematic diagram of the Yezo group deposits, demonstrating the Plankotonic foramifera and depostional environment.

The Yezo supergroup, located in the Ishikari belt was primarily deposited in a forearc basin environment in the inner trench slope, it will be discussed in detail further but predominantly it is a coarse grained sediment deposited in a shallow sea environment (Takashima et al, 2004) intermittent with turbidites (Fig VI.3). It covers numerous

geological stages but essentially, it is famous for its preservation of multiple oceanic anoxic event horizons such as the Cenomanian/Turonian oceanic anoxic event (Takashima et al, 2010). It should be noted that Cretaceous basins throughout Japan were developed through a pre-Cretaceous formed basement within localised zones, they developed through changes in the tectonic setting along the continental margin of East Asia (Takashima et al, 2004; Shigeta and Maeda, 2005).

VI.2.4 Stratigraphy of the Yezo group

Exposed in central Hokkaido (N. Japan), it was deposited 35-45^{o}N along a westwards subducting margin in the NE Asian continent during the Cretaceous, running centrally throughout Hokkaido in the Ishikari accretionary belt (Shigeta and Maeda, 2005). Stratified under an unusual nomenclature (Fig.VI.4) the Yezo basin has been stratigraphically simplified (Nishi et al, 2003; Takashima et al, 2004) by six alternations of mudstone-dominant units interbedded with sandstones. Albian-Aptian sequences show laminated mudstones structured in a slope fan channel fill, while deep water trace fossils show abyssal zones filling upwards in the in the Albian, up to bathyal zones (Nishi et al, 2003; Takashima et al, 2004).

Upper Cretaceous deposits show lateral variations, thickening to the North West. Rapid uplift in the Yezo forearc basin during the Albian-Turonian gave way to shallow marine, deltaic and even fluvial deposits (Takashime et al, 2004), following onwards within the Cenomanian-Campanian whereby formations exhibit slope fan and benthic bathyal environments. The final stage of the Yezo forearc basin deposited non-marine strata during the Campanian-Late Paleocene (Kawabe et al, 2003; Takashima et al, 2004; 2010). Back arc spreading in the mid-Miocene altered the majority of Pre-Neogene stratigraphy in Northern Japan. However sediments around the Yezo group were not altered by severe tectonic deformation or diagnesis (Ando, 2003).

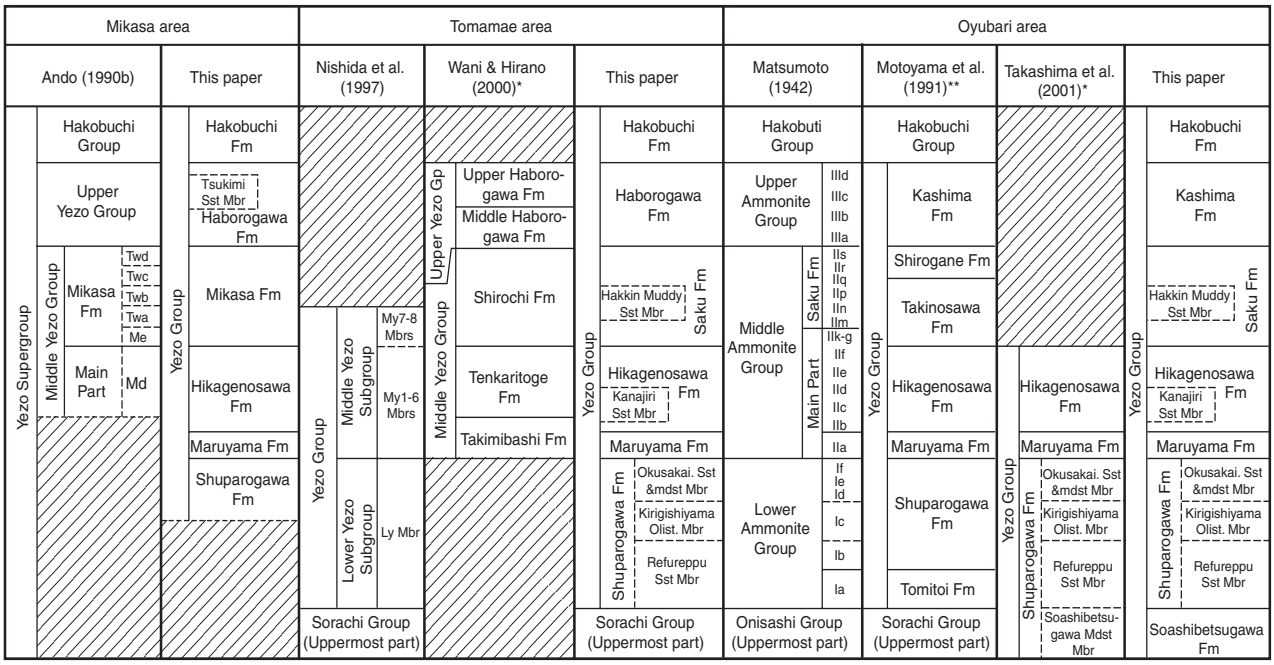

* Same definition is used in Nishi et al. (2003)
* *Same definition is used in Hasegawa & Saito (1993), Kaiho et al. (1993), Kaiho & Hasegawa (1994), Hasegawa (1995) and Hasegawa (1997)

Key units	Thickness	Lithofacies	Horizons	Age
KY-6	10–30 m	Tuffaceous coarse sandstone beds	Middle parts of the Kashima and Haborogawa formations (Tsukimi Sst Mbr)	Latest Santonian
KY-5	10–20 m	Greenish tuffaceous coarse sandstone beds with abundant *I. uwajimensis*	Lower parts of the Kashima and Haborogawa formations	Early Coniacian
KY-4	<300 m	Greenish gray tuffaceous muddy sandstone with abundant *Planolites* trace fossils and very thick felsic tuff beds	Middle part of the Saku Formation (Hakkin Muddy Sst Mbr)	Early Turonian
KY-3	100–300 m	Sandstone-conglomerate beds	Lower middle part of the Hikagenosawa Formation (Kanajiri Sst Mbr)	Latest Albian
KY-2	<82 m	Felsic tuff and tuffaceous sandstone beds	Maruyama Formation	Early Late Albian
KY-1	<400 m	Olistostrome or debris flow deposits occasionally containing "*Orbitolina*" limestone blocks	Middle part of the Shuparogawa Formation (Kirigishi. Olistostrome Mbr)	Late Aptian–Early Albian

Fig VI.4, Taken from Takashima et al, 2004, list of traceable key units witin the Yezo group, alongside the basin wide correlative stratigraphy.

The Yezo supergroup can be divided further into the eight varying sub-groups, all deposited during the late Cretaceous. Below are brief descriptions of each sub unit that will be utlised further within this chapter:-

Shuparogawa: Located along the Shuparo river in central Oyubari, the formation conformably overlies the Soashibetsugawa formation and is composed of alternating turbiditc sandstones and mudstones. These are further subdivided into three members known as the Refureppu Sandstone, Kirigishiyama Olistostrom and Okusakainosawa

Sandstone each characterised by its mix of sandstone to mudstone ratios. Deposited in a variety of environments from carbonate platforms to bathyal zone it represents a varying thickness of 800-2450m with fossil assemblages such as the *Globigerinelloides barri*, dating the section as Late Aptian-Early Albian in age (Nishi et al, 2003; Takashima et al, 2004).

Maruyama: Once again type casted from the Suparo river locality, it is characterised as a stratigraphic marker that extends throughout the Hokkaido region. Conformably lying on top of the Suparogawa formation, it is composed of tuffaceous sandstone beds, felsic volcaniclastic sandstones and conglomerates that were erupted episodically along the western Pacific/Asian continental margin. It has a variable thickness depending on exposure of 4-900m, with radiolarian ages of Early-late Albian (Nishi et al, 2003; Takashima et al, 2004).

Hikagenosawa: Conformably lying over the previous Maruyama formation, it is categorised by dark grey mudstones with alternating beds of sandstone and mudstone. Located in the Hukageno-sawa valley, Oyubari it ranges from 1900-2600m in thickness and is presumed to be Late Albian in age from ammonoid assemblages such as *Mortonicera rostratum*. This succession formed in the lower upper bathyal zone in oxygenated conditions (Nishi et al, 2003; Takashima et al, 2004).

Saku Formation: Contrived from the Abeshinai river section Teshionakagawa, it lies conformably over the previous Hikagenosawa section and is composed of alternating tubiditic sandstone and mudstone with a variable thickness of 1800-2300m in the Oyubari area. Abundant macrofossils point to a Middle Turonian to Upper Cenomanian age (Nishi et al, 2003; Takashima et al, 2004).

Mikasa Formation: Dominated by hummocky cross stratified sandstones that are divided into three successions of third order depositional sequences, this section is named from the North-West Katsurazawa Lake, Mikasa. The succession measures between 400-750m, thickening eastwards forming part of the Sorachi-Ikushumbetsu anticline (Fig.VI.2C). Interpreted as being deposited in depleted deltaic environments aged from Cenomanian to Turonian (Nishi et al, 2003; Takashima et al, 2004).

Kashima Formation: Overlying the Saku formation, it encompasses dark grey mudstones inter-calibrated with felsic volcaniclastic units measuring around 1670m in thickness, found within the Oyubari area. Fossils within this section such as *Contusotruncasa fornicata* and *Globotruncana arca* span from the Late Turonian to Campanian age and is named from the Kashima Village section southern Oyabari (Nishi et al, 2003; Takashima et al, 2004).

Haborogawa Formation. Found within the Nakafutamata river section Tomamae, this formation is characterised by a bio-turbated mudstone coursing upwards to a muddy siltstone / sandstone mix. It stretches between 1950m-2250m in thickness and is deposited in a deep outer shelf to lower shore-face environment. It is proposed that this section is Coniacian-Campanian in age due to abundant microfossils such as *Marginotruncana pseudolinneiana* in the section (Nishi et al, 2003; Takashima et al, 2004).

Hakobuchi formation: Corresponding to the Hakobuch group, in the Shuaro River, Oyubari this section is dominated by third and fourth order depositional sequences sand and musdstone complexes, conformably overlying the Kashima formation. Formed in a variety of environments from shallow marine-shelf it spans a thickness from 20-450m and contains few macrofossils with no age diagnostic species, however, some formanifera show ages from the Campanian to Paleocene (Nishi et al, 2003; Takashima et al, 2004).

VI.2.5 Geological Areas

Samples were collected from two different sample sites within the Hokkaido region; the Kotanbetsu and Shumarinai river section. Both sample sites span the lower and upper Cretaceous period, incorporating key oceanic events during this time. Strata contains abundant marine macro- and micro- marine fossils, while the scarcity of age diagnostic fossils in the Upper Cretaceous sequence have prevented researchers from making stratigraphic correlation (particularly within the Turonian/Coniacian – Coniacian/Santonian). Additional sample sites such as the Hakkin river and Tomiuchi sections were also sampled, however we were unable to extract suitable age diagnostic minerals for these sections.

VI.2.6 Kotanbetsu Section

A large section of the Yezo super-group can be located along the Kotanbetsu river (Fig.VI.5), Tomamae region, Hokkaido, Japan. It spans a large sum of the Yezo group containing the Hikagenosawa formation, Saku formation and Haborogawa Formation. Within this section the widely traceable key units KY-5 and KY-6 are identifiable alongside key oceanic event horizons. Sample ashes were taken where available and will be dated later in this chapter.

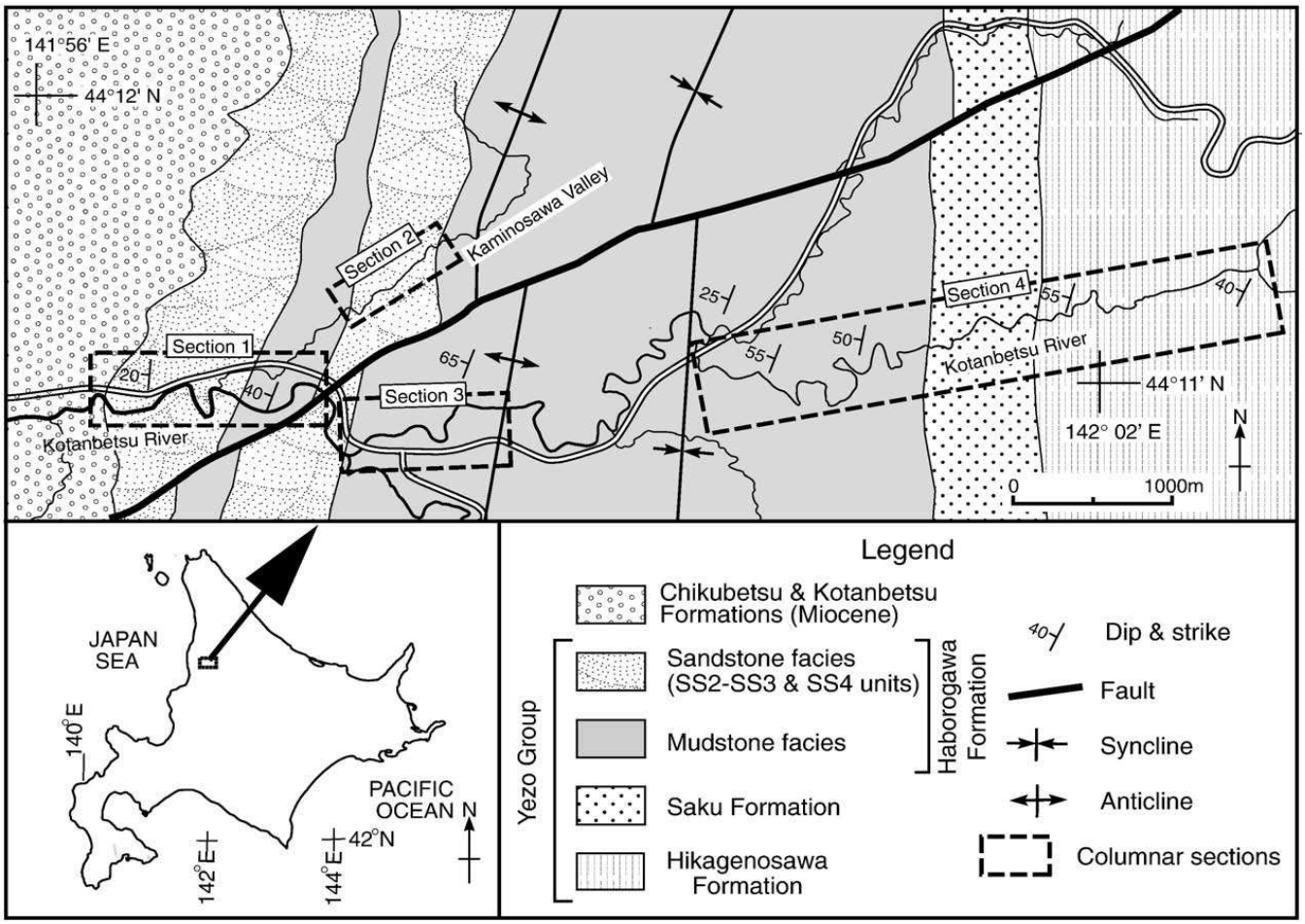

Fig.VI.5 Kotanbetsu river location and geological map taken from Takashima et al, 2010

Within the Kotanbetsu section there are multiple basin wide correlative beds (Fig.VI.6) that have been logged and stratigraphically defined. These marker beds (Fig.VI.6) help correlate to other key sections within the Yezo basin and sub groups. Defined by their lithology they are noted as the following:-

Sandstones

These marker beds represent a total of four shallowing events alongside global eustatic sea level changes with the depositional environment alternating from a continental slope to outer or inner shelf environment.

- *SS1:* A thick 180m sandstone sequence that coarsens upwards from bio-turbated sandy siltstone to a fine grained sandstone with hummocky cross stratification. This event correlates to the Pewsey Carbon isotope event in the late middle Turonian and considered to represent a glaciation induced rapid sea level fall (Takashima et al, 2004; 2010).

- *SS2*- Strongly bioturbated mudstone correlating to the major swallowing event around the Santonian/Campanian boundary. Both facies and C^{13} curve indicate a shallowing event marked by a transgression (Takashima et al, 2004; 2010).

- *SS3*-Bioturbated muddy sandstone exhibiting upward coarsening sequences correlating to sea level fall in the middle lower Campanian (Takashima et al, 2004, 2010).

- *SS4* Medium to coarse grained bioturbated sandstone similar to SS3 exhibiting vertical upwards grading, it is presumed to have occurred in the early–mid Campanian (Takashima et al, 2004; 2010).

Volcaniclastic horizons

Two volcaniclastic markers (Fig.VI6) in the lower and upper section of the Kotanbetsu river section are excellent stratigraphic markers and utilised for basin wide correlation. Located in the centre of the Haborogawa formation KY-5 consists of thick beds of volcaniclastic sandstones with abundant *Inoceramus uwajmensis* fossil*s* while KY-6 is clased as the Tsukimi Sandstone member and is a 20m thick volcaniclastic sandstone with interbedded dark grey mudstones with evidence of turbidic sequences (Takashima et al, 2004; 2010).

VI.3 Previous Work

Although not as extensive as other well defined Cretaceous basins, some specialised work has succeeded in correlating the NW pacific with global counterparts. Work by Obradovitch et al. (2002), Takishima et al. (2004; 2010), Nishi et al. (2003) and Quidelleur et al. (2011), have allowed us to understand correlative horizons giving way to age determined by radiometric dating and biostratigraphic interpretation.

VI.3.2 Carbon Isotope Curve

Carbon Isotope curves are used geologically for a variety of applications, one being that they act as great stratigraphic correlates on a global scale for events such as oceanic anoxic events. Heavy collaborations in the Cretaceous of European and North American counterparts has made a vast network array of stratigraphic reference points most notably the well developed δC^{13} curve (e.g. Voigt and Hilbrecht, 1997). The use of age diagnostic fossils coupled with numerous fossilised wood fragments, found within this region, allows the possibility to correlate towards other worldwide basins (Fig.VI.7). Previous studies and work by (Takishima et al, 2004) have developed a novel approach for creating a high resolution carbon isotope curve. Using a resolution of ~50 Kyr, planktonic foraminfera and bulk wood carbon isotopes has led to the production of a remarkable high resolution signal, revealing global events such as OAE2, decreasing levels in pCO_2, eustatic sea level rises showing great correlation to other global signatures such as the English chalk C curve (Fig. VI.7).

The carbon isotope curve (Fig.VI.7) was developed by extracting over 100 pieces of fossilised wood and fossil fragments, crushing them into a fine powder and analysed using the bulk rock method (Hasegawa and Saito, 1993) therby reducing isotopic noise. Total organic carbon levels were found to be 0.5-1.2 wt % higher than the Tethyan and Atlantic regions (i.e English chalk section) with isotpic values varying between 19-27‰, showing isotopic event excursions correlating to both stage boundaries and OAE horizons. Volcanic tuffs are then dated around the associated isotopic events helping to construct high fidelity ages for the Kotanebetsu section and adjoining areas (Takashima et al, 2010; Quidelleur et al, 2011).

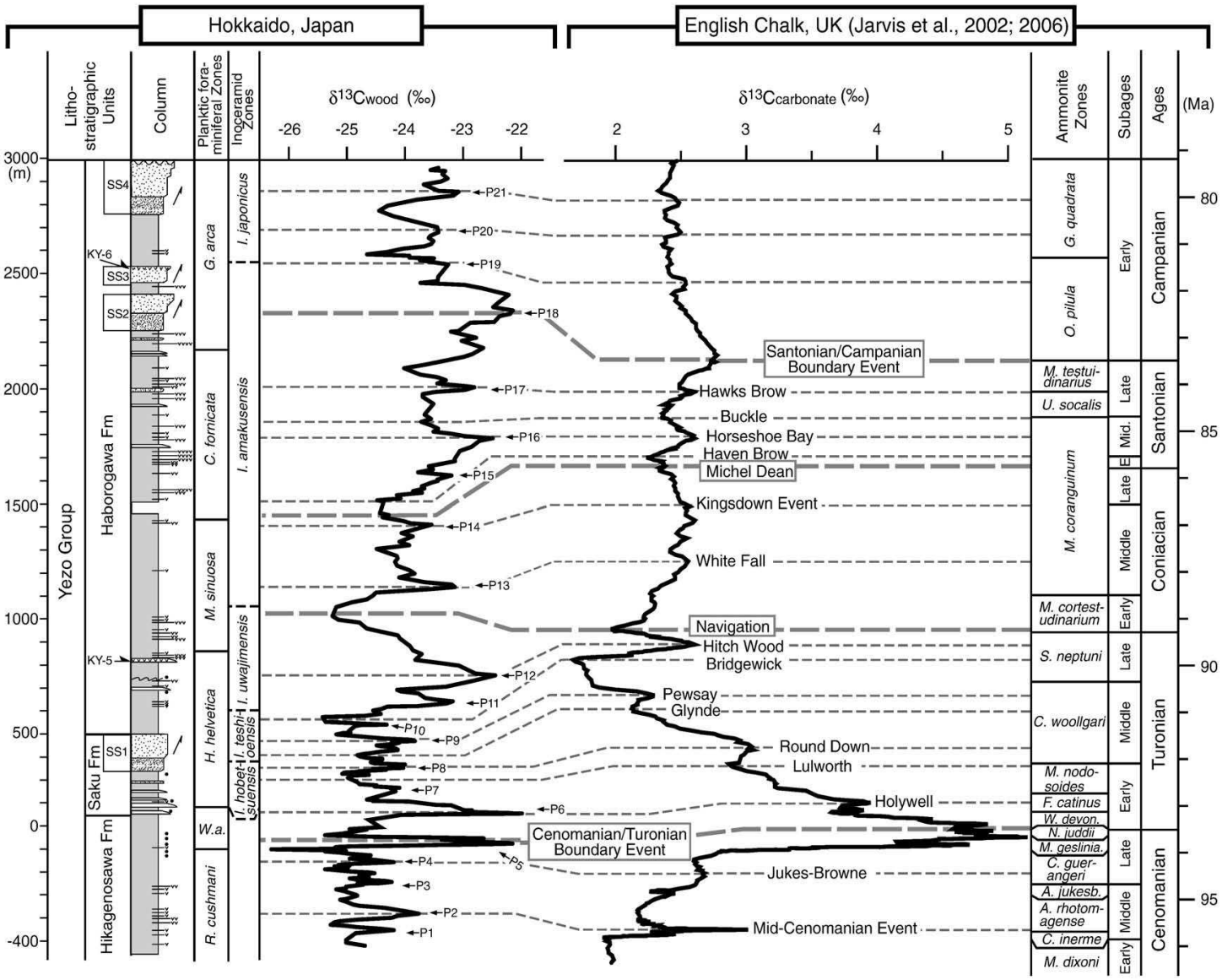

Fig.VI.7 Showing the correlated Carbon isotope curves for both the Kotanbetsu and English chalk Section. Figure also shows the position of key marker beds such as the SS# sandstones and volcaniclatistic depotsits (KY-#) alongside the stratrigraphic log of the Kotanbetsu section.

Oceanic anoxic events (Previosuly discussed in chapter 1) within the Yezo basin are recorded in the lithology and easily observed in the carbon isotope curve (Fig.VI.7). Although easily recognized in the European basins as laminated organic rich black shales within white limestone beds, it has been problematic when locating similar horizons in an terrigenous dark grey sandstone/mudstone beds such as in the Yezo basin. Higher average total organic carbon (TOC) levels within the section also hinder the ability to easily locate such horizons and is dependant on biostatigraphic and chemostratigraphic markers, correlated by Nishi et al. (2003).

OAE1

Previously discussed in chapter I, this oceanic anoxic event is split into multiple sub units from OAE1a through to OAE1d. Negative and positive $^{13}C_{org}$ excursions were measured within the Soashibetsugawa formation (Ando et al, 2002, 2003) corresponding to a global anoxic event (OAE1a) occurring for ~1 ma (119.5-120.5 Ma). Within the Yezo group, this excursion corresponds to the first occurrence of *Leupoldina cabri* in the 110m thick Soashibetsugawa formation, however, due to erosional or tectonic events the boundary that contains *Ticinella bejaouaensis* OAE1b marker bed is presumed missing in the Yezo formation. The basal part of the Hikagenosawa and the top part of the Shuparogawa formation contain the 300m thick *Biticinella breggiesnsis* zone characteristic of the OAE1c horizon and correlates well with the OAE1c horizon of Leckie et al. (2002).

The last of the OAE1 events (OAE1d) correlates with the lower middle Hikaganosawa formation exisitng within the *Rotalipora appenninica* zone in the uppermost Albian (Gale et al, 1996). This is recorded as a positive $^{13}C_{org}$ curve, correlating to the $^{13}C_{carbonate}$ excursion in the Tehyan atlantic region just below the KY3 sandstone member within the *Stoliczkaia dispar* ammonite chronozone (Nishi et al, 2003; Takashima et al, 2010).

Middle Cenomanaian event horizon.

Prelude to the OAE2 this event represents another perturbation in the carbon cycle, resolved by a major +0.7‰ $^{13}C_{carbonate}$, shift in the global organic rich layer associated with upper Cenomaninan organic rich shale in Central Italy type sections. Transpired to correlate with the 1.2‰ $^{13}C_{org}$ peak in the Hakkin-Zawa section (Hasegawa 1997) Oyubari. This event shows a stepwise benthic foraminiferaal extinction (43% reduction of calcareous species in Southern Oyubari (Hasegawa et al, 1993).

OAE2 (Bonarelli Event)

Previously stated in chapter 1 the Cenomanian-Turonian boundary anoxic event is the most documented of all the Cretaceous oceanic anoxic events occurring ~ 93.9 Ma and forms the latter anoxic event in the late cretaceous period (Jarvis et al, 2002). It is noted as a depletion event occurring nearly half a million years, causing the worldwide extinction of ~27% of all marine invertebrates. Boundary sediments within the English

chalk and Thetyan regions exhibit elevated $^{13}C_{org}$ values (Jarvis et al, 2002). In Hokkaido, this event is presumed to occur at the base of the Hakkin river section and middle Kotanbetsu section within the Saku formation Oyubari, represented by a $+^{13}C_{org}$ shift of 2.5‰ Takashima et al, (2010).

VI.3.3 Radiometric ages

Compared to similar aged counterparts such as the Western Interior Basin, catalogued ages for the North Pacific Hokkaido area are thinly spread. Datums within this area sourced from the volcanic felsic beds can easily be applied to integrated planktonic and formaminiferal biostatigraphy and developed carbon isotopes curves. Previous work has utilised the variety of suitable radiometric minerals such as zircons and sanidines to form a multi-disciplinary radiometric study of the area.

***Yezo Group (Quidelleur et al, 2011*)**

A total of seven felsic tuff horizons sourced from various formations within the Yezo group were sampled and analysed using U-Pb (ID-TIMS and LA-ICPMS) and $^{40}Ar/^{39}Ar$ dating techniques. Tuffs were chosen throughout the Cretaceous and those located at main stage boundaries were typically used.

Sample	Section	Formation	Boundary
TOM001	Horosari River	Kashima	Base Campanian
HKt003	Hakkin River	Saku	Base Turonian
HKt002	Hakkin River	Saku	Top Cenomanian
TNGt006	Tengunosawa Valley	Hikagenosawa	Base Cenomanian
SK069	Shumarinai River	Hikagenosawa	Base Cenomanian
TNGt005	Tengunosawa Valley	Hikagenosawa	Top Albian
TNG001.8	Tengunosawa Valley	Hikagenosawa	Upper Albian

Table. VI.1. Samples used within Quidelleur et al, (2011) study. Postions and formations for each are stated and used in Fig.VI.8.

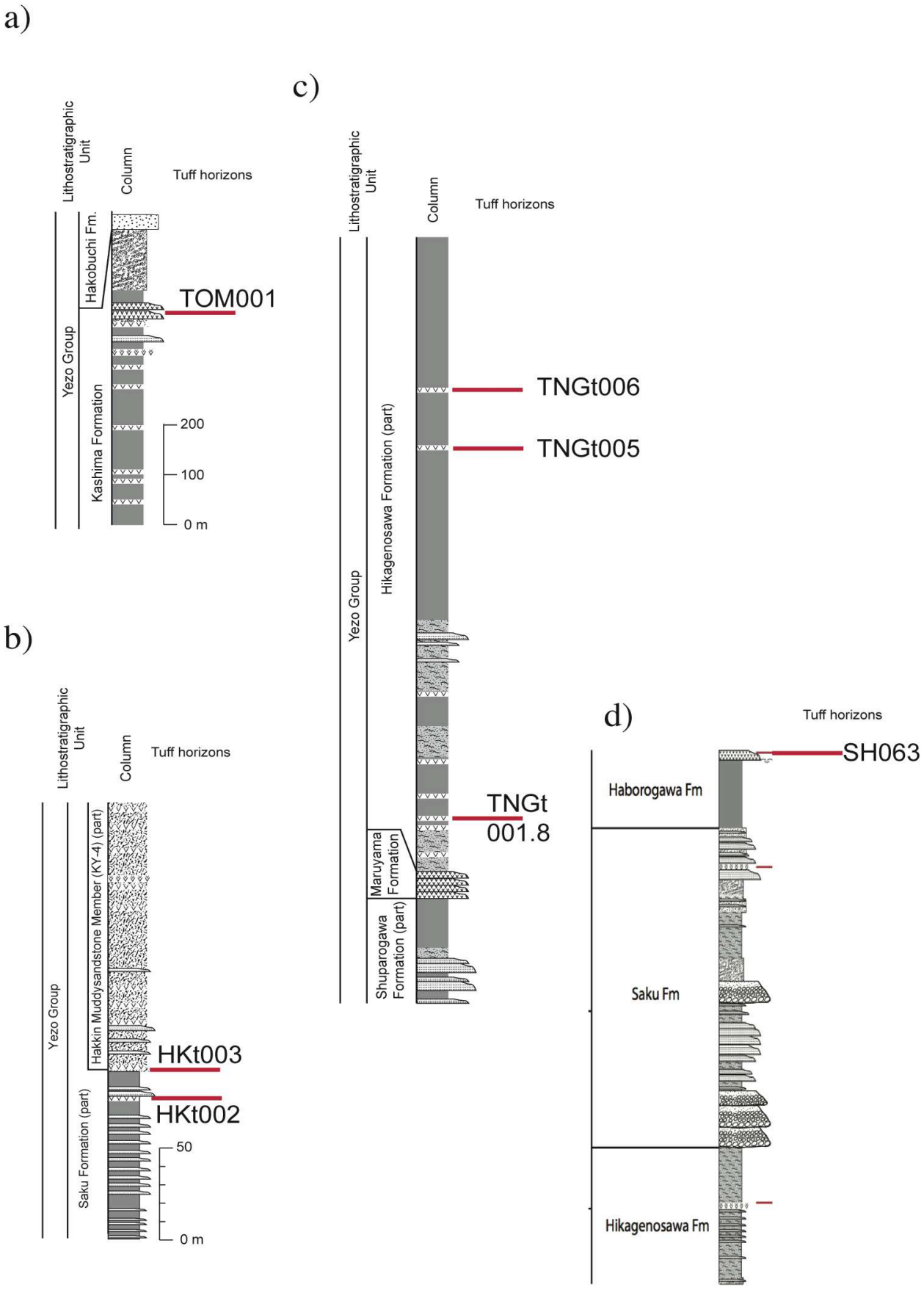

Fig. VI. 8. Biostratigraphy and position of dated tuff horizons (Quidelleur et al., 2011). (a) Tomichi section Hokkaido Japan. (b) Hakkin River section Hokkaido Japan. (c) Tengu section Hokkaido Japan (d) Shumarinai section, Hokkaido, Japan. Figure Taken from Quidelleur et al., 2011.

Hakkin river section: Two tuff samples located in the Hakkin river, Oyubari area. It spans the Cenomanian and Turonian boundary lying within the Saku Formation. Within this section the widely traceable key unit KY-4 is found.

Tengunosawa: Three samples within the Hikagenosawa stretching from the Upper Albian to the base of the Cenomanian (TNGt006, TNGt005 and TNGt001.8), they relate to various biochronological layers (Kawabe et al, 2003) such as *Thalmanninella globotruncanoides* (representing the base of the Cenomanian) and *Pseudothalmanninella subticinensis,* Upper albian (Nishi et al, 2003).

Shumarinai river: Sample SK069 exposed along the Shumariani River, its located at the occurrence of *M. Saxbii* and *Th. Globotruncanoides* relatable with samples dated by Obradovitch (1993) in the Western Interior Basin (Nishi et al, 2003).

Horosari River: The Tomiuchi tuff (TOM001) is located along the Horosari River bed, within the Kashima formation and correlates the traceable KY-6 sandstone unit relative to the *Globotruncana arca* foraminifera (Nishi et al, 2003).

Ages

Quidelleur et al. (2011)

Sample	Stage	ID-TIMS	LA-ICPMS	40Ar/39Ar	K/Ar
TOM001	Base Campanian	84.9±0.2		No Plateau	
HKt003	Base Turonian	94.3±0.3			
HKt002	Top Cenomanian		92.9±1.3		78.7±1.1
TNGt006	Base Cenomanian	97.0±04	98.0±2.1		85.2±1.2
SK069	Base Cenomanian	99.7±0.3		100.2±1.0	98.3±1.4
TNGt005	Top Albian		102.1±1.4		99.7±1.4
TNG001.8	Upper Albian			114.8±1.1	113.8±1.6

(Table.VI.2) Radiometric ages from the tuff localities Quidelleur et al. (2011)

Quidelleur et al. (2011) obtained an age of 84.9 ± 0.2 Ma for the base of the Campanian allowing an upper bound age for the Santonian-Campanian limit. Radiometric ages show good correlation between the chronometers and the U-Pb technique allowed identification that some of the K-Ar ages attained were altered by a thermal event through argon diffusion (Mark et al, 2008) allowing them to identify

reliable ages (Samples HKt002, TNGt006 and TNGT001.8). The sample SK069 yielded the most reliable datums for all three geochronometers, and five an age of 99.7 ± 0.3 Ma bracketed by the $^{40}Ar/^{39}Ar$ age of 100.2 ± 1.0 and 98.3 ± 1.4 Ma (Quidelleur et al, 2011).

Quidelleur et al. (2011), was able to constrain the Cenomanian-Turonian boundary limit as 94.3 ± 0.3 Ma from HKt003 just above the peak of the OAE2 ^{13}C horizon, bounded by an age of 93.0 ± 2.1 Ma slightly below the same formation HKt002 sample, within the 2nd phase of the OAE 2 ^{13}C excursion. The Albian Cenomanian limit was constrained for sample SK069 at the base o d the Cenomanian as 99.7 ± 0.3 Ma, with an upper Albian limit of 99.7 ± 1.3 Ma obtained from sample Tngt005.

Obradovitch et al. (2002)

Two $^{40}Ar/^{39}Ar$ ages were achieved from tuff deposits located in Central Hokkaido defining the Albian / Cenomanian boundary. Both tuff layers are located close to the Shumarinai river (Used in this study and that of Quidelleur et al, 2011) in both the Hotei-zawa and Kyoei-Sakin-zawa river. Using the defined planktonic foraminifera *Rotalipora globotrunanoides* as the position of the boundary, achieved ages of 98.98 ± 0.38 Ma and 99.16 ± 0.37 Ma place new constraints for this boundary.

These ages have allowed us to fully quantify some sections within the Yezo basin and will be discussed in detail within the next section. In our results we will document a similar methodology whereby we determine ages through sampled tuff horizons in the Kotanbetsu region. Both $^{40}Ar/^{39}Ar$ ages and U-Pb ages will be deduced and compared with previous ages attained in correlated horizons from the Carbon Isotope curved developed by Takashima et al, (2004).

VI.4 Sample Localities

A total of 10 different samples were extracted from the Yezo basin in a variety of locations (Fig.VI.9; Fig.V.10), covering the Lower and Upper Cretaceous. Here we propose to radiometrically date and calibrate these horizons to both the Cretaceous Timescale (GTS2012), carbon isotope curve (Takashima et al, 2010) and try to correlate the sections to the well defined North American counterparts. Previously discussed these various sample sections handle variable datable horizons, however, due to the shear length and continuity most samples will arise from the Kotanbetsu section.

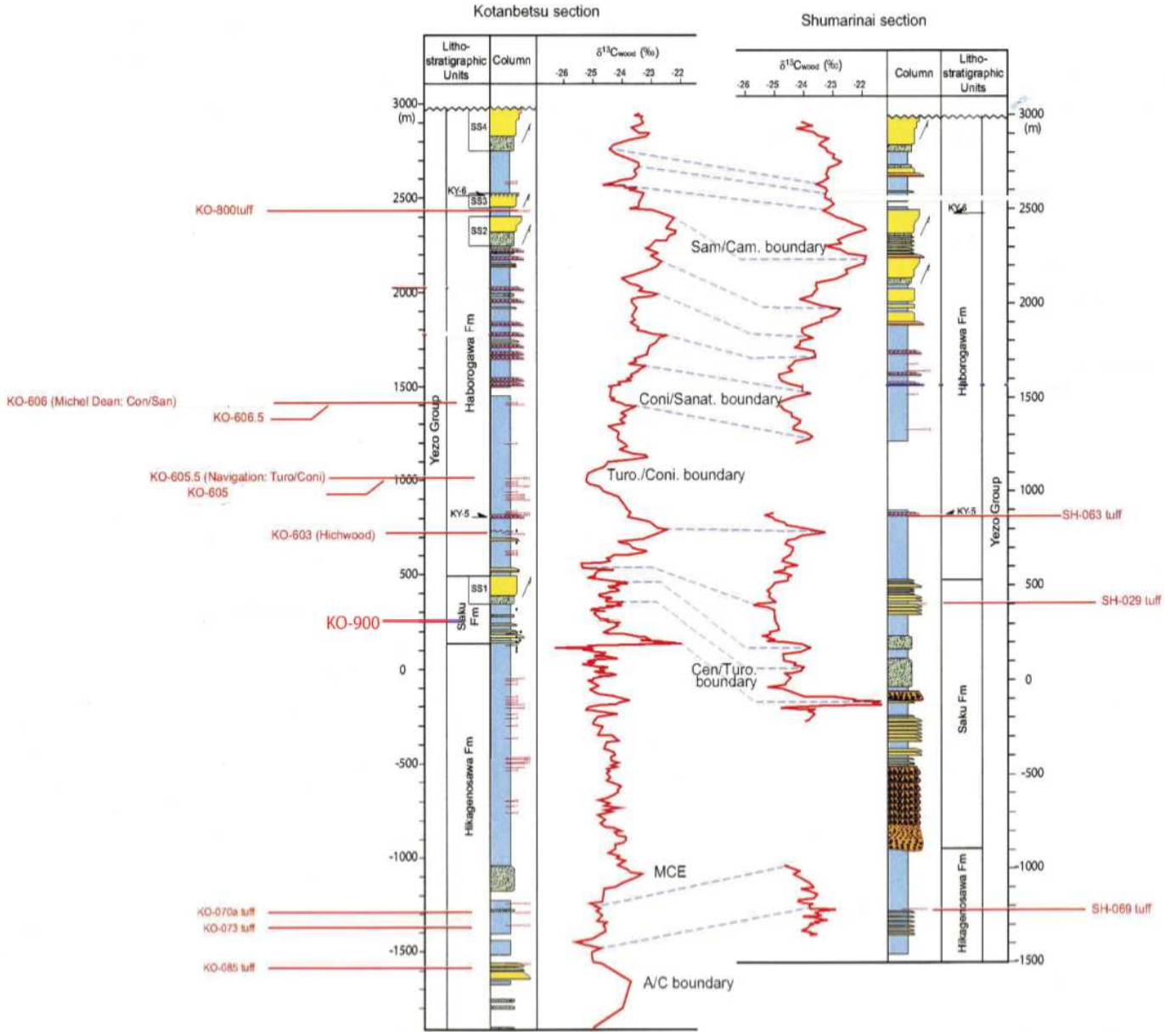

Fig.V1.9 Located within the Yezo Basin, Hokkaido, Japan this figure shows the combination of the Kotanbetsu Section alongside the Shumarinai river section. Each sample location is marked with the position relative to it's carbon isotope excursion (Takashima et al, 2010).

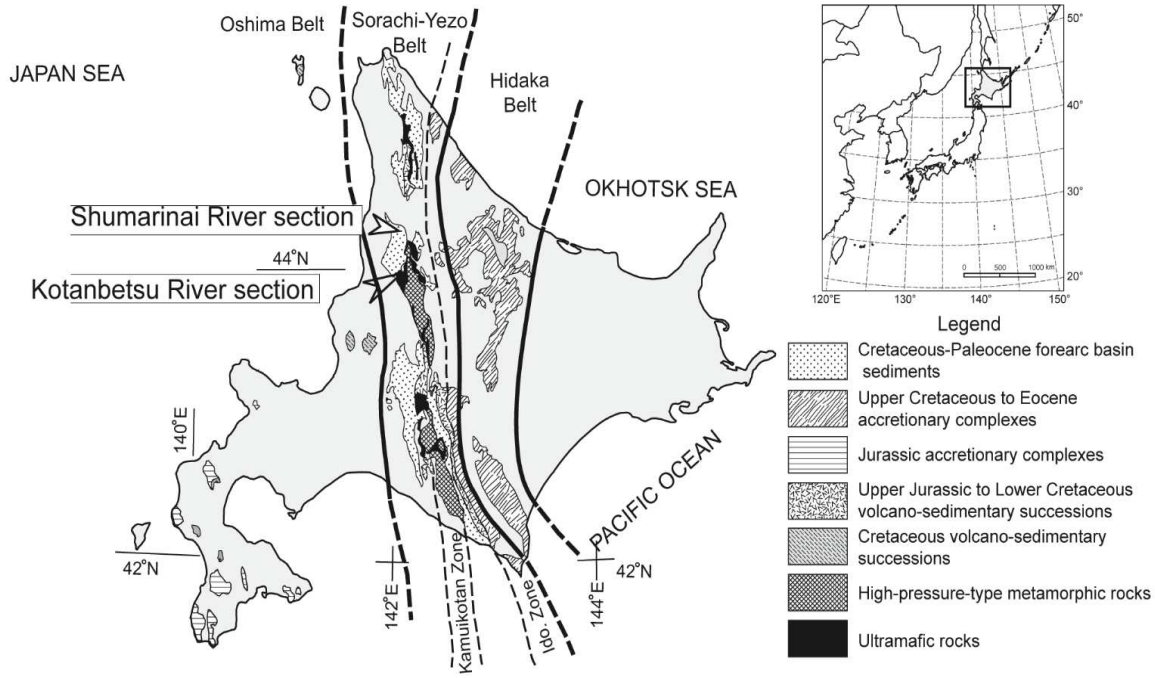

Fig.VI.10 Geological map and localities of sampled tuffs in the Shumarinai river section and Kotanbetsu river section, Hokkaido Japan.

Samples were collected and analysed on two main sections: the Kotanbetsu and Shumarinai sections. These are located in northern Hokkaido and exposed along river channels and contain much of the lithologies commonly associated with the Yezo group. The main Kotanbetsu river area is previously discussed earlier in this chapter, but should be noted that a total of 8 tuffaceous samples were analysed (Table VI. 3).

Shumarinai River site: This section is located in the North Tomamae area, N-NW Hokkaido (Fig.VI.10), and spans 3 main units of the Yezo supergroup: Haborogawa formation, the Saku formation and the Hikagenosawa formation (Fig.VI.9). Correlated by Takishmia et al, (2004; 2010) to the Kotanbetsu river section, it contains numerous key marker beds, such as the Sandstone SS# beds and has additionally been correlated using a carbon isotope curve against the Kotanbetsu section (Fig.VI.9), allowing rough stage boundaries to be assigned to the section. A total of two tuff horizons were sampled from this site and postions will be discussed later in this chapter (Table VI.3).

VI.5 Analytical Techniques

U-Pb Geochronology

Zircon Crystals were analysed from two well preserved tuff layers in the Kotanbetsu section, the first KO-605 (Turonian / Coniacian) located ~500m into the Haborogawa formation, the second KO-603 within the Turonian (Fig.VI.9). Whole zircon grains for sample KO-603 were separated in Japan, while zircons attained from KO-605 tuff were separated in Bern by the mineral separation technique involving whole rock crushing, followed by mineral density and Franz separation techniques. Whole zircon grains, fragments and tips of individual crystals were selected for high-precision U-Pb analyses. All grains were annealed and dissolved in two steps, following the chemical abrasion method (Mattinson. 2005). U/Pb isotope ratios were determined by ID-TIMS using a Thermo Fisher Triton+, equipped with a discrete-dynode MasCom electronic multiplier in ion-counting mode. All analyses were performed at the Institute of Geological Sciences at University of Bern, Switzerland. Total procedural Pb blanks range between 2.3 ± 0.8 and 0.50 ± 0.4 pg. Higher common Pb contents are attributed to an inherited component and corrected for using the common Pb composition from the two-stage model of Stacey and Kramers (1975). Mass fractionation factors in the electronic multiplier were constrained by using NBS982 for Pb and CRM-U500 for U. The tracer is enriched in ^{205}Pb and ^{235}U isotopes, and was calibrated using a certified gravimetrically mixed Pb-U solution (NBS982-IRMM056). Accuracy was performed by repeated analysis of the EARTHTIME 100, 500 and 2000 Ma synthetic solutions (Condon pers. comm.). All the U/Pb dates are reported with 2σ confidence levels. U/Pb isotopic data and dates are given in the supplementary data. All the age estimates plot on or near the Concordia line (Fig.VI 11a; 12a).

$^{206}Pb/^{238}U$ age estimates for single grains and grain tips for the two samples range from 89.31 ± 0.11 to 89.57 ± 0.11 Ma (2σ). The youngest population is interpreted to represent the time of deposition of the tuff as these crystals are considered to have the closest relationship to the time of eruption (e.g. Crowley et al, 2007). Furthermore, weighted mean statistics are useful to analyse if the distribution of ages within individual volcanic ashes is due to analytical uncertainties or dispersion in zircon

crystallisation. The mean square of weighted deviates (MSWD or reduced chi-square) is often used as a statistical test for the best fit of the calculated mean or regression line (e.g. Wendt and Carl, 1991). If MSWD is ~1, inhomogeneous samples will not contribute with additional scatter, meaning that the extent of the match between the observations and the estimates is purely analytical and thus in accord with the uncertainty variance.

KO-603 volcanic ash sample has 10 independent analysis (Fig.VI.11) yielding two separate populations and on older outlier (Fig.VI.11b). The youngest population has a mean age of 89.57 ± 0.11 Ma (MSWD 0.53) suggesting that the data are consistent with a null-hypothesis that all zircon grains crystallised synchronously. A second population clusters from age of 90.3 ± 0.11 Ma suggesting possibility of sub-million year recharge of the magma chamber. Zircon grain analyses obtained for the other sample, KO605 (Fig.VI.12) exhibits several populations (Fig.VI.12a) with the youngest defined as seven scattered zircon ages dated from the mean age of 89.31 ± 0.11 Ma with a MSWD value of 2.6 (Fig.VI.12c). This suggests possible errors outside of analytical uncertainty variance and that these zircons resided in the magma chamber and grew over a longer time period (antecrystic zircons).

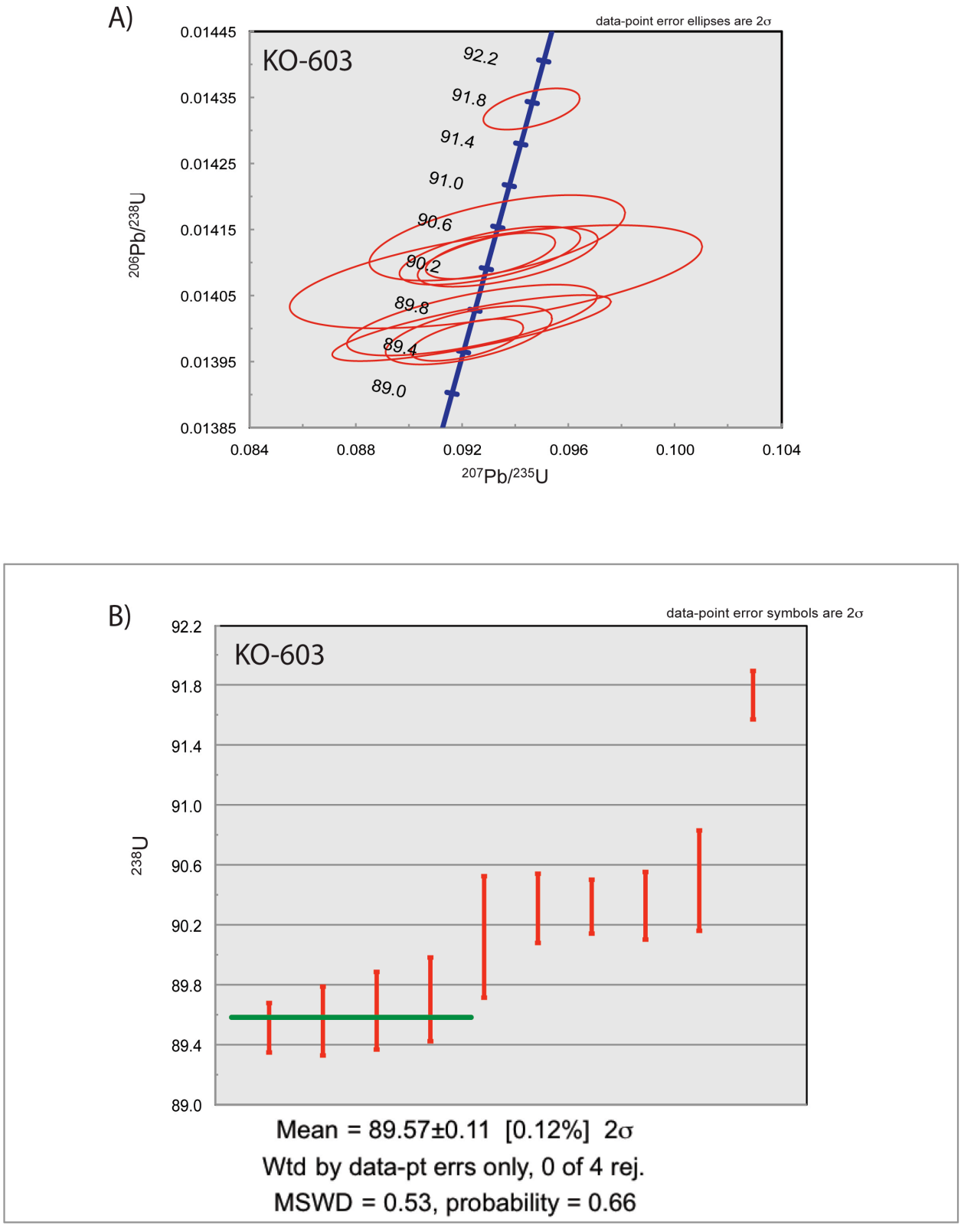

Fig.VI.11. Concordia diagram (a) and radiometric ages for each zircon (b) for Sample KO-603. Data point uncertainty ellipses and age uncertainties are given at the 2σ with decay constants included. Using the 4 youngest aged zircons we achieve a mean age of 89.57 ± 0.11 (2σ) MSWD 0.53.

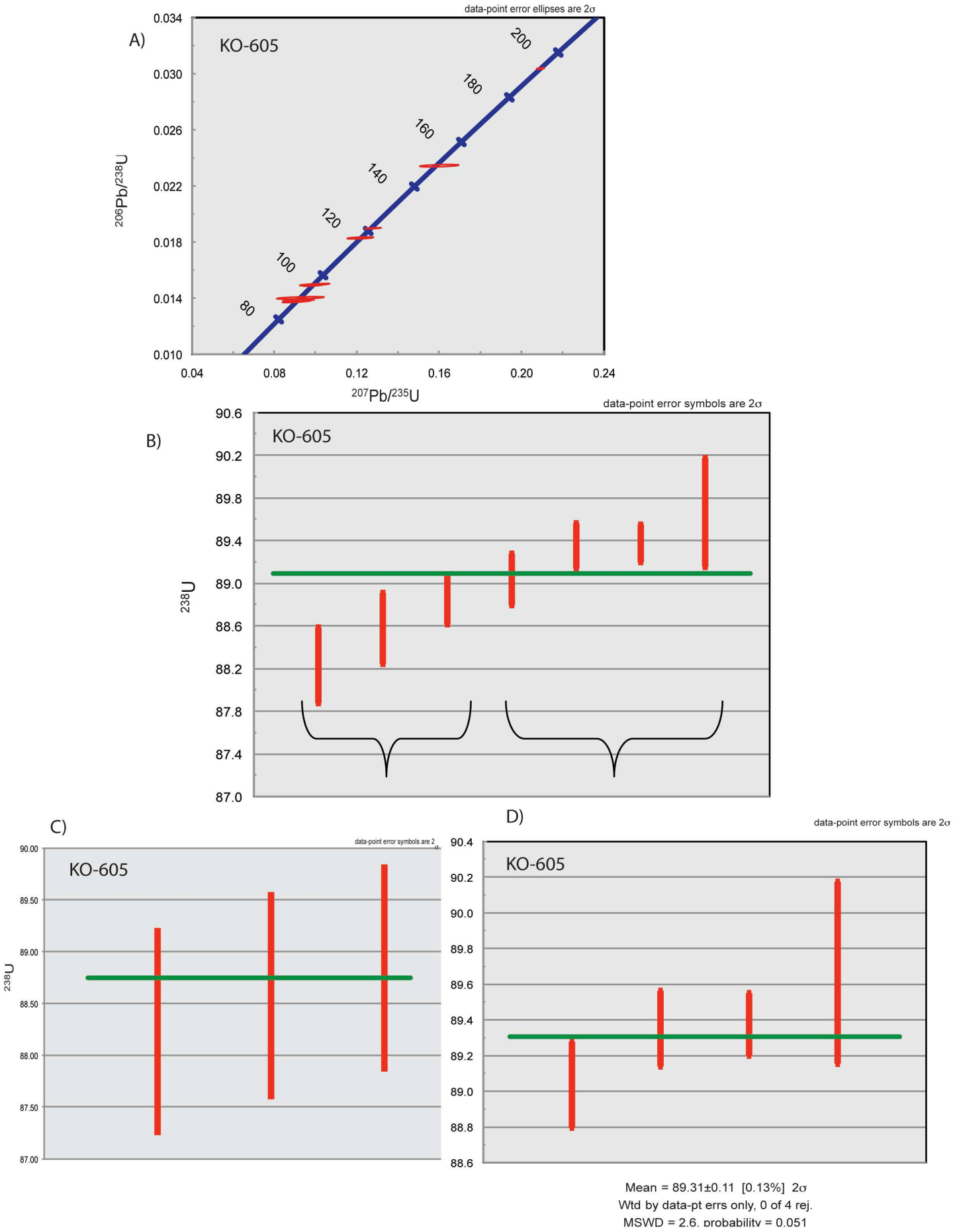

Fig.VI.12. Showing (A) Concordia diagram and radiometric ages for each zircon (B) , for Sample KO-605. Data point uncertainty ellipses and age uncertainties are given at the 2σ with decay constants included. Using the 4 reliable aged zircon in figure (D) we resolve an age of 89.31 ± 0.11 (2σ). With a MSWD of 2.6.

VI.5.2 $^{40}Ar/^{39}Ar$ Geochronology.

This technique has widely been adopted to both accurately date and detect any perturbations since emplacement. In total nine independent analysis from both the Kotanbetsu section and Shumarinai formation were performed. Samples were initially crushed and sieved into several size fractions. Following inspection, the crushed samples were washed ultrasonically with de-ionized water then separated using high density liquids (bromoform). Once in the density fractions, the samples were again cleaned by both water then using a 3 step acidic technique of HNO_{3conc}, followed by HF_{conc} then leached once more by HNO_{3conc}. About 0.2g of each sample was packaged into compact copper pellets and placed into 1cm vacuum sealed quartz tubes, tightly packed between two flux monitor samples for irradiation.

Samples were sent for irradiation in the cadmium shielded CLICIT facility of the Triga fast neutron reactor of the Oregon state university. Tubes were irradiated for 40 hours and flipped 180^{o} halfway during irradiation to reduce change in neutron flux across the Z-axis. J-factor determination was performed using 20mg aliquots of Fish Canyon Tuff sanidine (FCT), Taylor Creek Rhyolite sanidine (TCR). Measurements were completed on the $^{40}Ar/^{39}Ar$ multi-collector instrument developed in our laboratory and described in Coulié et al (2004).

Flux monitors were measured using total fusion and samples by step heating technique performed with a Nd-YAG infra-red laser and high frequency furnace respectively. The gas is first purified by 700^{o}C Ti foam followed by a getter and then transferred to an additional coal trap undergoing a second purification under an additional getter, before measured in the mass spectrometer. Unknowns were typically measured on average ~13 incremental steps set with the HF furnace and determined by the total argon released.

Mass discrimination was determined from a air pipette system, while blanks were determined on the same conditions as samples. Average $^{40}Ar/^{36}Ar$ atmospheric ratios of 304±1 were measured over the course of the two studies. Potassium interfering reactions were calculated using the values proposed by Renne et al. (1998): 7.0 x 10^{-4}, 1.2 x 10^{-2}, 7.2 x 10^{-4} and 2.68 x 10^{-4} for $[^{40}Ar/^{39}Ar]_K$, $[^{38}Ar/^{39}Ar]_K$, $[^{39}Ar/^{37}Ar]_{Ca}$ and $[^{36}Ar/^{37}Ar]_{Ca.}$ Age uncertainties and calculations follow McDougall and Harrison

$^{40}Ar/^{39}Ar$ Techniques, with ^{40}K decay constants and isotopic ratios of Steiger and Jager et al (1977). J-values were determined using the FCT and TCR ages of Kuiper et al. (2008) 28.201 ± 0.046 Ma and 28.53 ± 0.02 Ma respectively with a calculated J-Value uncertatinty of 0.44% from chapter II.

All samples were step-heated using an average of 12 temperature steps, results shown (Fig.VI.13-21) omitted any steps with low radiogenic $^{40}Ar^*$% additionally the primary and final steps were usually ignored in the final plateau ages due to low and high temperature abnormalities.

VI.5.3 Kotanbetsu section.

Six tuff layers were analysed within this section, including two samples in which a plateau could not be established (Fig 13.a;b). All samples show high radiogenic $^{40}Ar^*$ however exhibit a incremental upward age trend during ^{39}Ar releasel Individual step heating results are covered below. Samples KO-800, 605.5, 606.5 and 606 show constant increasing step ages suggesting that the sample experienced argon loss by diffusion (Mark et al, 2008), with three out of seven showing no attainable plateau age.

KO-900 – exhibits a strong saddle shaped spectrum (Fig.VI.13), offering higher ages on the low and high temperature steps could suggest the presence of excess argon whereby the ^{40}Ar is being held in two different lattice sites with contrasting thermal degassing behavior, and no reliable age spectrum can be derived. A plateau age, including 3 steps, of 106.1 ± 1.1 Ma can be defined for mid-temperature interval, but given the evidence for excess 40Ar* it should be considered only with caution.

KO-800 - Constantly increasing ages from 70Ma on low temperature steps up to an final age (Fig.VI.14) of around 90 Ma indicate that this sample exhibits signs of argon diffusion thus hindering determine a plateau age. Total gas age is determined as 83.92 ± 1.2 Ma, and can only be considered as a minimum value for this sample.

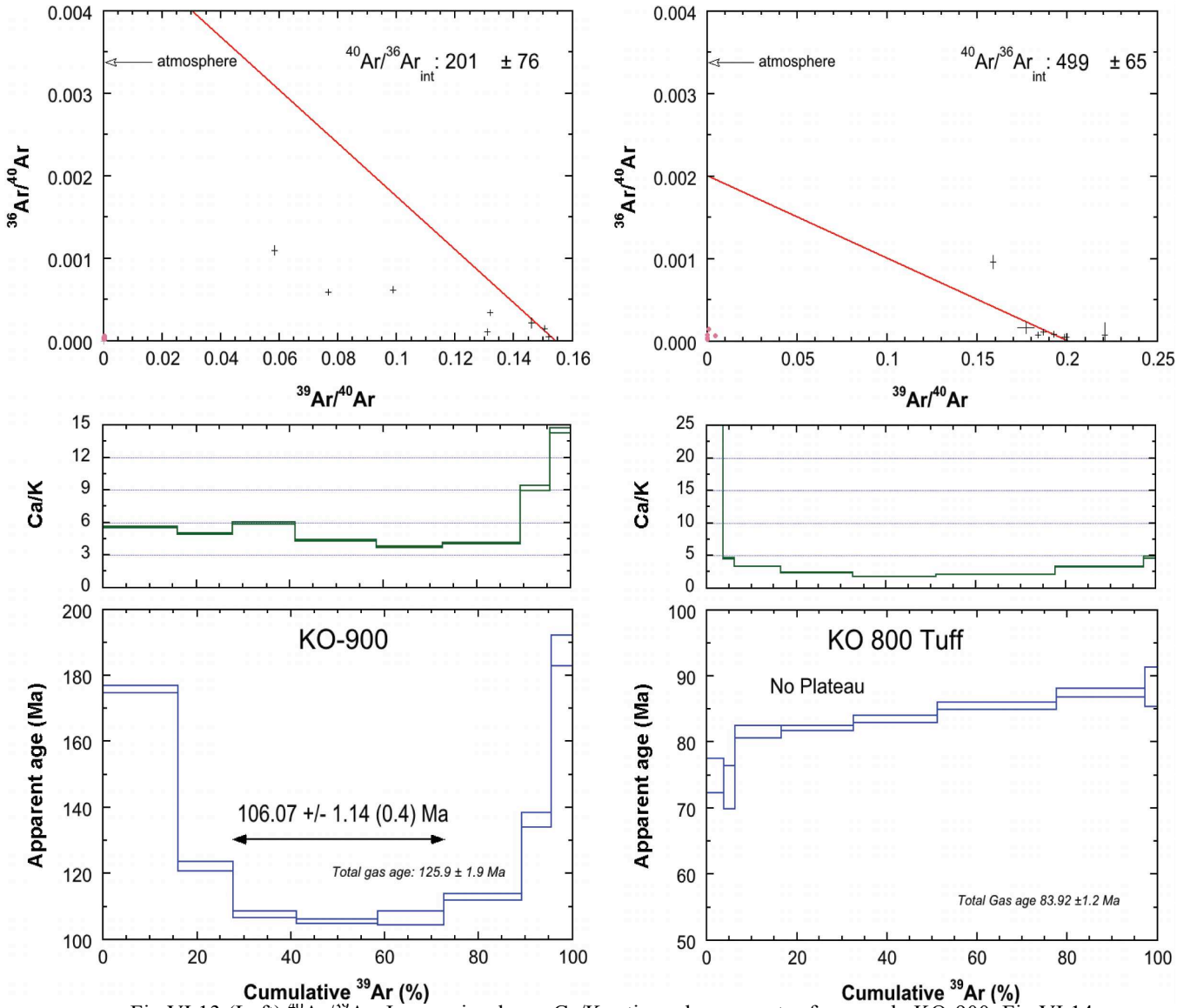

Fig.VI 13 (Left) $^{40}Ar/^{39}Ar$, Inverse isochron, Ca/K ratio and age spectra for sample KO-900. Fig.VI 14 (Right) $^{40}Ar/^{39}Ar$, Inverse isochron, Ca/K ratio and age spectra for sample KO 800 tuff.

KO-606.5 - This sample exhibits a two step spectrum whereby the first step averages is about 87 Ma, the second step utilising 40% of the total gas released displays an age of about 92 Ma. However, the age spectrum shows an increasing ages pattern suggesting that ^{40}Ar loss by diffusion was involved here.

KO-606 - Originating from the same tuff layer as KO-606.5, this sample shows again evidence of increasing ages throughout the step-heating process, with no possible defining plateau. $^{40}Ar/^{36}Ar$ ratios tend towards atmosphere however just fall under error. As KO-606.5 it shows a possible diffusion loss profile whereby this sample exhibits evidence of gas loss and excess argon. The relatively high Ca/K ratios suggest possibility of degassing from non-sanidine feldspars. Total gas age of 85.01 ± 1.47Ma falls within error of inferred ages, however this will be discussed in detail later.

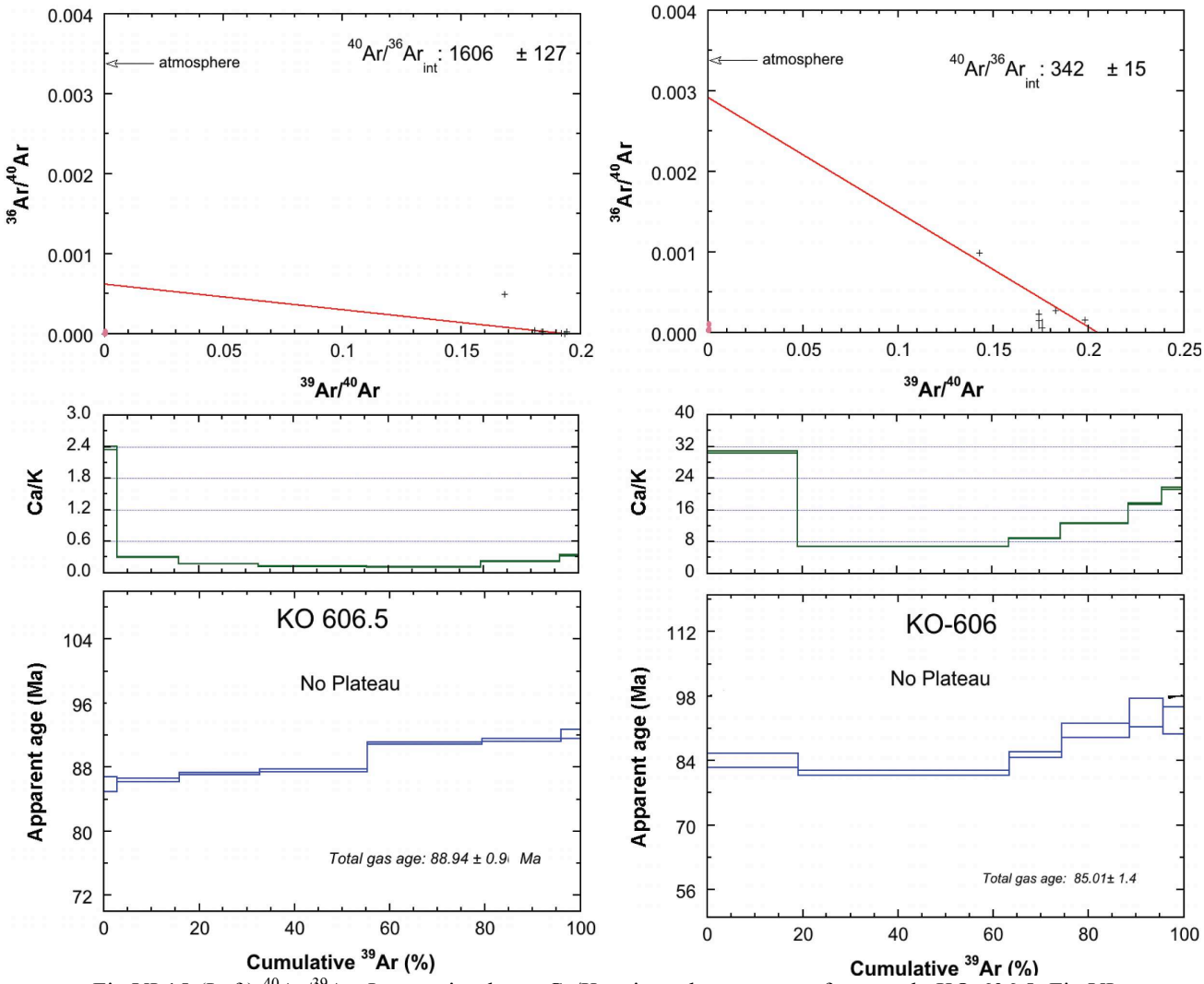

Fig.VI 15 (Left) $^{40}Ar/^{39}Ar$, Inverse isochron, Ca/K ratio and age spectra for sample KO-606.5. Fig.VI 16 (Right) $^{40}Ar/^{39}Ar$, Inverse isochron, Ca/K ratio and age spectra for sample KO-606 tuff.

KO-605.5 - This tuff sample was found within the Haborogawa formation and presumed to occur around the Turonian-Coniacian boundary. This sample again exhibits an upwards stepping trend (Fig.VI.17), however a 50% portion of ^{39}Ar released can be utilised to define an age of 87.95 ± 0.88 Ma. All individual steps utilized within the plateau age contain all $^{40}Ar^*$ over 90%. Inverse isochron trends towards atmosphere within error 324 ± 93. This sample will be discussed further combining the achieved U-Pb ages.

KO-073 - Analysed through seven different temperature steps, this sample exhibits a suitable plateau (utilising 4 out of the 7 possible steps, Fig. VI.18) relating to 70% of the total ^{39}Ar released. Mean plateau age is given as 92.6 ± 1.1 Ma, with total gas age of 94.3 ± 1.8 Ma. The first and last steps were not included in the final calculation, and should be noted that a slight increasing age tendancy is also present for this sample, suggesting ^{40}Ar loss effects. Inverse isochron trends positively towards atmospheric ratios and fall within error (332.5 ± 112).

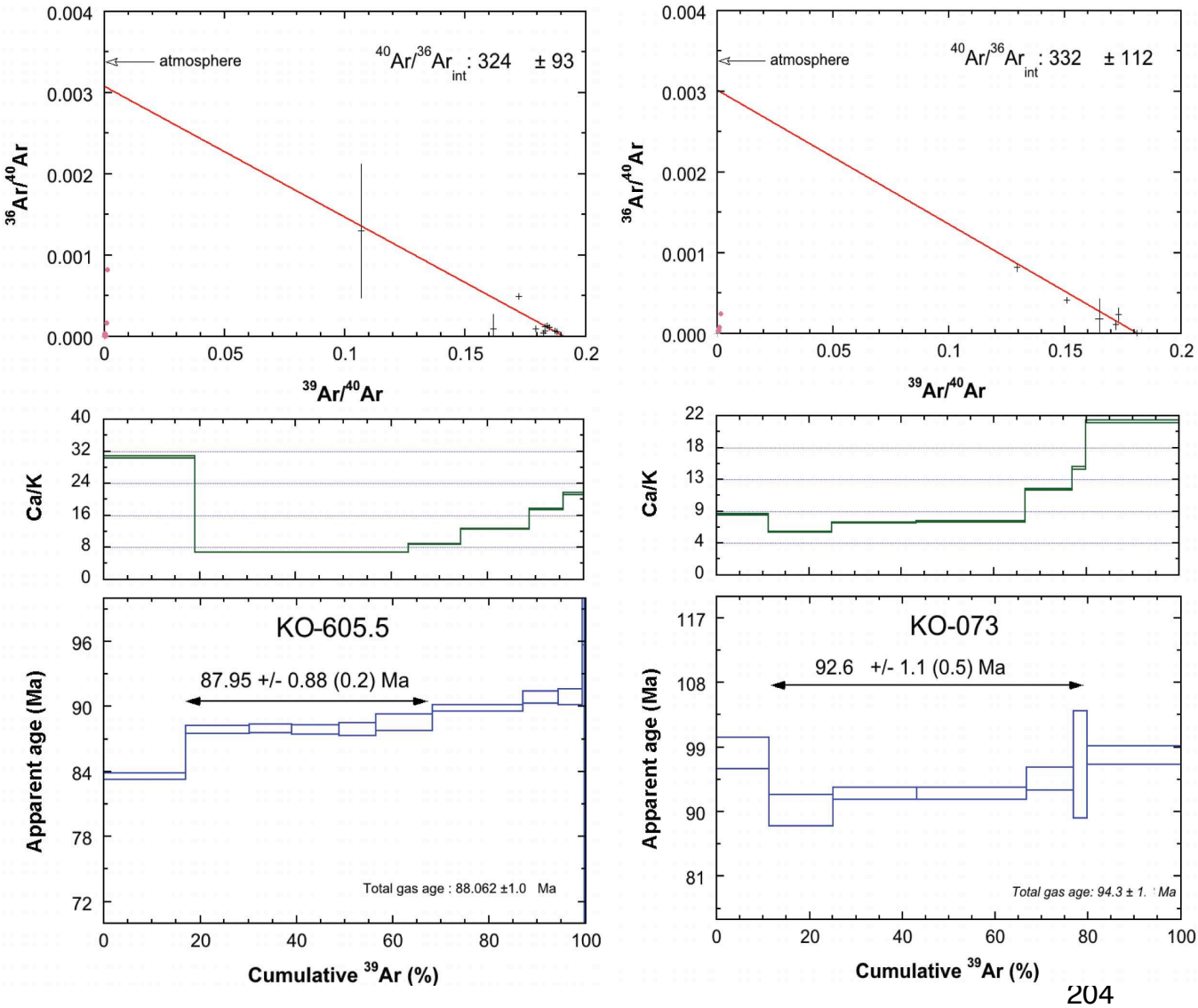

(Previous page) Fig.VI 17 (Left) $^{40}Ar/^{39}Ar$, Inverse isochron, Ca/K ratio and age spectra for sample KO-605.5. Fig.VI 18 (Right) $^{40}Ar/^{39}Ar$, Inverse isochron, Ca/K ratio and age spectra for sample KO-073 tuff.

KO-85 - Exhibits a complicated saw tooth spectrum (Fig.VI.19) which could be related to the decreptiation of fluid inclusions containing $^{40}Ar_{excess}$. In total 8 out of the plausible 15 steps carrying ~60% of the total ^{39}Ar released were chosen due to contributing factors such as $^{40}Ar^*$ values higher than 90%. A plateau age is given as 98.9 ± 1.1 Ma following a total gas age of 99.7 ± 1.6 Ma. Inverse isochron shows a trend towards atmosphere within error, although shows some evidence of possible excess argon.

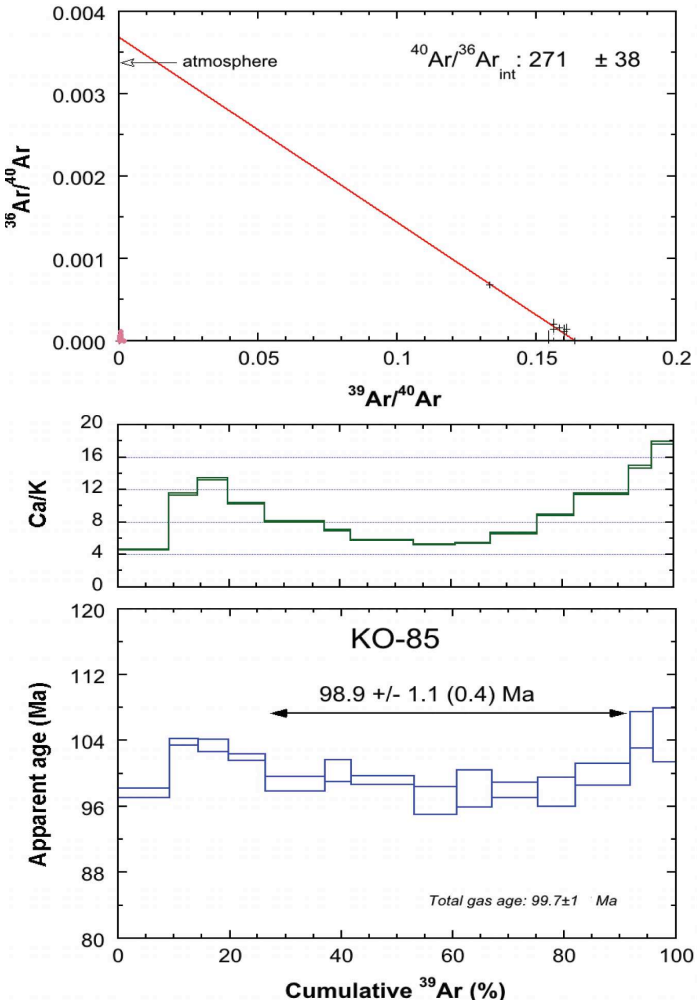

Fig.VI 19 (Left) $^{40}Ar/^{39}Ar$, Inverse isochron, Ca/K ratio and age spectra for sample KO-85.

VI.5.4 Shumarinai Section

Just two tuffs were sampled and analysed within this section and both exhibit signs of low $^{40}Ar^*$ levels, thus not as high as expected for Cretaceous sanidine crystals. Out of the two samples analysed only one plausible plateau age could be accounted for. The table and figures below correspond to the samples analysed in this section (Fig.VI.20-21)

SHO-029 – This age spectrum plateau exhibits a horseshoe trend (Fig.VI.20) typical of a the possibility of excess argon, however generally only the very low and high temperatures show this trend. The plateau chosen utilises 6 out of the possible 9 steps leading to an intepred age of 96.9 ± 1.0 Ma with a total gas age of 102.4 ± 1.9 Ma. All steps utilised cover about 75% of the total ^{39}Ar released in this sample and all correspond to a radiogenic $^{40}Ar^*$ value of at least 85%. Based on this sample is hypothesized to occur close to the Pewsey event horizon (90.5 Ma), however using our age of 96.9 ± 0.98 Ma we obtain a much older age than expected. Located towards the top of the Saku formation it should be presumed to be within the Middle Turonian, however with this attained age we would be within the early-middle Cenomanian, thus indicating that the age achieved would be erroneous.

SHO-063 - This sample shows a steep inclined spectrum starting around 160 Ma eventually reaching 245 Ma, far too old for the apparent age of sediments presumed to be Late Cretaceous. The spectrum exhibits (Fig.VI.21) clear indication of excess argon and therefore a reliable age cannot be determined. This sample will be treated as an anomaly and will not be used further within the discussion.

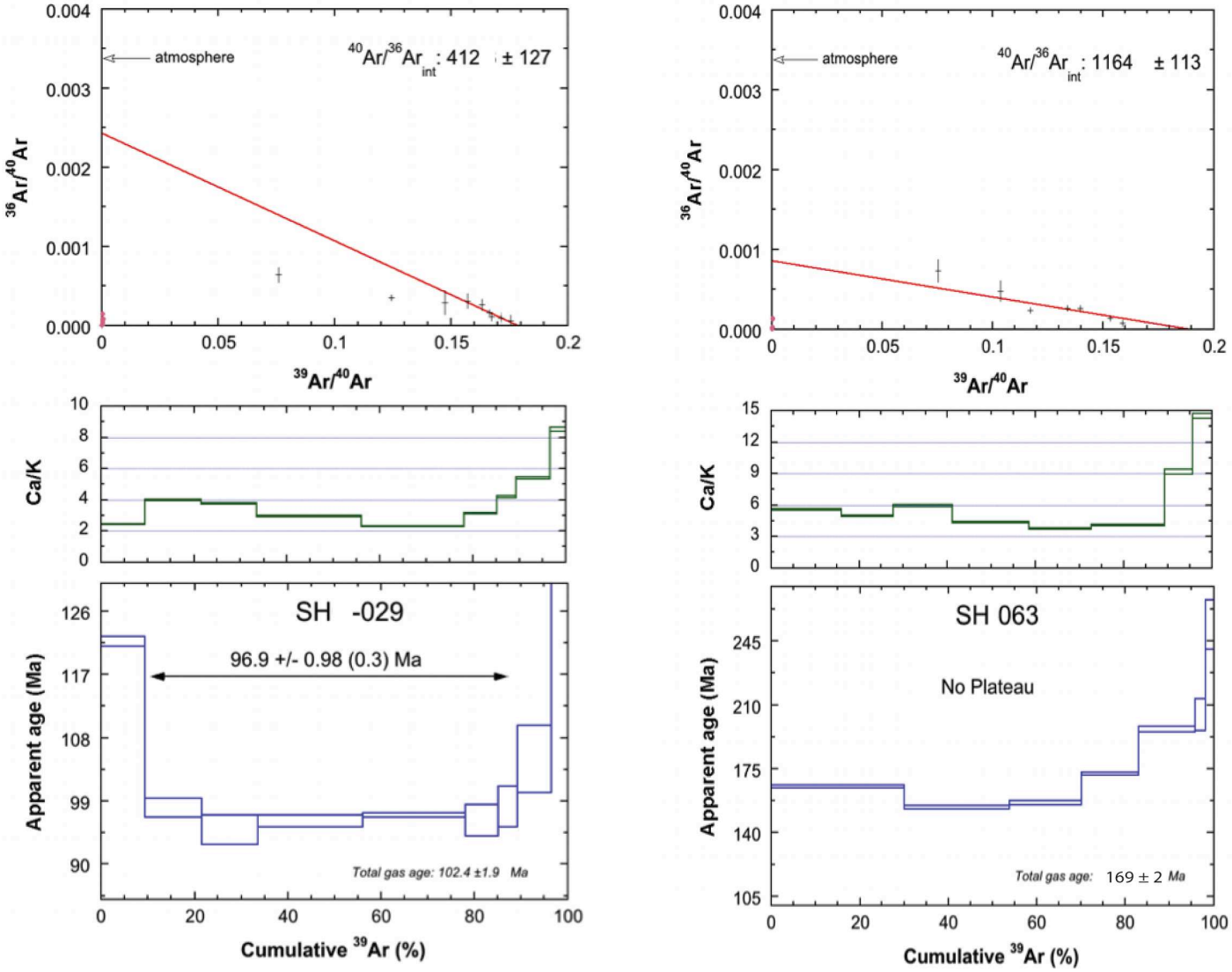

Fig.VI 20 (Left) $^{40}Ar/^{39}Ar$, Inverse isochron, Ca/K ratio and age spectra for sample SH029. Fig.VI 21 (Right) $^{40}Ar/^{39}Ar$, Inverse isochron, Ca/K ratio and age spectra for sample SH063 tuff.

VI.6 Discussion

Comparison on $^{40}Ar/^{39}Ar$ and U-Pb ages.

Due to difficulties in extracting suitable zircon grains from each tuff layer in the Kotanbetsu section, only one datable horizon can be compared with the $^{40}Ar/^{39}Ar$ ages achieved in this study. Additionally, all ages will be compared to that of the GTS2012 (Gradstein et al, 2012) boundary ages.

Kotanbetsu section,

The most studied of the two sections, the Kotanbetsu section spans 5 stage boundaries in which 7 tuffs were analysed. Table VI.3 shows the achieved age against the GTS2012 inferred ages attributed to the carbon isotope curve obtained for this section (Takashima et al, 2010).

Sample	Formation	Stage	Inferred age (GTS2012)	U-Pb Age (Ma)	Ar-Ar Plateau Age (Ma)	Total Gas age (Ma)
KO-800	Haborogawa	Campanian (KY-6)		-	No Plateau	83.92 ± 1.2
KO-606.5	Haborogawa	Coniacian-Santonian-	86.3 ± 0.5	-	No Plateau	88.94 ± 0.9
KO-606	Haborogawa	Coniacian-Santonian-	86.3 ± 0.5	-	No Plateau	85.01 ± 1.47
KO-605.5	Haborogawa	Turonian-Coniacian	89.8 ± 0.4	89.31 ± 0.11	88.0 ± 0.9	88.1 ± 1.1
KO-603	Haborogawa	Turonian-Coniacian	89.8 ± 0.4	89.57 ± 0.11	-	-
KO-073	Hikagenosawa	Albian-Cenomanian	100.5 ± 0.4	-	92.62 ± 1.1	94.3 ± 1.8
KO-85	Hikagenosawa	Albian-Cenomanian	100.5 ± 0.4	-	98.9 ± 1.1	99.7 ± 1.6
KO-900	Saku	Turonian		-	106.7 ± 1.14	125.9 ± 1.89

Table VI.3 showing the Sample localitly, type section and apparent age compared to measured ages from this study

From the base of the secion, $^{40}Ar/^{39}Ar$ plateau ages generally increase upwards, but remain younger than the inferred age (Table VI.3). Commonly, the $^{40}Ar/^{39}Ar$ ages yield much different datums than initially expected; regarding the KO-605.5 tuff layer

(jointly dated by both techniques), the $^{40}Ar/^{39}Ar$ technique obtains a slightly younger age than the U-Pb and can be attributed to residence time in the magma chamber causing older apparent U-Pb ages. Alternatively, since most samples are affected by argon loss to a variable extent, its more likely that the $^{40}Ar/^{39}Ar$ ages of KO-605.5 is rather slightly under-estimated. Notwithstanding, it can be noted that both U-Pb and $^{40}Ar/^{49}Ar$ ages overlap at the 2σ level. Given the high precision and accuracy of the former, only this age of 89.31 ± 0.11 Ma will be considered below for calibration of the Turonian-Coniacian boundary.

VI.6.2 The age of the Turonian-Coniacian boundary

The age of the Turonian-Coniacian (T-C) is defined as the lowest occurrence of the *Cremnoceramus rotundatus* inoceramid bivalve and assumed as the equivalent to the base of the *Scaphites preventricous* ammonite zone of the western interior basin, scaled by cycle statigraphy. High resolution integrated wood carbon isotope stratigraphy (Takashima et al, 2010) correlates the Navigation isotopic event to the inoceramid stratigraphy whereby the *Inoceramus uwajimensis*, references the Coniacian base. The Navigation event (Corresponding to a negative shift in $\delta 13C_{wood}$) excursion in the Kotanbetsu section correlates well against the Contessa section (Stoll & Schrag, 2000), Salzgitter-Salder (Voight & Hilbrecht, 1997) and the English Chalk, UK (Jarvis et al, 2006). GTS2012 ages for this boundary places it at 89.8 ± 0.4 Ma (Gradstein et al, 2012). In this study our U-Pb youngest zircon ages of 89.31 ± 0.11 Ma, obtained for sample KO-605 (Fig.VI.12 and Fig.VI.3) fall within error of the younger boundary age proposed in the GTS2012 published ages.

Sample KO-603 correlates to the Hitchwood isotopic event noted to occur in the Late Turonian, just before the Turonian-Coniacian boundary (Fig.VI.11). This horizon has been well constrained with reference alongside worldwide carbon isotope curves (Takashima et al, 2010) and occurs on the late Turonian boundary. We obtained a well constrained U-Pb age from the youngest population of zircons of 89.57 ± 0.11 Ma and straigraphically should fall older than the T-C boundary age of 89.8 ± 0.4 Ma, which is verified when uncertainties are accounted for. In addition, this age is older

that obtained for the above KO-605.5 Tuff (Table VI.3), however still falls within error.

Utilising the two U/Pb ages for these ash layers, we can constrain the age of the boundary to fall between these two ages (Fig.VI.22). Assuming that the Navigation excursion event occurred just before the Coniacian and the Hitchwood within the Late Turonian (Takashima et al, 2010) then the boundary is to be located between these two ages. Using the maximum age errors used for each ash layer we can assume therefore that the age of this boundary falls between the ages of 89.21 - 89.67 Ma and constraining the age of the boundary further to 89.44 ± 0.24 Ma by using the maximum and minimum age, both falling within the upper limits of the GTS2012 boundary age and reducing the C-T boundary age uncertainty to only 0.24 Ma. Note that since both U/Pb ages do not overlap within uncertainties no weighted mean can be calculated.

Siewert et al. (2011) integrated astrochronology with both $^{40}Ar/^{39}Ar$ and U-Pb of the orbitally forced rhythmic strata of the Niobrara formation near Pueblo, Colorado. Combining the results they obtained an age for the Turonian-Coniacian boundary as 89.68 ± 0.12/0.32 Ma with all total radioisotopic, astrochronologic and geological uncertainties involved. The age associated in Siewert et al. (2011) for this boundary falls within error of our calculated ages (Fig.VI.22), therefore we can utilise our previous age range again to reduce the age constraint for the boundary. We can therefore define the boundary for the Turonian-Coniacian boundary to be between 89.56 Ma but before 89.68 Ma, thus leading to the boundary age of 89.62 ± 0.04 Ma thus in the upper half of the proposed Siewert et al. (2011) age.

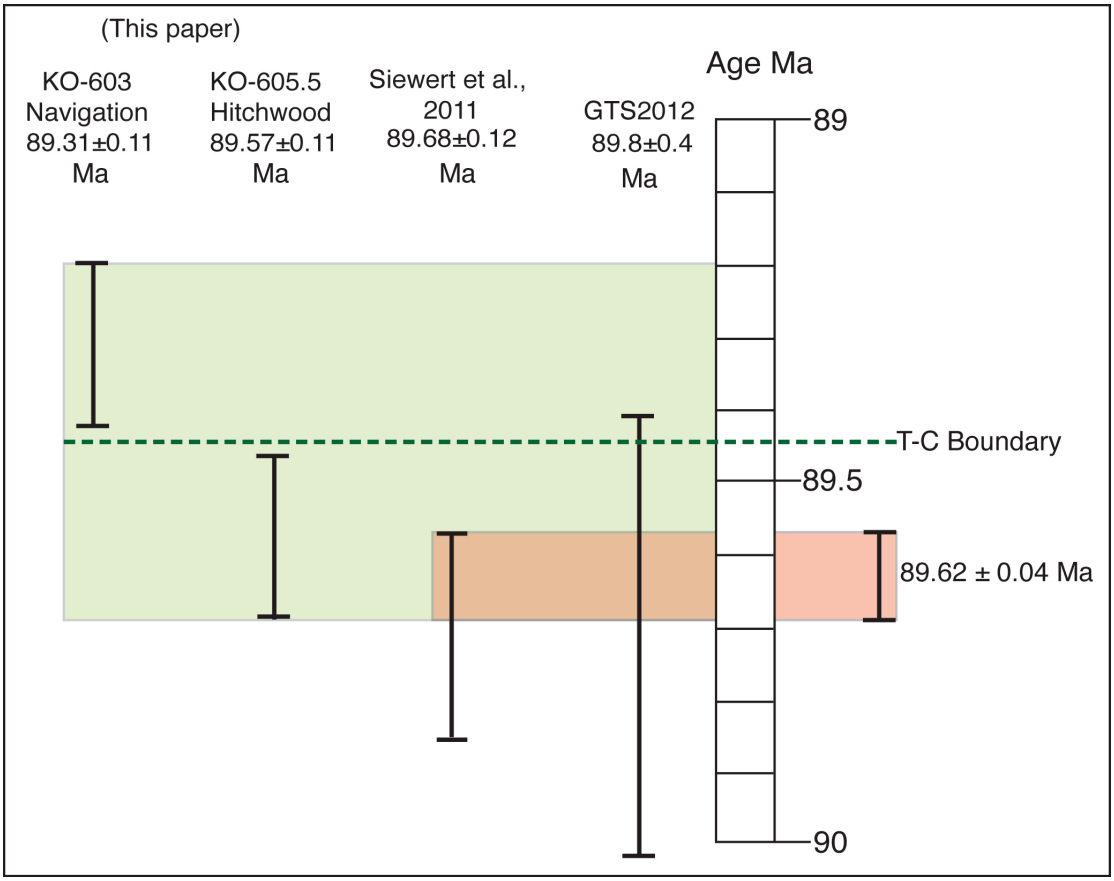

Fig.VI.22 Schematic ages attained from this study compared to the age associated with GTS2012 and Siewert et al (2011). The green box represents the age range for the T-C boundary from this study (89.44 ± 0.24 Ma) while the red box indicates the age using the published boundary age propsed by Siewert et al. (2011). Using this we achieve an age for the T-C as 89.62 ± 0.04 Ma, falling within error to the T-C boundary age published in GTS 2012 (Gradstein et al, 2012).

Albian Cenomanian boundary

Relatively little data is published within the Kotanbetsu section for this timeframe, and no carbon isotope curve is currently available that extends towards the lower half of the Hikagenosawa formation. However, two individual tuff layers were analysed (KO-073, KO-85) by $^{40}Ar/^{39}Ar$ step heating techniques and we can deduce where the position of the boundary could be located.

The Albian-Cenomanian boundary is calculated as 100.5 ± 0.4 Ma (GTS2012) and is the result from the combination of two dated horizons located at the top of the Albian in the Western Interior seaway alongside a spline fit astronomical tuning of Gale et al. (1995), with a GSSP located 0.25 Myr below the base of the N. *carcitanense* subzone relating to the *Mantelliceras mantelli* Zone. The correlation to the WIB and Japanese

sections is determined as the *Mantellicera mantelli* zone dated using ID-TIMS and LA-ICPMS U-Pb techniques as 99.7 ± 0.3 and 99.7 ± 1.3 Ma. Using the ash bed located in the Tengu section Japan, Quidelleur et al. (2011), was able to quantify and correlate the age. Therefore using this, we can locate the rough approximation of the Albian-Cenomanian boundary within the Kotanbetsu section.

$^{40}Ar/^{36}Ar$ step heating techniques show two plausible age plateaus of 92.62 ± 1.1 Ma and 98.9 ± 1.1 Ma for KO-073 and KO-85 respectively. Utilising the age of GTS2012 (Gradstien et al, 2012) we fall outside error and assume that the boundary is below the KO-85 tuff horizon. However, comparing recently acquired ages from Quidelleur et al. (2011) in the nearby sections (Hokkaido, Japan) of 99.7 ± 1.3 Ma we fall in agreement. Therefore, the boundary of the Albian-Cenomanian must be located close to the lowest samples ash (KO-85) in the Kotanbetsu section, rather than near the KO-073 tuff horizon as proposed by Takishima et al, (2010).

VI.7 Conclusion

We have been able to successfully obtain and apply new $^{40}Ar/^{39}Ar$ and U-Pb ages towards the Kotanbetsu section, Hokkaido, (Japan) within the Yezo basin. However, due to the positions of the tuff layers and references for certain stage boundaries we have not been able to independently date stage boundaries, thus only able to acquire ages for certain isotopic events, useful for the continuation of collaboration of the Yezo basin with it's global counterparts. Future work on the Kotanbetsu section will hopefully yield some biostratigraphic data towards the Albian-Cenomanian boundary allowing us to both correlate with other Japanese and global sections.

Using our approach we can deduce that the Turonian – Coniacian boundary recorded in the GTS2012 timescale and ages acquired from both this study (samples KO603 and KO605.5) and Siewert et al, (2011) are within error, moreover, we have been able to succesfully calibrate this boundary age, suggesting an age of 89.62 ± 0.04 Ma, greatly reducing both the age range and uncertainity to previously published ages. Once again these suitable bondary ages continue to endorse the carbon isotope curve correlations published by Takishama et al. (2010).

The majority of our $^{40}Ar/^{39}Ar$ age spectra show strong evidence of excess argon and demonstrate that our samples experienced reheating. Additionally, $^{40}Ar/^{39}Ar$ age spectrums achieved from Obradovitch et al. (2002) and Quidelleur et al. (2011) also prove difficulties in dating these Japanese sections using this method. The limitations within the $^{40}Ar/^{39}Ar$ dating method such as the J-Value determination and debatable ages for flux monitors (Kuiper et al, 2008; Renne et al, 2010) keeps the total uncertainties associated with this technique still relatively large ~1%, therefore when dealing with such small time variations and the need to differentiate between two events such as the Hichwood and Navigation isotopic excursion events, we need data points that do not overlap, to determine plausible reliable ages The resulting ages acquired and used in this study are dependant on the low uncertainties associated with U-Pb ages, demonstrating that the U-Pb dating techniques are the dominant technique for calibrating the Cretaceous timescale.

VII Conclusions

Conclusion

The newly revised geologic time scale (GTS2012, Gradstein et al, 2012) incorporates the most current work of timescale calibration, both small and large increases from ages proposed in GTS2004 highlights improvements in timescale calibration work such as enhancements in radiometric dating technique such as the age of the fluence monitor standard.

Derived Cretaceous boundary ages relied heavily on a correct biostratigrapic interpretation from the European to the North American Sections (Obradovitch, 1993), alongside spline fit ages attached with assumptions in constant spreading ridge rates of the M1 Hawaii ridge. Advancements in biostratigraphy and radiometric technique has allowed this improvement on the Upper Cretaceous but still hinders the Lower Cretaceous boundary ages.

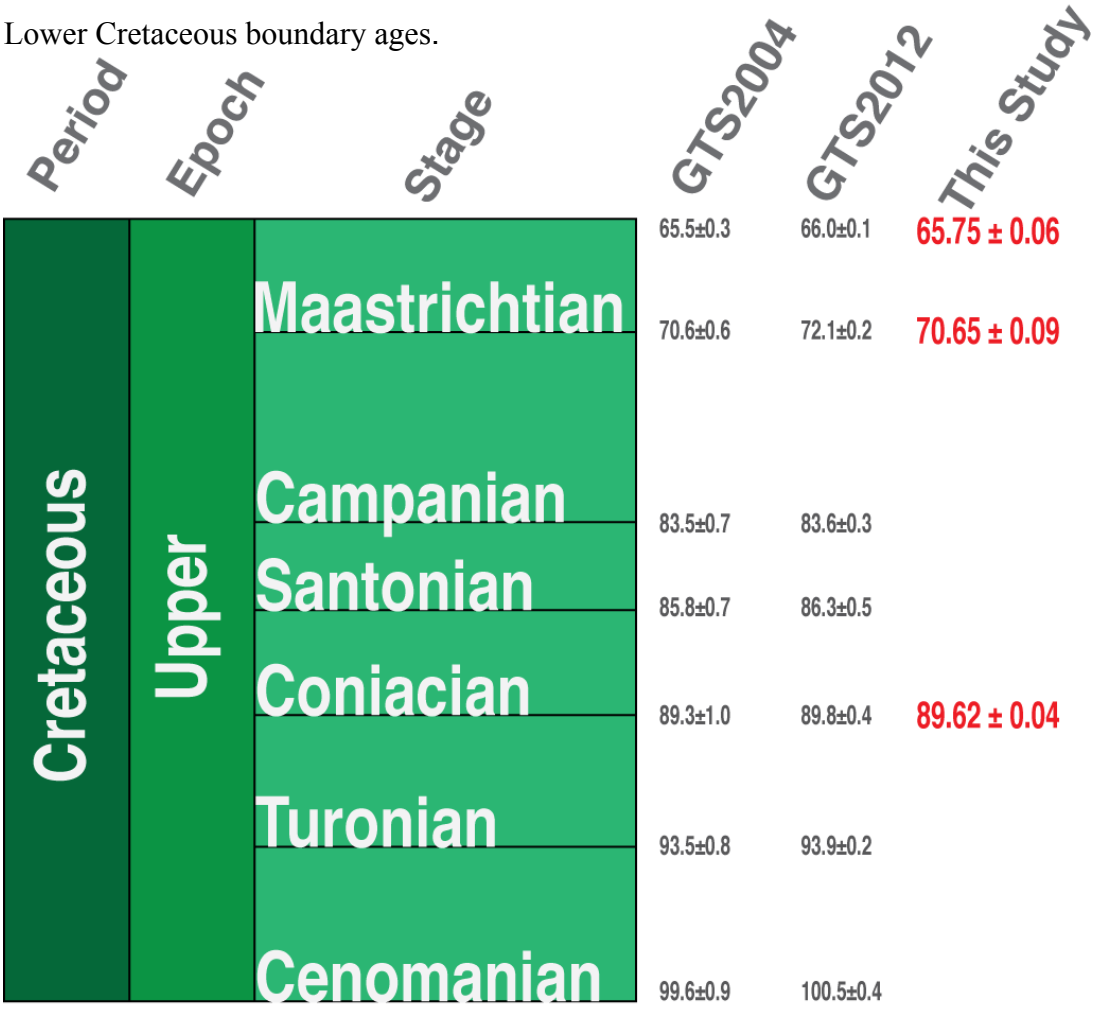

Fig.VII.1 Newly constrained boundary ages from this project alongised GTS2012 and GTS2004 boundary ages

Newly defined ages

Ages calculated in this project (Fig.VII.1) have been continually compared to the most recent published GTS2012 time scale, utilising these ages we observe 3 plausible boundary ages, all independently differ to those proposed in GTS2012.

K/Pg

Our K/Pg age is derived from a multitude of geochronological techniques, and successful stratigraphic interpretations in the Red Deer River section (Alberta, Canada) achieving an age of 65.75 ± 0.06 Ma. We were able to cyclostratigraphically tune sediments in a non-marine, fluvial environment utilising high resolution proxy records suggesting a 11-12 precession related cyclicity form the base of C29r using a period of 21Ka. This age is not consistent with the ages published in GTS2012 and the revised Renne et al. (2013) age of 66.043 ± 0.011 Ma, using this age we can deduce an age of the C29r of 65.988 ± 0.31 Ma. Assuming the $^{40}Ar/^{39}Ar$ is inter-calibrated with the cyclostratigraphy, the apparent age for C29r deduced by Husson et al. (2011) suggests that the K/Pg boundary falls between eccentricity maxima and minima yielding an age of the C29r between 65.89 ± 0.08 and 66.30 ± 0.08 Ma. To improve our achieved age we suggest a revised palaeomagnetic constraint within the Red Deer section.

Campanian Maastrichtian.

Our work suggests that the boundary previously placed in the Morrin Bridge section is inaccurate with regards to the position associated by Eberth. (2011) and Lerbekmo et al. (2005). Difficulties in the boundary definition coupled with complexities in the magnetostratigraphy and bio-stratigraphy has hampered the placement in western Canada. Compared with the Knudsens's farm section (K/Pg) we were unable to fully quantify a reliable magnetostratigraphy as we obtained a strong overprint on each sample, however we are able to see small cyclostratigraphic stacking of short eccentricity cycles with some evidence of precession controlled horizons. The age estimate of this boundary is given as 70.65 ± 0.09 Ma and falls outside estimation propose by Voigt et al. (2012) and Husson et al. (2011) thus producing an ~1.4Myr younger age. This highlights the need for possible improvements in the bio-

stratigraphic and magnetostratigraphic interpretation for the Red deer section and rather than define a new boundary age these ages presented can constitute important ages constraints in Western Canada

Turonian-Coniacian ages.

The global correlation of the Cretaceous period has successfully been implemented using a variety of bio-stratigraphic and geochemical methods. Carbon isotope curve developed by Nishi et al. (2004) Takashima et al. (2010) has allowed us to correlate suitable horizons in the Northwest Pacific. However ash tuff ages in the Kotanbetsu river section (Hokkaido, Japan) have proven difficult to ascertain. $^{40}Ar/^{39}Ar$ step heating spectra constantly exhibit strong evidence of excess argon with only few suitable age spectra usable. Similarly zircons were difficult to extract and analyse yielding unsuitable minerals for the U-Pb radiometric dating method. However we successfully dated two ash tuff layers falling either side of the Turonian-Coniacian boundary, yielding an age range for the boundary between 89.31 ± 0.11 Ma - 89.57 ± 0.11 Ma or a boundary age of 89.44 ± 0.24. This age falls within error of the proposed GTS2012 age of 89.8 ± 04 Ma. Additionally through improvements in the U-Pb dating method we can reduce the error associated with this boundary utlising the published age of Siewert et al. (2011) we can reduce again this age to 89.62 ± 0.04 Ma. This age coupled with the well constrained Carbon Isotope curve yield a very plausible datum for the proposed boundary and could be included in further geologic timescale work.

Cyclostratigraphy

In this study we have developed new cyclostratigraphic interpretations for strata in a non-marine fluvial environment, thus demonstrating astronomical forcing in an highly active environment. Using this method alongside radiometric ages we can help enhance the astronomical solution. Whereby the astronomical solution proposed by Laskar. (2003; 2011) is reliable up to ~100myrs, assuming that the eccentricity is the only stable cycle past this age, we can utilise radiometric data as a positive feedback approach to help enhance this method and help us ascertain the best fit astronomical solution, based on stratigraphic interpretations, and determine the stability of the solution past 100 Ma.

Throughout this study we have attempted to date numerous ash beds using the $^{40}Ar/^{39}Ar$ techniques, however we are often hampered by evidence of excess argon and relatively large uncertainties (compared with the U-Pb technique). Evidence from this study and previous published work (e.g. Quidelleur et al, 2011) has demonstrated that for Cretaceous timescale work, the U-Pb dating method still is the preferred calibrating tool for the Cretaceous timescale, although this study has also highlighted the power of the $^{40}Ar/^{39}Ar$ technique and the continued effort to quantify the uncertainties in this field.

Future work

Work by Eberth (in progress), is currently attempting to correlate WIB lithologies from Alberta on a larger basin wide scale by following bentonitic layers across basin wide boreholes using techniques such as gamma log tracing. By continuing to date these individual bentonite layers and swarms, we are helping to improve both the time domain but also the evolution and interpretation of the Western Interior Basin. High fidelity sequencing of strata is becoming a highly useful tool for industrial purposes, tracing age defined horizons alongside seismic surveys allowing a new high definition of understanding of the location of unconventionals and optimising new play concepts for better resource recovery. Improving ages in this area will continue help trace similar horizons into areas of study such as Wyoming, Saskatchewan and Montana, allowing for this mass understanding of strata to help produce an integrated stratigraphic framework model useful for both academic and industrial purposes.

VIII. Bibliography

A

Aguado, R., Company, M., Tavera, J.M. (2000) - The Berriasian/Valanginian boundary in the Mediterranean Region: New Data from the Caravaca and Cehegin Sections, SE Spain. Cretaceous Research 21, 1–21.

Albarede, F. (1995) - Introduction to Geochemical Modeling. Cambridge University Press, Cambridge, pp.543.

Aldrich, L.T and Nier A.O. (1948) - Argon 40 in Potassium Minerals. Phys. Rev. 74, 876-877.

Alexander, E.C., Mickelson G.M., Lanphere M.A. (1978) - MMhb-l: A new $^{40}Ar/^{39}Ar$ dating standard. U.S. Geol. Surv. Open-File Rept. 78-701.

Allan, J., Carr, J. (1945) - Geology and coal occurrences of Wapiti-Cutbank area, Alberta. Research Council of Alberta, Report, vol. 48. 50 pp.

Allen, P.A., Homewood, P., Williams, G.D. (1986) - Foreland basins: an introduction; in Foreland Basins, (ed.) P.A. Allen and P. Homewood. Int. Ass. Sed. Sp. Pub. 8, 3–12.

Alvarez, W., Arthur, M.A., Fischer, A.G., Lowrie, W., Napoleone, G., Premoli Silva., I, Roggenthen, W.M. (1977) - Upper Cretaceous-Paleocene magnetic stratigraphy at Gubbio, Italy. V. Type section for the Late Cretaceous-Paleocene geomagnetic reversal time scale. Geol. Soc. Am. Bull. 88, 383-389.

Alvarez, L.W., Alvarez, W., Asarao, F., Michel, H.V. (1980) - Extraterrestrial causes of the Cretaceous / Tertiary extinction. Science 208, 1095–1108.

Ando, H. (2003) - Shallow-marine sedimentary facies distribution and progradational sequences of the Mikasa Formation Middle Yezo Group (Upper Cretaceous). The Journal of the Geological Society of Japan 96, 453–469.

Arthur, M.A., Dean, W.E., Pratt, L.M. (1988) - Geochemical and climatic effects of increased marine organic carbon burial at the Cenomanian/Turonian boundary. Nature 335: 714–717.

B

Bachmann, O., Dungan, M.A., Lipman, P.W. (2000) - Voluminous lava like precursor to a major ash-flow tuff low column pyroclastic eruption of the Pagosa Peak Dacite, San Juan volcanic field, Colorado. Journal of Volcanology and Geothermal Research 98, 153-171

Bachmann, O., Dungan, M.A., Lipman, P.W. (2002) - The Fish Canyon magma body, San Juan volcanic field, Colorado: rejuvenation and eruption of an upper-crustal batholith. Journal of Petrology 43: 1469–503.

Bachmann, O., Oberli, F., Dungan, M.A., Meier, M., Mundil, R., Fischer, H. (2007) - Ar-^{40}Ar-^{39}Ar and U-Pb dating of the Fish Canyon magmatic system, San Juan Volcanic field, Colorado: evidence for an extended crystallization history. Chemical Geology, 236, 134-166.

Bahlburg, H., Dobrzinski, N. (2011) - A review of the Chemical Index of Alteration (CIA) and its application to the study of Neoproterozoic glacial deposits and climate transitions. In: Arnaud, E., Halverson, G.P. Shields-Program. The Geological Record of Neoproterozoic Glaciations. Geol. Soc. London, Memoir 36, 81-92.

Baksi, A.K., Archibald, D.A., Farrar, E. (1996) - Intercalibration of ^{40}Ar/^{39}Ar dating standards. Chem. Geol. 129, 307-324.

Barchi, P., Bonnemaison, M., Galbrun, B., Renard, M. (1997) – Tercis (Landes, Sud- Ouest France): point stratotypique global de la limite Campanien– Maastrichtien: resultats magnétostratigraphiques et premières données sur la nannoflore calcaire. Bull. Soc. Géol. Fr. 168, 133–142.

Barrera, E., Savin, S.M., Thomas, E., Jones, C.E. (1997) - Evidence for thermohaline-circulation reversals controlled by sea-level change in the latest Cretaceous. Geology, 25, 715–718.

Barrera, E., Savin, S.M. (1999) - Evolution of late Campanian–Maastrichtian marine climates and oceans. In: Barrera, Evolution of the Cretaceous Ocean-Climate System. Geol. Soc. Am. Sp. Pap. 332, Boulder, 245-282.

Bassinot, F.C., Laurent, D., Vincet, E., Quidelleur, X., Shackelton, N., Lancelot, Y (1994) - The astronomical theory of climate and the age of the Brunhes-Matuyama magnetic reversal. Earth and Planetary Science Letters 126 91-108.

Batenburg, S..J, Sprovieri, M., Gale, A.S., Hilgen, F.J., Hüsing, S., Laskar, J., Liebrand, D., Lirer, F., Orue- Etxebarria., X, Pelosi., N, Smit., J. (2012) - Cyclostratigraphy and astronomical tuning of the Late Maastrichtian at Zumaia (Basque country, Northern Spain). Earth Planet. Sc. Lett. 359-360, 264-278.

Beaumont, C., Quinlan, B., Hamilton, J. (1988) - Orogeny and stratigra- phy: Numerical models of the Paleozoic in the eastern interior of North America: Tectonics, 7, 389–416.

Beaumont, C., Quinlan, G.M., Stockmal, G.S. (1993) - The evolution of the Western Interior Basin: causes, consequences and unsolved problems. In Evolution of the Western Interior Basin. Edited by W.G.E. Caldwell and E.G. Kauffman. Geological Association of Canada, Special Paper 39, 97–117.

Beckinsale, R. D,. Gale, N.H. (1969) - A reappraisal of the decay constants and branching ratio of ^{40}K. Earth and Planetary Science Letters 6: 289–94.

Beerbower, J.R. (1964) - Cyclothems and cyclic deposition mechanisms in alluvial plain sedimentation. Kansas Geol. Surv. Bull. 169, 169.

Begemann, F., Ludwig, K.R., Lugmair, G.W., Min, K., Nyquist, L.E., Patchett, P.J., Renne, P.R., Shih, C-Y, Villa, I.M., Walker, R.J. (2001) - Call for an improved set of decay constants for geochronological use. Geochimica et Cosmochimica Acta 65: 111- 121.

Berger, A., Loutre, M.F. (1991) - Insolation values for the climate of the last 10 million years. Quaternary Sciences Review, Vol. 10.

Berger, A.L., Loutre, M.F., Laskar, J. (1992) - Stability of the astronomical frequencies over the Earth's history for paleoclimate studies. Science 255: 560–6.

Berggren, W.A., Hilgen, F.J., Langereis, C.G. (1995) - Late Neogene (Pliocene–Pleistocene) chronology: new perspectives in high-resolution stratigraphy. Geological Society of America Bulletin, 107: 1272–87.

Blanc, E., Bulot, L.G., Paicheler, J.C. (1994) - La coupe de reference de Monbrun-les-Bains (Drome, SE France): Un stratotype potentiel pour la limite Berriasien-Valanginien. Comptes rendus de l'Acade´mie des Sciences, Paris, Serie II. Sciences de la Terre et des Planetes 318: 101–8.

Bourrouilh, R., Richert, J.P., Zolnai, G. (1995) - The North Pyrenean Aquitaine Basin, France evolution and hydrocarbons. AAPG Bull.79, 831-853

Burnett, D.S., Lippolt, H.J., Wasserburg, G.J. (1966) - The relative isotopic abundance of ^{40}K in terrestrial and meteoritic samples. J. Geophys. Res. 71, 1249-1269.

Bralower, T.J., Premoli Silva, I., Malone, M.J., and the Shipboard Scientific Party. (2002) - Site 1210B. Proceedings of the Ocean Drilling Program, Initial Reports 198, 1–89.

Brinkman, D. (2003) - A review of non-marine turtles from the Late Cretaceous of Alberta. Canadian Journal of Earth Sciences 40, 557–571.

C

Caldwell, W.G.E,. Kauffman, E.G. (1993) - Evolution of the Western Interior Basin. Geological Association of Canada, Special Paper 39,.

Cande, S.C,. Kent, D.V. (1992) - A new geomagnetic polarity time scale for the Late Cretaceous and Cenozoic. Journal of Geophysical Research 97: 13 917–51.

Cande, S.C,. Kent, D.V. (1995) - Revised Calibration of the geomagnetic polarity timescale for the Late Cretaceous and Cenozoic. Journal of Geophysical reearch vol. 100 pages 6093-6095.

Carlisle, D.B. (1995) - Dinosaurs, Diamonds, and Things From Outer Space: The Great Extinction. Stanford University Press, Stanford, 241.

Cassignol, C, and Gillot, P-Y. (1982) - Range and effectiveness of unspiked potassium-argon dating: Experimental groundwork and applications. In Numerical dating in stratigraphy (ed. G. S. Odin), pp. 159-179. Wiley, Chichester.

Catuneanu, O., Galloway, W.E., Kendall, G.St.C., Miall, A.D., Posamentier, H.W., Strasser, A., Tucker, M. (2011) - Sequence stratigraphy: Methodology and nomenclature: Newsletters on Stratigraphy, 44,173–245.

Cebula, G.T., Kunk, M.J., Mehnert, H.H., Naeser, C.W., Obradovich, J.D., Sutter, J.F. (1986) - The Fish Canyon Tuff, a potential standard for the $^{40}Ar/^{39}Ar$ and fission-track dating methods. Terra Cognita 6, 139-140.

Cecil, C.B., Edgar, N.T. (2003) - Climate controls on stratigraphy. SEMP special publication 77, 275.

Channell, J.E.T., Cecca, F., Erba, E. (1995) - Correlations of Hauterivian and Barremian (Early Cretaceous) stage boundaries to polaritychrons. Earth and Planetary Science Letters 134: 125–40.

Channell, J.E.T., Erba, E., Nakanishi, M., Tamaki, K. (1995b), Late Jurassic–Early Cretaceous time scales and oceanic magnetic anomaly block models. In W. A. Berggren, D. V. Kent, and J. Hardenbol, eds, Geochronology, Time Scales and Global Stratigraphic Correlations. A Unified Temporal Framework for a Historical Geology. Society of Economic Paleontologists and Mineralogists Special Publication, Vol. 54. Tulsa, OK: SEMP, pp. 51–63.

Channell, J. E.T., Hodell, D.A., Singer, B.S., Xuan, C. (2010) - Reconciling astrochronological and $^{40}Ar/^{39}Ar$ ages for the Matuyama-Brunhes boundary and late Matuyama Chron. G-cubed . Journal of geophysics.

Charlier, B.L.A, Wilson, C.J.N, Lowenstern, J.B, Blake, S, Van Calsteren, P.W, Davidson, JP (2005) - Magma generation at a large, hyper- active silicic volcano (Taupo, New Zealand) revealed by U-Th and U-Pb systematics in zircons. J. Petrol. 46, 3-32.

Chen Y.L., Luo Z.H., Zhao J.X., Li Z.H., Zhang H.F., Song B. (2005) - Petrogenesis and dating of the Kangding complex, Sichuan province: Science in China, Series D, 48, 622–634.

Chenet, A.L., Quidelleur, X., Fluteau, F., Courtillot, V., Bajpai, S. (2007) - $^{40}K/^{40}Ar$ dating of the main Deccan Large Igneous Province: Further Evidence of KTB Age and short duration. Earth Planet. Sci. Lett. 263, 1–15.

Chenet, A.L., Fluteau, F., Courtillot, V., Gerard, M., Subbarao, K.V. (2008) - Determination of rapid Deccan eruptions across the KTB using paleomagnetic secular variation: (I) Results from 1200 m thick section in the Mahabaleshwar escarpment. J. Geophys. Res. 113, B04101.

Cobban, W.A., Walaszczyk, I., Obradovich, J.D., McKinney, K.C. (2006) - A USGS zonal table for the Upper Cretaceous middle Cenomanian–Maastrichtian of the Western Interior of the United States based on ammonites, inoceramids, and radiometric ages. USGS Open-File Report 1250, 45.

Cooper, R.A., Sadler, P.M. (2010) - Facies preference prdictts extinction risk in Ordovician graptolites. Paleobiology 36 (2), 167-187.

Couch, S., Sparks, R.S.J., Carroll, M.R. (2001) - Mineral disequilibrium in lavas explained by convective self-mixing in open magma chambers: Nature, 411, 1037–1039.

Coulié, E., Quidelleur, X., Gillot, P-Y., Courtillot, V., Lefèvre, J-C., Chiesa, S. (2003) - Comparative K-Ar and $^{40}Ar/^{39}Ar$ dating of Ethiopian and Yemenite Oligocene volcanism: implications for timing and duration of the Ethiopian Traps. Earth Planet. Sci. Lett. 206, 477–492

Coulié, E., Quidelleur, X., Lefèvre, J-C., Gillot,P.J. (2004) – Exploring the muticollection approach for the $^{40}Ar/39Ar$ dating technique. Geochemistry Geophysics Geosystems.

Courtillot, V., Besse, J., Vandamme, D., Montigny, R., Jaeger, J.J., Cappetta, H. (1986) - Deccan flood basalts at the Cretaceous/Tertiary boundary. Earth Planet. Sci.Lett. 80, 361–374.

Courtillot, V., Feraud, G., Maluski, H., Vandamme, D., Moreau, M.G., Besse, J. (1988) - Deccan flood basalts and the Cretaceous/Tertiary boundary. Nature 333, 843– 846.

Coquand, H. (1871) - Sur le Klippenkalk du departement du Varet des Alpes-Maritimes. Bulletin de la Societe Geologique de France 2.

Crampton, J.S., Schiøler, P., Roncaglia, L. (2006) - Detection of Late Cretaceous eustatic signatures using quantitative biostratigraphy. Geol. Soc. Am. Bull. 118, 975–990.

Crowley, J.L., Schoene, B., Bowring, S.A. (2007) - U-Pb dating of zircon in the Bishop Tuff at the millennial scale. Geology 35, 1123– 1126.

D

Dalrymple, G.B. (1969) - $^{4O}Ar/^{36}Ar$ analyses of historic lava flows. Earth Planet. Sci. Lett. 6, 47-55.

Dalrymple, G.B., Lanphere, M.A. (1969b) - Potassium-argon dating. Freeman, San Francisco

Dalrymple, G.B., Alexander, E.C., Jr, Lanphere, M.A., Kraker, G.P. (1981) - Irradiation of samples for $^{40}Ar/^{39}Ar$ dating using the Geological Survey TRIGA reactor. U.S. Geol. Surv, Prof Paper. 1176.

Dalrymple, G.B., Duffield, W.A. (1988) - High precision $^{40}Ar/^{39}Ar$ dating of Oligocene rhyolites from the Mogollon-Datil volcanic field using a continuous laser system. Geophys. Res. Lett. 15, 463-466.

Dawson, F.M., Evans, C., Marsh, R., Richardson, R. (1994) - Uppermost Cretaceous-Tertiary strata of the Western Canada Sedimentary Basin; in Geological Atlas of the Western Canada Sedimentary Basin, (comp.) G.D. Mossop and I. Shetsen; Calgary, Canadian Society of Petroleum Geologists and Alberta Research Council, p. 387– 406.

DeCelles, P.G. (2004) - Late Jurassic to Eocene evolution of the Cordilleran thrustbelt and foreland basin system, western U.S: American Journal of Science, 304, 105–168.

DeCelles, P.G., Currie, B.S. (1996) - Long-term sediment accumulation in the Middle Jurassic—Early Eocene Cordilleran retroarc foreland-basin system: Geology, 24, 591–594.

Desmares, D., Grosheny, D., Beaudoin, B., Gardin, S., Gauthier-Lafaye, F. (2007) - High resolution stratigraphic record constrained by volcanic ash beds at the Cenomanian–Turonian boundary in the Western Interior Basin, USA. Cretaceous Res. 28, 561–582.

Dinarès-Turrell, J., Baceta, J.I., Pujalte, V., Orue-Etxebarria, X., Bernaola, G., Lorito, S. (2003) - Untangling the Palaeocene climatic rhythm: an astronomically calibrated Early Palaeocene magnetostratigraphy and biostratigraphy at Zumaia (Basque basin, northern Spain). Earth Planet. Sci. Lett. 216, 483–500.

Duffield, W.A., Dalrymple, G.B. (1990) - The Taylor Creek Rhyolite of New Mexico: a rapidly emplaced field of lava domes and flows. Bull. Volcanol. 52, 475--487.

Duncan, R.A., Pyle, D.G. (1988) - Rapid eruption of the Deccan flood basalts at the Cretaceous/Tertiary boundary. Nature 333, 841– 843.

E

Eberth, D.A., Currie, P.J. (2005) - Vertebrate taphonomy and taphonomic modes. In Dinosaur Provincial Park: A Spectacular Ancient Ecosystem Revealed. Edited by, P.J. Currie and E.B. Koppelhus. Indiana University Press, 453-477.

Eberth, D.A. (2010) - A revised regional stratigraphy and stratigraphic architecture for the Horseshoe Canyon Formation: Outcrop and surface Canadian Society of Petroleum Geology, Joint Annual Convention, Calgary, 50.

Eberth, D. A. (2011) - Edmontosaurus bonebeds from the Horseshoe Canyon Formation of Alberta: Paleobiological implications.

Embry, A.F. (1993) - Transgressive–regressive (T–R) sequence analysis of the Jurassic succession of the Sverdrup basin, Canadian Arctic Archipelago. Canadian Journal of Earth Sciences 30, 301–320.

Embry, A.F. (1997) - Global sequence boundaries of the Triassic and their identification in the Western Canada Sedimentary Basin. Canadian Society of Petroleum Geologists Bulletin 45: 415–533.

Erba, E. (1996) - The Aptian Stage. Bulletin de l'Institut Royal des Sciences Naturelles de Belgique, Sciences de la Terre, Supplement 66: 31–43.

F

Fanti, F. and Catuneanu, O. (2008) - Sequence stratigraphy of the fluvial Wapiti Formation, Grande Prairie region, Alberta.

Fiet, N., Beaudoin, B., Parize, O. (2001) - Lithostratigraphic analysis of Milankovitch cyclicity in pelagic Albian deposits of cen-tral Italy: implications for the duration of the stage and substages. Cretaceous Research, 22: 265-27.

Fiet, N., Quidelleur, X., Parize, O., Bulot, L.G., Gillot, P.-Y. (2006) - Lower Cretaceous stage durations combining radiometric data and orbital chronology: towards a more stable relative time scale. Earth Planet. Sci. Lett. 246, 407–417.

Flemings, P. (1991) - Large-scale stratigraphic architecture, eustatic variation and unsteady tectonism: a theoretical approach. Journal of Geophysical Research 96, 6681–6699.

Frakes, L.A., Francis, J.E., Syktus, J.L. (1992) - Climate Modes of the Phanerozoic: The History of the Earth's Climate Over the Past 600 Million Years. Cambridge: Cambridge University Press.

Frakes, L.A., (1999) - Estimating the global thermal state from Cretaceous sea surface and continental temperature data. In: Barrera, E., Johnson, C.C.Eds., Evolution of the Cretaceous Ocean-Climate System. Geol. Soc. Am. SP Boulder, Colorado.

Frank, T.D., Arthur, M.A. (1999) - Tectonic forcings of Maastrichtian ocean-climate evolution. Paleoceanography 14, 103– 117.

G

Gale, A.S., Kennedy, W.J., Burnett, J.A., Caron, M., Kidd, B.E. (1996) - The Late Albian to Early Cenomanian succession at Mont Risou near Rosans (Drome, SE France): an integrated study (ammonites, inoceramids, planktonic foraminifera, nannofossils, oxygen and carbon isotopes). Cretaceous Research 17: 515–606.

Garner, E.L., Machlan, L.A., Barnes, I.L. (I975) - The isotopic composition of lithium, potassium, and rubidium in some Apollo 11, 12, 14, 15, and 16 samples. Geochim. Cosmochim. Acta Suppl. 6 Proceedings of the Sixth Lunar Science Conference), 1845-1855.

Gibson, D.W. (1977) - Upper Cretaceous and Tertiary coal-bearing strata in the Drumheller-Ardley region, Red Deer River Valley, Alberta. Geological Survey of Canada, 76-35.

Gill, J.R., Cobban, W.A., Schultz, L.G. (1972) - Stratigraphy and composition of the Sharon Springs Member of the Pierre Shale in western Kansas. U.S. Geol. Surv. Prof. Paper 728.

Gillot, P-Y., Cornette, Y. (1986) - The Cassignol technique for potassium-argon dating, precision and accuracy: examples from late Pleistocene to recent volcanics from southern Italy. Chem. Geol. 59, 205–222.

Gillot, P.Y., Cornette, Y., Max, N., Floris, B. (1992) - Two reference materials, trachytes MDO-G and ISH-G, for argon dating (K-Ar and $^{40}Ar/^{39}Ar$) of Pleistocene and Holocene rocks. Geostand. Newsl. 16, 55–60.

Gordy, P.L., Edwards, G. (1962) - Age of the Howell Creek Intrusions. Journal of the Alberta Society of Petroleum Geologists, 10: 369–372.

Gradstein, F.M., Ogg, J.G., Smith, A.G. (2004) - A Geologic Time Scale 2004. Cambridge University Press, Cambridge, U.K, 589.

Gradstein, F.M., Ogg, J.G., Smith, A.G. (2012) - A Geologic Time Scale 2004. Cambridge University Press, Cambridge, U.K

Grieve, R.A.F., Alexopoulos, J. (1988) - Microscopic planar features in quartz from Scollard Canyon, Alberta, and the Cretaceous–Tertiary boundary event. Can. J. Earth Sc. 25, 1530–1534.

Grippo, A., Fischer, A., Hinnov, L.A., Herbert, T.D., Silva, I. (2004) - Cyclostratigraphy and Chronology of the Albian stage (Piobbico core, Italy). In B. D'Argenio, A. G. Fischer, I. Premoli Silva, H. Weissert, and V. Ferreri, eds, Cyclostratigraphy: An

Essay of Approaches and Case Histories, Society of Economic Paleontologists and Mineralogists Special Publication, Vol. 81. Tulsa, OK: SEPM.

H

Hancock, J.M., Kauffman, E.G. (1989) - Use of eustatic changes of sea level to fix Campanian–Maastrichtian boundary in Western Interior of USA. In Proceedings of the 28th International Geological Congress, Washington, D.C, Vol 2, 23.

Hancock, J.M., Gale, A.S., Gardin, S. (1996) - The Campanian Stage. Bulletin de l'Institut Royal des Sciences Naturelles de Belgique, Sciences de la Terre, Supplement 66: 103–9.

Hamblin, A.P. (2004) - The Horseshoe Canyon Formation in southern Alberta: surface and subsurface stratigraphic architecture, sedimentology, and resource potential. Geol. Surv. Can. Bull. 578, 180.

Hart, M., Amedro, F., Owen, H. (1996) - The Albian stage and substage boundaries. Bulletin de l'Institut Royal des Sciences Naturelles de Belgique, Sciences de la Terre, Supplement 66: 45–56.

Hasegawa, T. (1999) - Planktonic foraminifera and biochronology of the Cenomanian – Turonian (Cretaceous) sequence in the Oyubari area, Hokkaido, Japan. Paleontol. Res. 3, 173–192.

Haq, B.U., Hardenbol, J., Vail, P.R. (1987) - Chronology of fluctuating sea levels since the Triassic. Science 235: 1156–67.

Hay, W.W., Eucher, D.L., Diner, R. (1993) - Physical oceanography and water masses in the Cretaceous Western Interior seaway in Caldwells. Evolution of the Western Interior Basisn Geological Association of Canada Special Paper 39 p 297-318.

Hayashi, K., Nishi, H., Takashima, R., Tomosugi, T., Kawabe, F. (2011) - Geology and foraminiferal biostratigraphy of Upper Cretaceous sequences in southern central Hokkaido. Japan. J. Geol. Soc. Japan 117, 14–34.

Heller, P.L., Angevine, C.L., Paola, C. (1988) - Two-phase model of foreland-basin sequences. Geology, 16: 501–504.

Herbert, T.D., (1992) - Paleomagnetic calibration of Milankovitch cyclicity in Lower Cretaceous sediments. Earth and Planetary Science Letters 112: 15–28.

Herbert, T.D., D'Hondt, S.L., Premoli-Silva, I., Erba, E., Fischer, A.G. (1995) - Orbital chronology of Cretaceous–Early Palaeocene marine sediments. In W. A. Berggren, D. V. Kent, and J. Hardenbol, eds, Geochronology, Time Scales and Global Stratigraphic Correlations: A Unified Temporal Framework for a Historical Geology, Society of Economic Paleontologists and Mineralogists Special Publication, Vol. 54. Tulsa, OK: SEPM, pp. 81–94.

Hess, J.C., Lippolt, H.J., Gurbanov, A.G, Michalski, I. (1993) - The cooling history of the late Pliocene Eldzhurtinskiy granite (Caucasus, Russia) and the thermochronological potential of grain-size/age relationships. Earth Planet. Sci. Lett. 117, 393-406.

Hildebrand, A.R., Penfield, G.T., Kring, D.A., Pilkington, M., Camargo, Z.A., Jacobsen, S.B., Boynton, W.V. (1991) - Chicxulub Crater: A possible Cretaceous/Tertiary boundary impact crater on the Yucatan Penninsula, Mexico. Geology 19, 867-871.

Hilgen, F.J. (2008) - Recent progress in the standardization and calibration of the Cenozoic Time Scale. Newslett. Strat. 43, 15-22.

Hilgen, F.J., Lourens, L.J., Kuiper, K.F. (2010) - Evaluation of the astronomical time scale for the Paleocene and earliest Eocene. Earth Planet. Sc. Lett. 300, 139-151.

Holmes, A. (1937), The Age of the Earth. London: Harper. The Age of the Earth. London: Nelson. 1947, The construction of a geological time-scale. Transactions Geological Society of Glasgow 21: 117–52. 1960, A revised geological time-scale. Transactions of the Edinburgh Geological Society 17: 183–216.

Holmes, A. (1960) - A revised geological time-scale: Transactions of the Edinburgh Geological Society, 17, 183-216.

Hurford, A.J., Hammerschmidt, K. (1985) - $^{40}Ar/^{39}Ar$ and K/Ar dating of the Bishop and Fish Canyon Tuffs: Calibration ages for fission- track dating standards. Chern. Geol. (Isot. Geosci. Section) 58, 23-32.

Husson, D., Galbrun, B., Laskar, J., Hinnov, L., Thibault, N., Gardin, S., Locklair, R. (2011) - Astronomical Calibration of the Maastrichtian (Late Cretaceous) Earth Planet. Sci. Lett, 305, 328-340.

Irish, E.J.W. (1970) - The Edmonton Group of south-central Alberta. Bull. Can. Petrol. Geol. 18, 125-155.

Izett, G., Dalrymple, G.B., Snee, L.W. (1991) - $^{40}Ar/^{39}Ar$ age of K–T boundary tektites from Haiti. Science 252, 159– 1543.

Jarvis, I., Gale, A.S., Jenkyns, H.C., Pearce, M.A. (2006) - Secular variation in Late Cretaceous carbon isotopes: A new $d^{13}C$ carbonate reference curve for the Cenomanian-Campanian (99.6-70.6Ma). Geological Magazine 143, 561-608.

Jeletzky, J.A. (1968) - Macrofossil zones of the marine Cretaceous of the Western Interior of Canada and their correlation with the zones and stages of Europe and the Western Interior of the United States. Geol. Surv. Can, 67-72.

Jenkins, D.G, (1967) - Planktonic foraminiferal zones and new taxa from the lower Miocene to the Pleistocene of New Zealand. New Zealand Journal of Geology and Geophysics 10: 1064–78.

Jenkyns H.C., Gale A.S., Corfield R.M. (1994) - Carbon-isotope and oxygen-isotope stratigraphy of the English Chalk and Italian Scaglia and its paleoclimatic significance. Geol Mag 131:1–34.

Jenkyns H.C. (2003) - Evidence for rapid climate change in the Mesozoic-Palaeogene greenhouse world. Philos Trans R Soc Ser A 361: 1885–1916.

Jerzykiewicz, T. (1985) - Stratigraphy of the Saunders Group in the central Alberta Foothills - a progress report. In: Current Research, Part B, Geol. Surv. Can. Paper 85, 247-258.

Jordan. T. E. (1981) - Thrust loads and foreland basin evolution, Cretaceous western United States. Bull. Am. Assoc. Petrol. Geol. 65, 2506-2520.

K

Kamikuri, S., N, Nishi., I., Motoyama. (2004) - Middle Miocene to Pleistocene radiolarian biostratigraphy in the Northwest. Island ArcVol. 13, No. 1, p. 191-22

Kauffman E.G. (1969) - Form function and evolution in Moore R.C ed., Treatise on invertebrate paleontology Part N 129-205.

Kaufman, A.J,. Knoll, A.H. (1995) - Neoproterozoic variation in the C-isotopic composition of seawater: stratigraphic and biogeochemical implications. Precambrian Research 73: 27–49.

Kauffman, E.J., Kennedy, W.J., Wood, C.J., with contributions by Dhondt, A.V, Hancock, J. M, Kopaevich, L. F, and Walaszczyk, I, (1996) - The Coniacian stage and substage boundaries. Bulletin de l'Institut Royal des Sciences Naturelles de Belgique, Sciences de la Terre, Supplement, 66: 81–94.

Karakitsios, V., Tsikos, H., Van Breugel, Y., Koletti, L., Damste, J.S.S,. Jenkyns H.C. (2007) - First evidence for the late Cenomanian Oceanic Anoxic Event (OAE2, or "Bonarelli"event) from the Ionian Zone, western continental Greece. International Journal of Earth Sciences (Geol. Rundsch), vol. 96, p. 343-35

Karner, D.B,. Renne, P.R. (1998) - $^{40}Ar/^{39}Ar$ geochronology of Roman volcanic province tephra in the Tiber River valley: Age calibration of middle Pleistocene sea-level changes. Geological Society of America, Bulletin 110(6): 740-747

Kawabe, F., Takashima, R., Wani, R., Nishi, H., Moriya, K. (2003) - Upper Albian to Lower Cenomanian biostratigraphy in the Oyubari area, Hokkaido, Japan: toward a Cretaceous biochronology for the North Pacific. Acta Geol. Pol. 53, 81–91.

Keller, G,T., Adatte, W., Stinnesbeck, M., Affolter, L., Schilli, Lopez-Oliva, J.G. (2002) - Multiple spherule layers in the late Maastrichtian of northeastern Mexico. GSA Special Paper 356, 145-162.

Keller, G., Stinnesbeck, W., Adatte, T., Stueben, D. (2003) - Multiple impacts across the Cretaceous-T ertiary boundary. Earth Sc. Rev. 62, 327-363.

Keller, G,T., Adatte, W., Stinnesbeck, M., Rebolledo-Vieyra, J., Urrutia Fucugauchi, U. Kramar, Stüben, D. (2004) - Chicxulub impact predates the K-T boundary mass extinction. PNAS 101, 3753- 3758.

Keller, G. (2008) - Cretaceous climate, volcanism, impacts and biotic effects. Cretaceous Research. 29, 754–771.

Keller, G,A,. Sahni., Bajpai, S. (2009) - Deccan volcanism, the KT mass extinction and dinosaurs. J. Biosci. 34, 709-728.

Keller, G. (2012) - The Cretaceous- Tertiary Mass Extinction, Chicxulub Impact, and Deccan Volcanism. Earth and Life, International Year of Planet Earth, 759-793

Kendall, B.R.F. (1960) - Isotopic composition of potassium. Nature (London) 186,225-226.

Kennedy, W.J., Walaszczyk, I., Cobban, W.A. (2000) - Pueblo, Colorado, USA, candidate global boundary stratotype section and point for the base of the Turonian Stage of the Cretaceous and for the Middle Turonian substage, with a revision of the Inoceramidae (bivalve). Acta Geologica Polonica 50: 295–334.

Khidir, A., Catuneanu, O. (2003) - Sedimentology and diagenesis of the Scollard sandstones in the Red Deer Valley area, central Alberta. Bulletin of Canadian Petroleum Geology, v. 51, 45-69.

Kiminami, K., Kito, N., Tajika, J. (1985) - Mesozoic group in Hokkaido: stratigraphy and age and their significance. Earth Sci. (Chikyu Kagaku) 39:1–17.

Kiminami, K., Niida, K., Ando, A., Kito, N., Iwata, I., Miyashita, S., Tajika, J., Sakakibara, M. (1992) -Cretaceous – Paleogene arc- trench systems in Hokkaido. In: Suzuki, K., Adachi, M. (Eds.), 29th IG.

Kolodny., Y. (1985) - Oxygen isotope variations in phosphate of biogenic apatites. IV. Mammal teeth and bones. Earth Planet. Sci. Lett., 75: 29‑36

Kowallis, B.J., Christiansen, E.H., Deino, A.L., Kunk, M.J., Heaman, L.M. (1995) - Age of the Cenomanian–Turonian Boundary in the Western Interior of the United-States. Cretaceous Res. 16, 109–129.

Kuiper, K., Deino, A., Hilgen, F.J., Krijgsman, W., Renne, P.R., Wijbrans, J.R. (2008) - Synchronizing rock clocks of Earth history. Science 320, 500–504.

Kulp, J.L. (1961) - Geologic time-scale. Science 133: 1105–14

Langenberg, W., Pana, C, (2006) - Coalbed methane resources and reservoir charactersitscs fromt eh Alberta Plains, Canada. International Journal of Coal Geology, 651-2: 93-113.

Larson, R.L., Hilde, T.W.C. (1975) - A revised time scale of magnetic reversals for the Early Cretaceous and Late Jurassic: J. Geophys. Res., v. 80, 2586

Larson, D.W., Brinkman, D.B., Phil, R.B. (2010) - Faunal assemblages from the upper Horseshoe Canyon Formation, an early Maastrichtian cool-climate assemblage from Alberta, with special reference to the Albertosaurus sarcophagus bonebed. Can. J. Earth Sc. 47, 1159-1181.

Laskar, J. (1990) - The chaotic motion of the solar system: A numerical estimate of the size of the chaotic zones. Icarus 88, 266-291.

Laskar, J., Robutel, P., Joutel, F., Gastineau, M., Correia, A.C.M., Levrard, B. (2004) - A long term numerical solution for the insolation quantities of the Earth. Astron. Astrophys. 428, 261–285.

Laskar, J., Fienga, A., Gastineau, M., Manche, H. (2011) - La2010: A new orbital solution for the long-term motion of the Earth. Astron. Astrophys. 532-589.

Leckie, R.M., Bralower, T.J., Cashman, R. (2002) - Oceanic anoxic events and plankton evolution: biotic response to tectonic forcing during the mid-Cretaceous. Paleoceanography 17.

Lerbekmo, J.F. (1985) - Magnetostratigraphic and biostratigraphic correlations of Maastrichtian to early Paleocene strata between south-central Alberta and southwestern Saskatchewan. Bull. Can. Petrol. Geol. 33, 213–226.

Lerbekmo, J.F., Coulter, K.C. (1985) - Late Cretaceous to early Tertiary magnetostratigraphy of a continental sequence: Red Deer Valley, Alberta, Canada. Can. J. Earth Sc. 22, 567–583.

Lerbekmo, J.F., St. Louis, R.M. (1986) - The terminal Cretaceous iridium anomaly in the Red Deer Valley, Alberta, Canada. Can. J. Earth Sc. 23, 120–124.

Lerbekmo, J.F., Sweet, A.R., Duke, M.J.M. (1996) - A normal polarity subchron that embraces the K/T boundary; a measure of sedimentary continuity across the boundary and synchroneity of boundary events. Geol. Soc. Am, Spec. Pap. 307, 465–476.

Lerbekmo, J.F. (2002) - "The Dorothy bentonite: an extraordinary case of secondary thickening in a late Campanian volcanic ash fall in central Alberta", Canadian Journal of Earth Sciences, 39 Pg 1745-1754.

Lewy, Z., Odin, G.S. (2001) - Magnetostratigraphy across the Campanian– Maastrichtian boundary at Tercis les Bains in comparison with northern Germany, the Apennines (Central Italy) and North America; biostratigraphical and geo-chronological constraints. In: Odin, G. S. (Ed.), The Campanian– Maastrichtian Stage Boundary – characterization at Tercis les Bains (France) and correlation with Europe and other continents. Developments in Paleontology and Stratigraphy 19, Elsevier, 175–186.

Ludwig, K.R. (1991) - Isoplot - a plotting and regression program for radiogenic isotope data USGS Open- File report, 91-445.

Li, L., Keller, G. (1998) - Maastrichtian climate, productivity and faunal turnovers in planktic foraminifera in South Atlantic DSDP sites 525 and 21. Marine Micropaleontology 33, 55-86.

Li, L., Keller, G., Stinnesbeck,W. (1999) - The late Campanian and Maastrichtian in northwestern Tunisia: palaeoenvironmental inferences from lithology, macrofauna and benthic foraminifera. Cret. Res. 20, 231–252.

Lipman, P.W., Steven, T.A., Mehnert, H.H., (1970) - Volcanic history of the San Juan mountains, Colorado, as indicated by potassium-argon dating. Geological Society of America Bulletin 81, 2329–2351.

Lourens, L.J., Hilgen, F.J., Laskar, J., Shackleton, N.J., Wilson, D. (2004) - The Neogene Period. In: Gradstein, F.M., Ogg, J.G., Smith, A.G. (Eds.), A Geologic Time Scale 2004. Cambridge University Press, Cambridge, p. 409-440

Lowenstern, J.B., Persing, H.M., Wooden, J.L., Lanphere, M., Donnelly-Nolan, J., Grove, T .L. (2000) - U-Th datingof single zircons from young granitoid xenoliths: New tools for understanding volcanic processes. Earth Plan. Sc. Lett. 183, 291–302

Ludwig, K.R. (1991) - Isoplot—a plotting and regression program for radiogenic isotope data. USGS Open- File report, 91-445.

M

MacLeod, K.G. (1997) - Deep sea paleotemperature record of extreme warmth during the Cretaceous. Geology 30: 123–6.

Maeda, H., Shigeta, Y., Okamoto, T., Kase, T., Uemura, K. (2003) - Upper Cretaceous stable carbon isotope stratigraphy of terrestrial organic matter from Sakhalin, Russian Far East:a proxy for the isotopic composition of paleoatmospheric CO2-Palaeogeograhpy Palaeoclimatology, Palaeocology 189:97-115

Mahon, K.I. (1996) - The New "York" regression: Application of an improved statistical method to geochemistry, International Geology Review, 38, 293-30.

Mahood, G.A., McWilliams, M., (1998) - New ages for the climactic eruptions at Yellow-stone: single-crystal Ar-40rAr-39 dating identifies contamination. Geology 26, 343–346.

Mark, D.F, Kelley, S.P., Lee, M.R., Parnell, J., Sherlock, S.C., Brown, D.J. (2008) - Ar–Ar dating of authigenic K-feldspar: Quantitative modelling of radiogenic argon-loss through subgrain boundary networks. Geochimica et Cosmochimica Acta, 72, 2695–2710.

Mattinson, J.M. (2005) - Zircon U–Pb chemical-abrasion (CA-TIMS) method: combined annealing and multi-step dissolution analysis for improved precision and accuracy of zircon ages. Chemical. Geology. 220, 47–56.

McArthur, J.M., Thirlwall, M.F., Gale, A.S., Chen, M., Kennedy, W.J. (1993) - Strontium isotope stratigraphy in the Late Cretaceous: numerical calibration of the Sr isotope curve and intercontinental correlation for the Campanian. Paleoceanography 8: 859–73.

McArthur, J.M., Kennedy, W.J., Chen, M., Thirlwall, M.F., Gale, A.S. (1994) - Strontium isotope stratigraphy for late Cretaceous time: direct numerical calibration of the Sr isotope curve based on the US Western Interior. Palaeogeogr-. Palaeoclimatol-. Palaeoecol-. 108, 95-119.

McDougall, I, and Roksandic, Z. (1974) - Total fusion $^{40}Ar/^{39}Ar$ ages using HIFAR reactor. Geologicsl. Society. Austria. J. 21, 81-89.

McDougall, I. (1985), K–Ar and $^{40}Ar/^{39}Ar$ dating of the hominid-bearing Pliocene–Pleistocene sequence at Koobi Fora, Lake Turkana. Geological Society of America Bulletin 96: 159–75.

McDougall, I. and Harrison, T. M, (1999) - Geochronology and Thermochronology by the $^{40}Ar/^{39}Ar$ Method. Oxford: Oxford University Press.

McLean, D.M. (1985) - Deccan traps mantle degassing in the terminal Cretaceous marine extinctions. Cret. Res. 6, 235-259

McNeil, D., Caldwell, W. (1981) - Cretaceous rocks and their foraminifera in the Manitoba Escarpment. Geological Association of Canada, Special Paper 21, 439.

Menegatti, A.P., Weissert, H., Brown, R.S. (1998) - High resolution δ13C-stratigraphy through the early Aptian "Livello Selli" of the Alpine Tethys. Paleoceanography 13: 530–45.

Merrihue, C., Turner, G. (1966) - Potassium–argon dating by activation with fast neutrons. Journal of Geophysical Research 71: 2852–2857.

Meyers, S.R., Siewert, S.E., Singer, B.S., Sageman, B.B., Condon, D.J., Obradovich, J.D., Jicha, B.R., Sawyer, D.A. (2012) - Intercalibration of radioisotopic and astrochonologic time scales for the Cenomanian-Turonian boundary interval, Western Interior Basin, USA, Geology, 40, 7-10.

Min, K,R., Mundil, P.R., Renne., Ludwig., K.R. (2000) - A test for systematic errors in 40Ar/39Ar geochronology through comparison with U/Pb analysis of a 1.1-Ga rhyolite, Geochim. Cosmochim. Acta 64, 73-98.

Molina, E., Alegret, L., Arenillas, I., Arz, J.A., Gallala, N., Hardenbol, J., von Salis, K., Steurbaut, E., Vandenberghe, N., Zaghbib-Turki, D. (2006) - The Global Boundary Stratotype Section and Point for the base of the Danian Stage (Paleocene, Paleogene, "Tertiary", Cenozoic) at El Kef, Tunisia - original definition and revision. Episodes 29, 263–273.

N

Naylor, R. S. (1971) - Acadian Orogeny: An abrupt and brief event. Science 172, 558-559.

Neall, V.E, (1977) - Genesis and weathering of andosols in Taranaki, New Zealand. Soils Science 123, 400-408.

Nesbitt, H.W., Young, G.M. (1982) - Early Proterozoic climates and plate motions inferred from major element chemistry of lutites. Nature, 199, 715-717.

Nier, A.L.T., Aldrich. (1948) -Argon 40 in potassium minerals. Phys. Rev. 74, 876-77

Nishi, H., Takashima, R., Hatsugai, T., Saito, T., Moriya, K., Ennyu, A., Sakai, T. (2003) - Planktonic foraminiferal zonation in the Cretaceous Yezo Group, Central Hokkaido, Japan. J. Asian Earth Sci. 21, 867–886.

O

Oberli, F., Fischer, H., Meier, M. (1990) - High-resolution 238U–206Pb zircon dating of Tertiary bentonites and Fish Canyon Tuff; a test for age "concordance" by single-crystal analysis. Seventh international conference on Geochronology,

cosmochronology and isotope geology. Seventh International Conference on Geochronology, Cosmochronology and Isotope Geology. Geological Society of Australia, Special Publication Canberra, 27, p 74.

Oberli, F., Bachmann, O., Meier, M., Dungan, M.A. (2002) - The Fish Canyon Tuff: Ar–Ar versus U–Pb age discrepancy re-assessed. Geochimica et Cosmochimica. Acta 66.

Obradovich, J. (1993) - A Cretaceous time scale. In: Kauffman, E.G Caldwell, W.G.E. (Eds.), Evolution of the Western Interior Basin Geol. Associated Cananadian Special Paper 39, 379–396.

Obradovich, J.D., Matsumoto, T., Nishida, T., Inoue, Y. (2002) - Integrated biostratigraphic and radiometric study on the Lower Cenomanian Cretaceous of Hokkaido, Japan. Proc. Jpn Acad. B Phys. Biol. Sci. 78, 149–153.

Odin, G.S. (2001) - The Campanian–Maastrichtian Stage Boundary- characterization at Tercis les Bains (France) and correlation with Europe and other continents. Developments in Paleontology and Stratigraphy 19, Elsevier, 881.

Odin, G.S., Arz, J.A., Caron, M., Ion, J., Molina, E. (2001b) - Campanian-Maastrichtian planktonic foraminifera at Tercis les Bains (Landes, France): synthetic view and potential for global correlation. In: Odin, G. S. (Ed.), The Campanian– Maastrichtian Stage Boundary – characterization at Tercis les Bains (France) and correlation with Europe and other continents. Developments in Paleontology and Stratigraphy 19, Elsevier, 379–395.

Odin, G.S., Courville, P., Machalski, M., Cobban, W.A. (2001c) - The Campanian-Maastrichtian ammonite fauna from Tercis (Landes, France): a synthetic view

Odin, G.S. (2001c.), The Campanian-Maastrichtian Stage Boundary – characterization at Tercis les Bains (France) and correlation with Europe and other continents. Developments in Paleontology and Stratigraphy 19, Elsevier, 550–560.

Odin, G.S., Lamaurelle, M.A. (2001d) – The global Campanian-Maastrichtian stage boundary. Episodes 24, 229-238.

Ogg, J.G., Steiner, M.B., Company, M., Tavera, J.M. (1988) - Magnetostratigraphy across the Berriasian–Valanginian stage boundary (Early Cretaceous) at Cehegin (Murcia Province, southern Spain). Earth and Planetary Science Letters 87: 205–15.

Ogg, J.G., Hasenyager II, R.W., Wimbledon, W.A., (1994) - Jurassic–Cretaceous boundary: Portland–Purbeck magnetostratigraphy and possible correlation to the Tethyan faunal realm. Geobios Memoire Special 17: 519–27.

Okada, H., Whitaker, J.H., McD, Smith, A.J. (1982) - The Shimanto Belt of Japan: Cretaceous - lower Miocene active-margin sedimentation: Geological Society of London Special Publication 10, p. 5-26.

Olsen, P. E., Kent, D.V. (1999) - Long-period Milankovitch cycles from the Late Triassic and Early Jurassic of eastern North America and their implications for the calibration of the Early Mesozoic time-scale and the long-term behaviour of the planets. Philosophical Transactions of the Royal Society of London, series 357: 1761–86

Onstott, T.C., Miller, M.L., Ewing, R.C., Arnold, G.W., Walsh, D.S. (1995) - Recoil refinements: Implications for the $^{40}Ar/^{39}Ar$ dating technique. Geochim. Cosmochim. Acta 59, 1821-1834.

P

Paillard, D., Labeyrie, L., Yiou, P. (1996) - Macintosh program performs time-series analysis. Eos Trans. Am. Geophys. Union 77, 379– 397.

Pälike, H,J., Laskar., Shackleton, N.J. (2004) - Geological constraints on the chaotic diffusion of the solar system. Geology 32, 929-932.

Palmer, A.R. (1999) - A proposed nomenclature for stages and series for the Cambrian of Laurentia. Canadian Journal of Earth Sciences 35:323–8.

Pancost, R.D., Crawford, N., Magness, S., Turner, A., Jenkyns, HC., Maxwell, J.R. (2004) - Further evidence for the development of photic-zone euxinic conditions during Mesozoic oceanic anoxic events. J Geol Soc Lond 161:353–364.

Porter, J.W., Price, R.A., McCrossan, R.G. (1982) - The Western Canada Sedimentary Basin. Phil. Tran. Royal Soc. Lon. A305, 169-182.

Price, J.R., Velbel, M.A. (2003) - Chemical weathering indices applied to weathering profiles developed on heterogeneous felsic metamorphic parent rocks. Chem. Geol. 202, 397-416.

Q

Quidelleur, X., Paquette, J.L., Fiet, N., Takashima, R., Tiepolo, M., Desmares, D., Nishi, H., Grosheny, D. (2011) - New U-Pb (ID-TIMS and LA-ICPMS) and $^{40}Ar/^{39}Ar$ geochronological constraints of the Cretaceous geologic time scale calibration form Hokkaido (Japan) Chemical. Geology.

Quinney, A. (2011) - The Upper Cretaceous Horseshoe Canyon Formation: using paleosols to reconstruc ancient environments, climate, and record of sea level chang in a dinosaur-dominated terrestrial ecosystem. Thesis University of Calgary.

R

Rahmani, R.A. (1988) - Estuarine tidal channel and nearshore sedimentation of a Late Cretaceous epicontinental sea, Drumheller, Alberta, Canada. In: Tide-influenced Sedimentary Environments and Facies. P.L. de Boer, A. van Gelder, and S.D. Nio. Dordrecht, Reidel Publishing Co, 433-471.

Rayleigh, Lord, and Ramsay, W. (1895) - Argon, a new constituent of the atmosphere. R. Soc. Lond. Phi/.Trans. Ser. A 186, 187-241.

Rawson, P. F. (1983) - The Valanginian to Aptian stages: current definitions and outstanding problems. Zitteliania 10: 493–500.

Reboulet, S. and Atrops, F. (1999) - Comments and proposals about the Valanginian–Lower Hauterivian ammonite zonation of southeastern France. Ecologae Geologicae Helvetiae 92: 183–97.

Reid, M.R., Coath, C.D., Harrison, T.M., McKeegan, K.D. (1997) - Prolonged residence times for the youngest rhyolites associated with Long Valley Caldera: 230Th- 238U microprobe dating of young zircons. Earth Plan. Sc. Lett. 150, 27-39.

Reiners, P.W., Farley,K.A. (1999) - Hediffusion and U–Th/Pb thermochronometry of titanite. Geochim. Cosmochim. Acta 63, 3845–3859.

Reiners, P.W., Farley, K.A., Hickes, H.J. (2002) - He diffusion and (U–Th)/Pb thermo-chronometry of zircon: initial results from Fish Canyon Tuff and Gold Butte, Nevada. Tectonophysics 349, 297–308.

Renevier, E, (1864) - Notices geologique et paleontologiques sur les Alpes Vaudoises, et les regions environnantes. I. Infralias et Zone a`Avicula contorta (Ét. Rhaetien) des Alpes Vaudoises. Bulletin de la Socie´te´ Vaudoise des Sciences Naturelles, Laussane 8: 39–97.

Renne, P.R. and Basu, A.R. (1991) - Rapid eruption of the Siberian Traps flood basalts at the Permo–Triassic boundary. Science 253: 176–9.

Renne, P.R., Deino, A.L., Walter, R.C. (1994) - Intercalibration of astronomical and radioisotopic time. Geology 22(9): 783–6. Renne, P. R, Zhang, Z, Richards, M. A, Black, M. T, and Basu, A. R, 1995, Synchrony and causal relations between Permian–Triassic boundary crises and Siberian flood volcanism. Science 269: 1413–16.

Renne, P.R., Sharp, W.D., Deino, A.L., Orsi, G., Civetta, L. (1997) - $^{40}Ar/^{39}Ar$ dating into the historical realm: calibration against Pliny the Younger. Science 277: 1279–80.

Renne, P.R., Deino, A.L., Sharp, W.D. (1998a) - $^{40}Ar/^{39}Ar$ Dating of the 79 AD eruption of Vesuvius and someimplications. In Joint Annual Meeting of the Geological Association of Canada and the Mineralogical Association of Canada with the Society of Economic Geologists Program with Abstracts, Vol. 23. Ottawa: Geological Association of Canada.

Renne, P.R., Swisher III, C.C., Deino, A.L., et al, (1998b) - Intercalibration of standards, absolute ages and uncertainties in $^{40}Ar/^{39}Ar$ dating. Chemical Geology 145: 117–52.

Renne, P.R,, Mundil, R., Min, K., Ludwig, K.R., (1999) - Progress report on high resolution comparison of argon/argon and uranium/lead systems. In 9th Goldschmidt Conference, Volume LPI Contribution 971. Houston, TX: Lunar and Planetary Institute, 243–4.

Renne, P.R., Ludwig, K.R., Karner, D.B. (2000) - Progress and challenges in geochronology. Science Progress 83: 107–21.

Renne, P.R., Mundil, G., Balco, K., Min., Ludwig, K.R. (2010) - Joint determination of ^{40}K decay constants and $^{40}Ar/^{40}K$ for the Fish Canyon sanidine standard, and improved accuracy for $^{40}Ar/^{39}Ar$ geochronology, Geochim. Cosmochim. Acta 74, 5349-5367.

Renne, P.R., Deino, A.L., Hilgen, F., Kuiper, K., Mark, D., Mitchell III, W.S., Morgan, L.E., Mundil, R., Smit, J. (2013) - Time Scales of Critical Events Around the Cretaceous-Paleogene Boundary. Science 339, 684-687.

Ricci J., Quidelleur X., Pavlov V., Orlov S., Shatsillo A. Courtillot, V. (2013) - New $^{40}Ar/^{39}Ar$ and K-Ar ages of the Viluy traps (Eastern Siberia): Further evidence for a relationship with the Frasnian-Famennian mass extinction. Palaeogeography, Palaeoclimatology, Palaeoecology, 386, 531-540.

Rivera, T., Storey, M., Zeeden, C., Hilgen, F., Kuiper, K. (2011) - A refined astronomically calibrated $^{40}Ar/^{39}Ar$ age for Fish Canyon sanidine. Earth Planet. Sc. Lett. 311, 420-426.

Roddick, J.C. (1983). High precision intercalibration of $^{40}Ar–^{39}Ar$ standards. Geochimica et Cosmochimica Acta 47: 887–98.

S

Sageman, B.B., Meyers, S.R., Arthur, M.A. (2006) - Orbital time scale and new C-isotope record for Cenomanian–Turonian boundary stratotype. Geology 34, 125–128.

Samson, S.D, and Alexander, E.C, Jr. (1987) - Calibration of the interlaboratory $^{40}Ar/^{39}Ar$ dat-ing standard, MMhb-l. Chern. Geol. Isotope. Geoscience Section. 66, 27-34.

Sarna-Wojcicki, A.M., Pringle, M.S. Wijbrans, J. (2000) - New $^{40}Ar/^{39}Ar$ age of the Bishop Tuff from multiple sites and sediment rate calibration for the Matuyama-Brunhes boundary. Journal of Geophysical Research 105

Scaillet, S. (2000) - Numerical error analysis in $^{40}Ar/^{39}Ar$ dating. Chemical Geology 162: 269–98.

Schmitz, M.D., Bowring, S.A. (2001) - U–Pb zircon and titanite systematics of the Fish Canyon Tuff. An assessment of high- precision U–Pb geochronology and its application to young volcanic rocks. Geochimica et Cosmochimica Acta 65 (15), 2571–2587.

Schulte, P. (2010) - The Chicxulub asteroid impact and mass extinction at the cretaceous-paleogene boundary. Science 327, 1214-1218.

Schwarz, H., Trieloff, M. (2007) – Intercalibration of $^{40}Ar/^{39}Ar$ age standards NL-25, HB3gr hornblende, GA1550, SB-3, HD-B1 biotite and BMus/2 muscovite. Chemical Geology, 242, 218-231.

Selby, D., Nesbitt, B.E., Muehlenbachs, K., Prochaska, W. (2000) - Hydrothermal alteration and fluid chemistry of the Endako porphyry molybdenum deposit, British Columbia. Economic Geology 95: 183–201.

Selby, D., Mutterlose, J., Condon, D.J. (2009) - U-Pb and Re-Os Geochronology of the Aptian/Albian and Cenomanian/Turonian stage boundaries: Implications for timescale calibration, osmium isotope seawater composition and Re-Os systematics in organic-rich sediments. Chemical Geology 265: 394-409.

Self, S., Blake, S., Sharma, K., Widdowson, M., Sephton, S. (2008) - Sulfur and Chlorine in Late Cretaceous Deccan Magmas and Eruptive gas release. Science 319, 1654–1657.

Seller. (2005) - Glossary of Geology (3rd ed.) Washington, D.C.: American Geological Institute. 1972. P.16.

Sharma, A., Rajamani, V. (2000) - Major element, REE, and other trace element behavior in amphibolite weathering under semiarid conditions in southern India. J. Geol. 108, 487-498.

Sheldon, E., Ineson, J., Bown, P. (2010) - Late Maastrichtian warming in the Boreal Realm: Calcareous nannofossil evidence from Denmark. Palaeogeography Palaeoclimatoly Palaeoecololgy. 295, 55–75.

Shepheard, W.W., Hills, L.V. (1970) - Depositional environments, Bearpaw-Horseshoe Canyon (Upper Cretaceous) transition zone, Drumheller Badlands, Alberta. Bull. Canandian Petrololgy Geology. 18, 166-215.

Siewert, S.E., Singer, B.S., Meyers, S.R., Sageman, B.B., Condon, D.J., Jicha, B.R,. Obradovich, J.D., Sawyer D.A. in review, Integrating $^{40}Ar/^{39}Ar$, U-Pb, and astronomical clocks in the Cretaceous Niobrara Formation, Western Interior Basin, USA.

Silva, P., R, Coccioni. (1994) - Hauterivian-Barremian chronostratigraphy based on ammonites, nannofossils, planktonic foraminifera and magnetic chrons from the Mediterranean domain. — Cretaceous Research. 15 457-467.

Simmons, M.D., Sharland, P.R., Casey, D.M., Davies, R.B., Sutcliffe, O.E. (2007) - Arabian plate sequence stratigraphy: Potential implications for global chronostratigraphy. GeoArabia 12, 101-130.

Sinclair, H.D., Tomasso, M., (2002) - Depositional evolution of coned Turbidite Basins. Journal of Sedimentary Research 72, 451–456.

Singer, B.S, Sageman, B.B, Siewert, S.E, Condon, D.J, Obradovich, J.D, Jicha, B.R, Sawyer, D.A, Meyers, S.R, (2009) - Implications of new $^{40}Ar/^{39}Ar$ and U–Pb ages for Cenomanian–Turonian OAE2. GSA Meeting, Portland: Geological Society of America Abstracts with Programs, 41, 421.

Skinner. (1995) - Upper Missourian–lower Wolfcampian (upper Kasimovian–lower Asselian) conodont biostratigraphy of the midcontinent, USA. Journal of Paleontology 69: 1139–54.

Smit, J., Hertogen, J. (1980) - An extraterrestrial event at the Cretaceous-Tertiary boundary. Nature 285, 198- 200.

Spell, T.L. and McDougall, I. (2003) - Characterization and calibration of ^{40}Ar–^{39}Ar dating standards. Chemical Geology 198: 189–211.

Srivastava, S.K. (1970) - Pollen biostratigraphy and paleoecology of the Edmonton Foramtion Maestrichtian, Alberta, Canada. Palaeogeography, Palaeoclimatology, Palaeoecology, 7: 221-276.

Stacey, J.S., Kramers, J.D. (1975) - Approximation of terrestrial lead isotope evolution by a two-stage model. Earth Planet. Sc. Lett. 26, 207– 221.

Stanley, Steven M. Earth System History. New York: W.H. Freeman and Company, (1999) - ISBN 0-7167-2882-6.

Steiger, R.H, and Jager, E. (1977) - Subcommission on geochronology: Convention on the use of decay constants in geo and cosmochronology. Earth Planet. Sci. Lett. 36, 359-362.

Steven, T.A., Mehnert, H.H., Obradovich, J.D. (1967) - Age of volcanic activity in the San Juan Mountains, Colorado. U.S. Geol. Survey. Prof Paper 575, 47-55.

Stockmal, G. S., Beaumont, C., Nguyen, M., Lee, B. (1987) - Mechanics of thin-skinned thrust-and- fold belts: insights from numerical models, in whence the Mountains Inquiries into the Evolution of Orogenic Systems: A Volume in Honor of Raymond A. Price, Geological Society of America, Spec. Paper 433, 63-99.

Stoll, H. M., D.P. Schrag. (2000) - Coccolith Sr/Ca as a new indicator of coccolithophorid calcification and growth rate Geochem. Geophys. Geosyst., vol.1.

Stott, D. (1961) - Dawson Creek map area, British Columbia. Geological Survey of Canada Paper, vol. 61. 10.

Straight, W.H., Eberth, D.A. (2002) - Testing the utlitiy of vertbrate remains in recognizing patterns in fluvial deposits: an example from the lower Horseshow Canyon Formation, Alberta. PALAIOS 17: 472-490.

Strasser, A., Hillgärtner, H., Hug, W., Pittet, B. (2000) - Third- order depositional sequences reflecting Milankovitch cyclicity. Terra Nova 12, 303-311.

Sugimura, A., Uyeda, S. (1973) “Island Arc” Japan and its Environments. Amsterdam: Elsevier. 247.

Sweet, A.R., McNeil, D.H. (1996) - Shoreface of the Bearpaw Sea in the footwall of the Lewis thrust, southern Canadian Cordillera, Alberta: Geological Survey of Canada, Paper 1996-A, p. 155–163.

Sweet, A.R., Braman, D.R., Lerbekmo, J.F. (1999) - Sequential palynological changes across the composite Cretaceous– Tertiary (K–T) boundary claystone and contiguous strata, western Canada and Montana, U.S.A. Can. J. Earth Sc. 36, 743–768.

Swisher, C.C., Grajales-Nishimura, J., Montanari, A. (1992) - Coeval $^{40}Ar/^{39}Ar$ ages of 65.0 million years ago from Chicxulub Crater melt rock and Cretaceous-Tertiary boundary tektites. Science 257, 954–958.

Swisher, C.C., Dingus, L., Butler, R.F., (1993) - $^{40}Ar/^{39}Ar$ dating and magnetostratigraphic correlation of the terrestrial Cretaceous–Paleogene boundary and Puercan mammal age, Hell Creek– Tullock Formations, Eastern Montana. Can. J. Earth Sci. 30, 1981–1996.

T

Taira, A., Tashiro, M. (1987) - Late Paleozoic and Mesozoic accretion tectonics in Japan and eastern Asia. In Historical Biogeography and Plate Tectonic Evolution of Japan and Eastern Asia.

Taira, A., Tokuyama, H., Soh, W. (1989) - Accretion tectonics and evolution of Japan. In The Evo- lution of the Pacific Ocean Margins, Oxford Monogr. Geol. Geophys, ed. Z Ben-Avrham, 8:100–123. Oxford, UK: Oxford Univ. Press. 234 pp.

Taira, A., Kiyokawa, S., Aoike, K., Saito, S. (1997) - Accretion tectonics of the Japanse islands and evolution of continental crust. Earth Planetary Science Letter. 325:467–78

Taira, A. (2001a) - Tectonic evolution of the Japanese island arc system. Annu. Rev. Earth Planetary. Science. 29, 109–134.

Taira, A., Eguchi, N., Aoike, K., Ienaga, M. (2001b) - Plate tectonics of the Japanese island arc and the deformation of the eastern margin of the Japan Sea. In Active Faults and Seismotec- tonics of the Eastern Margin of the Japan Sea, ed. M Ohtake, A

Takashima, R., Kawabe, F., Nishi, H., Moriya, K., Wani, R., Ando, H. (2004) - Geology and stratigraphy of forearc basin sediments in Hokkaido, Japan: Cretaceous environmental events on the north-west Pacific margin. Cretaceous Research. 25, 365–390.

Takashima, R., Nishi, H., Yamanaka, T., Hayashi, K., Waseda, A., Obuse, A., Tomosugi, T., Deguchi, N., Mochizuki, S. (2010) - High-resolution terrestrial carbon isotope and planktic foraminiferal records of the Upper Cenomanian to the Lower Campanian in the Northwest Pacific. Earth Planetary Science. Letters. 289, 570–582.

Takashima, R., Nishi, H., Yamanaka, T., Tomosugi, T., Fernando, A.G., Tanabe, K., Kawabe, F., Hayashi, K., (2011). Global impact of the Pacific Ocean on carbon and sulphur cycle perturbations during Oceanic Anoxic Event 2. Nature Communications2-234 doi: 10.1038/ncomms1233.

Tanaka, K. (1960) - Cretaceous deposits in the Tomiuchi District, Southern Central Hokkaido. Bulletin. Geology. Survey. Japan 11, 543–554.

Taylor S.R., McLennan S.M. (1985) - The Continental Crust: Its Composition and Evolution. Blackwell, Oxford.

Taylor, J.F., (1997) - Upper Cambrian biomeres and stages, two distinctly different and equally vital stratigraphic units. Abstracts with Program. In 2nd International Trilobite Conference, August 1997, St. Catharine's, p. 47.

Therrien, F., Eberth, D.A., Braman, D.R., Zelenitsky, D.K. (2007) - High-resolution organic carbon isotope record across the Cretaceous– Tertiary boundary in south- central Alberta: implications for the post-impact recovery rate of terrestrial ecosystems and use of δ13C as a boundary marker. Can. J. Earth Sci. 44, 529–542.

Torrence, C., Compo, G.P. (1998) - A practical guide to wavelet analysis, Bull. Am. Meteorol. Soc. 79, 61-78.

Toshimitsu, S., Maiya, S., Inoue, Y., Takahashi, T. (1998) - Integrated megafossil foraminiferal biostratigraphy of the Santonian to lower Campanian (Upper Cretaceous) succession in northwestern Hokkaido, Japan. Cretaceous Res. 19, 69–85.

Toshimitsu, S., Hasegawa, T., (2000) - Notes on stratigraphy of the upper Santonian to lower Campanian (Upper Cretaceous) of Azumi of Hobetsu Town and Noborikawa of Yubari City, central Hokkaido. Bulletin Hobetsu 16, 1–17.

Tsikos H., Jenkyns H.C., Walsworth-Bell B., Petrizzo, M.R., Forster, A., Kolonic, S., Erba, E., Premoli Silva I, Baas, M., Wagner, T., Sinninghe Damsté J.S. (2004a) - Carbon-isotope stratigraphy recorded by the Cenomanian– Turonian oceanic anoxic event: correlation and implications based on three key-localities. J Geological Society London 161:711–720.

Tsikos, H., Karakitsios, V., van Breugel, Y., Walsworth-Bell, B., Bombardiere, L,, Petrizzo, M.R., Sinninghe Damsté, JS., Schouten, S., Erba, E., Premoli Silva, I., Farrimond P, Tyson, R.V., Jenkyns H.C. (2004b) - Organic-carbon deposition in the Cretaceous of the Ionian Basin, NW Greece: The Paquier event (OAE 1b) revisited. Geology Magazine 141:401–416.

V

Vail, P.R., Audemard, F., Bowman, S.A., Eisner, P.N., Perez-Cruz, C. (1991) - The stratigraphic signatures of tectonics, eustasy and sedimentology - an overview. In: Cycles and Events in Stratigraphy (G. Einsele et al, eds), 617-659. Springer, Berlin.

Verbeek, A.A., Schreiner, G.D.L. (1967) - Variations in ^{39}K:^{41}K ratio and movement of potassium in a granite-amphibolite contact region. Geochim. Cosmochim. Acta 31, 2125- 2133.

Villeneuve, M. (2004) Radiogenic isotope geochronology. in: Gradstein, F.M, Ogg J.G, and Smith, A.G, eds, A Geologic Time Scale-2004,Cambridge University Press, p. 87-95.

Voigt S., and H. Hilbrecht (1997) - Late Cretaceous carbon isotope stratigraphy in Europe: correlation and relations with sea level and sediment stability, Palaeogeography, Palaeoclimatology, Palaeoecology, 134, 39-59.

Voigt, S., Gale, A.S., Jung, C., Jenkyns, HC. (2012) - Global correlation of Upper Campanian -Maastrichtian successions using carbon- isotope stratigraphy: development of a new Maastrichtian timescale. Newslett. Strat. 45, 25-53.

W

Wendt, I., Carl, C. (1991) - The statistical distribution of the mean squared weighted deviation. Chem. Geol. 86, 275–285.

Westerhold, T., Röhl, U., Raffi, I., Fornaciari, E., Monechi, S., Reale, V., Bowles, J., Evans, H.F. (2008) - Astronomical calibration of the Paleocene time. Palaeogeogr. Palaeoclimatol. Palaeoecol. 257, 377–403.

Westerhold, T, Röhl, U, Laskar, J, (2012) - Time scale controversy: accurate orbital calibration of the early Paleogene, Geochem. Geophys. Geosyst, 13,

Wicander, R. (2000) - Devonian acritarchs and related forms. Courier Forschungsinstitut Senckenberg 220: 195–204.

Wijbrans, J.R. (1985) - Geochronology of meta-morphic terrains by the $^{40}Ar/^{39}Ar$ age spectrum method. Ph.D. dissertation, Australian National University, Canberra.

Wijbrans, J.R, McDougall, I. (1986) - $^{40}Ar/^{39}Ar$ dating of white micas from an Alpine high-pressure metamorphic belt on Naxos (Greece): The resetting of the argon isotopic system. Contrib. Mineral. Petrol. 93, 187-194.

Wijbrans, J.R., Pringle, M.S., Koppers, A.A.P., Scheveers, R. (1995) - Argon geochronology of small samples using the Vulkaan argon laser- probe. Koninklijke Nederlandse Akademie van Wetenschappen, Amsterdam 98, 185-218.

Wilde, S.A., Valley, J.W., Peck, W.H., Graham, C.M. (2001) - Evidence from detrital zircons for the existence of continental crust and oceans on the Earth 4.4 Gyr ago. Nature 409. 175–78

Williams, G.L., Brinkhuis, H., Pearce, M.A., Fensome, R.A., Weegink, J.W. (2000) Southern Ocean and global dinoflagellate cyst events compared: index events for the Late Cretaceous–Neogene. In N. F. Exon, J. P. Kennett, M. J. Halone, et al, eds, Proceedings of the Ocean Drilling Program, Scientific Results, Vol. 189.

Whitney, J.A., Stormer Jr, J.C. (1985) - Mineralogy, petrology, andmagmatic conditions from the Fish Canyon Tuff, central San Juan volcanic field, Colorado. Journal of Petrology 26, 726–762.

Wood, C.J., Morter, A.A., Gallois, R.W. (1994) - Upper Cretaceous stratigraphy of the Trunch Borehole (TG 23 SE 8). In R. S. Arthurton, S. J. Booth, A. N. Morigi, et al, Geology of the Country around Great Yarmouth. Memoir for 1:50 000 geological sheet 162 (England and Wales). London: British Geological Survey/Her Majesty's Stationery Office.

Z

Zakharov, V.A., Bown, P., Rawson, P.F. (1996) - The Berriasian Stage and the Jurassic–Cretaceous boundary. Bulletin de l'Institut Royal des Sciences Naturelles de Belgique, Sciences de la Terre, Supplement 66: 7–10.

Appendix A

Chapter II. Standards

Sample#	Sample	Province	phase	Weight (g)	Plat.Age	Un. °Plat.
451	NCD Small	Standard	Sanidine	0.2031	28.018	0.126
452	PPD SMALL	Standard	Sanidine	0.2015	HT: 28.572	0.128
					LT:28.145	*0.106*
453	NCD Large	Standard	Sanidine	0.2013	28.412	0.046
454	PPD LARGE	Standard	Sanidine	0.1989	HT: 28.366	0.089
					LT:27.92	*0.122*
456	FCT	Standard	Sanidine	0.2018	28.004	0.069
461	FCT	Standard	Sanidine	0.1998	28.119	0.074

Sample 451 | NCD Small | Irradiate for 40h

40/39	38/39	37/39	36/39	39Ar (10-12.mol)	% 40Ar*	40Ar*/39Ar	Er.4039	Age(Ma)	Er.An.	Er.Tot.	Cl/K	Er.Cl/K	Ca/K	Er.Ca/K
2.12804	0.01025	0.45281	0.0017	2.93066	78.07107	1.66192	0.01547	28.40832	0.26242	0.38511	-0.00057	0.00025	0.91498	0.01109
1.77879	0.01174	0.55585	0.00053	2.22411	93.59522	1.66552	0.02395	28.46941	0.40614	0.4947	-0.00009	0.00043	1.12327	0.01395
1.77515	0.01151	0.46785	0.00062	4.03869	91.69	1.62819	0.01607	27.83609	0.27271	0.38816	-0.00016	0.00015	0.94537	0.01021
1.85726	0.01219	0.36353	0.00082	3.24254	88.52497	1.64457	0.02787	28.11398	0.47279	0.54896	0.00002	0.00021	0.73453	0.00958
1.93336	0.01081	0.26699	0.00111	4.93945	84.16684	1.62756	0.01602	27.82545	0.27171	0.38739	-0.00038	0.00014	0.53942	0.00586
1.84035	0.01199	0.12552	0.00067	3.5927	89.75137	1.65188	0.01881	28.23807	0.31912	0.42466	-0.00004	0.00013	0.25357	0.00378
1.83791	0.01118	0.0698	0.00067	2.67809	89.47145	1.64448	0.04689	28.11253	0.79543	0.84292	-0.00026	0.00037	0.141	0.00813
1.86086	0.01226	0.08644	0.00074	3.47962	88.60636	1.64894	0.01837	28.18813	0.31153	0.41866	0.00003	0.0002	0.17461	0.00393
1.89634	0.01242	0.18145	0.00091	1.92507	86.59801	1.6424	0.01879	28.07724	0.31878	0.42337	0.00007	0.00027	0.36657	0.01069
1.98447	0.01523	0.35685	0.00117	0.65229	83.91786	1.66576	0.1218	28.47331	2.06564	2.08486	0.00084	0.00132	0.72102	0.01677
2.13153	-0.00592	0.81455	0.00093	0.21586	90.15437	1.9228	0.20337	32.82727	3.4407	3.45604	-0.005	0.0053	1.64635	0.07991
3.95329	0.03538	1.62658	0.01208	0.06087	12.9708	0.51338	1.30962	8.82331	22.4533	22.45347	0.00588	0.00828	3.28954	0.16449

Sample 452 | PPD Small | Irradiate for 40h

40/39	38/39	37/39	36/39	39Ar (10-12.mol)	% 40Ar*	40Ar*/39Ar	Er.4039	Age(Ma)	Er.An.	Er.Tot.	Cl/K	Er.Cl/K	Ca/K	Er.Ca/K
3.66618	0.01622	1.20166	0.00738	1.17956	43.06096	1.58006	0.05284	26.95484	0.89476	0.9339	0.0008	0.00043	2.42945	0.02971
1.89877	0.01075	0.48868	0.00092	1.77566	87.66496	1.66514	0.02248	28.39494	0.38026	0.47326	-0.00039	0.00018	0.98748	0.01399
1.92108	0.0116	0.35365	0.00102	5.66463	85.79615	1.64863	0.00737	28.11552	0.12473	0.30559	-0.00016	0.00012	0.71456	0.00772
2.78053	0.01196	0.20708	0.00388	9.40446	59.36485	1.6509	0.01403	28.15394	0.23743	0.36662	-0.00021	0.0001	0.41836	0.00419
2.5202	0.01188	0.11025	0.00289	4.67029	66.45223	1.67486	0.0127	28.5593	0.21488	0.35561	-0.00018	0.0001	0.22272	0.003
2.03538	0.01161	0.04627	0.00105	4.86413	84.96815	1.72948	0.01321	29.48319	0.22331	0.36795	-0.00016	0.00015	0.09347	0.00742
1.91788	0.01145	0.03149	0.00082	6.24754	87.45513	1.67732	0.01023	28.60091	0.17306	0.33237	-0.0002	0.00013	0.06361	0.00408
1.93347	0.01149	0.0524	0.00091	3.21388	86.31746	1.66899	0.02701	28.45996	0.45699	0.53718	-0.00019	0.00011	0.10586	0.00246
2.01719	0.01324	0.2022	0.00125	1.15877	82.46061	1.66363	0.06445	28.36937	1.09037	1.12612	0.00028	0.00052	0.4085	0.0138

Sample 453 | NCD Large | Irradiated for 40h

40/39	38/39	37/39	36/39	39Ar (10-12.mol)	% 40Ar*	40Ar*/39Ar	Er.4039	Age(Ma)	Er.An.	Er.Tot.	Cl/K	Er.Cl/K	Ca/K	Er.Ca/K
2.9188	0.00946	0.06187	0.00434	0.97001	56.24101	1.64163	0.04642	28.04669	0.78686	0.83463	-0.00093	0.00061	0.12499	0.01781
1.8144	0.01056	0.10592	0.00057	2.56876	91.18157	1.65453	0.01619	28.26523	0.27435	0.39232	-0.00043	0.00024	0.21398	0.00848
1.75795	0.01169	0.07038	0.00039	4.68209	93.71279	1.64751	0.0114	28.14632	0.19318	0.33958	-0.0001	0.00014	0.14218	0.00675
1.77889	0.01117	0.05073	0.00039	3.47959	93.7209	1.66726	0.0087	28.481	0.1475	0.31875	-0.00025	0.00023	0.10248	0.00674
1.86455	0.01134	0.03028	0.00069	7.44338	89.16736	1.66261	0.00916	28.40221	0.1552	0.32171	-0.00022	0.0001	0.06117	0.00194
1.91345	0.01141	0.01758	0.00085	5.65284	86.83674	1.6616	0.01179	28.38515	0.19985	0.34533	-0.00021	0.00009	0.03552	0.00385
1.84949	0.01108	0.0091	0.00064	5.61818	89.69578	1.65892	0.00885	28.33974	0.15007	0.31872	-0.00029	0.0001	0.01838	0.00414
1.80719	0.0118	0.00922	0.0005	9.94038	91.81531	1.65928	0.00777	28.34588	0.13162	0.31052	-0.00008	0.00006	0.01862	0.00359
1.78504	0.01169	0.00896	0.00041	10.60358	93.29307	1.66533	0.00471	28.44828	0.0798	0.29332	-0.00011	0.00008	0.01809	0.00119
1.79082	0.01178	0.01401	0.00041	7.88995	93.31244	1.67107	0.0075	28.5457	0.12718	0.31046	-0.00008	0.0001	0.02829	0.00276
1.85644	0.01195	0.00689	0.0006	1.38319	90.42285	1.67866	0.03482	28.67422	0.59005	0.65504	-0.00005	0.00038	0.01391	0.03964
1.94767	0.02194	-0.03915	0.00095	0.2954	85.35082	1.66231	0.18729	28.39713	3.17445	3.18693	0.0027	0.00295	-0.07909	0.09122

Sample#	Sample	Province	phase	Weight (g)	Plat.Age	Un. °Plat.
451	NCD Small	Standard	Sanidine	0.2031	28.018	0.126
452	PPD SMALL	Standard	Sanidine	0.2015	HT: 28.572	0.128
					LT:28.145	*0.106*
453	NCD Large	Standard	Sanidine	0.2013	28.412	0.046
454	PPD LARGE	Standard	Sanidine	0.1989	HT: 28.366	0.089
					LT:27.92	*0.122*
456	FCT	Standard	Sanidine	0.2018	28.004	0.069
461	FCT	Standard	Sanidine	0.1998	28.119	0.074

Sample 454 PPD Large Irradiated for 40h

40/39	38/39	37/39	36/39	39Ar (10-12.mol)	% 40Ar*	40Ar*/39Ar	Er.4039	Age(Ma)	Er.An.	Er.Tot.	Cl/K	Er.Cl/K	Ca/K	Er.Ca/K
2.37511	0.01031	0.95269	0.00285	1.23206	67.74642	1.61016	0.0478	27.4844	0.80968	0.85439	-0.0006	0.0006	1.92576	0.03252
1.82232	0.01209	0.1296	0.00075	2.25637	88.42577	1.61155	0.03944	27.50795	0.66809	0.72172	-0.00001	0.00024	0.26182	0.01153
1.96586	0.01091	0.06786	0.00114	6.10682	83.15268	1.63475	0.01067	27.90093	0.18066	0.33059	-0.00036	0.0001	0.13708	0.01016
2.32578	0.01141	0.0419	0.00237	4.7621	69.98315	1.6277	0.02102	27.7816	0.35597	0.45024	-0.00029	0.00015	0.08465	0.02138
2.58344	0.01139	0.02822	0.0032	3.61093	63.49554	1.6404	0.02546	27.99663	0.43116	0.51291	-0.00033	0.00019	0.05701	0.00921
2.36247	0.01182	0.01545	0.00245	6.15385	69.35045	1.6384	0.01835	27.96276	0.31077	0.41661	-0.00018	0.00012	0.03121	0.00453
1.97646	0.01119	0.03385	0.00115	6.54286	82.94725	1.63946	0.01667	27.98072	0.28237	0.39601	-0.00028	0.00011	0.06838	0.04092
1.85591	0.01157	-0.00313	0.00065	9.67624	89.6621	1.66405	0.00908	28.39705	0.15375	0.32097	-0.00015	0.00006	-0.00632	0.00719
1.8049	0.01155	0.00181	0.00049	15.13306	91.9757	1.66007	0.00696	28.32968	0.11782	0.30478	-0.00015	0.00004	0.00365	0.00196
1.81061	0.01099	-0.00084	0.00048	4.18535	92.13005	1.66811	0.02009	28.46591	0.34017	0.44213	-0.0003	0.00012	-0.00169	0.02871
1.85229	0.01123	0.00021	0.00061	2.1311	90.19236	1.67062	0.04249	28.50837	0.71943	0.77303	-0.00024	0.00024	0.00041	0.03237
1.90932	0.0106	-0.00819	0.00079	0.98843	87.73579	1.67515	0.07309	28.58502	1.23743	1.26952	-0.00043	0.00055	-0.01654	0.07368

Sample 456 FCT Irradiated for 40h

40/39	38/39	37/39	36/39	39Ar (10-12.mol)	% 40Ar*	40Ar*/39Ar	Er.4039	Age(Ma)	Er.An.	Er.Tot.	Cl/K	Er.Cl/K	Ca/K	Er.Ca/K
2.06115	0.01276	0.12171	0.0013	2.91376	81.80487	1.68627	0.02124	28.62953	0.35779	0.45683	0.00015	0.00023	0.24589	0.02444
1.83708	0.0101	0.32056	0.00041	1.31988	94.73906	1.74084	0.06804	29.54848	1.1455	1.1824	-0.00054	0.00066	0.64767	0.05191
1.74348	0.01157	0.23831	0.0004	6.18647	94.19942	1.64263	0.01056	27.89434	0.17799	0.32909	-0.00014	0.00012	0.48146	0.00845
1.7706	0.01143	0.1459	0.0005	3.83296	92.3021	1.63448	0.01728	27.75693	0.29118	0.40082	-0.00018	0.0002	0.29476	0.03366
1.82216	0.0111	0.11705	0.00061	6.55563	90.5063	1.64931	0.0092	28.00687	0.15501	0.31821	-0.00028	0.00009	0.23646	0.00824
1.74205	0.0108	0.05738	0.00033	7.59893	94.5884	1.64784	0.0129	27.98215	0.21731	0.35259	-0.00035	0.00011	0.1159	0.00717
1.71279	0.01094	0.01479	0.00019	6.16154	96.83395	1.65858	0.01113	28.16305	0.18755	0.33655	-0.0003	0.00022	0.02987	0.02215
1.70919	0.01093	0.0094	0.0002	7.9298	96.53798	1.65003	0.00743	28.01906	0.12523	0.30493	-0.00031	0.00014	0.019	0.02256
1.69877	0.01195	0.02271	0.00015	5.03043	97.40109	1.65465	0.01611	28.09688	0.27139	0.38907	-0.00002	0.00017	0.04588	0.01932
1.75074	0.01647	0.30962	0.00033	0.61352	95.72594	1.67628	0.07977	28.46134	1.34374	1.37309	0.00123	0.00083	0.62557	0.09585
1.90501	0.02795	1.49995	0.00126	0.08715	86.66402	1.65274	0.57452	28.06474	9.68033	9.68433	0.00438	0.0049	3.03317	0.78988
3.2625	0.03884	4.228	0.01363	0.02377	-13.21524	-0.43246	2.56169	-7.41614	44.02002	44.02009	0.00681	0.0196	8.56665	3.89574

Sample 461 FCT Irradiated for 40h

40/39	38/39	37/39	36/39	39Ar (10-12.mol)	% 40Ar*	40Ar*/39Ar	Er.4039	Age(Ma)	Er.An.	Er.Tot.	Cl/K	Er.Cl/K	Ca/K	Er.Ca/K
1.94602	0.00966	0.1345	0.00087	0.68109	87.33986	1.69981	0.04367	28.91199	0.73683	0.79068	-0.00069	0.00122	0.27171	0.1977
1.74119	0.01197	0.4525	0.0006	0.91745	91.84371	1.59969	0.0514	27.22186	0.86806	0.90913	-0.00003	0.00035	0.91434	0.08633
1.69545	0.0133	0.30277	0.00019	1.87993	98.12763	1.66407	0.03082	28.30876	0.52019	0.59118	0.00035	0.00043	0.61172	0.11238
1.68679	0.0114	0.25845	0.00023	2.06183	97.15324	1.63908	0.02737	27.8869	0.46217	0.53868	-0.00018	0.00026	0.52216	0.0676
1.69054	0.01187	0.18255	0.00018	4.74399	97.68579	1.65163	0.01708	28.09883	0.28829	0.40105	-0.00004	0.00005	0.3688	0.05588
1.68161	0.01187	0.15991	0.00017	3.9521	97.80563	1.6449	0.01584	27.98515	0.26738	0.3855	-0.00004	0.00013	0.32306	0.01585
1.68819	0.0124	0.10107	0.0001	3.92255	98.60292	1.66472	0.01587	28.31979	0.26782	0.38818	0.00011	0.00011	0.20418	0.03794
1.68543	0.01074	0.04888	0.0001	3.2977	98.46129	1.65956	0.01804	28.23266	0.30451	0.41376	-0.00035	0.00013	0.09874	0.02628
1.67924	0.01134	0.00486	0.00012	6.154	97.82092	1.64266	0.00955	27.94734	0.16124	0.32079	-0.00019	0.00012	0.00982	0.01214
1.67746	0.01109	0.01652	0.00007	12.1596	98.74438	1.65642	0.00645	28.17965	0.1089	0.30007	-0.00025	0.00005	0.03338	0.00712
1.70237	0.01153	0.12552	0.00018	2.8798	97.4358	1.65887	0.03333	28.22094	0.56257	0.62841	-0.00014	0.00026	0.25358	0.06058
1.96607	0.0059	0.75142	0.00125	0.44874	84.17728	1.65588	0.23614	28.17051	3.98604	3.99582	-0.00175	0.00095	1.51869	0.32573
7.42082	0.01098	0.15322	0.01547	0.03863	38.56196	2.86193	1.48508	48.41499	24.78891	24.79351	-0.00108	0.02027	0.30953	3.92707

Appendix B

Chapter IV K/Pg

Fig. 1. Panoramic picture of the alternations observed in a parallel section at the Red Deer River. Same amount of alternations from the Scollard Tuff to the Cretaceous/Palaeogene boundary are observed, suggesting for a regional continuity in the sedimentary deposits.
Supplementary tables.

Table.1 Lithological and chemical proxies used in this work for developing the cyclostratigraphic framework at the Knudsen's Family Farm section.

Fig.2 $^{40}Ar/^{39}Ar$ Table and figures SVI.2

Fig.3 Directions and projects of Paleomagnetic directions.

Table 4. U and Pb isotope results and calculated ages for zircons from the Coal nr. 13.

Table SVI-T5. U and Pb isotope results and calculated ages for zircons from the Coal nr. 14

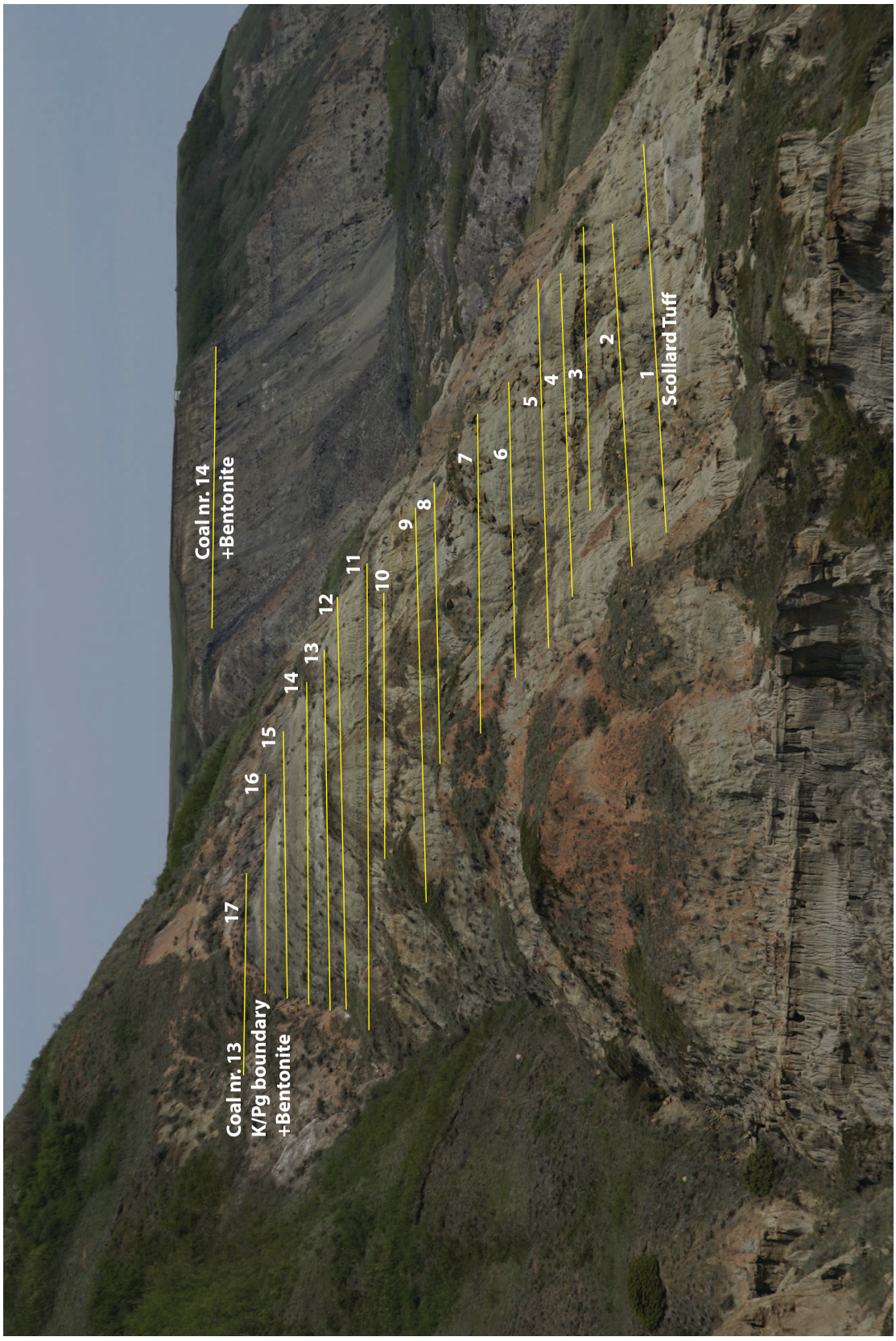
Coal nr. 14
+Bentonite
Coal nr. 13
K/Pg boundary
+Bentonite
Scollard Tuff
1
2
3
4
5
6
7
8
9
10
11
12
13
14
15
16
17

Fig. SIII-1

Supplementary Table SIII-T1. Lithological and chemical proxies used for developing the cyclostratigraphy at the Knudsen's Family Farm Section

Stratigraphic Height (cm)	Index of Alteration(1)	Fe#	Blueness or b*(D65)	Sr/(Rb+Sr)	Cr/V	Magnetic Susceptibility (no norm)	Silica-Titania Index(2)
-10	1.830	0.9980	6.15	0.8360	14.36	1.0807E-07	0.9600
10	1.857	0.9907	7.59	0.8527	13.33	1.0969E-07	0.9733
30	1.883	0.9833	9.03	0.8693	12.30	1.1131E-07	0.9866
50	1.860	0.9804	11.80	0.8757	12.40	1.0895E-07	0.9909
70	1.829	0.9797	14.64	0.8629	19.52	9.6088E-08	0.9634
90	2.000	0.9667	10.67	0.8697	25.85	9.1495E-08	0.9554
110	1.850	0.9920	7.27	0.8109	20.22	8.3937E-08	0.9762
130	1.562	0.9804	9.06	0.8296	18.93	1.0877E-07	0.9784
150	1.494	0.9810	11.43	0.8449	20.72	1.1618E-07	0.9668
170	1.527	0.9805	12.01	0.8416	21.20	1.1641E-07	0.9625
190	1.622	0.9755	10.82	0.8227	19.99	1.1344E-07	0.9675
210	1.686	0.9657	10.89	0.8195	18.82	1.1924E-07	0.9680
230	1.718	0.9510	12.27	0.8327	17.70	1.3414E-07	0.9640
250	1.751	0.9386	13.57	0.8418	16.97	1.4628E-07	0.9605
270	1.790	0.9415	14.36	0.8255	18.70	1.4102E-07	0.9600
290	1.829	0.9471	15.06	0.8047	20.87	1.3273E-07	0.9600
310	1.844	0.9512	15.41	0.7979	21.87	1.2726E-07	0.9600
330	1.832	0.9536	15.38	0.8059	21.65	1.2478E-07	0.9600
350	1.819	0.9538	14.99	0.8085	21.50	1.2165E-07	0.9595
370	1.800	0.9399	12.29	0.7766	21.81	1.1436E-07	0.9561
390	1.780	0.9235	9.17	0.7387	22.20	1.0634E-07	0.9521
410	1.731	0.9205	7.21	0.7264	19.11	9.8336E-08	0.9500
430	1.670	0.9361	7.29	0.7523	14.43	9.5624E-08	0.9512
450	1.715	0.9752	11.47	0.8332	21.84	1.1849E-07	0.9602
470	1.691	0.9882	9.47	0.8373	20.74	9.1232E-08	0.9731
490	1.715	0.9802	9.43	0.8224	19.90	8.2071E-08	0.9704
510	1.796	0.9584	12.56	0.8083	21.45	1.0188E-07	0.9527
530	1.795	0.9555	13.41	0.8196	22.61	1.0992E-07	0.9500
550	1.793	0.9546	13.01	0.8341	23.02	1.1483E-07	0.9500
569	1.868	0.9421	8.40	0.8369	19.61	1.1319E-07	0.9493
589	1.893	0.9135	11.64	0.8247	19.87	1.1058E-07	0.9435
609	1.889	0.9029	14.90	0.8233	21.37	1.1115E-07	0.9419

Supplementary Table SIII-T1. Lithological and chemical proxies used for developing the cyclostratigraphy at the Knudsen's Family Farm Section

Stratigraphic Height (cm)	Index of Alteration(1)	Fe#	Blueness or b*(D65)	Sr/(Rb+Sr)	Cr/V	Magnetic Susceptibility (no norm)	Silica-Titania Index(2)
629	1.865	0.9153	16.39	0.8364	23.31	1.1518E-07	0.9459
649	1.841	0.9274	17.16	0.8444	24.59	1.1787E-07	0.9500
669	1.816	0.9382	13.09	0.8170	21.39	1.1137E-07	0.9549
689	1.762	0.9529	9.25	0.8001	18.91	1.1722E-07	0.9615
709	1.542	0.9911	12.58	0.8856	25.67	2.0362E-07	0.9769
729	1.513	0.9984	13.82	0.9004	25.42	2.0473E-07	0.9778
749	1.526	0.9989	14.39	0.8978	23.46	1.8637E-07	0.9756
769	1.540	0.9993	14.96	0.8951	21.50	1.6800E-07	0.9734
789	1.553	0.9998	15.53	0.8924	19.55	1.4963E-07	0.9712
809	1.569	0.9944	14.86	0.8885	18.50	1.0774E-07	0.9700
829	1.540	0.9838	13.28	0.8864	19.36	5.9718E-08	0.9666
849	1.170	0.9824	15.22	0.9069	26.30	1.5749E-07	0.9392
869	0.735	0.9828	17.83	0.9316	34.42	2.8333E-07	0.9072
889	1.049	0.9678	18.36	0.9159	32.94	2.6770E-07	0.9223
909	1.760	0.9519	13.92	0.8538	22.97	1.4771E-07	0.9599
929	1.890	0.9568	7.45	0.8005	16.99	1.0341E-07	0.9604
949	1.847	0.9690	7.81	0.8042	17.27	9.8014E-08	0.9638
969	1.771	0.9826	9.51	0.8190	18.78	1.0022E-07	0.9678
989	1.757	0.9764	9.89	0.8268	19.48	1.0151E-07	0.9685
1009	1.817	0.9468	8.73	0.8265	19.21	1.0172E-07	0.9651
1029	1.877	0.9172	7.56	0.8262	18.95	1.0192E-07	0.9618
1049	1.892	0.9079	6.68	0.8307	17.76	1.0210E-07	0.9600
1069	1.852	0.9231	6.15	0.8411	15.48	1.0226E-07	0.9600
1089	1.800	0.9409	6.26	0.8558	13.58	1.0549E-07	0.9614
1109	1.664	0.9777	11.01	0.9021	14.45	1.3134E-07	0.9727
1129	1.586	0.9996	13.93	0.9301	15.48	1.4459E-07	0.9811
1149	1.598	0.9989	13.52	0.9285	16.05	1.3707E-07	0.9836
1169	1.611	0.9982	13.10	0.9267	16.61	1.2950E-07	0.9861
1189	1.623	0.9974	12.67	0.9250	17.18	1.2193E-07	0.9886
1209	1.643	0.9932	12.93	0.9180	18.27	1.1563E-07	0.9855
1229	1.673	0.9847	14.02	0.9045	20.01	1.1087E-07	0.9755
1249	1.726	0.9681	13.23	0.8840	20.52	1.0293E-07	0.9700

Supplementary Table SIII-T1. Lithological and chemical proxies used for developing the cyclostratigraphy at the Knudsen's Family Farm Section

Stratigraphic Height (cm)	Index of Alteration(1)	Fe#	Blueness or b*(D65)	Sr/(Rb+Sr)	Cr/V	Magnetic Susceptibility (no norm)	Silica-Titania Index(2)
1269	1.806	0.9413	10.09	0.8548	19.51	9.1032E-08	0.9700
1289	1.873	0.9172	7.55	0.8312	18.65	8.1140E-08	0.9690
1309	1.849	0.9133	9.59	0.8498	18.98	8.6573E-08	0.9606
1329	1.806	0.9136	12.59	0.8771	19.55	9.5190E-08	0.9506
1349	1.769	0.9151	15.27	0.8997	20.11	1.0356E-07	0.9423
1369	1.779	0.9256	15.51	0.8861	20.61	1.0998E-07	0.9475
1389	1.799	0.9380	15.24	0.8649	21.10	1.1599E-07	0.9555
1409	1.817	0.9435	14.51	0.8508	21.30	1.1699E-07	0.9590
1429	1.832	0.9402	13.18	0.8457	21.12	1.1162E-07	0.9568
1449	1.848	0.9369	11.85	0.8405	20.95	1.0622E-07	0.9546
1469	1.863	0.9335	10.53	0.8354	20.77	1.0083E-07	0.9524
1489	1.803	0.9252	10.05	0.8348	20.57	9.4190E-08	0.9504
1509	1.262	0.8834	14.93	0.8638	20.45	7.9766E-08	0.9500
1529	1.544	0.8854	9.92	0.8577	22.65	7.9518E-08	0.9500
1549	1.538	0.9074	8.25	0.8817	22.53	8.5926E-08	0.9413
1569	1.035	0.9429	13.51	0.9435	19.28	9.4955E-08	0.9288
1589	1.585	0.9906	14.14	0.8994	20.59	9.4109E-08	0.9693
1609	1.792	0.9976	13.90	0.8389	24.12	1.0282E-07	0.9698
1629	1.912	0.9792	11.99	0.8030	25.16	9.5595E-08	0.9533
1649	1.897	0.9341	13.10	0.8475	20.85	1.0524E-07	0.9500
1669	1.801	0.9525	11.73	0.8290	20.49	1.0107E-07	0.9500
1689	1.757	0.9593	9.69	0.8141	19.59	9.4488E-08	0.9471
1708	1.799	0.9327	7.97	0.8250	16.92	9.1307E-08	0.9407
1728	1.855	0.9265	8.51	0.8120	17.73	9.6479E-08	0.9363
1748	1.915	0.9249	9.54	0.7936	19.33	1.0351E-07	0.9323
1768	1.933	0.9236	11.36	0.8026	20.72	1.1121E-07	0.9343
1788	1.953	0.9073	10.55	0.8200	17.76	1.0076E-07	0.9357
1808	1.996	0.8922	7.56	0.8083	13.72	8.1867E-08	0.9309
1828	1.965	0.9064	8.30	0.8089	15.62	8.6154E-08	0.9328
1848	1.933	0.9208	9.07	0.8095	17.56	9.0568E-08	0.9348
1868	1.901	0.9352	9.83	0.8101	19.49	9.4983E-08	0.9368
1888	1.869	0.9496	10.59	0.8107	21.43	9.9398E-08	0.9388

Supplementary Table SIII-T1. Lithological and chemical proxies used for developing the cyclostratigraphy at the Knudsen's Family Farm Section

Stratigraphic Height (cm)	Index of Alteration(1)	Fe#	Blueness or b*(D65)	Sr/(Rb+Sr)	Cr/V	Magnetic Susceptibility (no norm)	Silica-Titania Index(2)
1908	1.853	0.9560	11.30	0.8128	22.18	1.0239E-07	0.9383
1928	1.858	0.9515	11.92	0.8169	21.30	1.0343E-07	0.9343
1948	1.864	0.9469	12.55	0.8211	20.42	1.0446E-07	0.9303
1968	1.870	0.9423	13.17	0.8253	19.53	1.0549E-07	0.9263
1988	1.876	0.9377	13.79	0.8295	18.64	1.0652E-07	0.9224
2008	1.886	0.9346	13.36	0.8237	18.11	1.0454E-07	0.9228
2028	1.899	0.9336	11.45	0.8038	18.08	9.8357E-08	0.9294
2048	1.912	0.9326	9.53	0.7838	18.05	9.2151E-08	0.9361
2068	1.907	0.9340	8.84	0.7781	18.40	9.0663E-08	0.9410
2088	1.874	0.9387	9.86	0.7924	19.28	9.5828E-08	0.9435
2108	1.842	0.9434	10.89	0.8069	20.17	1.0104E-07	0.9460
2128	1.809	0.9482	11.93	0.8214	21.06	1.0625E-07	0.9485
2148	1.821	0.9401	12.02	0.8176	21.29	1.0488E-07	0.9459
2168	1.895	0.9138	10.78	0.7879	20.58	9.4101E-08	0.9360
2188	1.915	0.9048	10.94	0.7807	20.17	9.0356E-08	0.9317
2208	1.856	0.9210	13.14	0.8065	20.21	9.6817E-08	0.9356
2228	1.805	0.9355	14.99	0.8291	20.33	1.0252E-07	0.9390
2248	1.833	0.9322	13.55	0.8209	21.10	1.0057E-07	0.9364
2268	1.881	0.9246	11.31	0.8054	22.03	9.6765E-08	0.9324
2288	1.877	0.9257	9.55	0.8015	22.30	9.6657E-08	0.9327
2308	1.816	0.9381	9.34	0.8122	21.46	1.0064E-07	0.9404
2328	1.867	0.9412	11.50	0.7902	20.06	9.3625E-08	0.9499
2348	1.883	0.9458	8.05	0.7538	19.43	8.6195E-08	0.9500
2368	1.854	0.9442	8.25	0.7681	19.15	8.6837E-08	0.9500
2388	1.814	0.9411	9.36	0.7949	18.94	8.9464E-08	0.9500
2408	1.774	0.9380	10.48	0.8218	18.74	9.2091E-08	0.9500
2428	1.734	0.9349	11.59	0.8487	18.53	9.4719E-08	0.9500
2448	1.715	0.9372	12.65	0.8659	18.85	1.0084E-07	0.9513
2468	1.726	0.9476	13.61	0.8687	19.96	1.1217E-07	0.9546
2488	1.738	0.9581	14.57	0.8714	21.07	1.2356E-07	0.9580
2508	1.750	0.9686	15.53	0.8740	22.18	1.3495E-07	0.9613
2528	1.761	0.9791	16.49	0.8767	23.29	1.4634E-07	0.9646

Supplementary Table SIII-T1. Lithological and chemical proxies used for developing the cyclostratigraphy at the Knudsen's Family Farm Section

Stratigraphic Height (cm)	Index of Alteration(1)	Fe#	Blueness or b*(D65)	Sr/(Rb+Sr)	Cr/V	Magnetic Susceptibility (no norm)	Silica-Titania Index(2)		
2548	1.773	0.9896	17.45	0.8794	24.40	1.5773E-07	0.9680		
2568	1.790	0.9896	17.34	0.8724	24.56	1.5845E-07	0.9684		
2588	1.816	0.9738	15.61	0.8508	23.28	1.4288E-07	0.9645		
2608	1.842	0.9578	13.86	0.8290	21.98	1.2714E-07	0.9605		
2628	1.868	0.9419	12.11	0.8072	20.69	1.1140E-07	0.9565		
2648	1.894	0.9259	10.36	0.7854	19.39	9.5660E-08	0.9525		
2668	1.892	0.9167	10.14	0.7794	19.78	8.9560E-08	0.9500		
2688	1.848	0.9181	12.30	0.7976	22.79	9.8389E-08	0.9500		
2708	1.799	0.9243	13.95	0.8116	24.43	1.0435E-07	0.9511		
2728	1.745	0.9379	14.77	0.8189	23.91	1.0556E-07	0.9539		
2748	1.691	0.9516	15.59	0.8260	23.35	1.0673E-07	0.9568		
2768	1.574	0.9635	16.08	0.8393	23.74	1.1192E-07	0.9566		
2788	0.817	0.9565	13.25	0.9165	33.85	1.5853E-07	0.9249		
2808	0.386	0.9503	10.98	0.9629	40.79	1.8648E-07	0.9026		
2828	0.738	0.9534	10.98	0.9343	38.67	1.6765E-07	0.9083		
2847	1.100	0.9566	11.01	0.9047	36.44	1.4824E-07	0.9142		
2867	1.461	0.9598	11.04	0.8751	34.21	1.2883E-07	0.9202		
2887	1.823	0.9630	11.07	0.8456	31.98	1.0942E-07	0.9262		
2907	2.005	0.9650	11.54	0.8431	27.11	1.0024E-07	0.9388		
2927	1.899	0.9650	12.73	0.8841	18.00	1.0752E-07	0.9620		
2947	1.789	0.9650	13.93	0.9258	8.84	1.1502E-07	0.9853		
2967	1.716	0.9688	14.62	0.9512	3.59	1.2001E-07	0.9998		
2987	1.700	0.9787	14.49	0.9504	4.69	1.2094E-07	1.0000		
3007	1.686	0.9887	14.36	0.9493	5.89	1.2182E-07	1.0000		
3027	1.660	0.9980	13.97	0.9492	6.88	1.2041E-07	1.0000		
3047	1.504	1.0000	10.93	0.9609	5.70	9.4094E-08	1.0000		
3067	1.313	1.0000	7.17	0.9757	3.92	6.0952E-08	1.0000		
3087	1.122	1.0000	3.40	0.9906	2.13	2.7809E-08	1.0000		
3107	1.000	1.0000	1.00	1.0000	1.00	1.2997E-08	1.0000	----------	K/Pg Boundary
3127	1.213	0.9719	4.02	0.9875	4.05	2.8568E-08	0.9973		
3147	1.368	0.9514	6.23	0.9783	6.28	4.4598E-08	0.9953		
3167	1.524	0.9308	8.44	0.9691	8.51	6.0627E-08	0.9933		

Supplementary Table SIII-T1. Lithological and chemical proxies used for developing the cyclostratigraphy at the Knudsen's Family Farm Section

Stratigraphic Height (cm)	Index of Alteration(1)	Fe#	Blueness or b*(D65)	Sr/(Rb+Sr)	Cr/V	Magnetic Susceptibility (no norm)	Silica-Titania Index(2)
3187	1.680	0.9102	10.65	0.9599	10.75	7.6656E-08	0.9913
3207	1.783	0.9048	12.66	0.9497	12.97	8.6704E-08	0.9893
3227	1.796	0.9250	14.32	0.9377	15.19	8.6683E-08	0.9873
3247	1.808	0.9456	15.98	0.9257	17.40	8.6502E-08	0.9853
3267	1.820	0.9661	17.64	0.9137	19.62	8.6321E-08	0.9833
3287	1.832	0.9867	19.30	0.9017	21.83	8.6140E-08	0.9813
3307	1.845	0.9977	19.54	0.8990	22.00	8.2309E-08	0.9772
3327	1.859	0.9923	17.37	0.9121	18.67	7.2240E-08	0.9696
3347	1.873	0.9866	15.15	0.9255	15.28	6.2065E-08	0.9619
3367	1.886	0.9809	12.93	0.9389	11.89	5.1890E-08	0.9542
3387	1.900	0.9752	10.72	0.9522	8.50	4.1715E-08	0.9465
3407	1.914	0.9695	8.50	0.9656	5.11	3.1540E-08	0.9388
3427	1.925	0.9624	6.51	0.9779	2.07	2.2986E-08	0.9320
3447	1.903	0.9376	7.16	0.9774	3.14	3.3787E-08	0.9348
3467	1.872	0.9076	8.58	0.9731	5.41	5.0229E-08	0.9406
3487	1.841	0.8776	10.01	0.9688	7.68	6.6670E-08	0.9463
3507	1.808	0.8704	11.45	0.9519	10.41	7.7964E-08	0.9510
3527	1.774	0.9033	12.93	0.9126	13.92	8.0190E-08	0.9538
3547	1.740	0.9370	14.41	0.8729	17.45	8.2244E-08	0.9567
3567	1.712	0.9675	15.46	0.8341	20.43	8.3295E-08	0.9588
3587	1.772	0.9587	11.26	0.8055	16.50	7.1956E-08	0.9516
3607	1.851	0.9375	5.95	0.7820	10.95	5.8602E-08	0.9417
3627	1.860	0.9074	6.45	0.7827	10.79	6.6104E-08	0.9333
3647	1.848	0.8747	8.68	0.7907	12.25	7.9853E-08	0.9253
3667	1.839	0.8562	10.45	0.7991	13.69	8.9192E-08	0.9209
3687	1.837	0.8634	11.40	0.8082	15.09	9.0573E-08	0.9230
3707	1.835	0.8712	12.34	0.8173	16.50	9.1792E-08	0.9252
3727	1.833	0.8789	13.28	0.8264	17.91	9.3010E-08	0.9274
3747	1.830	0.8857	14.18	0.8359	19.06	9.4326E-08	0.9291
3767	1.817	0.8797	14.69	0.8507	16.90	9.6909E-08	0.9233
3787	1.801	0.8697	15.07	0.8671	13.72	9.9879E-08	0.9153
3807	1.592	0.8669	13.80	0.8837	11.60	9.2839E-08	0.9115

Stratigraphic Height (cm)	Index of Alteration(1)	Fe#	Blueness or b*(D65)	Sr/(Rb+Sr)	Cr/V	Magnetic Susceptibility (no norm)	Silica-Titania Index(2)
3827	1.028	0.8774	9.51	0.9009	11.42	6.7343E-08	0.9153
3847	0.529	0.8897	5.39	0.9170	11.48	4.3666E-08	0.9184
3867	0.977	0.9215	4.50	0.9183	13.96	4.9345E-08	0.9100
3887	1.721	0.9595	4.61	0.9151	17.20	6.4145E-08	0.8981
3907	2.136	0.9851	5.91	0.9093	19.27	7.7774E-08	0.8970
3927	1.939	0.9877	9.46	0.8987	19.16	8.9215E-08	0.9165
3947	1.741	0.9872	12.89	0.8875	19.07	1.0012E-07	0.9353
3967	1.743	0.9534	14.11	0.8715	19.87	1.0441E-07	0.9367
3986	1.807	0.9090	14.63	0.8539	20.94	1.0663E-07	0.9327
4006	1.863	0.8797	13.55	0.8364	21.31	1.0349E-07	0.9301
4026	1.903	0.8790	9.43	0.8192	20.32	9.0189E-08	0.9300
4046	1.940	0.8793	5.53	0.8034	19.34	7.7409E-08	0.9302
4066	1.936	0.8832	5.48	0.8055	19.08	7.5270E-08	0.9326
4086	1.919	0.8883	6.68	0.8134	19.05	7.6537E-08	0.9358
4106	1.903	0.8934	7.88	0.8213	19.01	7.7805E-08	0.9390
4126	1.886	0.8986	9.08	0.8292	18.98	7.9072E-08	0.9422
4146	1.869	0.9037	10.28	0.8372	18.94	8.0340E-08	0.9454
4166	1.852	0.9088	11.48	0.8451	18.91	8.1607E-08	0.9486
4186	1.835	0.9139	12.67	0.8530	18.87	8.2875E-08	0.9518
4206	1.819	0.9190	13.87	0.8609	18.83	8.4142E-08	0.9550
4226	1.802	0.9241	15.07	0.8688	18.80	8.5410E-08	0.9582
4246	1.785	0.9292	16.27	0.8767	18.76	8.6677E-08	0.9614
4266	1.768	0.9344	17.47	0.8846	18.73	8.7945E-08	0.9646
4286	1.752	0.9395	18.66	0.8925	18.69	8.9212E-08	0.9678
4306	1.653	0.9423	19.05	0.9013	17.96	8.9918E-08	0.9653
4326	1.392	0.9406	17.82	0.9116	15.82	8.9506E-08	0.9517
4346	1.126	0.9388	16.55	0.9220	13.65	8.9063E-08	0.9377
4366	0.860	0.9370	15.28	0.9324	11.48	8.8620E-08	0.9237
4386	0.594	0.9352	14.01	0.9428	9.31	8.8178E-08	0.9097
4406	0.465	0.9360	13.29	0.9473	8.46	8.8349E-08	0.9029
4426	0.612	0.9420	13.67	0.9401	10.28	8.9760E-08	0.9104
4446	0.766	0.9481	14.09	0.9325	12.18	9.1206E-08	0.9184

Supplementary Table SIII-T1. Lithological and chemical proxies used for developing the cyclostratigraphy at the Knudsen's Family Farm Section

Stratigraphic Height (cm)	Index of Alteration(1)	Fe#	Blueness or b*(D65)	Sr/(Rb+Sr)	Cr/V	Magnetic Susceptibility (no norm)	Silica-Titania Index(2)
4466	0.921	0.9543	14.50	0.9249	14.08	9.2653E-08	0.9264
4486	1.075	0.9604	14.91	0.9173	15.98	9.4099E-08	0.9344
4506	1.230	0.9665	15.33	0.9097	17.87	9.5545E-08	0.9424
4526	1.385	0.9726	15.74	0.9021	19.77	9.6992E-08	0.9504
4546	1.539	0.9788	16.16	0.8945	21.67	9.8438E-08	0.9584

1. Nesbit, H.W., Young, G.M. 1982. Early Proterozoic climates and plate motions inferred from major element chemistry in lutites. Nature 299, 715-717.
2. de Jayawardena, U.S., Izawa, E. 1994. A new crititcal index of weathering for metamophic silicate rocks in tropical regions: a study from Sri Lanka. Eng. Geol. 36, 303-310.

Sample: 440 Scolle E

Irradiation Duration: 40

Sanidine

Results:

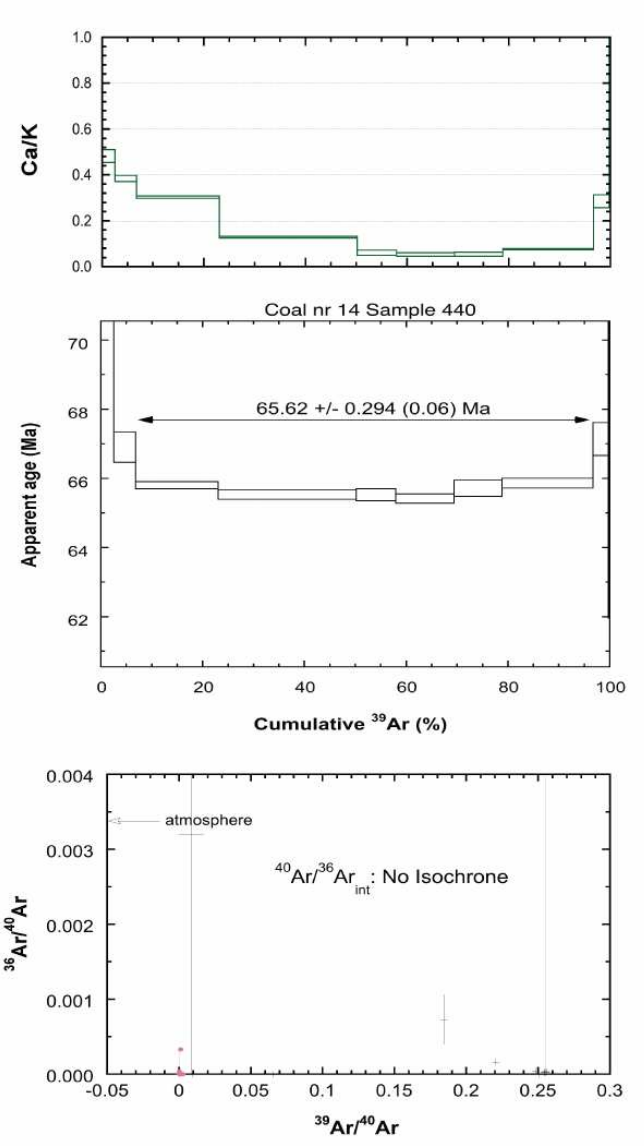

40/39	38/39	37/39	36/39	39Ar (10-12	% 40Ar*	40Ar*/39Ar	Er.4039	Age(Ma)	Er.An.	Er.Tot.	Cl/K	Er.Cl/K	Ca/K	Er.Ca/K
120.02757	2.00058	4.41109	0.38823	0.00058	4.71077	5.67224	193.76921	94.95796	3159.96642	3159.96656	0.53241	1.10181	8.93879	80.11193
4.53779	0.01602	0.23886	0.00084	1.1467	94.92879	4.30841	0.05639	72.57857	0.93111	1.17177	0.00107	0.00047	0.48258	0.02791
4.03077	0.01189	0.19029	0.00025	1.92903	98.50382	3.971	0.02922	66.99892	0.4839	0.81653	-0.00004	0.00032	0.38444	0.01303
3.92467	0.01133	0.14983	0.00013	7.36462	99.30195	3.89769	0.00701	65.78431	0.11615	0.65635	-0.00019	0.00014	0.30268	0.005
3.92264	0.0118	0.06385	0.00016	12.29091	98.90373	3.87982	0.00891	65.488	0.14763	0.65986	-0.00006	0.00006	0.12898	0.00317
3.91648	0.01213	0.03002	0.00013	3.5312	99.04712	3.87924	0.01148	65.4785	0.19027	0.6706	0.00003	0.0002	0.06064	0.01088
3.92355	0.01214	0.02638	0.00018	5.16544	98.691	3.87226	0.00892	65.36277	0.14795	0.65876	0.00003	0.00019	0.05329	0.00744
3.93301	0.01163	0.0267	0.00014	4.29539	98.94916	3.89176	0.01566	65.68595	0.25954	0.6953	-0.00011	0.00009	0.05393	0.00903
3.9289	0.012	0.03786	0.0001	8.09867	99.30217	3.90159	0.00972	65.84894	0.16108	0.66638	0	0.0001	0.07648	0.00265
3.99521	0.00713	0.14138	0.00007	1.36262	99.76746	3.98632	0.03144	67.25265	0.5207	0.84079	-0.00135	0.00054	0.28562	0.02811
5.42626	0.00253	0.59501	0.00433	0.10952	77.26458	4.19438	0.55268	70.69478	9.13504	9.16131	-0.00284	0.00714	1.20244	0.42127
15.35346	-0.292	-0.35328	0.02833	0.01226	45.2838	6.95086	6.29987	115.69011	101.56366	101.56984	-0.08566	0.03724	-0.71345	3.02621
107.33549	-0.19251	-0.05722	0.31623	0.00657	12.93672	13.88512	18.99237	224.15416	288.3205	288.32821	-0.07308	0.08755	-0.11557	3.23735

Sample: 468 K/Pg

Irradiation Duration: 60

Sanidine

Results:

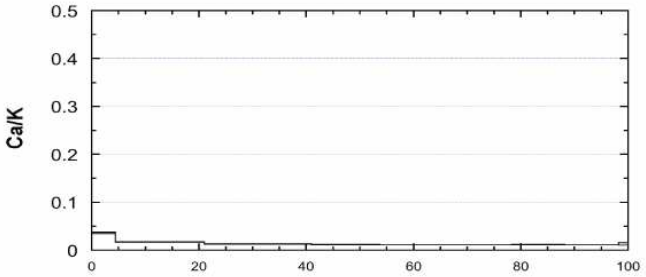

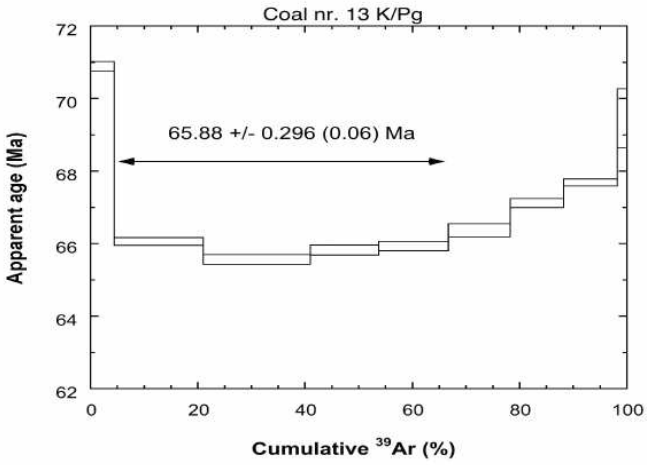

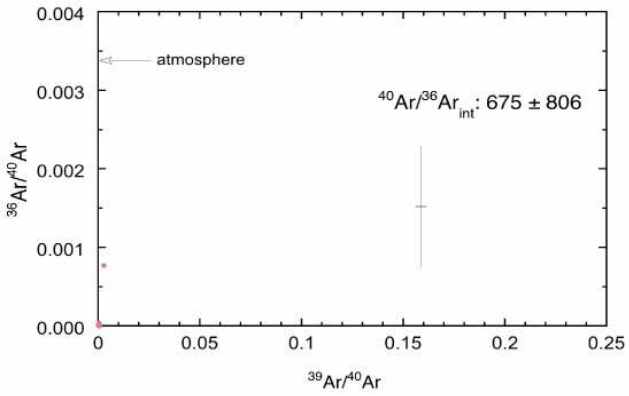

40/39	38/39	37/39	36/39	39Ar (10-14	40Ar*	40Ar*/39Ar	Er.4039	Age(Ma)	Er.An.	Er.Tot.	Cl/K	Er.Cl/K	Ca/K	Er.Ca/K
2.88253	0.01125	0.01803	0.00022	5.02189	97.75885	2.81796	0.00536	70.89093	0.13232	0.70764	-0.00022	0.00012	0.03641	0.0012
2.63863	0.01114	0.00874	0.00005	19.06486	99.38956	2.62254	0.00434	66.06365	0.10726	0.6575	-0.00024	0.00005	0.01765	0.00032
2.62659	0.01134	0.00647	0.00008	23.0377	99.08443	2.60255	0.00534	65.56907	0.13221	0.65735	-0.00019	0.00004	0.01306	0.00023
2.62472	0.01134	0.00575	0.00004	14.6421	99.55661	2.61309	0.00551	65.8299	0.13625	0.66064	-0.00019	0.00005	0.01161	0.00046
2.63253	0.01118	0.00567	0.00005	14.94142	99.42052	2.61729	0.00509	65.9337	0.12581	0.65954	-0.00023	0.0001	0.01145	0.00016
2.65723	0.0109	0.00575	0.00008	13.33383	99.15654	2.63483	0.00736	66.36742	0.18195	0.67654	-0.00031	0.00005	0.01161	0.00027
2.68874	0.01097	0.00588	0.00008	11.35595	99.1248	2.66522	0.00501	67.11901	0.12375	0.67038	-0.00029	0.00005	0.01187	0.00028
2.71492	0.01133	0.00567	0.00009	11.61923	99.0198	2.68832	0.00404	67.68984	0.09996	0.67184	-0.00019	0.00005	0.01145	0.00015
2.81229	0.01078	0.00663	0.00018	1.99815	98.14072	2.76001	0.03312	69.4607	0.81761	1.06433	-0.00035	0.00019	0.01339	0.00242
6.30076	0.04212	0.03872	0.00959	0.04599	55.06211	3.46943	1.4332	86.89067	35.04323	35.0535	0.00784	0.01178	0.07822	0.11354

Sample: 472

Irradiation Duration: 60

Sanidine

Results:

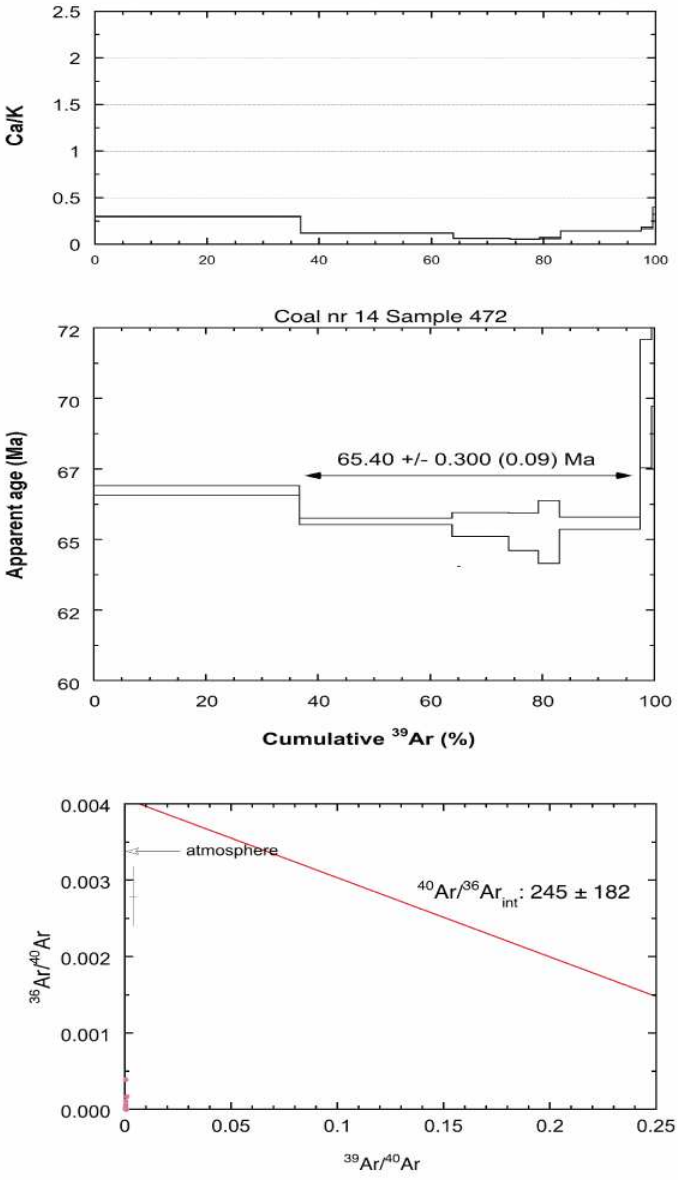

40/39	38/39	37/39	36/39	39Ar (10-12	% 40Ar*	40Ar*/39Ar	Er.4039	Age(Ma)	Er.An.	Er.Tot.	Cl/K	Er.Cl/K	Ca/K	Er.Ca/K
2.6025	0.01181	0.14892	0.00009	17.74448	99.41124	2.58745	0.00643	66.47863	0.1623	0.67256	-0.00005	0.00004	0.30085	0.00316
2.56716	0.01148	0.06175	0.00009	13.15341	99.15647	2.54562	0.00416	65.42294	0.1051	0.65105	-0.00015	0.00004	0.12475	0.00149
2.56855	0.01139	0.03305	0.0001	4.90073	98.93232	2.54119	0.01619	65.31112	0.40867	0.76055	-0.00017	0.00014	0.06677	0.00157
2.57307	0.0101	0.02771	0.00015	2.55457	98.3802	2.53145	0.02508	65.06529	0.63319	0.89963	-0.00053	0.00018	0.05597	0.00197
2.57794	0.01108	0.03377	0.00017	1.8269	98.18282	2.53115	0.04224	65.05785	1.06646	1.24324	-0.00026	0.00023	0.06821	0.00561
2.58205	0.01134	0.07162	0.00015	6.95203	98.48814	2.54314	0.00829	65.36058	0.20926	0.67516	-0.00019	0.0001	0.14468	0.00178
2.68978	0.01198	0.08813	-0.00003	0.98477	100.54011	2.70448	0.08647	69.42821	2.17761	2.28163	0	0.00036	0.17803	0.00857
2.95876	0.03192	0.18018	0.00042	0.24655	96.26011	2.84848	0.14738	73.05102	3.70417	3.77272	0.0055	0.00177	0.36402	0.03738
248.09994	-0.14899	0.09296	0.69221	0.0026	17.55733	43.56264	31.79441	883.61249	509.88816	509.93602	-0.08058	0.11794	0.18779	0.3082

Sample number	Stratigraphic Height (M)	Declination	Inclination
35.1	42.5	20.1	13
34.3	37.5	176	-29
37.4	37.4	274.1	-4.1
37.3	37.3	52.1	-9.1
27.7	27.7	157.5	-26.4
27.3	27.3	174.1	-4.1
25.2	15.8	229.9	-36.8
26	15.4	174	-2
24.2	15	155	-32.6
24.1	14.9	177.7	-75.5
22	12	303	58
21.1	11.5	155.8	-9.8
12.1	8.5	110.1	-23.7
t3	7.8	135	-20.3
t4	7.7	133.3	-64.4
14.1	7.3	157.1	-23.9
15.1	6.8	108	-68.5
15.2	6.7	140	-60.3
10.1	6.4	343	39.5
10.2	6.2	350	51.5
1.1	4	324	26.8
2.1	3.8	210	-71.5
3.2	3.5	343	61.6
8.1	1.9	309.7	69.7
10.2	1.3	346	41
10.1	1.2	342	41.8
11.1	0.2	14.2	42.8
11.2	0.1	10.3	34.3

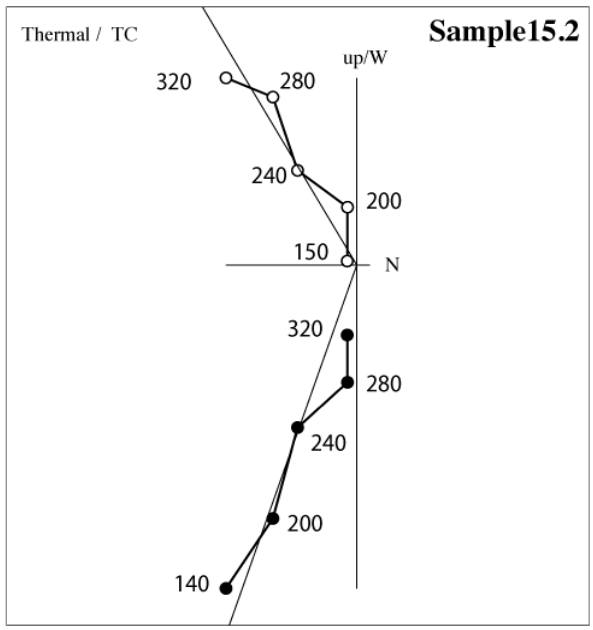

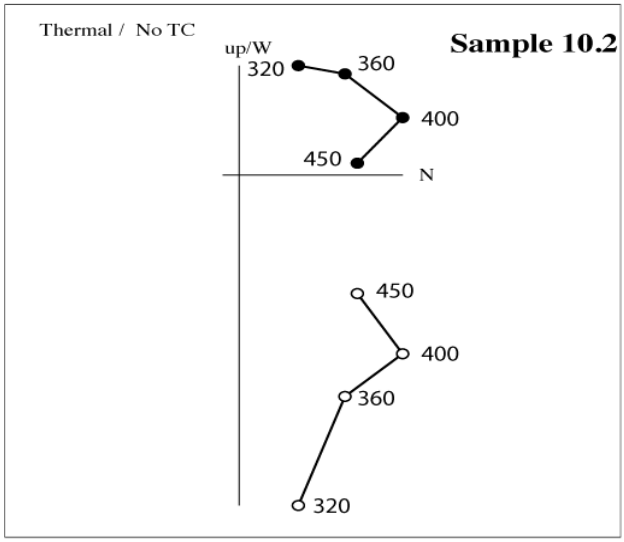

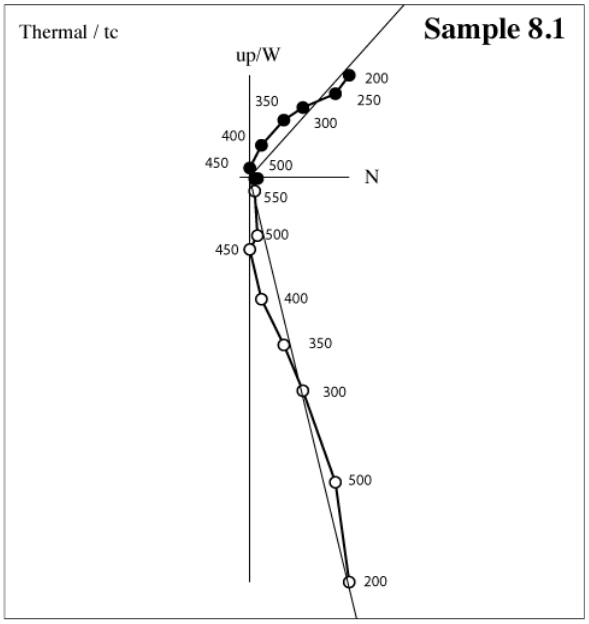

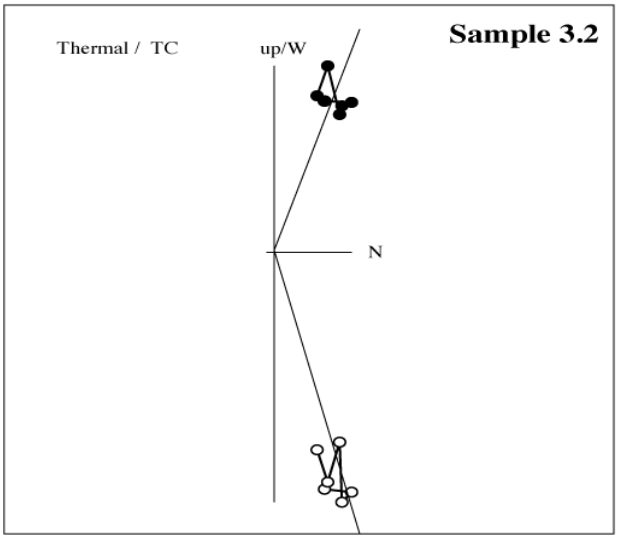

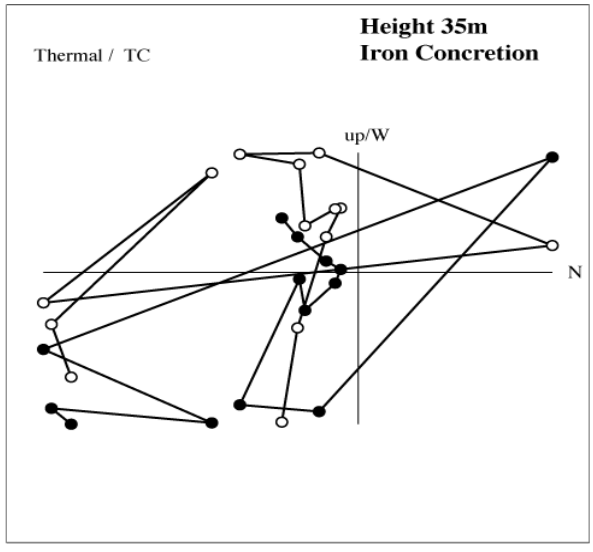

		Compositional Parameters								Radiogenic Isotope Ratios								Isotopic Ages					
Sample	Wt. mg	U ppm	Th/U	Pb ppm	206Pb* x10-13 mol	mol % 206Pb*	Pb*/Pbc	Pbc (pg)	206Pb/204Pb	208Pb/206Pb	207Pb/206Pb	% err	207Pb/235U	% err	206Pb/238U	% err	corr. coef.	207Pb/206Pb	±	207Pb/235U	±	206Pb/238U	±
(a)	(b)	(c)	(d)	(c)	(e)	(e)	(e)	(e)	(f)	(g)	(g)	(h)	(g)	(h)	(g)	(h)		(i)	(h)	(i)	(h)	(i)	(h)
Coal 14																							
3TF	0.01	43.50	0.432	0.609	0.185	0.9056	2.90	1.56	199.12	0.1385	0.0474	2.13	0.0667	2.24	0.0102	0.17	0.66	67.185	50.662	65.528	1.421	65.483	0.112
7MF	0.01	119.95	0.375	1.369	0.510	0.9677	8.77	1.40	572.53	0.1202	0.0473	1.09	0.0666	1.16	0.0102	0.16	0.47	66.226	26.034	65.508	0.737	65.488	0.105
6RF	0.01	35.36	0.571	0.523	0.151	0.8974	2.73	1.40	183.25	0.1840	0.0476	4.02	0.0671	4.22	0.0102	0.26	0.78	81.411	95.457	65.940	2.695	65.514	0.169
10RF	0.01	56.20	0.403	0.727	0.239	0.9308	3.96	1.47	266.75	0.1292	0.0473	2.17	0.0667	2.28	0.0102	0.24	0.48	66.752	51.670	65.553	1.446	65.520	0.158
1TF	0.01	41.40	0.340	0.575	0.176	0.9037	2.72	1.54	192.37	0.1091	0.0474	2.20	0.0668	2.30	0.0102	0.25	0.44	67.328	52.334	65.657	1.461	65.612	0.163
2RF	0.01	118.99	0.411	1.414	0.508	0.9578	6.87	1.80	447.56	0.1316	0.0473	1.49	0.0668	1.53	0.0102	0.24	0.25	65.575	35.384	65.647	0.971	65.649	0.154
9TF	0.01	27.56	0.350	0.419	0.118	0.8753	2.04	1.38	148.90	0.1121	0.0474	2.19	0.0670	2.32	0.0103	0.23	0.60	67.921	52.145	65.821	1.481	65.763	0.150
6MF	0.01	56.35	0.359	0.712	0.241	0.9362	4.30	1.34	290.40	0.1152	0.0473	2.06	0.0669	2.17	0.0103	0.24	0.50	65.786	48.900	65.788	1.380	65.788	0.160
5RF	0.01	39.85	0.280	0.566	0.170	0.8933	2.39	1.67	174.47	0.0897	0.0473	1.71	0.0670	1.81	0.0103	0.25	0.47	66.509	40.593	65.839	1.154	65.820	0.164
9RF	0.01	55.99	0.341	0.694	0.239	0.9407	4.65	1.23	316.86	0.1093	0.0473	2.12	0.0670	2.23	0.0103	0.19	0.59	66.144	50.518	65.836	1.421	65.828	0.124
1MF	0.01	41.40	0.318	0.553	0.177	0.9160	3.14	1.34	220.32	0.1019	0.0473	1.97	0.0670	2.09	0.0103	0.23	0.55	66.416	46.891	65.875	1.330	65.860	0.148
7TF	0.01	38.19	0.368	0.517	0.163	0.9156	3.16	1.24	219.16	0.1180	0.0474	3.80	0.0671	3.91	0.0103	0.27	0.45	67.317	90.452	65.912	2.498	65.874	0.174
3MF	0.01	40.01	0.402	0.577	0.172	0.8966	2.59	1.61	182.33	0.1289	0.0473	2.73	0.0671	2.87	0.0103	0.23	0.63	66.062	64.943	65.982	1.831	65.980	0.149
4TF	0.01	33.27	0.395	0.495	0.143	0.8869	2.33	1.49	165.86	0.1267	0.0474	2.73	0.0674	2.84	0.0103	0.21	0.57	68.014	64.850	66.218	1.821	66.169	0.138
2TF	0.01	25.99	0.481	0.426	0.112	0.8602	1.86	1.49	132.37	0.1543	0.0474	3.91	0.0674	4.07	0.0103	0.33	0.54	68.011	92.893	66.246	2.611	66.197	0.215
3RF	0.01	37.25	0.341	0.532	0.160	0.8979	2.55	1.50	181.69	0.1094	0.0474	1.58	0.0674	1.65	0.0103	0.22	0.37	67.120	37.582	66.234	1.058	66.210	0.147
6TF	0.01	37.19	0.515	0.534	0.160	0.9068	2.99	1.34	202.48	0.1650	0.0474	4.08	0.0675	4.25	0.0103	0.24	0.71	66.956	97.145	66.281	2.729	66.262	0.161
4MF	0.01	27.58	0.333	0.487	0.119	0.8273	1.40	2.03	108.30	0.1069	0.0474	3.20	0.0677	3.37	0.0104	0.33	0.56	67.535	76.003	66.540	2.170	66.513	0.217
2MF	0.01	27.42	0.508	0.443	0.119	0.8694	2.02	1.47	141.62	0.1628	0.0474	4.07	0.0679	4.16	0.0104	0.28	0.38	67.081	96.724	66.698	2.688	66.687	0.183
8TF	0.01	38.00	0.366	0.530	0.166	0.9129	3.01	1.32	208.31	0.1172	0.0474	2.61	0.0684	2.67	0.0105	0.25	0.26	69.141	62.140	67.135	1.733	67.079	0.166

(a) Samples are labels for fractions composed of single zircon grains or fragments; all fractions annealed and chemically abraded after Mattinson (2005).
(b) Nominal fraction weights estimated from photomicrographic grain dimensions, adjusted for partial dissolution during chemical abrasion.
(c) Nominal U and total Pb concentrations subject to uncertainty in photomicrographic estimation of weight and partial dissolution during chemical abrasion.
(d) Model Th/U ratio calculated from radiogenic 208Pb/206Pb ratio and 207Pb/235U age.
(e) Pb* and Pbc represent radiogenic and common Pb, respectively; mol % 206Pb* with respect to radiogenic, blank and initial common Pb.
(f) Measured ratio corrected for spike and fractionation only.
SEM analyses, based on analysis of NBS982 and CRM-U500.
(g) Corrected for fractionation, spike, and common Pb; up to 1 pg of common Pb was assumed to be procedural blank: 206Pb/204Pb = 18.55 ± 0.90%; 207Pb/204Pb = 15.62 ± 0.52%; 208Pb/204Pb = 38.45 ± 0.75% (all uncertainties 1-sigma). Excess over blank was assigned to initial common Pb.
(h) Errors are 2-sigma, propagated using the algorithms of Schmitz and Schoene (2007) and Crowley et al. (2007).
(i) Calculations are based on the decay constants of Jaffey et al. (1971). 206Pb/238U and 207Pb/206Pb ages corrected for initial disequilibrium in 230Th/238U using Th/U [magma] = 3.
(j) Corrected for fractionation, spike, and blank Pb only.

Appendix C

Chapter V. C-M

Table -T1. Chemical and lithological proxies used for developing the cyclostratigraphy at the Morrin Bridge section.

Table T2. U and Pb isotope results and calculated ages for zircons from the bentonite at the top of the section.

Fig. T1&2 Paleomagnetic curie temperature graph and $^{40}Ar/^{39}Ar$ data

Table T3. U and Pb isotope results and calculated ages for zircons from the bentonite at the bottom of the section.

Table SIV-T1. Chemical and lithological proxies used to develop the cyclostratigraphy at the Morrin Bridge section.

Stratigraphic Height (cm)	CAI(%)(1)	Vogt Index (2)	Fe#	K/Si	Zr/Al	Ti/Al	100*Rb/Ti	L*(D65)
-150	50.35	1.20	0.960	0.42	0.240	0.390	0.390	42.69
-140	56.69	3.59	0.926	0.73	0.310	0.548	0.979	39.83
-130	58.70	4.54	0.930	0.77	0.320	0.575	1.025	40.63
-120	59.88	5.16	0.938	0.76	0.319	0.578	0.987	41.83
-110	60.45	5.30	0.934	0.76	0.314	0.572	0.986	41.65
-100	60.93	5.35	0.928	0.76	0.308	0.564	0.992	41.23
-90	61.40	5.39	0.922	0.76	0.302	0.556	0.998	40.81
-80	61.87	5.44	0.916	0.76	0.296	0.548	1.004	40.39
-70	62.31	5.49	0.912	0.76	0.289	0.543	1.010	40.04
-60	62.56	5.52	0.918	0.75	0.276	0.554	1.021	40.09
-50	62.78	5.55	0.927	0.74	0.262	0.568	1.032	40.22
-40	62.99	5.57	0.935	0.73	0.248	0.582	1.044	40.35
-30	60.90	5.13	0.948	0.69	0.274	0.576	1.020	38.63
-20	56.06	4.14	0.965	0.64	0.348	0.544	0.955	34.72
-11	51.22	3.14	0.982	0.58	0.422	0.513	0.889	30.81
-1	47.65	2.54	0.995	0.54	0.477	0.492	0.857	27.34
9	53.79	4.96	0.981	0.68	0.387	0.550	1.074	27.15
19	60.98	7.54	0.961	0.82	0.279	0.618	1.318	27.97
29	60.53	6.36	0.941	0.86	0.260	0.625	1.365	31.32
39	58.70	4.61	0.924	0.87	0.260	0.622	1.369	34.79
49	58.93	4.82	0.929	0.88	0.260	0.632	1.370	34.87
59	59.60	5.47	0.939	0.88	0.260	0.646	1.370	34.20
69	60.21	6.08	0.949	0.89	0.262	0.660	1.370	33.58
79	60.25	6.47	0.955	0.90	0.276	0.683	1.375	33.30
89	60.17	6.80	0.960	0.90	0.293	0.708	1.380	33.11
99	60.09	7.13	0.965	0.91	0.311	0.733	1.385	32.92
109	60.03	7.44	0.969	0.92	0.326	0.753	1.389	32.74

Table SIV-T1. Chemical and lithological proxies used to develop the cyclostratigraphy at the Morrin Bridge section.

Stratigraphic Height (cm)	CAI(%)(1)	Vogt Index (2)	Fe#	K/Si	Zr/Al	Ti/Al	100*Rb/Ti	L*(D65)
119	60.21	7.45	0.968	0.91	0.319	0.735	1.388	32.64
129	60.45	7.40	0.965	0.91	0.306	0.708	1.385	32.55
139	60.68	7.35	0.963	0.90	0.294	0.681	1.383	32.47
149	60.87	7.25	0.959	0.89	0.282	0.655	1.379	32.37
159	60.64	6.74	0.948	0.89	0.274	0.644	1.365	32.11
169	60.31	6.12	0.935	0.90	0.267	0.637	1.349	31.82
179	54.95	4.86	0.927	0.92	0.284	0.642	1.282	35.28
189	34.96	2.26	0.942	0.98	0.372	0.681	1.011	53.10
199	59.97	6.17	0.925	0.86	0.264	0.616	1.115	41.93
209	64.99	7.24	0.931	0.84	0.246	0.617	1.127	37.58
219	64.32	7.51	0.943	0.84	0.254	0.637	1.112	35.25
229	63.65	7.77	0.956	0.85	0.261	0.657	1.097	32.92
239	63.10	8.01	0.966	0.86	0.268	0.674	1.082	30.80
248	64.03	7.94	0.957	0.85	0.259	0.661	1.065	31.06
258	65.38	7.78	0.942	0.83	0.247	0.638	1.048	32.02
268	66.74	7.62	0.927	0.81	0.234	0.616	1.030	32.98
278	67.28	7.34	0.915	0.80	0.224	0.598	1.004	33.90
288	57.45	5.55	0.932	0.81	0.237	0.629	0.868	34.38
298	44.46	3.30	0.959	0.84	0.257	0.675	0.699	34.71
308	33.07	1.25	0.981	0.86	0.275	0.712	0.550	35.64
318	43.30	1.88	0.945	0.77	0.268	0.611	0.673	44.71
328	59.50	3.31	0.894	0.66	0.259	0.476	0.871	55.72
338	63.30	3.89	0.893	0.64	0.335	0.474	0.913	57.72
348	63.06	4.20	0.909	0.66	0.438	0.516	0.906	56.79
358	62.83	4.51	0.925	0.68	0.542	0.558	0.898	55.86
368	62.59	4.82	0.941	0.70	0.646	0.600	0.890	54.93
378	62.24	5.08	0.956	0.72	0.740	0.638	0.878	53.88

Stratigraphic Height (cm)	CAI(%)(1)	Vogt Index (2)	Fe#	K/Si	Zr/Al	Ti/Al	100*Rb/Ti	L*(D65)
388	59.93	4.57	0.965	0.72	0.683	0.613	0.800	51.04
398	56.95	3.80	0.971	0.72	0.573	0.568	0.701	47.57
408	53.97	3.03	0.977	0.71	0.463	0.522	0.601	44.11
418	51.00	2.25	0.983	0.71	0.354	0.476	0.502	40.64
428	48.52	1.59	0.986	0.71	0.248	0.430	0.420	37.72
438	55.10	2.83	0.947	0.71	0.204	0.389	0.667	44.61
448	64.16	4.66	0.896	0.70	0.186	0.356	1.017	54.64
458	56.65	4.03	0.908	0.73	0.203	0.450	1.010	55.12
468	42.86	2.48	0.945	0.77	0.233	0.593	0.867	51.99
478	29.81	1.01	0.979	0.81	0.262	0.729	0.731	49.04
488	32.02	1.16	0.977	0.80	0.276	0.721	0.726	49.91
498	40.25	1.95	0.959	0.77	0.283	0.656	0.773	52.31
508	48.48	2.75	0.942	0.74	0.291	0.591	0.821	54.70
517	56.45	3.52	0.925	0.72	0.298	0.529	0.868	57.00
527	58.54	3.76	0.930	0.72	0.293	0.525	0.915	57.28
537	58.18	3.79	0.943	0.73	0.283	0.545	0.961	56.72
547	57.89	3.83	0.956	0.74	0.273	0.564	1.007	56.10
557	59.17	4.09	0.954	0.73	0.273	0.563	1.027	53.94
567	61.14	4.43	0.946	0.71	0.277	0.553	1.037	51.10
577	63.10	4.78	0.938	0.69	0.281	0.543	1.047	48.26
587	65.07	5.13	0.930	0.67	0.285	0.533	1.057	45.42
597	66.67	5.44	0.922	0.65	0.288	0.523	1.066	42.65
607	57.97	4.62	0.911	0.65	0.270	0.511	1.027	41.86
617	44.50	3.28	0.899	0.67	0.243	0.499	0.968	41.98
627	31.04	1.94	0.886	0.69	0.216	0.486	0.908	42.10
637	18.34	0.68	0.875	0.71	0.189	0.475	0.851	42.16
647	30.92	1.94	0.901	0.71	0.204	0.508	0.900	40.15

Table SIV-T1. Chemical and lithological proxies used to develop the cyclostratigraphy at the Morrin Bridge section.

Stratigraphic Height (cm)	CAI(%)(1)	Vogt Index (2)	Fe#	K/Si	Zr/Al	Ti/Al	100*Rb/Ti	L*(D65)	
657	55.32	4.38	0.945	0.69	0.238	0.562	0.998	37.20	
667	64.00	5.17	0.951	0.69	0.245	0.571	1.041	36.90	
677	64.84	5.15	0.938	0.68	0.239	0.558	1.058	37.91	Maastrichtian
687	65.63	5.13	0.925	0.68	0.233	0.545	1.074	38.92	-------- Campanian
697	64.89	5.27	0.937	0.68	0.274	0.577	1.043	39.47	Boundary
707	63.33	5.47	0.961	0.69	0.338	0.631	0.989	39.83	
717	61.68	5.09	0.970	0.70	0.377	0.657	0.980	42.35	
727	60.01	4.41	0.970	0.72	0.402	0.666	0.994	46.02	
737	59.81	4.06	0.977	0.67	0.453	0.660	0.967	49.54	
747	60.48	3.91	0.985	0.58	0.513	0.644	0.920	52.72	
757	65.07	4.86	0.939	0.64	0.334	0.550	1.035	43.55	
767	65.53	4.97	0.923	0.67	0.243	0.507	1.113	42.58	
776	62.43	4.26	0.943	0.63	0.277	0.516	1.117	50.13	
786	62.71	4.20	0.940	0.61	0.300	0.520	1.052	48.90	
796	64.91	4.53	0.926	0.59	0.315	0.520	0.950	42.69	
806	64.35	4.73	0.950	0.57	0.324	0.499	1.003	45.45	
816	63.20	4.87	0.973	0.55	0.322	0.471	1.099	51.42	
826	65.96	4.99	0.911	0.56	0.285	0.464	1.011	49.44	
836	67.31	4.83	0.865	0.57	0.245	0.456	0.874	46.11	
846	62.04	3.57	0.908	0.56	0.205	0.433	0.615	40.46	
856	56.21	2.23	0.960	0.55	0.166	0.409	0.350	34.67	
866	56.59	2.86	0.971	0.58	0.184	0.406	0.574	37.78	
876	60.99	4.76	0.956	0.64	0.238	0.416	1.114	46.57	
886	63.29	5.67	0.947	0.68	0.257	0.438	1.291	48.19	
896	64.19	5.93	0.942	0.69	0.252	0.468	1.226	45.02	
906	65.10	6.20	0.937	0.71	0.247	0.498	1.161	41.85	
916	65.98	6.46	0.932	0.72	0.242	0.528	1.097	38.70	

Table SIV-T1. Chemical and lithological proxies used to develop the cyclostratigraphy at the Morrin Bridge section.

Stratigraphic Height (cm)	CAI(%)(1)	Vogt Index (2)	Fe#	K/Si	Zr/Al	Ti/Al	100*Rb/Ti	L*(D65)
936	61.31	5.31	0.949	0.76	0.265	0.591	1.121	39.01
946	58.13	4.51	0.961	0.79	0.281	0.623	1.153	40.02
956	54.96	3.72	0.973	0.81	0.297	0.655	1.185	41.03
966	51.80	2.93	0.985	0.83	0.313	0.686	1.216	42.04
976	52.76	3.09	0.980	0.83	0.309	0.694	1.184	43.13
986	56.81	3.96	0.964	0.81	0.289	0.684	1.105	44.26
996	60.85	4.83	0.947	0.80	0.269	0.674	1.024	45.40
1006	61.60	4.43	0.948	0.77	0.232	0.606	0.836	46.39
1016	59.75	3.04	0.963	0.74	0.182	0.491	0.562	47.26
1026	52.39	1.93	0.976	0.72	0.210	0.468	0.385	45.06
1035	40.59	1.06	0.985	0.73	0.299	0.518	0.285	40.40
1045	37.71	1.06	0.992	0.74	0.393	0.589	0.375	38.46
1055	42.23	1.80	0.995	0.76	0.489	0.679	0.620	38.78
1065	46.76	2.54	0.998	0.78	0.585	0.768	0.866	39.10
1075	50.57	2.89	0.984	0.77	0.555	0.769	0.966	38.77
1085	53.75	2.90	0.954	0.74	0.416	0.693	0.939	37.87
1095	56.94	2.91	0.924	0.71	0.276	0.616	0.913	36.98
1105	58.54	3.06	0.923	0.68	0.225	0.572	0.950	39.50
1115	58.70	3.34	0.946	0.63	0.253	0.556	1.046	45.12
1125	59.16	3.57	0.963	0.60	0.270	0.540	1.111	49.01
1135	61.33	3.54	0.936	0.62	0.226	0.527	1.005	43.09
1145	53.37	2.85	0.936	0.74	0.308	0.644	0.812	38.52
1155	35.40	1.58	0.968	0.95	0.519	0.887	0.561	36.73
1165	17.43	0.30	1.000	1.17	0.730	1.130	0.310	34.93

1. Nesbit, H.W., Young, G.M. 1982. Early Proterozoic climates and plate motions inferred from major element chemistry in lutites. Nature 299, 715-717.
2. Vogt, T. 1927. Sulitjelmafeltets geologi og petrografi . Norges Geologiske Undersokelse 121, 1-560.

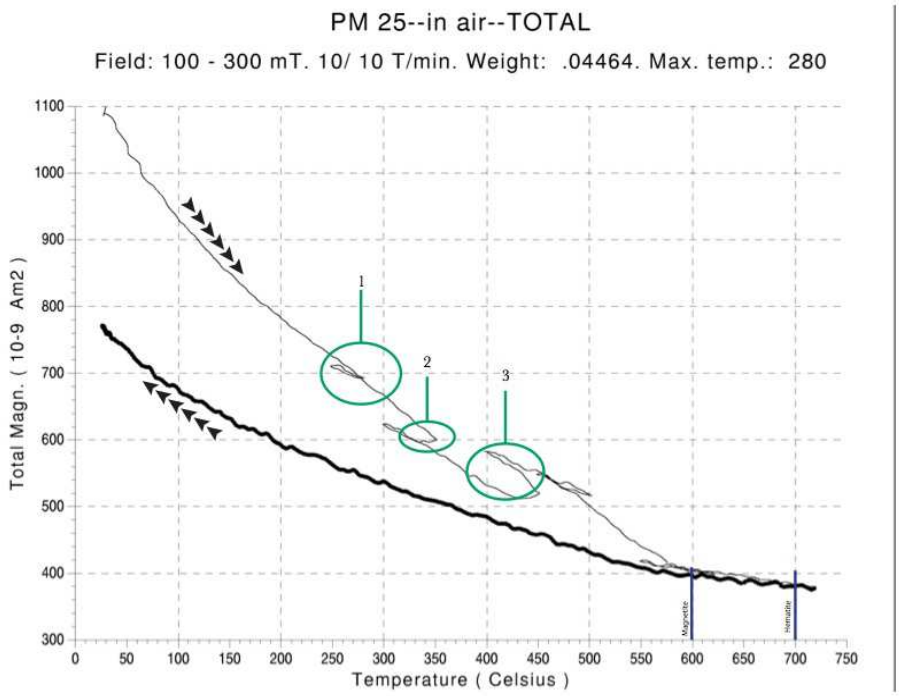

(Above) Curie temperature graph of a typical Morrin Bridge sample. The graph indicates (1,2,3) the difficulty of interpreting these samples and how even at low temperatures ~250oc the mineralogy is being chemically altered to alter the ferromagnetic minerals such as Greigite, thus distorting the signal. No suitable magnetostratigraphy could be deduced from this section.

Next Page 40Ar-39Ar age spectrums for all four samples, each sample hampered as no plateau can be attained . In addition, all isochrones are outside error to $^{36}Ar/^{40}Ar$ atmospheric ratio. All samples exhibit saddle shaped spectrum indicating the presence of excess argon, therefore these results were not included as only high precision ages can be utlised to fix cyclostratigraphic interpretations to the closest cycle.

Sample Number	Sample	Locality	Mineral	Mass (g)	Size Fraction	Age Plat (Ma)	Un. °Plat.	Total Gas Age (Ma)	Total Gas age Unc
444	MB1A	Knudends	Sanidine	0.2004	125-250	no-plateau		98.002	1.63
467	MB-1.5	Standard	Sanidine	0.2008	60-125	no plateau	no plateau	111.552	2.01
469	MB-32	Canada	Sanidine	0.1066	125-250	no plateau	no plateau	98.447	0.6
471	MB-3	Canada	Sanidine	0.1058	125-250	no plateau	no plateau	189.328	0.96

Sample 444 MB1A Morrin Bridge Irradiated for 40h

40/39	38/39	37/39	36/39	39Ar (10-12.mol)	% 40Ar*	40Ar*/39Ar	Er.4039	Age(Ma)	Er.An.	Er.Tot.	Cl/K	Er.Cl/K	Ca/K	Er.Ca/K
9.01898	0.0109	3.61519	0.006	0.96678	83.51402	7.55177	0.09799	125.38992	1.57174	1.98435	-0.00057	0.00079	7.32175	0.07756
5.98781	0.01569	8.64393	0.0036	0.35087	93.65674	5.64311	0.24694	94.51192	4.02941	4.13328	0.00096	0.00208	17.57008	0.1769
5.51487	0.01302	2.56367	0.00131	1.02467	96.67622	5.34143	0.04184	89.5826	0.68453	1.11012	0.00025	0.00058	5.1882	0.05273
5.36305	0.00801	3.08764	0.0015	1.0172	96.29674	5.17595	0.10825	86.87307	1.77389	1.96622	-0.00114	0.00086	6.25093	0.06298
5.45032	0.0088	2.74391	0.00157	0.46474	95.43982	5.21208	0.12308	87.46499	2.01618	2.18951	-0.00093	0.00158	5.55366	0.06253
6.10229	0.00653	1.74612	0.00242	0.75699	90.53482	5.53166	0.06259	92.69239	1.02225	1.36431	-0.00162	0.00115	3.53161	0.03895
6.52595	0.00963	1.46469	0.00296	0.53955	88.37674	5.77351	0.11485	96.63837	1.87182	2.09502	-0.00079	0.00208	2.96179	0.03545
6.95142	0.00994	1.11489	0.00283	0.90149	89.239	6.20836	0.06166	103.71171	1.00104	1.42052	-0.0007	0.00069	2.25389	0.03124
6.77824	0.02735	1.82731	0.00308	0.45608	88.68847	6.01944	0.04742	100.6421	0.77113	1.24612	0.00412	0.00147	3.69603	0.03742
6.4505	0.02499	4.69898	0.0062	0.14437	77.37067	5.00774	0.39187	84.11465	6.43112	6.48342	0.00335	0.00218	9.52417	0.12527

Sample 467 MB-1.5 Morrin Bridge Irradiated for 60h

40/39	38/39	37/39	36/39	39Ar (10-12.mol)	% 40Ar*	40Ar*/39Ar	Er.4039	Age(Ma)	Er.An.	Er.Tot.	Cl/K	Er.Cl/K	Ca/K	Er.Ca/K
5.65001	0.01004	0.55364	0.00159	2.53999	92.45713	5.22592	0.03772	133.04394	0.92575	1.58177	-0.00062	0.00029	1.1188	0.01112
4.02487	0.01052	1.63546	0.0006	1.2336	98.81023	3.98167	0.0557	102.24572	1.39066	1.70939	-0.00042	0.00056	3.30752	0.03296
3.81068	0.01144	1.77211	0.00096	3.05804	96.18932	3.67015	0.02184	94.45187	0.54748	1.07076	-0.00018	0.00011	3.58424	0.03556
4.08486	0.01131	1.20277	0.00178	1.42111	89.42839	3.65619	0.07363	94.10171	1.84641	2.06153	-0.00027	0.00064	2.43171	0.02537
4.70775	0.01153	0.84403	0.00223	0.92682	87.40372	4.11726	0.07568	105.62737	1.88585	2.14686	-0.00024	0.00064	1.70597	0.0188
5.13411	0.00932	0.89347	0.00313	0.57413	83.32605	4.2808	0.09162	109.69812	2.27797	2.51434	-0.00089	0.001	1.80598	0.02076
5.82505	0.01316	1.54197	0.00381	0.5471	82.75537	4.8259	0.18125	123.19965	4.47267	4.62849	0.00015	0.00187	3.11825	0.03193
6.63871	0.01578	3.41851	0.00488	0.2767	82.36511	5.48147	0.16849	139.30488	4.12093	4.33352	0.00084	0.0013	6.92243	0.07733
11.14339	0.0371	5.41711	0.01408	0.08756	66.49684	7.43902	0.8467	186.55715	20.17268	20.25039	0.00632	0.00702	10.98541	0.13663
18.79102	-0.04552	7.4249	0.03261	0.04505	51.85008	9.79553	1.72556	241.8453	39.87085	39.93505	-0.01762	0.01339	15.0789	0.268
59.84265	-0.00565	8.87379	0.08148	0.02117	60.93688	36.70073	5.14506	776.01692	88.41484	88.63949	-0.00906	0.01556	18.04032	0.71902

Sample 469 MB-32 Morrin Bridge Irradiated for 60h

40/39	38/39	37/39	36/39	39Ar (10-12.mol)	% 40Ar*	40Ar*/39Ar	Er.4039	Age(Ma)	Er.An.	Er.Tot.	Cl/K	Er.Cl/K	Ca/K	Er.Ca/K
3.74596	0.01003	0.02795	0.00065	2.11037	94.93766	3.5564	0.02223	91.04841	0.5551	1.04713	-0.00058	0.00062	0.05646	0.00125
3.7398	0.011	0.02484	0.00038	6.60019	97.01351	3.62818	0.01669	92.83959	0.41624	0.99605	-0.0003	0.0001	0.05017	0.00094
3.72063	0.01112	0.0174	0.00049	9.12183	96.1177	3.57623	0.00875	91.5436	0.21843	0.91893	-0.00027	0.0001	0.03515	0.00057
3.86118	0.01115	0.01455	0.00081	7.16223	93.82256	3.6227	0.00719	92.70294	0.17927	0.92122	-0.00028	0.00013	0.02938	0.00078
3.99428	0.01124	0.01184	0.00071	7.25036	94.78235	3.78591	0.01026	96.76927	0.25522	0.97615	-0.00025	0.00008	0.02393	0.00068
4.24531	0.01131	0.00906	0.0006	13.77507	95.796	4.06687	0.01283	103.74801	0.318	1.05717	-0.00022	0.00006	0.01829	0.00022
4.42162	0.01099	0.00703	0.00053	8.29201	96.44848	4.26461	0.00973	108.64357	0.24047	1.08144	-0.00031	0.00006	0.0142	0.00018
4.8324	0.00652	0.0168	0.00132	0.70602	91.95479	4.44368	0.08689	113.06549	2.14301	2.40699	-0.00159	0.00111	0.03393	0.00809
7.0028	-0.01246	-0.00236	0.01201	0.04985	49.31399	3.45335	1.69356	88.47399	42.34173	42.35053	-0.0074	0.01124	-0.00476	0.03135
74.30156	0.38902	0.00132	0.21904	0.01114	12.88705	9.57529	5.36476	235.38517	123.63852	123.65822	0.09305	0.03143		

Sample 472 MB-3 Morrin Bridge Irradiated for 60h

40/39	38/39	37/39	36/39	39Ar (10-12.mol)	% 40Ar*	40Ar*/39Ar	Er.4039	Age(Ma)	Er.An.	Er.Tot.	Cl/K	Er.Cl/K	Ca/K	Er.Ca/K
8.19611	0.00995	0.01078	0.00061	2.66878	97.80279	8.01608	0.02949	198.1428	0.69039	1.99947	-0.0006	0.00018	0.02178	0.00224
7.36853	0.01092	0.0117	0.00055	5.89268	97.80493	7.20684	0.01378	179.09906	0.32605	1.73586	-0.00033	0.00009	0.02364	0.00049
6.16729	0.01112	0.00979	0.00036	7.1028	98.27375	6.06087	0.01205	151.78241	0.2895	1.48424	-0.00026	0.00011	0.01977	0.0007
6.22802	0.01136	0.00851	0.0006	5.60375	97.13938	6.0499	0.01558	151.51883	0.3742	1.50071	-0.00021	0.0001	0.01718	0.00108
6.14125	0.0119	0.00898	0.00065	4.25872	96.87861	5.94959	0.01689	149.10768	0.40621	1.48765	-0.00006	0.00017	0.01814	0.00088
6.39198	0.01145	0.00935	0.0006	2.54451	97.20376	6.21328	0.02156	155.43937	0.51687	1.57645	-0.00018	0.00025	0.01889	0.00118
6.55226	0.0107	0.00742	0.00071	4.57742	96.77868	6.34123	0.0133	158.50354	0.31837	1.55044	-0.0004	0.00014	0.015	0.00214
8.14046	0.01123	0.00514	0.00059	4.47681	97.8417	7.9648	0.01609	196.94183	0.37681	1.9034	-0.00024	0.00011	0.01039	0.00081
9.48052	0.01167	0.00536	0.00067	15.1567	97.90129	9.28159	0.02128	227.52649	0.49002	2.19308	-0.00013	0.00004	0.01083	0.00021
10.73236	0.01061	0.00266	0.00078	2.64579	97.8426	10.50084	0.04877	255.39074	1.1059	2.62563	-0.0042	0.00019	0.00537	0.00181
13.61152	0.00523	0.00592	0.00105	0.75217	97.70907	13.29974	0.10914	317.77299	2.39103	3.76909	-0.00193	0.00061	0.01195	0.00835
20.45808	0.00521	0.00791	0.0135	0.14985	80.49903	16.46865	0.46409	385.89235	9.79022	10.38836	-0.00258	0.00391	0.01598	0.02536

Table SIV-T2. U/Pb isotope data and dates for the Upper Bentonite.

		Compositional Parameters							Radiogenic Isotope Ratios								Isotopic Ages						
Sample	Wt. mg	U ppm	Th U	Pb ppm	206Pb* x10-13 mol	mol % 206Pb*	Pb* Pbc	Pbc (pg)	206Pb 204Pb	208Pb 206Pb	207Pb 206Pb	% err	207Pb 235U	% err	206Pb 238U	% err	corr. coef.	207Pb 206Pb	±	207Pb 235U	±	206Pb 238U	±
(a)	(b)	(c)	(d)	(c)	(e)	(e)	(e)	(e)	(f)	(g)	(g)	(h)	(g)	(h)	(g)	(h)		(i)	(h)	(i)	(h)	(i)	(h)
Top Bentonite																							
1R	0.01	63	0.33	0.85	0.2852	0.931	4.0	1.7	272.8	0.1049	0.0474	2.6	0.07082	2.7	0.01084	0.21	0.59	69.29	61.42	69.5	1.8	69.48	0.15
4T	0.01	34	0.56	0.53	0.1554	0.901	2.8	1.4	189.2	0.1779	0.0471	3.4	0.07050	3.6	0.01086	0.27	0.70	52.78	80.48	69.2	2.4	69.65	0.19
4M	0.01	95	0.44	1.20	0.4322	0.961	7.4	1.4	478.4	0.1399	0.0474	1.0	0.07121	1.1	0.01089	0.18	0.41	71.74	24.51	69.9	0.7	69.80	0.12
2T	0.01	46	0.46	0.65	0.2113	0.928	3.9	1.3	257.5	0.1466	0.0474	2.5	0.07139	2.6	0.01092	0.22	0.62	70.27	58.48	70.0	1.8	70.01	0.15
1M	0.01	58	0.53	0.81	0.2649	0.937	4.6	1.5	296.5	0.1697	0.0474	1.3	0.07144	1.4	0.01093	0.17	0.57	70.32	31.70	70.1	1.0	70.06	0.12
2R	0.01	18	0.34	0.35	0.0834	0.817	1.3	1.5	101.9	0.1074	0.0474	3.3	0.07143	3.5	0.01093	0.37	0.51	69.78	78.24	70.1	2.3	70.07	0.26
3M	0.01	106	0.39	1.32	0.4847	0.964	8.0	1.5	522.6	0.1253	0.0475	1.2	0.07164	1.3	0.01094	0.17	0.46	73.99	29.68	70.3	0.9	70.14	0.12
2M	0.01	34	0.46	0.53	0.1550	0.895	2.6	1.5	176.7	0.1476	0.0474	3.7	0.07152	3.9	0.01094	0.34	0.61	69.81	88.76	70.1	2.7	70.16	0.23
5M	0.01	45	0.44	0.66	0.2060	0.916	3.2	1.6	219.5	0.1414	0.0474	2.3	0.07158	2.4	0.01094	0.21	0.61	71.19	54.44	70.2	1.6	70.17	0.15
3T	0.01	18	0.47	0.34	0.0814	0.827	1.4	1.4	107.2	0.1520	0.0474	6.1	0.07182	6.4	0.01098	0.45	0.71	71.20	145.05	70.4	4.4	70.40	0.31
5T	0.01	24	0.34	0.40	0.1084	0.859	1.8	1.5	131.8	0.1099	0.0475	3.6	0.07192	3.8	0.01099	0.30	0.62	72.19	84.87	70.5	2.6	70.47	0.21
5R	0.01	47	0.49	0.69	0.2173	0.922	3.6	1.5	239.0	0.1580	0.0474	0.9	0.07218	1.0	0.01104	0.21	0.35	70.87	21.81	70.8	0.7	70.77	0.15
4R	0.01	28	0.49	0.47	0.1281	0.872	2.0	1.6	142.5	0.1578	0.0478	4.9	0.07276	5.1	0.01105	0.33	0.54	87.58	115.96	71.3	3.5	70.83	0.23
3R	0.01	28	0.48	0.48	0.1283	0.868	2.0	1.6	140.0	0.1540	0.0474	4.5	0.07244	4.7	0.01108	0.36	0.67	70.95	106.10	71.0	3.2	71.01	0.25

(a) Number and letter are labels for fractions composed of single zircon grains or fragments; all fractions annealed and chemically abraded after Mattinson (2005).
(b) Nominal fraction weights estimated from photomicrographic grain dimensions, adjusted for partial dissolution during chemical abrasion.
(c) Nominal U and total Pb concentrations subject to uncertainty in photomicrographic estimation of weight and partial dissolution during chemical abrasion.
(d) Model Th/U ratio calculated from radiogenic 208Pb/206Pb ratio and 207Pb/235U age.
(e) Pb* and Pbc represent radiogenic and common Pb, respectively; mol % 206Pb* with respect to radiogenic, blank and initial common Pb.
(f) Measured ratio corrected for spike and fractionation only.
SEM analyses, based on analysis of NBS-982.
(g) Corrected for fractionation, spike, and common Pb; up to 1 pg of common Pb was assumed to be procedural blank: 206Pb/204Pb = 18.50 ± 0.80%; 207Pb/204Pb = 15.62 ± 0.32%; 208Pb/204Pb = 38.02 ± 0.74% (all uncertainties 1-sigma). Excess over blank was assigned to initial common Pb.
(h) Errors are 2-sigma, propagated using the algorithms of Schmitz and Schoene (2007) and Crowley et al. (2007).
(i) Calculations are based on the decay constants of Jaffey et al. (1971). 206Pb/238U and 207Pb/206Pb ages corrected for initial disequilibrium in 230Th/238U using Th/U = 3.
(j) Corrected for fractionation, spike, and blank Pb only.

Table SIV-T2. U/Pb isotope data and dates for the Lower Bentonite.

U-Th-Pb isotopic data

		Compositional Parameters								Radiogenic Isotope Ratios								Isotopic Ages					
Sample	Wt. mg	U ppm	Th U	Pb ppm	206Pb* x10-13 mol	mol % 206Pb*	Pb* Pbc	Pbc (pg)	206Pb 204Pb	208Pb 206Pb	207Pb 206Pb	% err	207Pb 235U	% err	206Pb 238U	% err	corr. coef.	207Pb 206Pb	±	207Pb 235U	±	206Pb 238U	±
(a)	(b)	(c)	(d)	(c)	(e)	(e)	(e)	(e)	(f)	(g)	(g)	(h)	(g)	(h)	(g)	(h)		(i)	(h)	(i)	(h)	(i)	(h)
MB32																							
1RF	0.01	31	0.48	0.52	0.143	0.876	2.13	1.66	148.75	0.1552	0.0475	3.7	0.0722	3.8	0.0110	0.28	0.56	72.5	87.4	70.82	2.62	70.78	0.20
3MF	0.01	59	0.48	0.87	0.273	0.922	3.59	1.89	238.99	0.1546	0.0474	1.4	0.0722	1.5	0.0110	0.20	0.44	70.9	33.7	70.79	1.02	70.78	0.14
5MF	0.01	61	0.52	0.96	0.280	0.900	2.75	2.55	186.68	0.1654	0.0474	1.0	0.0723	1.1	0.0111	0.24	0.29	70.9	24.4	70.88	0.73	70.88	0.17
2MF	0.01	45	0.62	0.76	0.207	0.884	2.38	2.24	159.59	0.1974	0.0474	2.4	0.0724	2.5	0.0111	0.23	0.51	71.0	57.7	70.94	1.74	70.93	0.16
5RF	0.01	41	0.45	0.67	0.189	0.881	2.20	2.11	154.53	0.1431	0.0474	3.8	0.0724	4.0	0.0111	0.28	0.55	71.1	91.3	70.94	2.73	70.94	0.20
5TF	0.01	47	0.40	0.74	0.219	0.894	2.50	2.12	175.44	0.1286	0.0474	2.2	0.0724	2.4	0.0111	0.21	0.62	71.2	53.4	70.99	1.62	70.99	0.14
1MF	0.01	37	0.65	0.60	0.170	0.894	2.65	1.65	174.14	0.2075	0.0474	4.0	0.0725	4.2	0.0111	0.27	0.61	71.9	95.6	71.04	2.87	71.01	0.19
4MF	0.01	25	0.51	0.47	0.114	0.833	1.52	1.88	110.70	0.1648	0.0474	4.7	0.0726	4.9	0.0111	0.32	0.59	71.0	111.0	71.20	3.34	71.21	0.23
3RF	0.01	26	0.50	0.49	0.119	0.837	1.55	1.91	113.11	0.1589	0.0474	5.0	0.0727	5.2	0.0111	0.32	0.61	71.3	118.4	71.25	3.56	71.25	0.23
2T	0.01	51	0.60	0.76	0.236	0.924	3.81	1.58	245.29	0.1925	0.0474	2.1	0.0729	2.3	0.0111	0.13	0.89	71.4	51.1	71.45	1.56	71.45	0.10
1T	0.01	57	0.37	0.79	0.266	0.933	4.15	1.54	281.19	0.1182	0.0474	2.4	0.0731	2.5	0.0112	0.19	0.54	71.4	57.3	71.59	1.74	71.60	0.14
2R	0.01	65	0.39	0.90	0.301	0.933	4.17	1.74	280.41	0.1236	0.0469	2.9	0.0723	3.0	0.0112	0.24	0.40	45.6	69.5	70.86	2.05	71.61	0.17
2M	0.01	38	0.48	0.60	0.179	0.905	2.91	1.53	197.22	0.1551	0.0474	1.9	0.0731	2.0	0.0112	0.23	0.51	71.6	45.6	71.61	1.40	71.61	0.16
5R	0.01	36	0.37	0.56	0.166	0.893	2.44	1.63	173.30	0.1170	0.0474	2.8	0.0731	2.9	0.0112	0.26	0.58	71.6	66.3	71.64	2.03	71.64	0.18
3T	0.01	36	0.48	0.57	0.169	0.904	2.83	1.48	193.24	0.1543	0.0474	1.1	0.0731	1.2	0.0112	0.22	0.38	71.4	27.1	71.63	0.84	71.64	0.16
3M	0.01	46	0.49	0.72	0.217	0.909	2.99	1.80	201.18	0.1566	0.0475	3.5	0.0732	3.7	0.0112	0.30	0.55	73.0	84.1	71.75	2.56	71.71	0.21
1R	0.01	51	0.47	0.76	0.239	0.921	3.50	1.69	233.74	0.1508	0.0475	2.4	0.0733	2.5	0.0112	0.21	0.61	72.0	56.5	71.84	1.74	71.84	0.15
4M	0.01	75	0.40	1.05	0.349	0.934	4.21	2.01	283.35	0.1282	0.0475	1.1	0.0733	1.1	0.0112	0.18	0.44	72.0	25.6	71.87	0.79	71.87	0.13
4T	0.01	31	0.47	0.52	0.145	0.876	2.15	1.67	151.03	0.1504	0.0475	3.8	0.0734	3.9	0.0112	0.29	0.70	72.0	89.2	71.93	2.74	71.93	0.21
5T	0.01	41	0.42	0.61	0.192	0.914	3.20	1.46	218.16	0.1355	0.0475	1.9	0.0734	2.0	0.0112	0.19	0.61	72.1	46.0	71.95	1.42	71.95	0.14
5M	0.01	29	0.43	0.48	0.135	0.878	2.14	1.54	151.75	0.1382	0.0475	4.2	0.0735	4.4	0.0112	0.30	0.73	74.4	100.1	72.05	3.08	71.98	0.22
1M	0.01	56	0.43	0.79	0.260	0.933	4.16	1.53	277.27	0.1393	0.0475	1.5	0.0735	1.6	0.0112	0.18	0.55	72.0	35.4	72.01	1.10	72.01	0.13
4R	0.01	55	0.41	0.80	0.260	0.929	3.87	1.63	261.30	0.1299	0.0475	1.4	0.0739	1.5	0.0113	0.19	0.50	72.5	33.3	72.36	1.04	72.36	0.13

(a) Number and letter are labels for fractions composed of single zircon grains or fragments; all fractions annealed and chemically abraded after Mattinson (2005).
(b) Nominal fraction weights estimated from photomicrographic grain dimensions, adjusted for partial dissolution during chemical abrasion.
(c) Nominal U and total Pb concentrations subject to uncertainty in photomicrographic estimation of weight and partial dissolution during chemical abrasion.
(d) Model Th/U ratio calculated from radiogenic 208Pb/206Pb ratio and 207Pb/235U age.
(e) Pb* and Pbc represent radiogenic and common Pb, respectively; mol % 206Pb* with respect to radiogenic, blank and initial common Pb.
(f) Measured ratio corrected for spike and fractionation only.
SEM analyses, based on analysis of NBS-982.
(g) Corrected for fractionation, spike, and common Pb; up to 1 pg of common Pb was assumed to be procedural blank: 206Pb/204Pb = 18.50 ± 0.80%; 207Pb/204Pb = 15.62 ± 0.32%; 208Pb/204Pb = 38.02 ± 0.74% (all uncertainties 1-sigma). Excess over blank was assigned to initial common Pb.
(h) Errors are 2-sigma, propagated using the algorithms of Schmitz and Schoene (2007) and Crowley et al. (2007).
(i) Calculations are based on the decay constants of Jaffey et al. (1971). 206Pb/238U and 207Pb/206Pb ages corrected for initial disequilibrium in 230Th/238U using Th/U = 3.
(j) Corrected for fractionation, spike, and blank Pb only.

Appendix D

Chapter VI. Japan

VI.S.2 Japan. Detailed $^{40}Ar/^{39}Ar$ data sets.

Sample Number	Sample	Locality	Mineral	Size Fraction	Age Plat (Ma)	Total Gas Age (Ma)
438	KO-900	Kotanbetsu	Sanidine	125-250	106.6 ± 1.13	125.9 ± 1.89
428	KO-800	Kotanbetsu	Sanidine	125-250	no plateau	83.92 ± 1.2
435	KO-606.5	Kotanbetsu	Sanidine	125-250	no plateau	88.94 ± 0.9
433	KO-606	Kotanbetsu	Sanidine	125-250	no plateau	85.01 ± 1.47
431	KO-605.5	Kotanbetsu	Sanidine	125-250	88.0 ±0.9	88.1 ± 1.1
446	KO-073	Kotanbetsu	Sanidine	125-250	92.62 ± 1.1	94.3 ± 1.8
427	KO-085	Kotanbetsu	Sanidine	125-250	98.9 ±1.1	99.7 ± 1.6
450	SH-029	Shumarinai	Sanidine	125-250	96.9 ± 0.3	102.4 ± 1.9
437	SHO63	Shumarinai	Sanidine	125-250	no plateau	169 ± 2

Sample 438 KO-900 Kotanbetsu Irradiated for 40h

40/39	38/39	37/39	36/39	39Ar (10-12.mol)	% 40Ar*	40Ar*/39Ar	Er.4039	Age(Ma)	Er.An.	Er.Tot.	Cl/K	Er.Cl/K	Ca/K	Er.Ca/K
13.03322	0.01132	2.75096	0.00837	0.71166	82.69777	10.79957	0.07353	175.82833	1.1407	2.02679	-0.00058	0.00056	5.56797	0.07035
7.62636	0.00469	2.45424	0.00151	0.52442	96.68061	7.38627	0.09103	122.08573	1.45489	1.87356	-0.00207	0.00142	4.96635	0.07712
6.56621	0.00734	2.93883	0.00111	0.59824	98.51756	6.48259	0.05726	107.58514	0.92252	1.39349	-0.00131	0.0009	5.94902	0.09933
6.63555	0.00881	2.13745	0.00157	0.77413	95.54741	6.34987	0.03585	105.44566	0.57819	1.17616	-0.00094	0.00102	4.3243	0.06455
6.8458	0.00203	1.86494	0.002	0.62639	93.49804	6.40929	0.12924	106.40391	2.08346	2.32561	-0.00284	0.00105	3.77224	0.06313
7.56893	0.00708	2.02309	0.00313	0.73945	89.88772	6.81346	0.05941	112.90793	0.95426	1.45206	-0.0015	0.00099	4.09261	0.056
10.08921	0.01967	4.517	0.00742	0.2836	81.79943	8.27985	0.13882	136.31061	2.20113	2.56294	0.00181	0.00195	9.15411	0.22991
17.03184	0.02107	7.1364	0.02065	0.19688	67.4853	11.55335	0.30346	187.48384	4.67714	5.00465	0.00155	0.00328	14.48998	0.21677

Sample 428 KO-800 Kotanbetsu Irradiated for 40h

40/39	38/39	37/39	36/39	39Ar (10-12.mol)	% 40Ar*	40Ar*/39Ar	Er.4039	Age(Ma)	Er.An.	Er.Tot.	Cl/K	Er.Cl/K	Ca/K	Er.Ca/K
6.23452	0.0085	14.66242	0.00986	0.32222	71.85828	4.52783	0.1616	74.92882	2.61943	2.72031	-0.00129	0.00159	29.9341	0.29993
4.52068	0.02039	2.24895	0.00097	0.21336	97.55697	4.4174	0.19932	73.13792	3.2341	3.31258	0.00231	0.00474	4.55025	0.06909
5.01147	0.01522	1.64746	0.00071	0.88484	98.39405	4.93685	0.05786	81.54677	0.93451	1.22842	0.00088	0.0006	3.33181	0.03523
5.0389	0.01088	1.16042	0.00055	1.36834	98.59888	4.97246	0.02369	82.12177	0.38242	0.88924	-0.00032	0.00036	2.34602	0.02387
5.19479	0.01037	0.87143	0.0007	1.59403	97.31282	5.05837	0.03567	83.50826	0.57552	0.99858	-0.00048	0.00053	1.76139	0.01899
5.35603	0.01042	1.02259	0.00089	2.26474	96.60901	5.17822	0.03489	85.44083	0.56235	1.00628	-0.00047	0.00031	2.06716	0.02128
5.43252	0.00963	1.626	0.00089	1.67866	97.52104	5.30406	0.04085	87.46757	0.65756	1.07767	-0.00068	0.00038	3.28838	0.03368
5.63999	0.01626	2.34507	0.00161	0.2353	94.85631	5.35894	0.18278	88.35076	2.9409	3.06469	0.00113	0.00587	4.74505	0.1459

Sample 435 KO-606.5 Kotanbetsu Irradiated for 40h

40/39	38/39	37/39	36/39	39Ar (10-12.mol)	% 40Ar*	40Ar*/39Ar	Er.4039	Age(Ma)	Er.An.	Er.Tot.	Cl/K	Er.Cl/K	Ca/K	Er.Ca/K
5.94856	0.01015	1.17221	0.00323	0.82787	85.51564	5.09125	0.05704	85.89631	0.93987	1.25976	-0.00067	0.00057	2.36986	0.03139
5.1471	0.00997	0.14592	0.00013	3.84781	99.45797	5.11973	0.0129	86.36556	0.21256	0.86969	-0.00057	0.00013	0.29478	0.00649
5.17378	0.00854	0.08356	0.00003	4.98271	99.92674	5.1703	0.00924	87.19827	0.15207	0.86472	-0.00096	0.00012	0.16879	0.00447
5.20709	0.00796	0.05888	0.00006	6.71901	99.72432	5.19296	0.01115	87.57123	0.18348	0.87427	-0.00112	0.00007	0.11894	0.00423
5.77496	0.01194	0.05475	0.00018	25.83547	99.15324	5.72629	0.00626	96.32894	0.10258	0.94362	-0.00003	0.00004	0.11059	0.0014
5.42896	0.01176	0.05321	0.00011	7.09299	99.47859	5.40086	0.00919	90.99023	0.151	0.90009	-0.00007	0.00008	0.10748	0.00453
5.44904	0.01193	0.10947	0.00011	4.93332	99.53636	5.4242	0.01024	91.37369	0.16812	0.90671	-0.00002	0.00009	0.22115	0.00418
5.53604	0.01189	0.16229	0.00026	1.1804	98.80604	5.47058	0.03346	92.13531	0.54934	1.05289	-0.00004	0.00066	0.32787	0.01077

Sample 433 KO-606 Kotanbetsu Irradiated for 40h

40/39	38/39	37/39	36/39	39Ar (10-12.mol)	% 40Ar*	40Ar*/39Ar	Er.4039	Age(Ma)	Er.An.	Er.Tot.	Cl/K	Er.Cl/K	Ca/K	Er.Ca/K
6.93833	0.01504	14.96344	0.01085	0.94949	70.86088	4.97012	0.09008	84.03637	1.48817	1.69966	0.00049	0.00064	30.55535	0.30384
5.03907	0.01192	3.32888	0.00171	2.2212	95.16969	4.80719	0.03161	81.34265	0.52302	0.95192	-0.00007	0.00017	6.74048	0.06739
5.46171	0.01354	4.3773	0.00264	0.54712	92.07619	5.04484	0.03854	85.27037	0.63623	1.04807	0.00035	0.00047	8.87009	0.08967
5.72364	0.0121	6.22314	0.00297	0.708	93.28798	5.36351	0.09092	90.52368	1.49663	1.73764	-0.00004	0.0008	12.62732	0.12771
5.66486	0.0194	8.66614	0.00266	0.35422	98.22036	5.59898	0.18604	94.39577	3.05591	3.1913	0.00205	0.0025	17.61552	0.18148
5.70999	0.00616	10.53417	0.00367	0.21681	95.59655	5.50028	0.17847	92.77374	2.93411	3.0703	-0.00167	0.00212	21.44165	0.22527

Sample Number	Sample	Locality	Mineral	Size Fraction	Age Plat (Ma)	Total Gas Age (Ma)
438	KO-900	Kotanbetsu	Sanidine	125-250	106.6 ± 1.13	125.9 ± 1.89
428	KO-800	Kotanbetsu	Sanidine	125-250	no plateau	83.92 ± 1.2
435	KO-606.5	Kotanbetsu	Sanidine	125-250	no plateau	88.94 ± 0.9
433	KO-606	Kotanbetsu	Sanidine	125-250	no plateau	85.01 ± 1.47
431	KO-605.5	Kotanbetsu	Sanidine	125-250	88.0 ±0.9	88.1 ± 1.1
446	KO-073	Kotanbetsu	Sanidine	125-250	92.62 ± 1.1	94.3 ± 1.8
427	KO-085	Kotanbetsu	Sanidine	125-250	98.9 ±1.1	99.7 ± 1.6
450	SH-029	Shumarinai	Sanidine	125-250	96.9 ± 0.3	102.4 ± 1.9
437	SHO63	Shumarinai	Sanidine	125-250	no plateau	169 ± 2

Sample 431	KO-605.5	Kotanbetsu	Irradiated for 40h												
40/39	**38/39**	**37/39**	**36/39**	**39Ar (10-12.mol)**	**% 40Ar***	**40Ar*/39Ar**	**Er.4039**	**Age(Ma)**	**Er.An.**	**Er.Tot.**	**Cl/K**	**Er.Cl/K**	**Ca/K**	**Er.Ca/K**
5.80431	0.01042	1.27248	0.00318	3.53706	85.51962	4.96837	0.01724	83.57118	0.28334	0.86441	-0.00059	0.00026	2.57276	0.02575
5.31519	0.01061	0.62829	0.00046	2.74698	98.35059	5.22988	0.02277	87.8645	0.37342	0.93536	-0.0004	0.00029	1.26973	0.01334
5.33962	0.01199	0.5653	0.0005	1.82251	98.05117	5.23769	0.02414	87.99249	0.39576	0.94561	-0.00002	0.00049	1.14237	0.01339
5.40547	0.01205	0.47367	0.00073	2.05455	96.71505	5.22969	0.02689	87.86132	0.44094	0.96428	-0.00002	0.00045	0.95715	0.00999
5.43746	0.0116	0.42143	0.00081	1.58637	96.19769	5.2323	0.03605	87.90414	0.59106	1.04185	-0.00015	0.00047	0.85155	0.01381
5.45758	0.01433	0.40897	0.00074	2.43633	96.57147	5.27201	0.04688	88.55521	0.76836	1.15636	0.00061	0.00037	0.82637	0.0093
5.45778	0.01334	0.36222	0.00046	3.91876	98.03748	5.35207	0.01888	89.86691	0.30922	0.92959	0.00035	0.00019	0.73188	0.00799
5.47364	0.01095	0.48234	0.00034	1.525	98.86316	5.41329	0.03414	90.86946	0.55882	1.04767	-0.0003	0.00067	0.97467	0.01361
5.57105	0.01321	0.9892	0.00081	1.01779	97.10908	5.41385	0.04367	90.87859	0.7149	1.13867	0.00031	0.0007	1.99961	0.02536
6.17433	0.00348	3.88795	0.00163	0.11941	97.18415	6.01731	0.31209	100.73072	5.08118	5.17476	-0.0024	0.004	7.87571	0.11982
9.33757	0.00307	6.41118	0.01389	0.03175	61.47241	5.76665	2.28578	96.64497	37.29997	37.31183	-0.00312	0.01204	13.01065	0.36038

Sample 446	KO-073	Kotanbetsu	Irradiated for 40h												
40/39	**38/39**	**37/39**	**36/39**	**39Ar (10-12.mol)**	**% 40Ar***	**40Ar*/39Ar**	**Er.4039**	**Age(Ma)**	**Er.An.**	**Er.Tot.**	**Cl/K**	**Er.Cl/K**	**Ca/K**	**Er.Ca/K**
7.70422	0.00998	4.11531	0.00742	0.40316	75.74388	5.85282	0.13244	98.17052	2.16205	2.36377	-0.00089	0.00166	8.33762	0.09077
5.76071	0.01423	2.9267	0.00215	0.493	92.9684	5.36695	0.13232	90.22121	2.16961	2.34129	0.00055	0.00131	5.92442	0.06289
5.447	0.01148	3.56031	0.00079	0.6496	100.86621	5.50831	0.05139	92.53755	0.84165	1.23371	-0.00014	0.00091	7.21031	0.07453
5.50963	0.00907	3.6344	0.00102	0.84439	99.72417	5.50885	0.05277	92.54652	0.86411	1.24921	-0.00081	0.00063	7.36074	0.07333
5.79019	0.0002	5.83492	0.00217	0.36285	96.89568	5.63412	0.09983	94.59666	1.63295	1.87507	-0.00331	0.00071	11.83625	0.12013
6.03805	0.02623	7.28532	0.00301	0.10558	94.80225	5.75439	0.45815	96.56301	7.48605	7.54486	0.00391	0.00484	14.79395	0.18778
6.5831	0.01743	10.43324	0.00547	0.7246	87.98398	5.83592	0.07807	97.8946	1.27464	1.59143	0.00138	0.00122	21.23465	0.21498

Sample 427	KO-085	Kotanbetsu	Irradiated for 40h												
40/39	**38/39**	**37/39**	**36/39**	**39Ar (10-12.mol)**	**% 40Ar***	**40Ar*/39Ar**	**Er.4039**	**Age(Ma)**	**Er.An.**	**Er.Tot.**	**Cl/K**	**Er.Cl/K**	**Ca/K**	**Er.Ca/K**
7.49799	0.01867	2.28105	0.00568	0.34851	80.02888	6.01043	0.03773	97.61144	0.59646	1.12187	0.00159	0.00158	4.6153	0.05369
5.91074	0.01194	5.63056	-0.00008	0.19716	107.93018	6.40544	0.02392	103.8452	0.37679	1.07718	0.00007	0.00268	11.42003	0.12542
5.91244	0.0419	6.5559	0.00028	0.20358	107.34575	6.37685	0.04777	103.39482	0.75282	1.25559	0.0084	0.00282	13.30572	0.14668
5.89324	0.0115	5.07689	0.00011	0.25268	106.27424	6.28598	0.02318	101.96221	0.36563	1.05662	-0.00007	0.00307	10.29294	0.1108
5.92158	0.01252	3.97832	0.00058	0.40569	102.3959	6.08087	0.05492	98.72469	0.86763	1.29451	0.00017	0.00123	8.05929	0.09058
6.08246	0.01308	3.42539	0.00064	0.18067	101.35832	6.18032	0.08414	100.29513	1.32812	1.64793	0.00031	0.00385	6.93639	0.08853
6.10063	0.00369	2.83837	0.00077	0.4285	99.96301	6.11086	0.03498	99.19834	0.55244	1.11212	-0.00231	0.00138	5.74524	0.06347
6.20347	-0.00107	2.57598	0.00158	0.2849	95.76476	5.95178	0.10465	96.68399	1.6553	1.90427	-0.00367	0.00251	5.21315	0.06942
6.24371	0.00194	2.67317	0.00142	0.23985	96.64382	6.0458	0.14129	98.17041	2.23289	2.42873	-0.00283	0.00226	5.41022	0.06449
6.31145	0.00358	3.25842	0.00185	0.31533	95.39272	6.03483	0.05977	97.997	0.94471	1.34248	-0.00239	0.00204	6.59748	0.07481
6.38335	0.01755	4.37675	0.00247	0.25458	93.98276	6.01822	0.1118	97.73448	1.76728	2.00707	0.00148	0.00146	8.86899	0.09532
6.38658	0.01679	5.64581	0.00238	0.3733	95.96772	6.15408	0.08352	99.88082	1.31872	1.63803	0.00129	0.0008	11.45109	0.11751
6.3785	0.02281	7.26772	0.00166	0.15548	101.30802	6.49593	0.13998	105.2703	2.20359	2.42929	0.00302	0.00274	14.75802	0.18462
6.43565	-0.01551	8.731	0.0024	0.15315	99.71005	6.45759	0.20699	104.66666	3.25954	3.41448	-0.00767	0.00557	17.74819	0.18763
39.76121	-0.39074	12.10111	0.32238	0.00064	-137.18327	-55.02514	87.81804	-1283.1963	2984.58335	2984.64193	-0.12927	0.76751	24.65909	26.35223

Sample Number	Sample	Locality	Mineral	Size Fraction	Age Plat (Ma)	Total Gas Age (Ma)
438	KO-900	Kotanbetsu	Sanidine	125-250	106.6 ± 1.13	125.9 ± 1.89
428	KO-800	Kotanbetsu	Sanidine	125-250	no plateau	83.92 ± 1.2
435	KO-606.5	Kotanbetsu	Sanidine	125-250	no plateau	88.94 ± 0.9
433	KO-606	Kotanbetsu	Sanidine	125-250	no plateau	85.01 ± 1.47
431	KO-605.5	Kotanbetsu	Sanidine	125-250	88.0 ±0.9	88.1 ± 1.1
446	KO-073	Kotanbetsu	Sanidine	125-250	92.62 ± 1.1	94.3 ± 1.8
427	KO-085	Kotanbetsu	Sanidine	125-250	98.9 ±1.1	99.7 ± 1.6
450	SH-029	Shumarinai	Sanidine	125-250	96.9 ± 0.3	102.4 ± 1.9
437	SHO63	Shumarinai	Sanidine	125-250	no plateau	169 ± 2

Sample 450	SH-029	Shumarinai	Irradiated for 40h											
40/39	**38/39**	**37/39**	**36/39**	**39Ar (10-12.mol)**	**% 40Ar***	**40Ar*/39Ar**	**Er.4039**	**Age(Ma)**	**Er.An.**	**Er.Tot.**	**Cl/K**	**Er.Cl/K**	**Ca/K**	**Er.Ca/K**
8.04251	0.01183	1.19817	0.00313	0.52067	89.65813	7.21699	0.04073	121.69228	0.66413	1.35126	-0.00019	0.00151	2.42239	0.02489
5.96786	0.00562	1.97073	0.0012	0.67295	96.66785	5.7772	0.08151	98.06127	1.34654	1.65049	-0.0018	0.00115	3.98654	0.0448
5.6884	0.01534	1.86335	0.00086	0.65755	98.1038	5.58804	0.12394	94.93343	2.05117	2.25	0.00091	0.00103	3.76901	0.05023
5.82947	0.01224	1.45726	0.00098	1.24099	97.00557	5.66085	0.05176	96.13813	0.85598	1.26854	0.00004	0.00057	2.94677	0.03187
6.0074	0.01195	1.1361	0.00132	1.21778	95.01583	5.71265	0.01881	96.9946	0.31098	0.99422	-0.00007	0.00061	2.2968	0.02466
6.12354	0.01616	1.54088	0.00198	0.38717	92.44483	5.66719	0.13589	96.24288	2.24724	2.43484	0.00107	0.00279	3.11603	0.046
6.35853	0.01314	2.06737	0.00252	0.22963	90.85891	5.7859	0.17395	98.20503	2.87358	3.02837	0.00021	0.0015	4.18232	0.08588
6.77407	0.00917	2.65931	0.0027	0.40466	91.30425	6.19688	0.29224	104.98134	4.80951	4.91645	-0.00089	0.00083	5.3821	0.06728
13.1581	0.01477	4.21012	0.00957	0.19019	81.04167	10.69597	0.33993	177.54616	5.37379	5.63354	0.00033	0.00485	8.5303	0.12489

Sample 437	SH-063	Shumarinai	Irradiated for 40h											
40/39	**38/39**	**37/39**	**36/39**	**39Ar (10-12.mol)**	**% 40Ar***	**40Ar*/39Ar**	**Er.4039**	**Age(Ma)**	**Er.An.**	**Er.Tot.**	**Cl/K**	**Er.Cl/K**	**Ca/K**	**Er.Ca/K**
7.14506	0.01234	2.59481	0.00252	1.79855	92.45058	6.61802	0.03702	165.31094	0.88358	1.80996	0	0.00039	5.25133	0.05485
6.28432	0.01049	2.56687	0.0012	1.4262	97.57128	6.14305	0.04619	153.93824	1.10949	1.84612	-0.00045	0.00035	5.19467	0.05528
6.5188	0.01603	2.31618	0.00156	0.97628	95.72092	6.25028	0.04462	156.51215	1.07022	1.84196	0.00107	0.00057	4.6865	0.05184
7.46767	0.01381	2.2988	0.00252	0.77201	92.4552	6.91569	0.03331	172.40211	0.79192	1.82498	0.0004	0.00132	4.65127	0.05709
8.53359	0.01681	2.91474	0.00283	0.76454	92.89173	7.94367	0.0665	196.67829	1.55992	2.43012	0.00123	0.00046	5.90016	0.0684
9.61155	0.00511	6.27706	0.0063	0.14124	85.78571	8.28277	0.36593	204.61515	8.54594	8.76213	-0.00216	0.00217	12.73723	0.26182
13.15077	0.04998	12.82441	0.01298	0.11381	78.54035	10.42493	0.58889	253.96242	13.38189	13.58996	0.01012	0.00594	26.14673	0.38676

Abstract

$^{40}Ar/^{39}Ar$ Dating of the Late Cretaceous

As part of the wider European GTS Next project, I propose new constraints on the ages of the Late Cretaceous, derived from a multitude of geochronological techniques, and successful stratigraphic interpretations from Canada and Japan. In the Western Canada Sedimentary Basin, we propose a new constraint on the age of the K/Pg boundary in the Red Deer River section (Alberta, Canada). We were able to cyclostratigraphically tune sediments in a non-marine, fluvial environment utilising high-resolution proxy records suggesting a 11-12 precession related cyclicity. Assuming the $^{40}Ar/^{39}Ar$ method is inter-calibrated with the cyclostratigraphy, the apparent age for C29r suggests that the K/Pg boundary falls between eccentricity maxima and minima, yielding an age of the C29r between 65.89 ± 0.08 and 66.30 ± 0.08 Ma. Assuming that the bundle containing the coal horizon represents a precession cycle, the K/Pg boundary is within the analytical uncertainty of the youngest zircon population achieving a revised age for the K/Pg boundary as 65.75 ± 0.06 Ma.

The Campanian - Maastrichtian boundary is preserved in the sedimentary succession of the Horseshoe Canyon Formation and has been placed ~8 m below Coal nr. 10. Cyclostratigraphic studies show that the formation of these depositional sequences (alternations) of all scales are influenced directly by sea-level changes due to precession but more dominated by eccentricity cycles proved in the cyclostratigraphic framework and is mainly controlled by sand horizons, which have been related by autocyclicity in a dynamic sedimentary setting. Our work shows that the Campanian - Maastrichtian boundary in the Western Canada Sedimentary Basin coincides with ~2.5 eccentricity cycles above the youngest zircon age population at the bottom of the section and ~4.9 Myr before the Cretaceous - Palaeogene boundary (K/Pg), and thus corresponds to an absolute age of 70.65 ± 0.09 Ma producing an ~1.4 Myr younger age than recent published ages.

Finally, using advances with terrestrial carbon isotope and planktonic foraminifera records within central Hokkaido, Northwest Pacific, sections from the Cretaceous Yezo group were correlated to that of European and North American counterparts. Datable ash layers throughout the Kotanbetsu and Shumarinai section were analysed using both $^{40}Ar/^{39}Ar$ and U-Pb methods. We successfully dated two ash tuff layers falling either side of the Turonian - Coniacian boundary, yielding an age range for the boundary between 89.31 ± 0.11 Ma and 89.57 ± 0.11 Ma or a boundary age of 89.44 ± 0.24 Ma. Combining these U-Pb ages with recent published ages we are able to reduce the age limit once more and propose an age for the Turonian - Coniacian boundary as 89.62 ± 0.04 Ma.

Keywords:

Cretaceous, KT boundary, K/Pg, Argon dating, Ar/Ar dating, U-Pb dating, Uranium Lead dating, Campanian, Maastrichtian, Turonian, Coniacian, Paleomagnetism, Cyclostratigrahy, Geochronology Horseshoe canyon, Alberta, Western Interior Basin, Yezo group, Kotanbetsu, Fish Canyon Tuff, Taylor Creek Rhyolite.

Résumé

Datation $^{40}Ar/^{39}Ar$ du Crétacé Supérieur

Dans le cadre du projet Européen GTS Next, nous avons obtenu des nouvelles contraintes sur l'âge des étages du Crétacé Supérieur à partir de plusieurs techniques de géochronologie et d'interprétations stratigraphiques au Canada et au Japon. Dans le bassin sédimentaire du Western Interior Canada, nous proposons une nouvelle détermination de l'âge de la limite Crétacé - Tertiaire (K/Pg) enregistrée dans la coupe de Red Deer River (Alberta). Il a été possible de calibrer par cyclostratigraphie haute-résolution cette série sédimentaire fluviatile non-marine et d'identifier 11-12 cycles associés à la précession orbitale de la Terre. En considérant la technique $^{40}Ar/^{39}Ar$ intercalibrée avec la cyclostratigraphie, l'âge apparent de la base du chron magnétique C29r suggère que la limite K/Pg se trouve entre un minimum et un maximum de l'excentricité, avec une durée pour C29r de 66.30 ± 0.08 à 65.89 ± 0.08 Ma. En supposant que le cycle contenant le niveau de charbon soit associé à un cycle de précession, l'âge révisé de la limite Crétacé - Tertiaire est donné par la plus jeune des populations de zircon datée par U-Pb à 65.75 ± 0.06 Ma.

La limite Campanien – Maastrichtien est également enregistrée dans ce même bassin canadien, et se trouve à environ 8 m sous le niveau de charbon No. 10 dans la formation de Horseshoe Canyon. L'étude cyclostratigraphique montre que le dépôt de cette séquence sédimentaire est directement influencé par les changements du niveau marin dû à la précession et dominés par l'excentricité Notre travail montre que la position de la limite Campanien – Maastrichtien dans ce bassin sédimentaire du Western Canada est placée à environ 2.5 cycles d'excentricité au dessus d'un niveau de téphra de la base de la coupe dont l'âge U-Pb est donné par la plus jeune population des zircons, et ~4.9 Myr avant la limite Crétacé - Tertiaire. Nous en déduisons un âge absolu de 70.65 ± 0.09 Ma pour la limite Campanien – Maastrichtien, ce qui est ~1.4 Myr plus jeune que les études récemment publiées.

Enfin, à partir des isotopes du carbone et des foraminifères planctoniques enregistrés au centre d'Hokkaido (Pacifique Nord-Ouest), les coupes Crétacé du groupe Yezo ont été corrélée avec les séries européennes et nord-américaines. Plusieurs niveaux de téphra prélevés au sein des coupes de Kotanbetsu et Shumarinai ont été datés par les méthodes $^{40}Ar/^{39}Ar$ and U-Pb. Deux d'entre eux, placés de part et d'autre de la limite Turonien – Coniacien, ont donné des âges de 89.31 ± 0.11 et 89.57 ± 0.11 Ma, ce qui suggère un âge de 89.44 ± 0.24 Ma pour cette limite. En combinant notre résultat avec les âges récemment publiés, nous pouvons proposer un âge de 89.62 ± 0.04 Ma pour la limite Turonien – Coniacien.

Mots-clés :

Crétacé, Crétacé-Tertiaire, Limite K-T, Datation argon, Ar/Ar, Datation U-Pb, datation Uranium-Plomb, Campanien, Maastrichtien, Turonien, Coniacien, Paléomagnétisme, Cyclostratigraphie, Géochronologie, Horseshoe Canyon, Western Interior Basin, Alberta, Yezo Group, Kotanbetsu, Fish Canyon Tuff, Taylor Creek Rhyolite.